High Contrast Coherent Population Trapping Resonances in Cs Vapour Cells with A Simple-Architecture Laser System.

Xiaochi Liu

SPIM

Thèse de Doctorat

école doctorale **sciences pour l'ingénieur et microtechniques**

UFC UNIVERSITÉ DE FRANCHE-COMTÉ

THÈSE présentée par

Xiaochi LIU

pour obtenir le

Grade de Docteur de
l'Université de Franche-Comté

Spécialité : **Sciences Pour L'Ingénieur**

High Contrast Coherent Population Trapping Resonances in Cs Vapour Cells with A Simple-Architecture Laser System

Unité de Recherche :
FEMTO-ST, UMR CNRS 6174

Soutenue le 11 Décembre 2013 devant le Jury :

FRANCOIS VERNOTTE	Président	Professeur, Observatoire de Besançon, Institut UTINAM
NOEL DIMARCQ	Rapporteur	Directeur de Recherche CNRS, LNE-SYRTE, Observatoire de Paris
OLIVIER LLOPIS	Rapporteur	Directeur de Recherche CNRS, LAAS-CNRS, Toulouse
PIERRE WALLER	Examinateur	Ingénieur ESA-ESTEC, Noordwijk, The Netherlands
VINCENT GIORDANO	Examinateur	Directeur de Recherche CNRS, FEMTO-ST, Besançon
RODOLPHE BOUDOT	Examinateur	Chargé de Recherche CNRS, FEMTO-ST, Besançon

High Contrast Coherent Population Trapping Resonances in Cs Vapour Cells with A Simple-Architecture Laser System

Xiaochi Liu

FEMTO-ST, CNRS, Université de Franche-Comté,
26 chemin de l'Epitaphe 25030 Besançon Cedex, France.

December 13, 2013

Acknowledgements

I have performed my PhD thesis work in the Time and Frequency department of FEMTO-ST Institute where I have gained excellent scientific working experiences with many brilliant colleagues. At first, I would like to thank director of the Time and Frequency department and my advisor, Vincent Giordano, who not only have greeted me to the laboratory, and also helped me to prolong my funding until my thesis defense.

I wish to express my thanks to the members of my jury. I want to thank sincerely Noel Dimarcq and Olivier Llopis to accept as the reporters of my thesis. Thanks to François Vernotte who accepted to be the president of the jury. Thanks to Pierre Waller who accepted as the examiner of my thesis. I also want to thank the Region of Franch-Comté, for my thesis funding, I could completed my thesis in this three years.

I want to deeply thank Rodolphe Boudot, my co-advisor, a responsible and respected scientist. Without his knowledge and assistances, I could not carry out our experimental setup and obtain satisfying results. When I met the difficulties, he could always give illuminating opinions and helped me to solve the problems. It is such a great privilege to study and work with him.

I am very grateful to Jean-Marc Mérolla, a researcher in the Optics department of FEMTO-ST. He worked with us to develop some important optical components of our experiments. Thanks for his help, many experiments can be carried out.

I truly appreciated Emeric de Clercq and Stéphane Guérandel, serious scientists of CPT atomic clock in Systèmes de Référence Temps Espace of l'Observatore de Paris (SYRTE). They collaborated with us on the development of a laser system for the detection of CPT resonance in continuous wave regime and pulsed regime. Emeric helped us a lot on analysis of the theory of our experiments. Stéphane wrote the key LabVIEW programs for controlling our experimental components, which is very important for us to detect the expected results.

Thanks to Philippe Abbé and Cyrus Rocher for their work of mechanical structures and electric circuits of our experiment setups.

I am very glad to join our research group which is full of sympathetic people, such as Yann Kersale, Jacques Millo, Clément Lacroute, Eric Kroemer, Pierre-yves Bourgeois, Serge Grop and Benoît Dubois. Their passions make me get use to the new environment as quickly as possible.

I also want to thank Nicolas Ratier, maître de conférences de l'ENSMM, who shared the same office with me for 3 years, and thanks for his encouragements for me.

I am grateful to Chinese colleagues in our laboratory, Xin Xu, Ning Tan, Jie Zhang and Tinjian Luo. We have lunched together almost everyday, and we had lots of fun during our lunch time.

I also want to thank my dearest friends, Jun Li, Zhengnan Guo and Qiong Nie, who have helped me to get through a hard time in my life.

Finally, I want to thank my parents, Chi Zhang and Liheng Liu. Nothing I could accomplished would have been possible without them.

Contents

1 Introduction **6**

2 Basics on atomic clocks **9**

2.1 Atomic clock principle 9

2.2 Characterization of atomic clocks 11

2.2.1 Basics 11

2.2.2 Frequency instabilities in the time domain 11

2.2.3 Instabilities in the frequency domain 13

2.2.4 Inter-domains transition 14

2.3 Frequency stability of an atomic clock 17

2.4 Atomic clocks applications 18

2.4.1 Ultimate performances 18

2.4.2 Compact and embedded systems 18

2.5 Overview of compact atomic clocks 21

2.5.1 Cs beam atomic clock 21

2.5.2 Double-resonance Rb vapor cell clocks 23

2.5.3 CPT clocks 30

2.5.4 Cold atom compact clocks 41

2.5.5 Trapped ion clocks 47

2.5.6 Resume of compact atomic clocks 51

3 CPT Physics **52**

3.1 Three energy level Λ-system 52

3.2 Frequency stability performances: a first approach 54

3.3 CPT resonance linewidth 55

3.4 CPT resonance signal height 58

3.5 Frequency shifts 61

3.5.1 Zeeman shift . . . 61
3.5.2 Buffer gas collisional shift . . . 62
3.5.3 Light shift . . . 64
3.6 Optimized CPT pumping schemes . . . 68
3.6.1 Overview . . . 68
3.6.2 Theoretical analysis of push-pull optical pumping . . . 70
3.6.3 Absorption . . . 75
3.7 Ramsey interference . . . 76

4 Experimental Setup **79**
4.1 System architecture . . . 79
4.2 894.6 nm frequency-stabilized DFB laser . . . 79
4.2.1 Saturated absorption setup . . . 81
4.2.2 Characterization of the laser system . . . 82
4.3 Electro-optic modulator (EOM) . . . 86
4.3.1 Phase modulator . . . 86
4.3.2 Intensity Mach-Zehnder modulator . . . 87
4.3.3 Choice of the EOM . . . 90
4.3.4 MZ EOM Stabilization . . . 93
4.3.5 Laser Power Stabilization . . . 98
4.4 4.596 GHz Frequency Synthesizers . . . 100
4.5 Michelson system . . . 103
4.6 Physics Package . . . 106

5 Continuous and Ramsey spectroscopy with push-pull optical pumping **111**
5.1 CPT spectroscopy with PPOP in CW regime . . . 111
5.1.1 Zeeman Spectrum : PPOP versus circular polarization . . . 111
5.1.2 Impact of the mirror position . . . 115

5.1.3 Impact of the laser intensity . . . 116
5.1.4 Impact of the laser beam diameter . . . 121
5.2 Detection of CPT Ramsey fringes . . . 122
5.2.1 Experimental setup . . . 122
5.2.2 Pulsed interaction with a MZ EOM . . . 123
5.2.3 Detection and preliminary characterization of CPT Ramsey fringes . . . 125

6 Annex Works **129**

6.1 Dual-frequency and dual-polarization modulated laser system at 1.5 μm . . . 130
6.1.1 1550 nm DFB laser source . . . 132
6.1.2 Dual Phase Shift Key demodulator (DPSK) . . . 135
6.1.3 Laser system at 1550 nm . . . 138
6.1.4 Conclusion . . . 138
6.2 A high-performance frequency stability compact clock based on a Cs-Ne microcell . . . 140
6.2.1 Experimental setup . . . 140
6.2.2 Experimental investigations and results . . . 141
6.3 Effects of getters on hermetically sealed micromachined Cs-Ne cells for atomic clocks . . . 144
6.3.1 Introduction . . . 144
6.3.2 Micro Cs vapor cells . . . 144
6.3.3 Residual gas analysis . . . 147
6.3.4 CPT spectroscopy . . . 148
6.3.5 Conclusion . . . 150

7 Conclusion **152**

1 Introduction

Atomic clocks are known to be the most performing time and frequency references. Their basic goal, based on the Bohr's law, is to obtain a local oscillator (LO) signal that indicates an interval of time that is as perfect in its duration as the fundamental separation of the energy levels of an atom specie. Atomic clocks are of fundamental importance in a wide number of applications from fundamental research and the probe of fundamental physic constants [1] [2] to civil, industry or military applications with telecommunication systems, navigation and positioning systems and space explorations [3] [4].

Impressive improvements in timing precision have been realized since the demonstration of the first Cs beam clock developed in NPL by Essen and Parry [5]. The pioneering work of Rabi [6] was improved and updated thanks to revolutionizing concepts such as the separated oscillatory fields spectroscopy technique proposed by Ramsey [7], optical pumping [8], laser cooling [9] and trapping techniques or the advent of optical frequency combs [10] [11] that allowed to accelerate greatly the development and characterization of up-to-date state-of-the-art optical clocks [2] [12] [13] [14] [15] [16].

In parallel to the development of these ultimate performance metrology clocks, more and more accommodate applications require clocks with limited volume, power consumption and not extreme but nevertheless excellent frequency stability performances. For embedded and portable applications, the Defense Advanced Research Projects Agency (DARPA) project referred to as CSAC (Chip-Scale Atomic Clock), which ran during the 2000's was very successful and conducted to the development of a frequency standard on a chip, taking up 15 cm^3, using 30 mW of power, and exhibiting 10^{-11} frequency stability at one hour or even one day integration time [17]. CSACs are now commercially available [18]. Different projects in Europe were led in this frame too [19] [20]. The more recent Integrated Micro Primary Atomic Clock Technology (IMPACT) project (also a DARPA-funded project) has a greater focus on long-term stability. The volume and power requirements are slightly relaxed compared to the CSAC project, but the goal is to create a standard that has nearly the same stability as a cesium beam clock for strongly reduced volume and power [21]. The short term frequency stability of clocks developed in these projects remain modest, in the order of a few 10^{-11} at 1 s integration time. Better performances, at the level of 10^{-12} to 10^{-13} at 1 s, while keeping a modest volume of a few liters, are required in several fields such as telecommunications and satellite radio-navigation. In this domain, a valid alternative is represented by vapor cell clocks, well-known through commercially-available double-resonance Rb clocks [22], that were studied and developed in several research laboratories. These secondary frequency standards are based on cell technology that is well-established, reliable and widely exploited. Recently, due to better performing laser sources and innovative techniques to prepare and detect the atoms, several cell-based prototypes exhibiting unprecedented frequency stability have been developed [23] [24]. For the same category of applications, the pulsed Cs vapor cell clock based on Coherent Population Trapping (CPT) proposed by LNE-SYRTE, Observatoire de Paris also demonstrated recently impressive frequency stability performances [25], still at the level of a laboratory-prototype. This clock combines a specific interaction scheme and pulsed Ramsey-like interrogation to allow the detection of high-contrast and narrow Ramsey CPT fringes [26] with reduced sensitivity to light shift phenomena [27]. The main drawback of the latter clock, for potential industrial transfer, is the use of two phase-locked external cavity diode lasers for atomic preparation, interrogation and signal detection. This complexity is not compatible with the development of an industrial clock that requires low volume, simplicity and low-cost.

In that sense, the philosophy and main objective of my thesis was the demonstration of a simple-architecture, compact, single diode laser system for the detection of high-contrast CPT resonances in Cs vapor cells. The optical system we developed simply combines a Distributed Feedback (DFB) diode laser, an intensity Mach-Zehnder electro-optic modulator (MZ EOM) and a Michelson delay-line system. Advanced noise reduction techniques were implemented to make the system operate properly. CPT spectroscopy is done with an optimized CPT pumping scheme, named push-pull optical pumping (PPOP), initially proposed by Jau *et al.* in 2004 [28]. Our system allows the detection of very high contrast CPT resonances, about two orders of magnitude higher than with the use of standard interaction schemes. In the end of my thesis, we proposed an original upgrade of our system by driving the EOM in pulsed regime by making it operate as a fast light switch. This leads to make the atoms interact with a sequence of optical pulse trains and allows the detection of high-contrast and narrow Ramsey CPT fringes, all along with a simple system. While no efforts for integration of our system was done in the frame of my PhD thesis, we're confident that it is compatible to be reduced onto a A3 format optical breadboard. Encouraging results obtained in this thesis have allowed us to participate to an exciting European project, named MClocks, funded by EURAMET, led by Dr. S. Micalizio (INRIM, Italy), that started June, 2013, 1^{st} and that aims to develop compact and high-performance vapor cell microwave atomic clocks. This project will help to further develop, test and validate preliminary studies proposed in this manuscript.

In section 1, basic knowledge and concepts of atomic clocks is reported. Time and frequency metrology tools used to characterize the performances of an atomic clock are reminded. Recipes to respect to improve the frequency stability performances of an atomic clock are given. We also present an overview of compact atomic clocks developed worldwide to introduce the context of our work.

In section 2, we introduce basics of CPT physics. The impact of main experimental parameters on the resonance line (linewidth, signal) is studied in order to know how to optimize the short term frequency stability performances of a CPT atomic clock. Main frequency shifts, including the Zeeman shift, the light shift and the collisional shift, are introduced to point out key points to work to improve the mid and long term performances of a CPT clock. In such a clock, a static magnetic field is applied in order to split Zeeman transitions and to isolate the magnetic field-insensitive clock transition. It is pointed out that low CPT signals are detected in standard CPT clocks because atoms interact with circularly polarized light. This leads numerous atoms to be lost in extreme Zeeman magnetic sublevels with the highest angular momentum m_F. For this purpose, different optimized CPT pumping schemes were proposed in the literature such as lin $\perp$ lin[26] [27], Push-Pull Optical Pumping (PPOP) [28] and lin $\parallel$ lin [29] schemes. In our case, we analyze theoretically in detail the PPOP scheme that is found to be similar to the lin $\perp$ lin scheme under given conditions. A brief review of the Ramsey interference scheme is given to make easier the reading of section 5.

In section 3, we present the experimental setup we developed for the detection of high contrast CPT resonances and Ramsey fringes in Cs vapor cells using the push-pull optical pumping technique. The experimental setup is mainly divided into 4 key parts: a Distributed Feedback (DFB) diode laser tuned on the Cs D_1 line, a pigtailed Mach-Zehnder intensity Electro-Optic Modulator (MZ EOM) driven by a microwave

synthesizer for sidebands generation, a Michelson delay-line system to produce the PPOP scheme and the Cs vapor cell in which CPT interaction takes place. Each block of this setup is described in detail. Several advanced noise reduction techniques are proposed to make the future CPT clock operate properly.

In section 4, continuous (CW) and Ramsey CPT spectroscopy in different Cs vapor cells is reported. High-contrast CPT resonances up to 78 % are reported in the CW regime. The efficiency of the PPOP scheme to pump a maximum number of atoms in the clock transition is demonstrated. The impact of several experimental parameters on the CPT resonance is reported. It is shown that high contrasts are obtained with high laser intensities at the expense of the CPT line broadening, i.e a degradation of the clock short term frequency stability. Thus, we proposed a slightly modified scheme that allows to make the atoms interact with a sequence of optical pulse trains separated by a time T where atoms evolve freely. Preliminary studies demonstrate the detection of high-contrast and narrow Ramsey fringes.

In section 5, I report different annex works I participated to during my thesis. An all-fibered simple laser system at 1550 nm using a DFB laser, a pigtailed intensity EOM and a dual phase shift key (DPSK) demodulator was proposed at the beginning of my thesis to generate two orthogonally polarized optical sidebands frequency-splitted in the microwave domain. First results are shown. A compact table-top Cs CPT clock based on microfabricated cell with advanced frequency stability performance is reported. These performances are measured to be $3.8 \times 10^{-11}\ \tau^{-1/2}$ at 1 second and well below $10^{-11}\ \tau^{-1/2}$ until 50 000 seconds. Eventually, we characterized microfabricated cells in which are deposited at the wafer-level getters in order to reduce undesired impurities in the cell and to improve the microcell inner atmosphere. The impact of the presence of the getter is evaluated by different techniques including residual gas analysis and CPT spectroscopy.

In section 6 aims to give a conclusion on my work and to present its perspectives.

2 Basics on atomic clocks

2.1 Atomic clock principle

The normalized signal of a perfect clock is shown in Figure 1. We define the period T of the signal in seconds and the frequency $\nu_0 = 1/T$ in Hz, as the number of cycles per second.

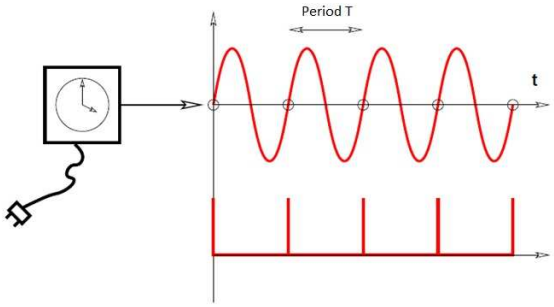

Figure 1: Typical signal of a perfect clock. Period: duration of one cycle; Frequency: number of cycles per second.

The periodic signal sent by an ideal clock should always keep the same frequency. Atomic clocks are the best candidate for ideal clocks because of their stable atomic transition. Atoms consist of a dense central nucleus surrounded by a cloud of negatively charged electrons. These electrons can change from one energy level E_1 to another E_2 ($E_2 > E_1$) by emitting or absorbing a photon whose energy must be exactly equal to the energy difference between the two levels such as (Bohr's law):

$$E_2 - E_1 = h\nu_{at} \tag{1}$$

where h is the Planck constant $(6.62606957(29) \times 10^{-34}$ J. s) and ν_{at} is the atomic transition frequency.

Energy exchange between atoms and light is realized through three different basic processes shown in figure 2: absorption, spontaneous emission and stimulated emission.

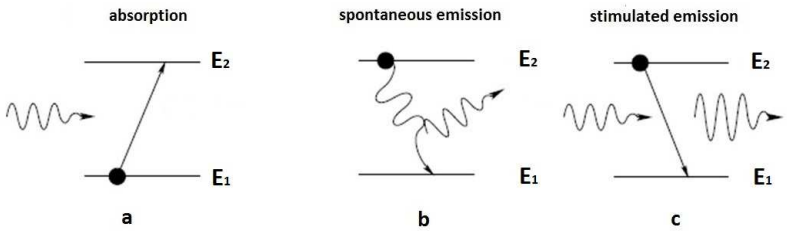

Figure 2: Basic processes for atomic transitions: (a) absorption; (b) spontaneous emission; (c) stimulated emission.

Absorption occurs when an atom in E_1 absorbs a photon whose energy is equal to the energy difference between two energy levels and is excited to E_2. Spontaneous emission occurs when an atom in E_2 decays to

E_1 by emitting a photon equal to the energy difference between both energy levels. Stimulated emission is the process by which an atom in the higher level E_2 drops to the lower level E_1 due to interaction with an incident photon equal to the energy difference $E_2 - E_1$. The photon created in this manner presents phase coherence with the incident photon. Stimulated emission is a basic quantum mechanical process used for the development of lasers or masers.
Since the atomic transition frequency ν_{at} is based on the Bohr's law and is an inherent property of atom, we can build an atomic clock by locking the frequency of a local oscillator to the atomic transition frequency. A simplified scheme of an atomic clock is shown in Figure 3.

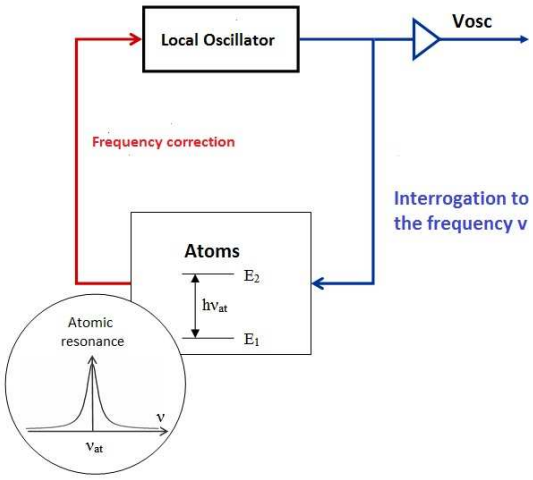

Figure 3: Simplified scheme of an atomic clock. ν_{at}: Atomic transition frequency; ν_{osc}: Frequency of the local oscillator.

In a passive atomic clock, a LO generates a periodic signal with frequency ν_{osc} to probe the atoms. An atomic resonance signal depending on the detuning $\delta_R = \nu_{osc} - \nu_{at}$ is generated. The amplitude of the signal reaches an extremum when the detuning δ_R equals zero, i. e when the frequency of the LO exactly equals the atomic transition frequency. An error signal generated in a feedback loop is then used to lock the frequency of the local oscillator to the atomic transition frequency.

2.2 Characterization of atomic clocks

2.2.1 Basics

Figure 4 shows an example of the time evolution of atomic clock frequency.

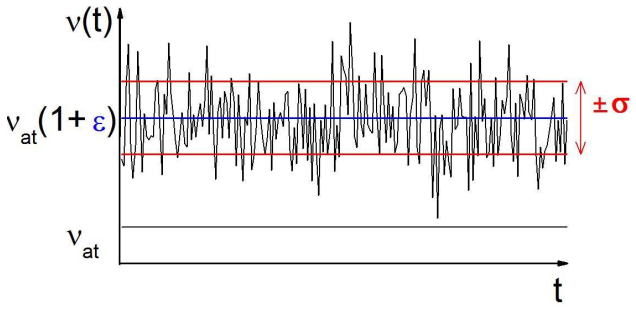

Figure 4: Typical frequency of a local oscillator when locked to an atomic resonance.

The frequency of the clock can be described by:

$$\nu_{osc} = \nu_{at}(1 + \varepsilon + y(t)) \tag{2}$$

where ε is difference between the frequency of local oscillator's signal and the ideal atomic transition frequency choosen and $y(t)$ is the signal relative frequency fluctuations.

Performances of an atomic clock are evaluated by two main parameters: accuracy and relative frequency stability. Accuracy is defined as the uncertainty of the evaluation of ε. This parameter describes how much the actual frequency of an atomic clock deviates from the exact atomic transition frequency, which is 9.192 631 770 GHz for Cs atomic clock. It is usually given by:

$$Accuracy = \frac{\overline{\nu} - \nu_{ref}}{\nu_{ref}} \tag{3}$$

where ν_{ref} presents the standard frequency of the reference source, and $\overline{\nu}$ is the actual averaged frequency of the clock.

2.2.2 Frequency instabilities in the time domain

In the time domain, the clock output signal can be given by:

$$V(t) = V_0 \sin(2\pi\nu_0 t + \varphi(t)) \tag{4}$$

where V_0 is the amplitude of the signal here assumed to be constant, ν_0 is clock signal frequency and $\varphi(t)$ represents phase fluctuations of the clock signal. From Equation 4, we can derive the instantaneous phase of the clock signal $\Phi(t)$:

$$\Phi(t) = 2\pi\nu_0 t + \varphi(t) \tag{5}$$

The instantaneous frequency of the clock is:

$$\nu(t) = \nu_0 + \frac{1}{2\pi}\dot{\varphi}(t) \tag{6}$$

The signal relative frequency fluctuations $y(t)$ can be expressed from the instantaneous frequency $\nu(t)$:

$$y(t) = \frac{\nu(t) - \nu_0}{\nu_0} = \frac{1}{2\pi\nu_0}\dot{\varphi}(t) \tag{7}$$

In the time domain, the frequency stability of a clock can be characterized from Allan deviation $\sigma_y(\tau)$ of the signal relative frequency fluctuations $y(t)$ in a given averaging time τ [30] [31] [32]. To calculate the Allan deviation, we measure the averaged frequencies in a fundamental interval τ. These measurements constitute a statistics result that presents frequency fluctuations of the source. We define the fractional frequency fluctuations averaged in τ, which presents the integration of $y(t) = \nu_0 + \frac{1}{2\pi\nu_0}\frac{d\varphi}{dt}$ between the instants t_k and t_{k+1}:

$$\overline{y}_k = \frac{1}{\tau}\int_{\tau_k}^{\tau_{k+1}} y(t)dt = \frac{\varphi(t_k + \tau) - \varphi(t_k)}{2\pi\nu_0\tau} \tag{8}$$

Allan deviation $\sigma_y(\tau)$, a two-sample deviation, is calculated by:

$$\sigma_y(\tau) = \sqrt{\frac{1}{2}\langle(\overline{y}_{k+1} - \overline{y}_k)^2\rangle} \tag{9}$$

The first advantage of using Allan deviation is that we can compare frequency stability performances of clocks with different frequencies. The slope of the curve on the Allan deviation plot is the signature of a type of noise, resumed on figure 5. Assuming that all experimental parameters are well controlled, the typical Allan deviation slope of an atomic clock is $\tau^{-1/2}$, signature of a white frequency noise.

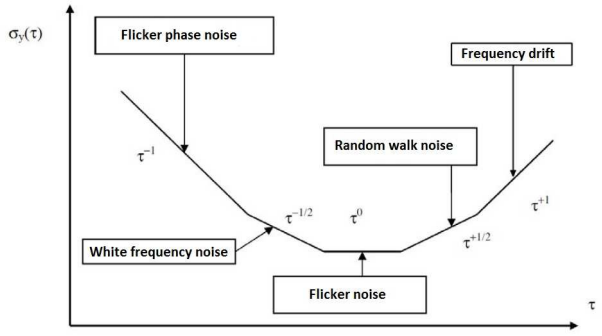

Figure 5: Allan deviation plot of different noises.

Figure 6 shows the basic scheme of frequency stability measurement of a clock. Signals of the source under test and a reference oscillator are mixed to generate a beatnote signal. The beatnote signal is sent to a frequency counter to count the beatnote frequency and to evaluate the relative frequency stability.

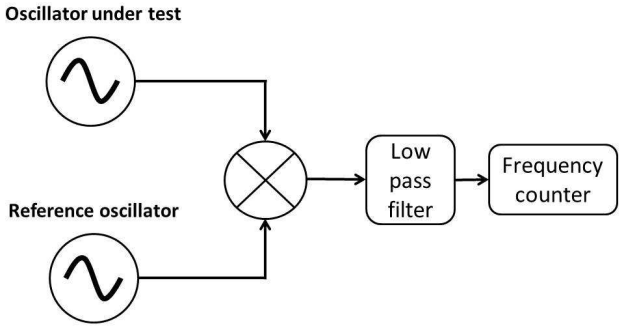

Figure 6: Basic scheme of frequency stability measurement.

2.2.3 Instabilities in the frequency domain

The spectral density of instantaneous frequency fluctuations $S_y(f)$ can be expressed with the spectral density of phase noise $S_\varphi(f)$ (rad^2/Hz or dBrad^2/Hz) as:

$$S_y(f) = \frac{1}{\nu_0^2} S_{\Delta\nu}(f) = \frac{1}{\nu_0^2} f^2 S_\varphi(f) \tag{10}$$

where $S_{\Delta\nu}(f)$ is the spectral density of frequency fluctuations (Hz^2/Hz).

Figure 7 shows the basic measurement scheme of phase noise of an oscillator.

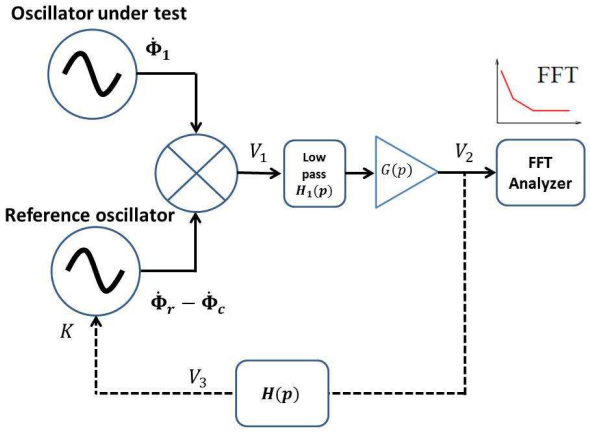

Figure 7: Basic scheme of phase noise measurement.

In this measurement setup, we assume that: $\dot{\Phi}_1(p)$ is the angular frequency fluctuations of the oscillator under test; $\dot{\Phi}_r(p)$ is the angular frequency fluctuations of the reference oscillator; $\dot{\Phi}_c(p)$ is the correction of the fluctuations applied on the reference oscillator; μ (measured typically in V/rad) is the sensitivity of the

mixer, which is used as a phase detector; $H_1(p)$ is the transfer function of the low-pass filter; $G(p)$ is the gain of the amplifier; $H(p)$ is the transfer function of the feedback loop; K is the sensibility of the electronic tuning of the reference oscillator; p is the symbolic variable equals $j2\pi f$ where f is the analyzed frequency.

If the input signals of the mixer is in quadrature, the output signal of the mixer $V_1(p)$ is proportional to the phase fluctuations between the oscillator under test and the reference oscillator. It can be described by:

$$V_1(p) = \frac{\mu}{p}(\dot{\Phi}_1(p) - \dot{\Phi}_r(p) - \dot{\Phi}_c(p)) \tag{11}$$

The low-pass filter is used to remove the carrier signal, $H(p) = 1$ at the low frequency. Then, the output signal of the amplifier is given by:

$$V_2(p) = \frac{\mu G(p)}{p}(\dot{\Phi}_1(p) - \dot{\Phi}_r(p) - \dot{\Phi}_c(p)) \tag{12}$$

At the output of the feedback loop $H(p)$, the correction signal of the fluctuations applied on the reference oscillator is:

$$\dot{\Phi}_c(p) = KV_3(p) = \frac{\mu G(p)H(p)}{p}(\dot{\Phi}_1(p) - \dot{\Phi}_r(p) - \dot{\Phi}_c(p)) \tag{13}$$

From Equation 11, 12 and 13, we can derive that:

$$V_2(p) = \frac{\mu G(p)}{p + \mu KG(p)H(p)}(\dot{\Phi}_1(p) - \dot{\Phi}_r(p)) = \frac{\mu G(p)}{1 + \frac{\mu KG(p)H(p)}{p}}(\dot{\Phi}_1(p) - \dot{\Phi}_r(p)) \tag{14}$$

If the term $\frac{\mu KG(p)H(p)}{p}$ in the Equation 14 is much larger than 1, we can approximate the Equation 14 to:

$$V_2(p) = \frac{\dot{\Phi}_1(p) - \dot{\Phi}_r(p)}{KH(p)} \tag{15}$$

In the other hand, if the gain of the feedback loop is very low, the Equation 14 can be rewritten:

$$V_2(p) = \mu G(p)(\dot{\Phi}_1(p) - \dot{\Phi}_r(p)) \tag{16}$$

Consequently, if the value of G, μ and K are adjusted suitably, we can obtain a output signal of the measurement setup which is proportional to the phase fluctuations. A FFT spectrum analyzer is used to measure the spectral density of phase noise $S_\varphi(f)$.

2.2.4 Inter-domains transition

From power spectral density of frequency noise, we can deduce Allan variance $\sigma_y^2(\tau)$ of frequency stability by:

$$\sigma_y^2(\tau) = 2\int_0^\infty S_y(f) \mid H(f) \mid^2 \frac{\sin^4(\pi f\tau)}{(\pi f\tau)^2} d\nu \tag{17}$$

where $\mid H(f) \mid^2 = \frac{1}{1+(f/f_c)^2}$ presents the transfer function of low pass filter in the measurement setup.

$S_y(f)$ can be described by the power law:

$$S_y(f) = \sum_{\alpha=-2}^{2} h_\alpha f^\alpha \tag{18}$$

$S_\varphi(f)$ can be described by the power law:

$$S_\varphi(f) = \sum_{\alpha=-4}^{0} b_\alpha f^\alpha \tag{19}$$

In a phase noise logarithmic plot, a term f^α is a straight line of slope α. Figure 8 shows the relation between power spectral density of phase noise $S_\varphi(f)$, power spectral density of frequency noise $S_y(f)$ and Allan variance $\sigma_y^2(\tau)$ of frequency stability [33].

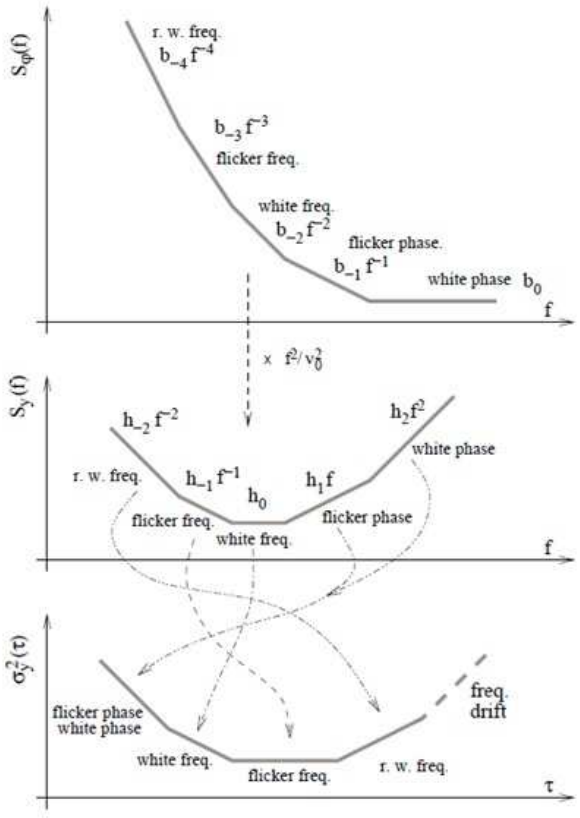

Figure 8: Power laws for spectra and Allan variance.

Table 1 resumes the relations between $S_\varphi(f)$, $S_y(f)$ and $\sigma_y^2(\tau)$.

Table 1: Relation of power spectral densities and Allan variance.

noise type	$S_\varphi(f)$	$S_y(f)$	$\sigma_y^2(\tau)$
white phase noise φ	b_0	$h_2 f^2$	$\propto \tau^{-2}$
flicker phase noise φ	$b_{-1} f^{-1}$	$h_1 f$	$\propto \tau^{-2}$
white frequency noise f	$b_{-2} f^{-2}$	h_0	$\frac{1}{2} h_0 \tau^{-1}$
flicker frequency noise f	$b_{-3} f^{-3}$	$h_{-1} f^{-1}$	$2\ln(2) h_{-1}$
random walk of frequency f	$b_{-4} f^{-4}$	$h_{-2} f^{-2}$	$\frac{4\pi^2}{6} h_{-2} \tau$

2.3 Frequency stability of an atomic clock

Figure 9 shows an example of an atomic resonance signal obtained with CPT in a Cs cell.

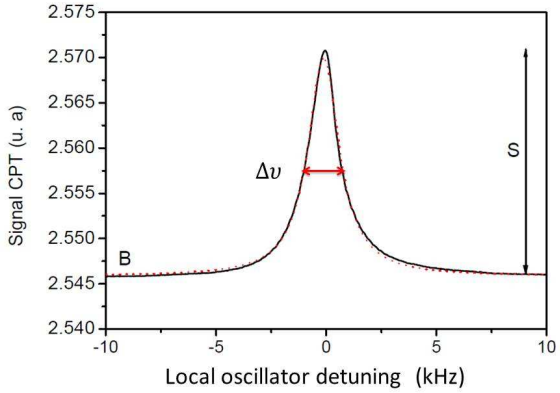

Figure 9: Example of an atomic resonance signal. The LO detuning is defined as the frequency difference between the atomic transition frequency and the local oscillator frequency.

The short term frequency stability $\sigma_y(\tau)$ of an atomic clock is given by:

$$\sigma_y(\tau) = K\frac{\Delta\nu}{\nu_0}\frac{1}{SNR}\tau^{-1/2} \tag{20}$$

where $K \simeq 1-2$ is a constant that depends on the modulation detection scheme, $\Delta\nu$ is the full width at half maximum (FWHM) of the atomic resonance signal, ν_0 is the clock frequency, SNR is the clock resonance signal-to-noise ratio in a 1 Hz bandwidth and τ is the averaging time of the measurement. We define the atomic Q-factor Q as:

$$Q = \frac{\nu_0}{\Delta\nu} \tag{21}$$

The contrast C of the resonance is defined as:

$$C = \frac{S}{y_0} \tag{22}$$

To improve the short term frequency stability performance, different methods can be considered. First of all, increasing the atomic transition frequency ν_0 is an effective way to improve the short term frequency stability. This idea has allowed to develop optical clocks that surpass greatly performance of best microwave atomic clocks [2] [12] [13] [14] [15] [16]. The stability can also be improved by decreasing the resonance linewidth $\Delta\nu$. This means that it is required to maximize the atom-field interaction time. In general, for atomic clocks based on alkali vapor cells (main study in this manuscript), there are two main methods for this purpose. The first one is to fill the cell with a pressure of buffer gas (Ne, Ar, N_2,..) in order to operate in the Dicke regime [34]. In this case, atoms experience multiple collisions against buffer gas atoms or molecules and the time for alkali atoms to reach the cell walls is increased. The second one consists to deposit an anti-relaxation coating on the cell inner windows to increase the coherence lifetime of atoms [35] [36]. Atoms experience multiple bounds against the cell walls before complete spin-depolarization. Additionally, the Ramsey interference scheme is a method widely used to narrow the resonance signal of atomic clocks [7].

This technique will be detailed later in the manuscript. Ultimately, laser-cooled atoms are the most efficient technique to slow down atoms and to allow the detection of very narrow resonances. Eventually, reaching a good short term frequency stability requires to detect the signal with the highest signal-to-noise ratio. This implies to concentrate the maximum number of atoms into the clock transition levels and to ensure relevant efforts to reduce the different noise sources of the system such as laser relative intensity noise (RIN), the laser frequency noise, the local oscillator phase noise, the detection noise, etc.
For long integration times, the clock frequency stability is degraded by the effect of environmental perturbations or/and internal components aging. Main contributions in vapor cell clocks are the Zeeman shift, the light shift and the collisional frequency shift. These frequency shifts will be detailed in the section devoted to CPT physics.

2.4 Atomic clocks applications

Atomic clocks are widely required by any application that needs a precise and stable clock. Different types of atomic clocks were proposed and produced. Each type of atomic clock has its own performance and volume, determining its field of application. We only focus in the manuscript on compact microwave atomic clocks.

2.4.1 Ultimate performances

The International System of Units (SI) strictly and precisely defines the second as the duration of 9 192 631 770 periods of the radiation corresponding to the transition between the two hyperfine levels of the ground state of ^{133}Cs atom assumed at rest and in a null magnetic field. The second is a key unit in metrology and some other basic units are defined from the second definition. For example, the definition of the meter is the distance traveled by light in vacuum in $\frac{1}{299\,792\,458}$ second. Consequently, devices that can generate and measure the second with high accuracy and frequency stability are very important. Besides the exact definition of the second, we need an universal time reference. Atomic clocks are used world wide to build International Atomic Time (TAI) and Coordinated Universal Time (UTC). The TAI is a high precision atomic coordinate time standard based on the notional passage of proper time on Earth's geoid. The UTC is the primary time standard from which the world regulates clocks and time. Fundamental physics, atomic and molecular physics researches, measurements of physical constants like Rydberg constant R_∞, hyperfine structure constant α, time variation of fundamental constants, properties of atoms and molecules, absolute frequency measurements or gravity measurements, also require ultra-precise measurement of frequencies and time.

2.4.2 Compact and embedded systems

Global navigation satellite system Global Navigation Satellite System (GNSS) such as GPS, GLONASS, BeiDou and GALILEO use atomic clocks to measure the signal propagation time $\Delta\tau$ between satellites and receivers. The propagation time $\Delta\tau$ allows to obtain a distance D between the satellite and the receiver. If the instant of signal emission and the spatial coordinates of the emission source are known, we can fix the position of the source by measuring the propagating time $\Delta\tau$. Uncertainty of 1 ns leads to an uncertainty of 30 cm positioning. A nominal GNSS is composed by 24 satellites orbiting the Earth to send the signal, ground tracking stations and users' receivers. The precision of positioning may be disturbed by two

Table 2: Atomic clocks embedded in GPS and GALILEO.

Performances	GPS	GALILEO	
Type of clocks	Rb II/IIA	RAFS	PHM
Embedded quantity	2	2	2
Frequency stability at 1 s	7×10^{-12}	3×10^{-12}	7×10^{-13}
Flicker	1×10^{-14}	3×10^{-12}	6×10^{-15}
Drift per day	$4 \sim 10 \times 10^{-14}$	2×10^{-13}	5×10^{-15}
Volume	/	2.4 L	28 L
Weight	6 kg	3.2 kg	18 kg

reasons: time fluctuations of signal propagating through atmosphere and desynchronization of time bases to transmit and receive. The time bases are given by atomic clocks. The time references of these systems are generated by the ground tracking stations in the Earth. The embedded atomic clocks in the satellites have worse performances than atomic clocks in the ground tracking stations because of limitations of volume and power consumptions. For this purpose, embedded atomic clocks must be calibrated when the satellites pass over the ground tracking stations every day. Today, the clocks installed in the GNSS systems (GPS or GALILEO) are Rb Atomic Frequency Standard (RAFS), Cs beam clocks and Passive Hydrogen Maser (PHM). Typical performances of these clocks are given in Table 2. Although the performances of the clocks embedded in GNSS can satisfy current requirements, developing better performance atomic clocks are a great benefit for next generations of satellites. Indeed, the proliferation of systems, the reduction of ionospheric contribution and the weight becomes more important for navigation systems. Additionally, better mid-long term frequency stability allows to relax the constraints of periodic calibration of ground tracking stations. Reliability and autonomy of navigation systems can be improved by using better performance atomic clocks. GNSS receiver today uses a quartz oscillator to synchronize with satellite's signal, the precision of positioning can be greatly improved if quartz oscillator is replaced by CSAC.

Deep space network Deep Space Network (DSN) is a world wide network of large antennas and communication facilities that supports interplanetary spacecraft missions and radar astronomy observations of the solar system and the universe. The network is constituted by three stations in Goldstone, Madrid and Canberra to track the path of probe 24h/24h. These stations are synchronized by atomic clocks. Usually, navigation of probe is realized by measuring Doppler velocity with a two-way link. This two-way link measures Doppler shift between the signal sent by antenna and the signal resent by probe with a transponder. Typically, these two-way links should be maintained for 7 to 8 hours to navigation of one probe. Atomic clocks that have frequency stability performance better than 10^{-14} for some days allows a precise enough navigation working with one way link from probe to antenna [4]. Such a configuration allows to track simultaneously a number of probes that orbit around the same plant [37].

Very large baseline interferometry Very Large Baseline Interferometry (VLBI) is a kind of astronomical interferometry used in radio astronomy. The VLBI can detect signal from an astronomical radio source by multiple radio telescopes in the Earth, then the distances between these radio telescopes can be calculated by the time difference between the detection of signal. By combining all the observations of these telescopes, we can emulate a telescope with a size equal to the maximum separation between these telescopes. Atomic

clocks in such a system are used to synchronize all the separate telescopes. The frequency stability requirements of the VLBI is about $10^{-13}\ \tau^{-1/2}$ that is currently satisfied by hydrogen maser. Today, compact atomic clocks exhibit short term frequency stability performance similar to hydrogen maser but with smaller volume. Consequently, developments of high performance, low power consumption compact atomic clocks could be meaningful for improving reliability and autonomy of VLBI.

Telecommunications With the development of telecommunication systems, data transmission becomes more and more important. To efficiently transfer the data and avoid the errors, high accuracy synchronization of different points of transfer is required. A high performance atomic clock embedded in every emitter and receiver can greatly improve the synchronization of telecommunication system. Table 3 shows atomic clocks performances required by different applications.

Table 3: Applications of atomic clocks and their requirements

Application	Short term frequency stability	Long term frequency stability	Constraints
Metrology	$10^{-13}\,\tau^{-1/2}$	10^{-16}	Laboratory-size
Fundamental physics	$10^{-13}\,\tau^{-1/2}$	10^{-16}	Laboratory-size
GNSS	$10^{-12}\,\tau^{-1/2}$	10^{-14}	Compact system
DSN	$10^{-12}\,\tau^{-1/2}$	$\leq 10^{-14}$	-
VLBI	$10^{-13}\,\tau^{-1/2}$	10^{-15}	-
GNSS receiver	$10^{-11}\,\tau^{-1/2}$	$\leq 10^{-13}$	Miniaturize clocks
Telecommunication	$10^{-11}\,\tau^{-1/2}$	$\leq 10^{-13}$	Miniaturize clocks

2.5 Overview of compact atomic clocks

Today, developments of compact atomic clocks are on the upswing. Compact atomic clocks emphasize compact volume, simple architecture and high performance. Compact atomic clocks are based on different atoms and preparation schemes have different volumes and performances. In the following section, a brief overview of main compact microwave atomic clocks is presented.

2.5.1 Cs beam atomic clock

The Cs beam clock is considered as the original frequency reference to define the duration of one second. According to the method of selection of atoms in clock, Cs beam clocks are divided into two types: Cs beam clocks based on magnetic deflection and based on optical pumping. Figure 10 shows a principle scheme of Cs beam clock based on magnetic deflection. Figure 11 shows a principle scheme of the Cs beam clock based on optical pumping (Jet Pompé Optiquement (JPO) developed by SYRTE).

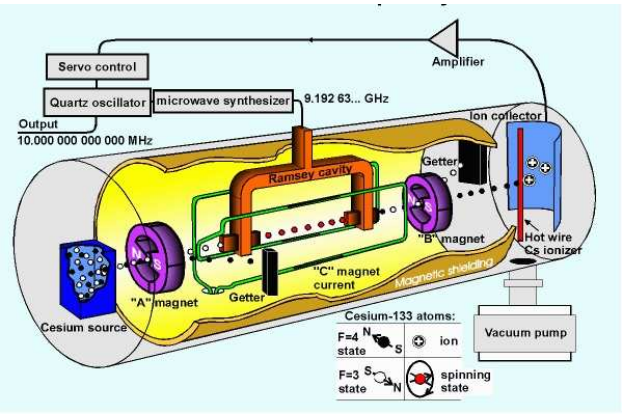

Figure 10: Principle scheme of Cs beam clock based on magnetic deflection. The figure is extracted from NRC website (http://inms-ienm.nrc-cnrc.gc.ca).

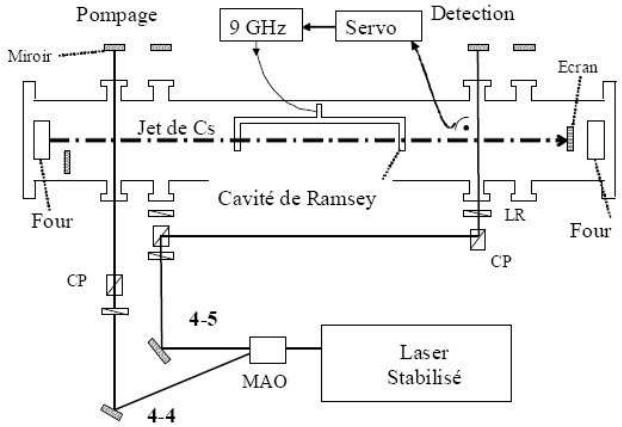

Figure 11: Principle scheme of Cs beam clock based on optical pumping. The figure is extracted from [39].

In a Cs beam clock, Cs atoms are heated to about 100 °C in an oven to generate a Cs beam. Microchannels are used to calibrate the Cs beam. The clock consumes about 1 gramme Cs atoms in one year with a Cs beam jet velocity of 200 m/s and an outflow of 10^{14} atoms/s. After the Cs beam is generated, the Cs atoms in an appropriate state are selected and sent into a resonant cavity. This selection is realized by a magnet (magnetic deflection) or a laser (optical pumping). The magnet selects the atoms by generating an inhomogeneous magnetic field. Atoms in expected state deflect an angle when passing though the magnetic field and are sent into the resonant cavity. Since the Cs atoms into the oven are distributed in 16 different Zeeman sublevels, the expected atoms are only about 1/16 of the total atoms. Magnetic deflection also depends on the atom velocity and magnetic field length. Atoms in the expected state can not enter the resonant cavity appropriate if they are too fast or too slow. This causes the number of atoms sent into resonance cavity is even smaller. Optical pumping technique can avoid this defect. In this case, the deflection angle of atoms is generated by momentum exchange with photons, which is much smaller than the one generated by magnetic deflection. Therefore, the optical pumping can increase number of atoms involved into interaction with microwave compared to the magnetic deflection. With the help of laser pumping, nearly all the atoms can be pumped into one hyperfine ground state. Once selected, atoms are sent in a Ramsey microwave resonant cavity. It is composed by two arms separated by a free-evolution zone whose length fixes the free-evolution time T. At the output of the resonant cavity, a resonance signal is detected by a heating wire (for magnetic deflection) or fluorescence optically. The signal detection is also improved thanks to the use of cycling transitions such as the $S_{1/2}|F = 4\rangle \longrightarrow P_{3/2}|F = 5\rangle$. An atomic resonance signal of the JPO Cs beam clock is shown in Figure 12.

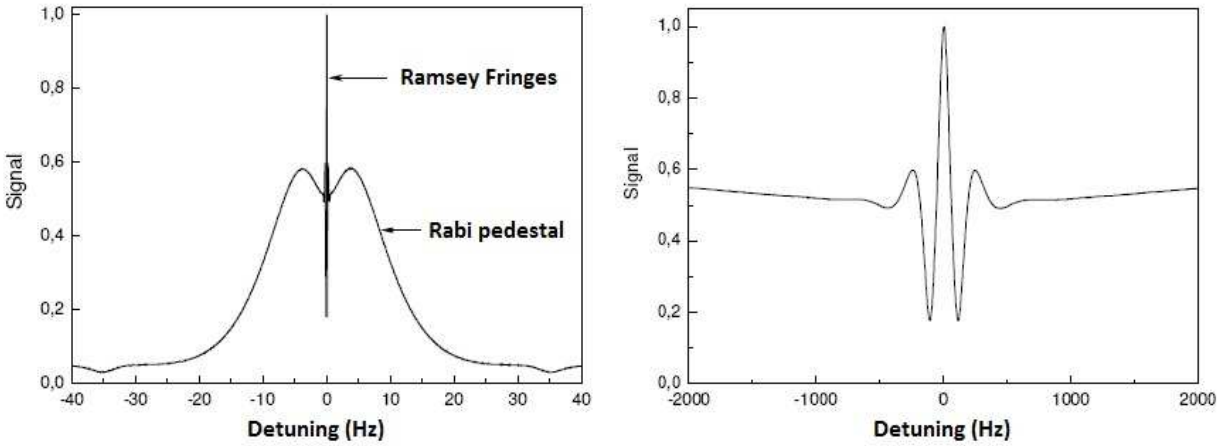

Figure 12: Atomic resonance signal of JPO Cs beam clock. The Rabi pedestal linewidth is 20 kHz, the central Ramsey fringe linewidth is 100 Hz. The figure is extracted from [39].

The JPO clock demonstrated a record of frequency stability of $3.5 \times 10^{-13}\ \tau^{-1/2}$ (Figure 13) and an accuracy of 6×10^{-15} [39].

Some industrial companies have produced commercial Cs beam clock with a reasonable size. Cs beam clocks act as a frequency reference source to calibrate new types of atomic clock in many laboratories. The best commercial Cs beam clock based on magnetic deflection is the 5071A clock developed by Symmetricom (Figure 14). It exhibits a relative frequency stability of $5 \times 10^{-12}\ \tau^{-1/2}$ and accuracy better than 2×10^{-13} with 30 liters volume. Its service life is about 7-8 years limited by the Cs atoms quantity.

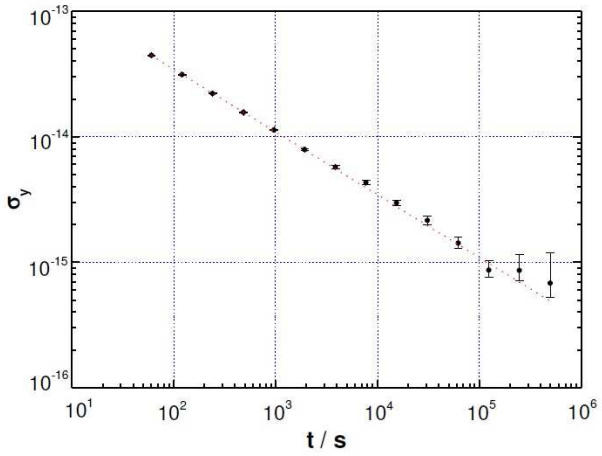

Figure 13: Frequency stability of JPO. The figure is extracted from [38]

Figure 14: Symmetricom 5071A clock Photo.

Up to date, no commercially-available Cs beam clocks based on optical pumping exist. The OSCC project, headed by Thales TED, aims to realize to realize a Cs beam clock using only one laser. This achieves a frequency stability of 3×10^{-12} at 1 second [40].

2.5.2 Double-resonance Rb vapor cell clocks

Continuous regime Rb clock The double-resonance Rb vapor cell clock is widely used in commercial and portable applications which require high accuracy and stability such as GPS, radar or VLBI. In such a clock, the core heart is a glass cell that contains alkali vapor and buffer gas to operate in the Dicke regime [34].
Figure 15 shows a principle scheme of the RAFS.

In such a clock, a spectral lamp emits a large spectrum that contains D_1 (795 nm) and D_2 (780 nm) lines of Rb. A hyperfine filter blocks the optical lines that can be resonant with the $|F = 2\rangle$ energy level of ^{87}Rb. The filtered optical field is sent into a cell containing Rb atoms vapor and buffer gas and then absorbed by the $|F = 1\rangle$ energy level of Rb atoms. The Rb atoms in the cell are excited by the optical field and relax

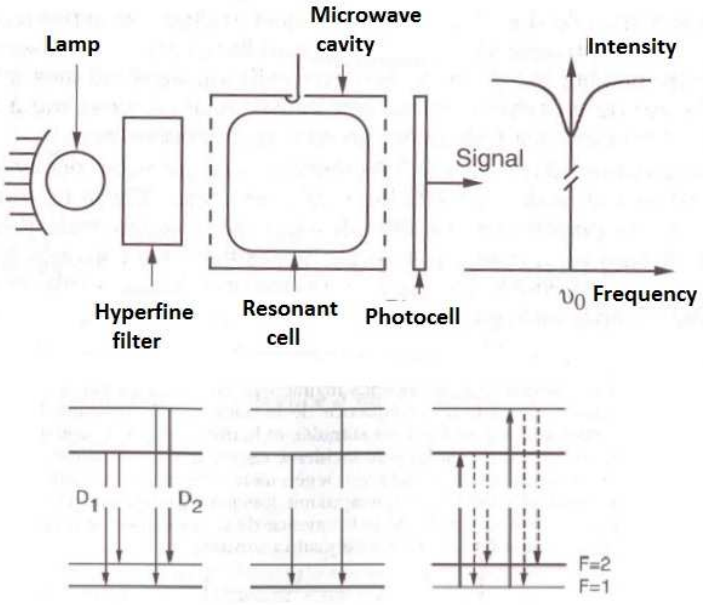

Figure 15: Principle scheme of a lamp-based RAFS.

separately until there is not any atom anymore in the $|F = 1\rangle$ energy level. When all the atoms are pumped into the $|F = 2\rangle$ energy level, the atoms vapor do not absorb the filtered optical field any more. Therefore, the transparency of the Rb vapor reaches a maximum and a photodiode at the output of cell can detect the light flux signal. If a microwave field resonant with the atoms radiates the vapor cell continuously, the atoms will repopulate the $|F = 1\rangle$ energy level and the absorption rate of Rb atoms will increase. If the spectral lamp is replaced by a laser source, the absorption rate of Rb atoms is even higher. The resonance signals detected by a RAFS have a typical linewidth of 1 kHz and 0.5 % contrast with spectral lamp and up to 25 % contrast with laser source [41] [42].

Atomic clocks based on Rb vapor cell were first commercially produced in the 1960s by the Perkin-Elmer company. These clocks played an important role in the compact navigation system, such as GPS and Deep Space Navigation (DSN) because of their compact volume and excellent stability performance. According to the performances, the best commercial RAFS is the RFS-IIF fabricated by the Perkin-Elmer with frequency stability of $2 \times 10^{-12}\ \tau^{-1/2}$ with a flicker level to 5×10^{-15} and drift to 2×10^{-13} for one day integration time. The RAFS developed by Dupuis *et al.,* has short term frequency stability performance of $10^{-12}\ \tau^{-1/2}$ to a 2×10^{-15} flicker level, and a drift to 2×10^{-14} for one day integration time [43]. The RAFS clock applied on the GALILEO project has frequency stability of $3 \times 10^{-12}\ \tau^{-1/2}$ with a level to 10^{-14} and then drift to 2×10^{-13} for one day [44]. The Rb Atomic Frequency Standard (RAFS) atomic clock fabricated by Symmetricom has 1 L level volume with a frequency stability of $2.5 \times 10^{-12}\ \tau^{-1/2}$ at 1 second [45]. These commercial Rb clocks usually use a Rb spectral lamp as a pumping source.

The performance of a Rb atomic clock can be improved by at least one order of magnitude by replacing spectral lamp with a diode laser. The best performance laboratory-prototype continuous regime RAFS was demonstrated by C. Stefanucci *et al.* in Université de Neuchatel [46]. Figure 16 shows the resonance signal of this RAFS. A compact magnetron cavity (Volume = 0.044 dm^3) operating with a TE_{011}-like mode is used in this RAFS. This cavity ensures an excellent microwave magnetic field homogeneity and the compactness of the whole system. This RAFS demonstrated a short term frequency stability of 2.4×10^{-13} at 1 second

integration time. Figure 17 shows the frequency stability performance of this RAFS.

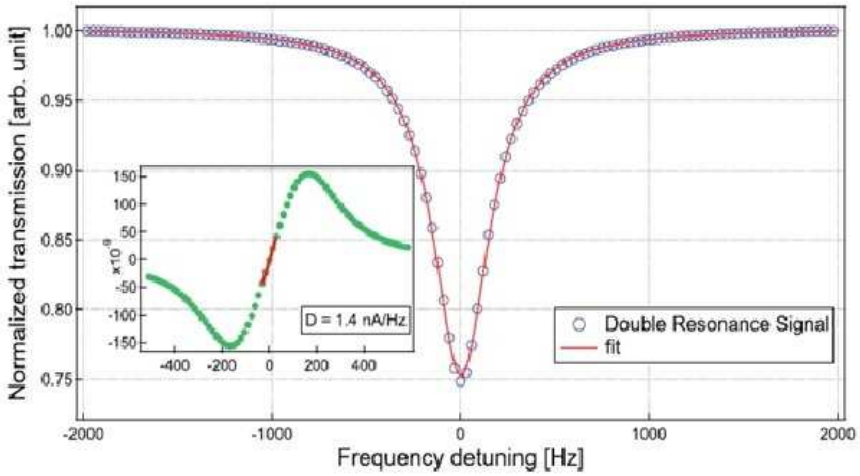

Figure 16: Resonance signal of the RAFS developed by C. Stefanucci *et al.*,. The figure is extracted from [46].

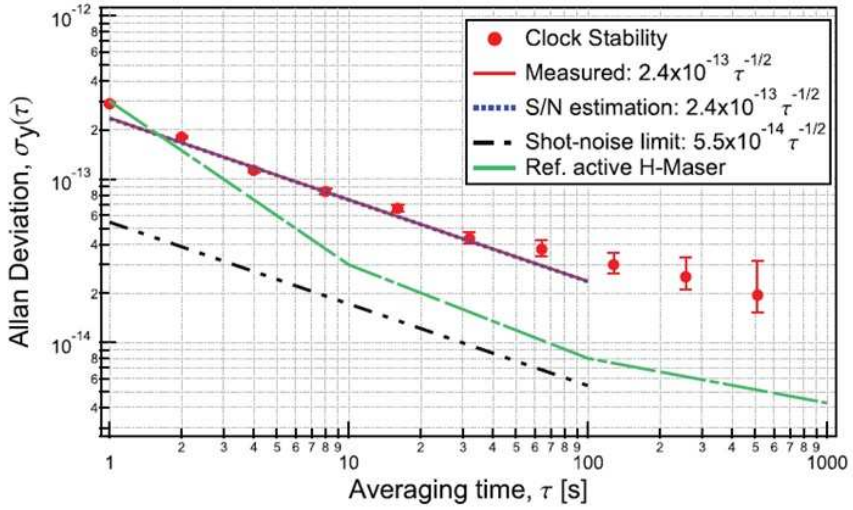

Figure 17: Frequency stability of the RAFS developed by C. Stefanucci *et al.*,. Solid line: the measured stability. Dotted line: the signal-to-noise estimated value. Dashed-dotted line: the shot-noise limit. Dashed line: the stability of an active H-maser, against which the clock is measured. The figure is extracted from [46].

Pulsed Optically Pumped (POP) Rb maser with microwave detection Pulsed Optically Pumped (POP) Rb maser developed by A. Godone *et al.* [47] in INRIM achieves a high performance of frequency stability by using the Ramsey technique to interrogate the atoms [7]. The Ramsey interaction permits clock signal linewidth independent from the laser intensity and the RF power and greatly reduces the cavity-pulling effect [48]. Additionally, the light shift is reduced in comparison with the classical double resonance continuous approach. Figure 18 shows the experimental setup of the pulsed Rb maser. It is divided into three main parts: the physics package, optics and electronics.

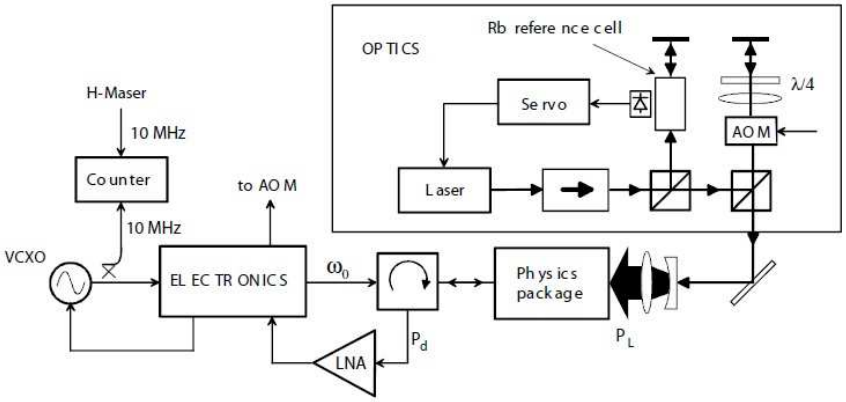

Figure 18: Experimental setup of pulsed Rb maser. LNA: low noise amplifier. The figure is extracted from [47].

The quartz cell (diameter=30 mm, length=18 mm) contains Rb vapor and buffer gases, Ar and N_2 in the pressure ratio 1.6 to 1 to minimize the collisional frequency shift, the total buffer gases pressure is 25 Torr. The operating temperature of the cell is stabilized around 63 °C in order to reach the highest atom number without increasing significantly the decay rates for spin exchange of atoms. An external cavity diode laser (ECDL) at 795 nm and a power up to 100 mW is used in the optic part. The laser is frequency locked to the Rb atomic transition observed in an external Rb vapor cell. The laser beam is sent to an acousto-optic modulator (AOM) to generate pulsed light sequence. The AOM also redshifts the laser frequency to match the absorption frequency of Rb in the physics package which is shifted by buffer gases. The laser beam at the input of the Rb cell is expanded to a diameter of 20 mm to cover as many atoms as possible. In electronic section, a microwave synthesizer is used to generate two microwave pulses for the Ramsey interrogation. A heterodyne detector is enabled during the detection window. The error signal generated in a servo system is used to lock the quartz oscillator at 10 MHz to the Rb atomic transition. Figure 19 shows the Ramsey fringes detected by the experimental setup. The central fringe has a linewidth of 54 Hz.

Figure 20 shows the measured frequency stability of the pulsed Rb maser at high laser intensity (about 10mW/cm^2). The best performance of frequency stability of this system is achieved, which is 1.2×10^{-12} at 1 second after drift removal of 6×10^{-14} per day. This performance is close to the thermal noise limited stability, which is 1×10^{-12} at 1 second.

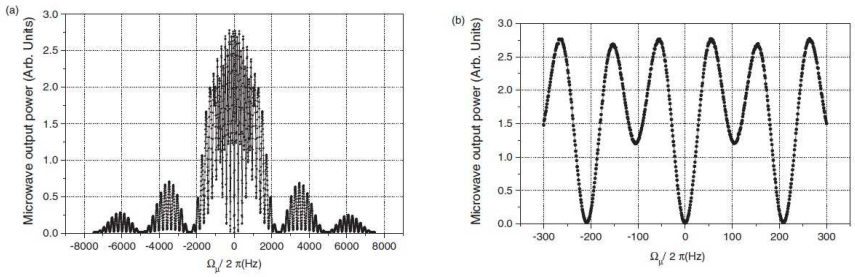

Figure 19: (a) Full pattern of Ramsey fringes; (b) central fringes. The figure is extracted from [47].

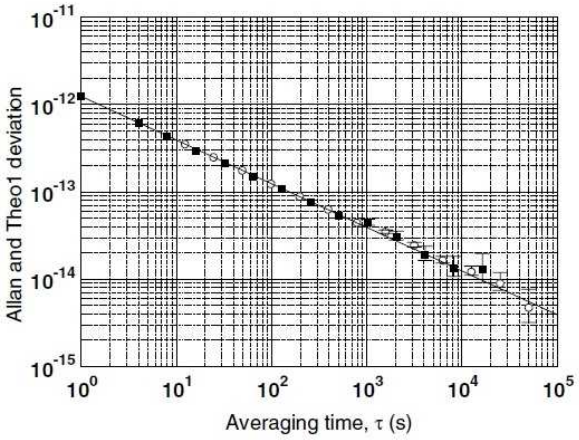

Figure 20: Frequency stability at high laser intensity. The figure is extracted from [47].

Pulsed Optically Pumped (POP) Rb clock with optical detection S. Micalizio *et al.* in INRIM has proposed a compact pulsed Rb vapor cell atomic clock prototype [23] with optical detection. Compared to the POP maser using passive maser for detection [47], this clock uses a laser as a probe in the detection. In this case, a higher signal-to-noise ratio of signal can be detected, because energy of optical photon is higher than energy of microwave photon, so the short term frequency stability can be improved. Moreover, the microwave cavity does not play a role in the detection and a high-Q cavity is no longer required. Thus, the mid-long frequency stability is also improved because cavity-pulling is negligible. Like the POP maser, Ramsey interference technique [7] is applied in this POP clock. Figure 21 shows the basic scheme of the POP clock.

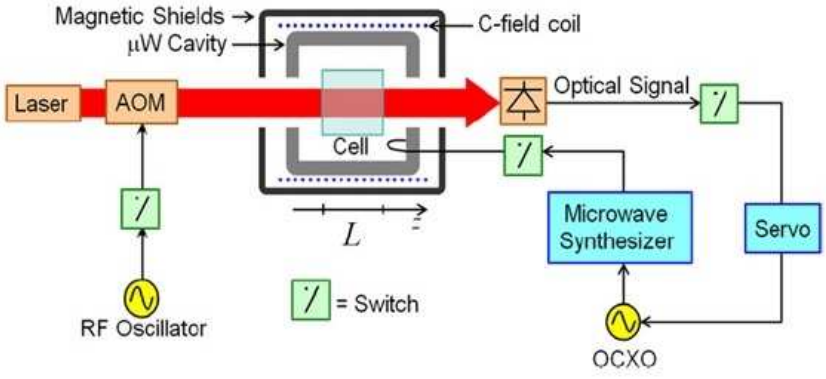

Figure 21: Basic scheme of the POP clock. The figure is extracted from [23].

The POP clock is divided into three main parts: physics package, optics and electronics. The physics package contains a quartz cell filled with Rb vapor and buffer gas, microwave cavity, magnetic shields and heaters. The quartz cell (Diameter = 20 mm, length = 20 mm) is filled with Rb vapor and a mixture of Ar and N_2 in the pressure ratio 1.6 with a total pressure of 25 Torr. The mixture of gases compensates collisional frequency shift at 65 °C. The microwave cavity is made of molybdenum and resonates on the electromagnetic mode TE_{011} at the Rb ground state hyperfine frequency. In the optic part, the clock uses a Distributed feedback (DFB) diode on Rb D_2 line (780 nm) as laser source. The laser diode is frequency locked to the Rb atomic transition $F = 1 \rightarrow F' = 1$. The laser beam is sent to an AOM that acts as an optical switch to generate the pulsed pumping sequence. Meanwhile, the laser frequency is redshifted to match the absorption frequency of Rb vapor shifted by buffer gas in the cell. The laser in this clock is not only used to pump the atoms, but also used to detect the resonance signal. The resonance signal detected by a photodetector is processed by a trans-impedance amplifier. Figure 22 shows the Ramsey fringes detected by the POP clock. The central Ramsey fringe linewidth is 150 Hz. Figure 23 shows the measured frequency stability of the POP clock, which is lower than $1.7 \times 10^{-13}\ \tau^{-1/2}$ at 1 second, and reaches nearly 10^{-15} for 10000 seconds. The frequency stability performance of the POP clock is close to the one of a Hydrogen Maser (T4S iMaser 3000 for example shown in figure 23).

For additional information, a polarization selective method was developed by M. Zhu for detecting a clock signal [49] with high contrast. Recently, this novel detection scheme was implanted to a POP clock developed in China by J. Lin *et al.*. They obtained a ultrahigh resonance contrast up to 90% [51]. This detection scheme is only suitable for the D_1 line. The frequency stability of the POP clock using this detection scheme was improved by an order of magnitude under equivalent conditions compared to a standard detection technique.

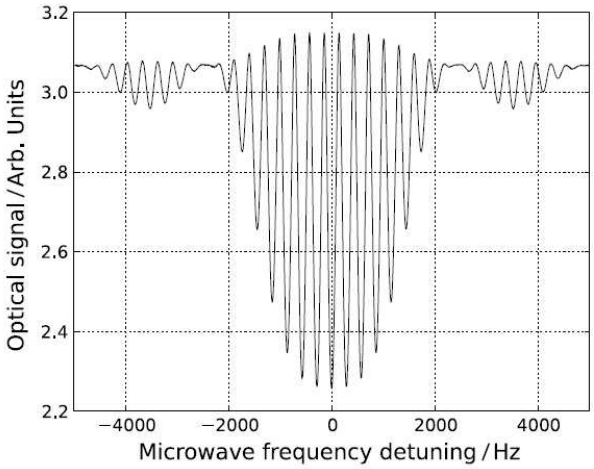

Figure 22: Ramsey fringes detected in the POP clock. The free evolution time T=3.3 ms. The figure is extracted from [23].

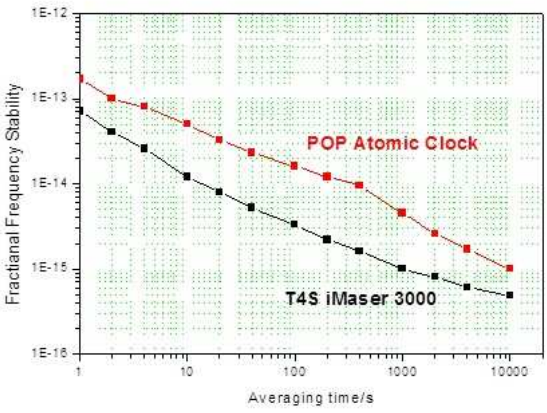

Figure 23: Frequency stability of POP clock and T4S iMaser 3000. Data of the figure are extracted from [23] and http://www.t4science.com/products/.

2.5.3 CPT clocks

Coherent Population Trapping (CPT) is a quantum interference process that occurs when a 3-energy level atomic system interacts with two phase coherent optical lines [52] [53]. If the frequency difference between both optical lines exactly equals the ground state hyperfine splitting of the atoms, the atoms do not absorb photons anymore and the transparency of atoms vapor reaches a maximum. Consequently, a CPT resonance signal can be detected by a photodiode. Atomic clocks based on CPT allow to generate resonance signal without a resonant cavity because the microwave signal that resonates with alkali atoms is optically carried. Consequently, CPT allows to realize ultra-compact or even miniature atomic clocks thanks to the development of MEMS techniques.

In 1976, G. Alzetta *et al.* first observed CPT line in an interaction between a multimode laser and Na atoms [52]. Theoretical explanation of the CPT phenomenon was made by E. Arimondo *et al.* [53]. In 1982, J. E. Thomas *et al.* observed the first Ramsey fringes on CPT resonance by combing two separated oscillating fields with CPT phenomenon in a Na atomic beam [54]. In the following decade, researches of atomic clocks based on CPT took place in different laboratories. Godone *et al.* developed a POP Rb maser exhibiting a frequency stability of $1.2 \times 10^{-12}\ \tau^{-1/2}$ for integration times up to 10^5 seconds [47]. An original pulsed Cs CPT clock was developed in LNE-SYRTE [26]. Eventually, thanks to the help of microfabrication techniques, the development of chip-scale atomic clocks became feasible.

A simplified scheme of a CPT atomic clock is shown in figure 24. A laser system generates two frequency-separated phase coherent optical lines. Both optical lines are resonant with the alkali atoms in a glass cell such that both ground state levels are connected to a common excited state. The glass cell contains a buffer gas used to reduce the linewidth of the resonance. A photodiode detects the transmitted optical power through the cell. The CPT resonance is detected in the bottom of the absorption line when both optical lines are exactly frequency-splitted by the atom ground state hyperfine splitting (9.192 GHz for Cs atom). The signal at the output of the photodiode is used to stabilize the laser frequency and to lock the local oscillator to the atomic transition frequency.

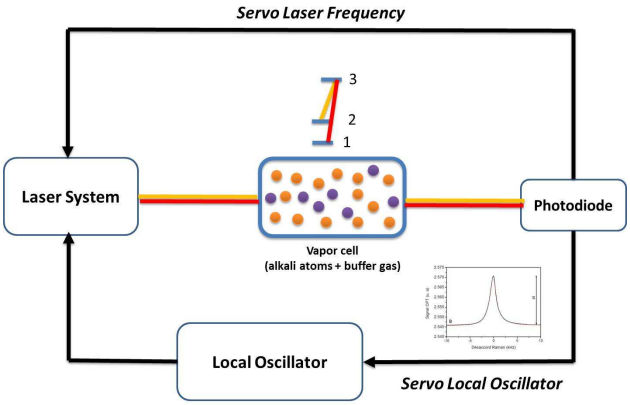

Figure 24: Simplified scheme of a CPT atomic clock.

Continuous Wave (CW) CPT clocks M. Zhu *et al.* developed a polarization-selective method for detecting high-contrast CPT resonances in a vapour cell [49]. The method uses a single laser beam with frequency modulation to induce CPT resonance and to control the AC Stark shift. The method provides a

CPT resonance signal with a high contrast of 22%.
Figure 25 shows the block diagram of the experimental setup.

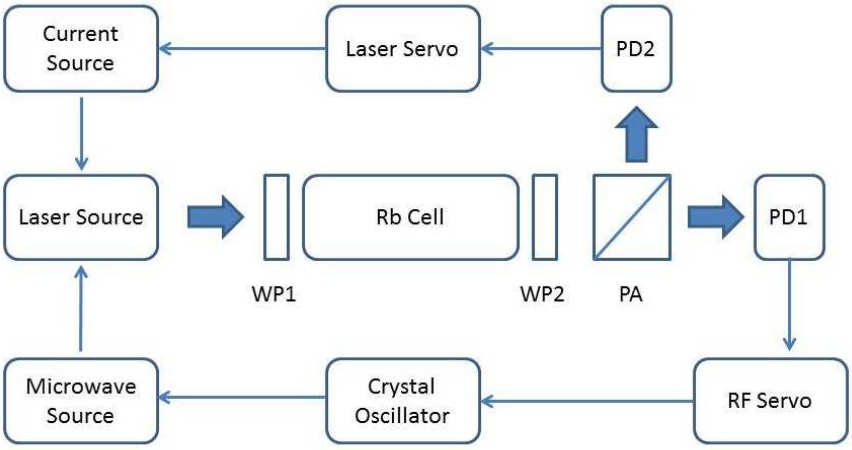

Figure 25: Block diagram of the CW CPT clock from M. Zhu. The figure is extracted from [49].

A single frequency diode laser is frequency modulated by coupling a microwave signal into the injection current. The ± 1 order sidebands serve as the CPT-generation and CPT detection frequencies while the higher order sidebands suppress the AC Stark shift. The first waveplate (WP1) converts the linear polarization of the laser output beam to the desired elliptical polarization so that most of the power is in the σ^+ polarization for CPT generation. The second waveplate (WP2), which is a combination of three linear waveplates, converts the circular polarizations of the laser fields emerging from the absorption cell into the desired linear polarizations, and provides the necessary relative phase shift between the two orthogonal polarizations. The waveplate WP2 and the polarization analyzer (PA) are aligned so that the polarization analyzer blocks most of the power in AC Stark shifts suppression frequency components and the CPT resonance signal is symmetric. Figure 26 shows the detected CPT resonance with this setup. The linewidth is 218 Hz and the contrast is 22 %. As shown in figure 27, this CPT-based rubidium vapour cell frequency standard demonstrated a measured short term frequency stability of $1.4 \times 10^{-12}\ \tau^{-1/2}$ up to 100 s. This is among the best short term frequency stability for a CW CPT clock we found in the literature.
For increased simplicity, CPT clocks are realized with VCSEL diode lasers whose injection current is directly modulated. Nevertheless, these diode lasers suffer from a relevant frequency noise and exhibit a wide linewidth (typically 100 MHz). Such clocks, as the one presented in figure 28, present a short term frequency stability in the range of $1 \times 10^{-11}\ \tau^{-1/2}$ when the VCSEL used operates on the alkali atom D_2 line. A relevant improvement can be expected with the use of a laser resonant on the alkali D_1 line.

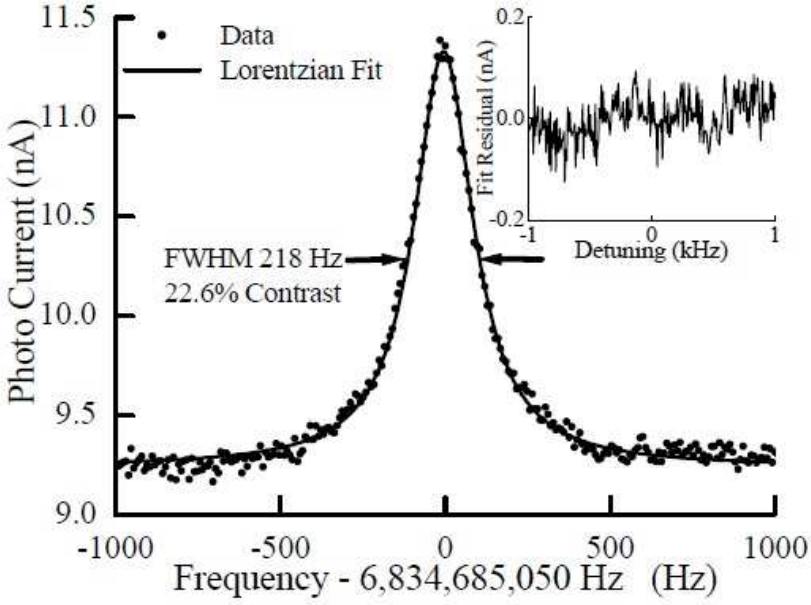

Figure 26: CPT resonance in the CW CPT from M. Zhu. The figure is extracted from [49].

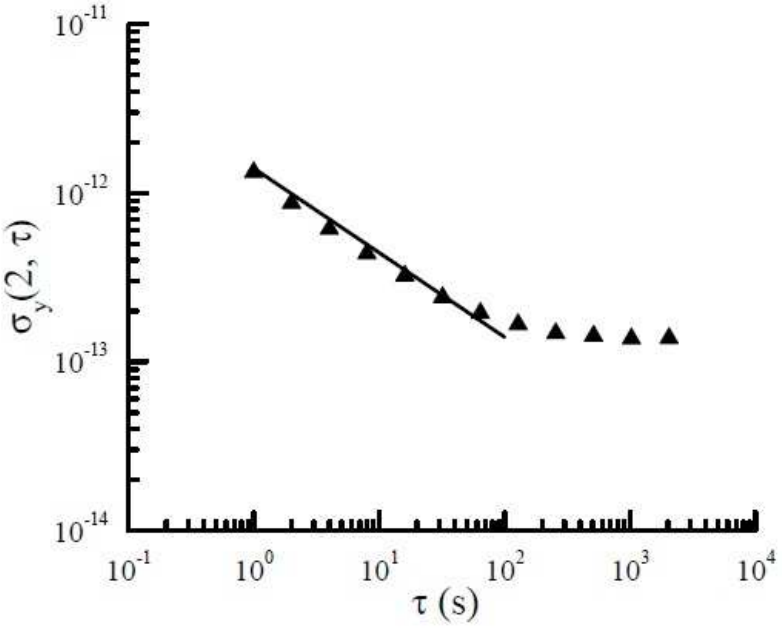

Figure 27: Allan deviation of the CW CPT clock from M. Zhu. The figure is extracted from [49].

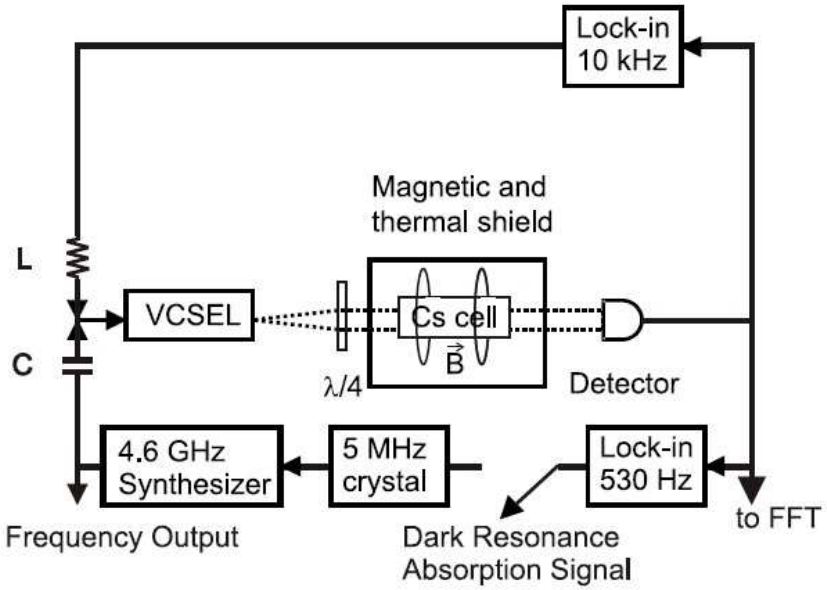

Figure 28: CPT resonance in a CW CPT clock with a modulated VCSEL. The figure is extracted from [50].

Pulsed Cs CPT clock Figure 29 shows the basic scheme and typical Ramsey fringes of the pulsed Cs CPT clock developed in the LNE-SYRTE. To the best of our knowledge, this pulsed Cs CPT clock is the best CPT clock in the world.

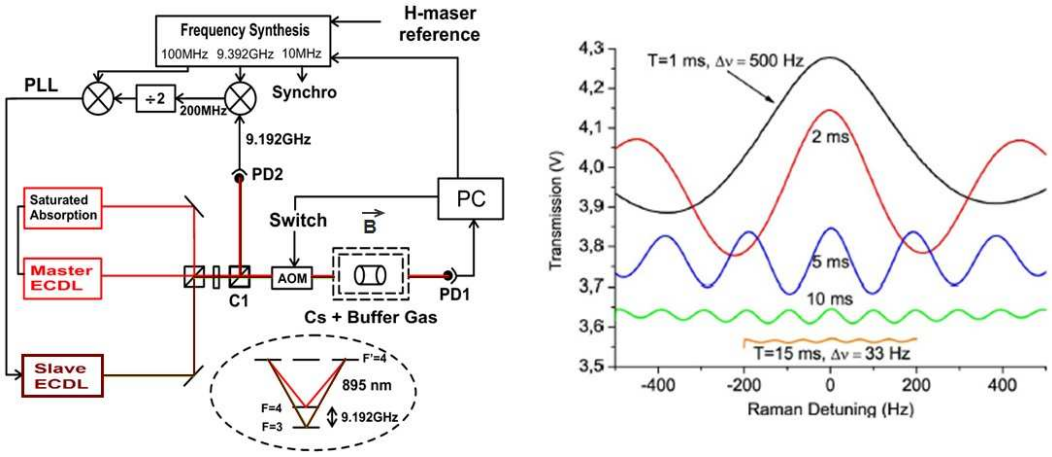

Figure 29: Principle scheme and Ramsey fringes of Pulsed Cs CPT clock for different free evolution times T. The figure is extracted from [25].

The pulsed CPT clock uses two phase-locked external cavity diode lasers (ECDL) to constitute the bichromatic light field required for CPT interaction. The master laser is frequency locked to the $F = 4 - F' = 4$ hyperfine component of the Cs D_1 line by a saturated absorption in an auxiliary Cs vapor cell. The slave laser is phase locked to the master laser with a frequency offset around 9.192 GHz with an optical phase lock loop. The laser beam is sent to an acousto-optic modulator (AOM) which acts as a light switch to realize Ramsey interrogation. This AOM is also used to compensate for the buffer gas frequency shift in the CPT cell. At the output of the AOM, the light field is sent through a cm-scale vapor cell filled with Cs atoms and a N_2-Ar buffer gas mixture. In this setup, atoms interact with a sequence of optical pulse trains. Each pulse is used both for CPT pumping and CPT detection. Each light pulse is separated by a time T where atoms evolve freely in the dark. High-contrast and narrow Ramsey fringes are detected by combination of lin $\perp$ lin interaction scheme and Ramsey-like temporal pulsed interrogation [26]. The clock signal is detected by a photodiode and processed to a computer to lock the local oscillator frequency. Figure 30 shows the frequency stability performance of the prototype. A short-term frequency stability of 7×10^{-13} at 1 s was demonstrated in [25][59]. More recently, these results were improved to $6.4 \times 10^{-13}\ \tau^{-1/2}$ as shown on figure 30.

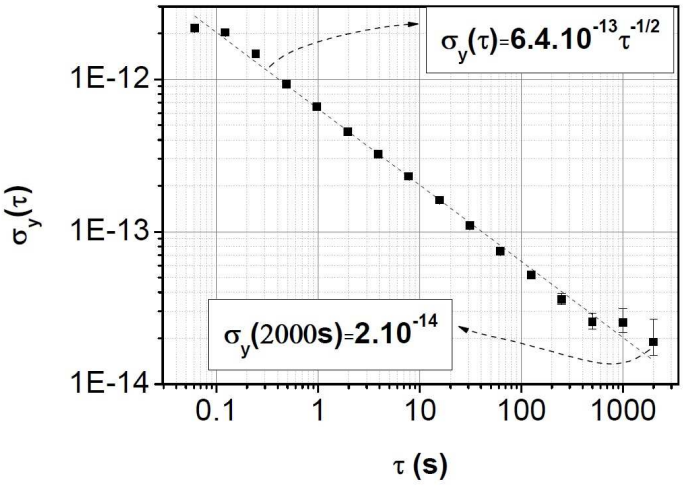

Figure 30: Frequency stability of the pulsed Cs CPT clock. Courtesy from J. M. Danet, SYRTE.

CPT maser The dark line signal, CPT signal, observed in the fluorescence spectrum of a three level system submitted to a Λ interaction scheme or the electromagnetically induced transparency (EIT) signal observed in the transmitted laser power are considered as interesting references for the realization of highly stable frequency standards. Alternatively to the optical signal, the oscillating magnetization induced in the medium can be used for the realization of a frequency standard: when the atoms are placed in an electromagnetic cavity, this magnetization is responsible for a coherent emission (CPT maser) observed in alkali-metal atoms at the ground-state hyperfine transition frequency. This is the basic principle of the CPT maser developed in INRIM and well-detailed in [48]. Figure 31 shows the CPT maser diagram.

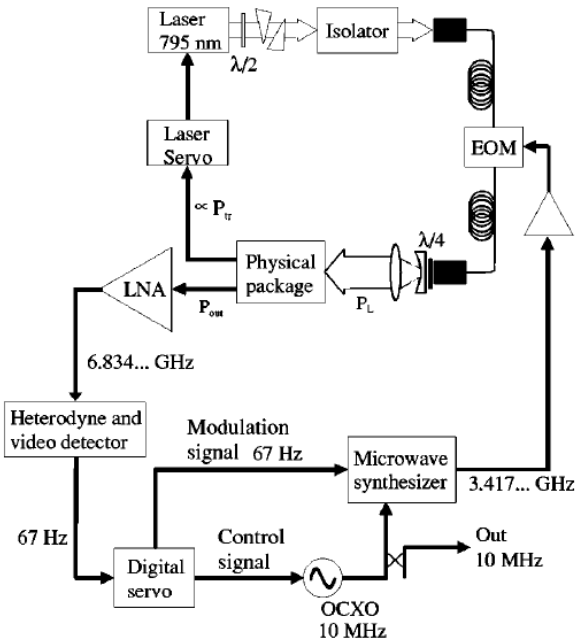

Figure 31: CPT maser block diagram. The figure is extracted from [48].

An external cavity diode laser resonant at 795 nm is coupled to a 5 GHz bandwidth EOM with a single-mode polarization maintaining fiber. The laser beam at the EOM output is expanded to a diameter of 2 cm and sent to the physics package through a quarter-wave plate to produce circular polarization. The total optical power coupled to the atoms is 1 mW. The quartz cell has a diameter of 28 mm and a length of 22 mm. It contains the Rb^{87} vapour and a mixture of buffer gases, Ar and N_2, in the ratio of 1.6 to 1 to minimize the linear temperature coefficient. The total buffer gas pressure is 25.7 Torr. A photodiode detects the transmitted laser intensity at the output of the cell. The cell operating temperature is 60 °C to have a high enough atomic density to reach a good signal-to-noise ratio without increasing the maser linewidth via spin-exchange and optical thickness of the vapour. The output microwave signal is sent to a double conversion heterodyne detector which provides the error control signal to the digital servo loop of the quartz oscillator at 10 MHz. A square wave frequency modulation may be used for the coherent detection of the maximum of the maser emission profile. The quartz oscillator is followed by a low phase noise frequency synthesizer.

Figure 32 shows the maser emission profile at the cavity output. Figure 33 shows the CPT maser clock relative frequency instability. A short term frequency stability of $3 \times 10^{-12}\ \tau^{-1/2}$, a value close to the

theoretical predication [48]. The fundamental noise contribution to the frequency stability of the CPT maser is the thermal additive noise estimated to be in this experiment 7×10^{-13} at 1 s. The thermal detection noise limit may be achieved in the short term (white frequency noise region). The medium term frequency stability is dominated by temperature drift and no flicker floor is observed at the level of 4×10^{-14}.

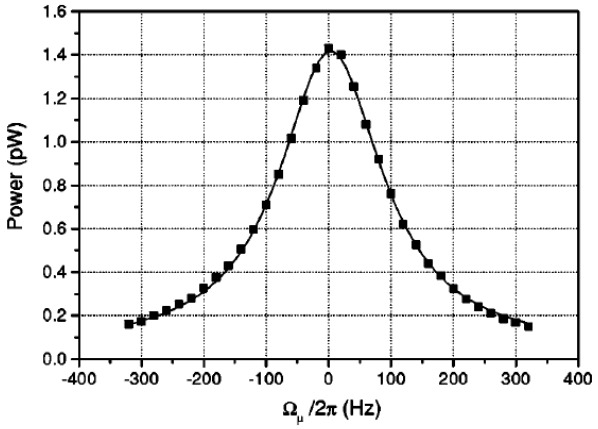

Figure 32: Maser emission profile at the cavity output. The figure is extracted from [48].

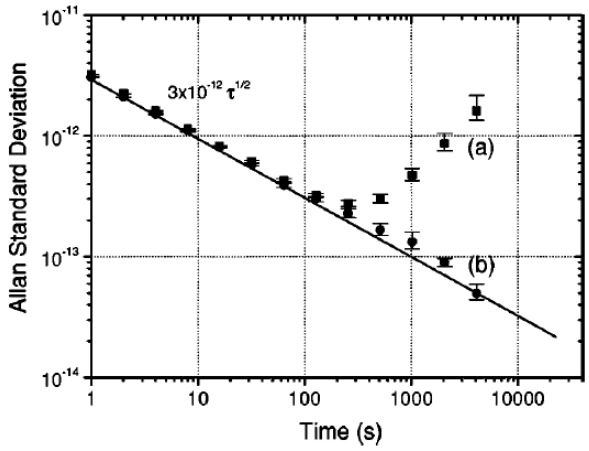

Figure 33: Allan deviation of the CPT maser with or without drift removed. The figure is extracted from [48].

Chip Scale Atomic Clocks (CSAC) Figure 34 shows the typical scheme of a miniature atomic clock [55]. Alkali atoms in a microfabricated cell interact with the laser beam from a VCSEL diode laser whose injection current is directly modulated by a local microwave signal with a frequency equal to the half of the ground state hyperfine splitting (4.596 GHz for the Cs atom). The output spectrum of the VCSEL contains two phase coherent optical lines frequency-splitted by 9.192 GHz required for CPT interaction. The carrier and the other higher order sidebands are still present and should be taken account for the light shift evolution. The output power of the laser is attenuated with a neutral density filter to maintain a laser power of about 10-20 μW at the input of the cell. The transmitted optical power through the cell is detected by a photodiode. The output signal of the photodiode is used in two main servo loops. The first one is used to stabilize the laser frequency on the bottom of the absorption line. For this purpose, the laser current is modulated at about 10 kHz and the signal is synchronously demodulated at the output of the photodiode with a lockin amplifier to increase the signal to noise ratio. The second loop is used to correct the local oscillator frequency using a similar synchronous modulation technique at a typical modulation frequency of a few 100 Hz. The frequency locked local oscillator acts as the reference signal to the RF system and provides an output signal to be compared with a hydrogen maser for frequency stability measurement. The first microfabricated atomic clock was demonstrated in NIST in 2004 [56]. In 2011, Symmetricom released the first commercially-available Chip Scale Atomic Clock based on CPT [57]. For information, figure 35 shows the frequency stability of 10 pre-production prototypes miniature clocks developed by R. Lutwak *et al.* [58]. All frequency stabilities are better than $3 \times 10^{-10}\ \tau^{-1/2}$ out to averaging intervals of $\tau > 100$ seconds. The latest commercially-available CSAC, SA.45s CSAC model fabricated by Symmetricom, demonstrates a frequency stability of 2.5×10^{-10} at 1 second with a volume < 17 cm^3 and total power consumption lower than 120 mW [18]. Figure 36 shows a photograph and a typical CPT resonance signal of the CSAC SA.45s model. The CPT resonance signal linewidth is 1313 Hz. Such atomic clocks can be applied on numbers of compact system, such as underwater sensor systems, GPS receivers, Backpack radios, unmanned vehicles, telecommunication systems and defense systems.

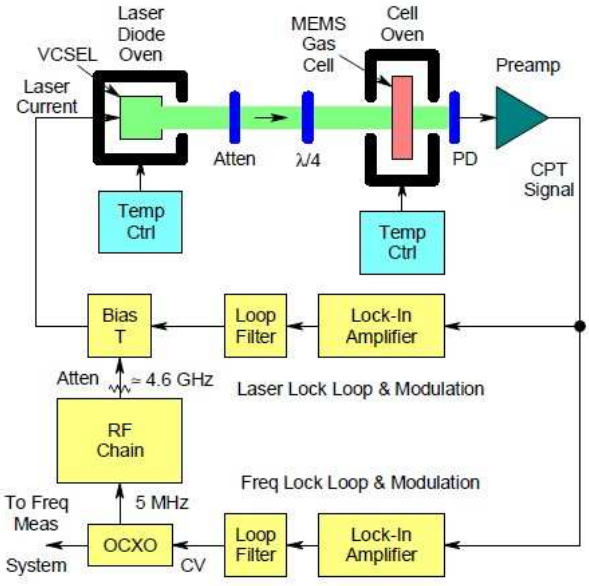

Figure 34: CSAC testbed scheme. Data of the figure is extracted from [55].

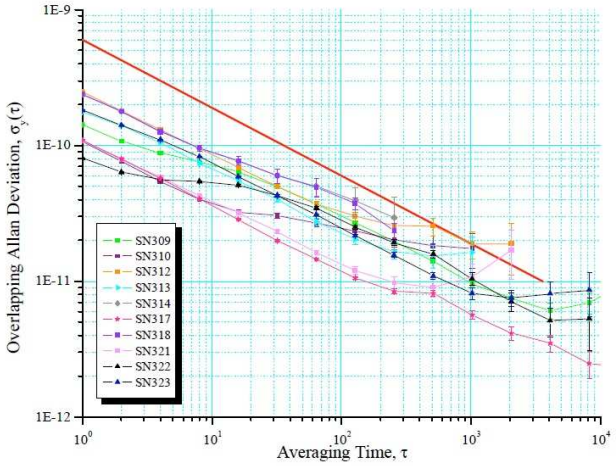

Figure 35: Frequency stability of 10 pre-production prototypes miniature clocks. The figure is extracted from [58].

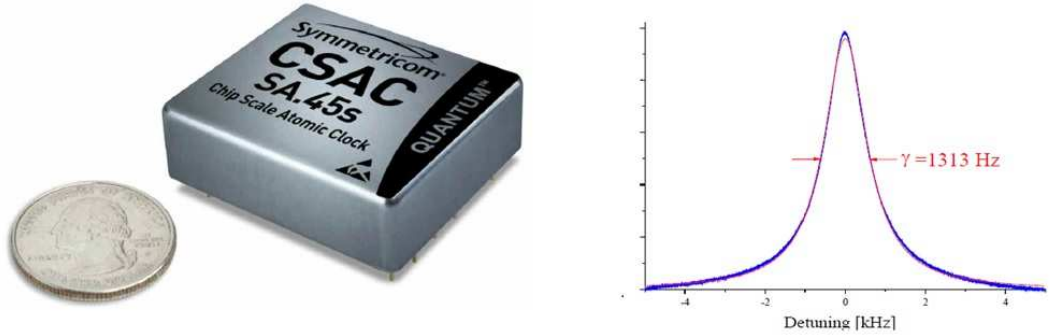

Figure 36: Photograph and typical CPT resonance signal of SA.45s CSAC. The figure is extracted from [18].

In Europe, the MAC-TFC project, led by FEMTO-ST from 2008 to 2012, allowed the development of the first European Cs miniature atomic clock. Figure 37 shows a photograph of the miniature atomic clock physics package prototype developed in this frame. In parallel, CSEM in Switzerland has demonstrated a well-advanced prototype of miniature atomic clock based on Rb atom shown on figure 38. This prototype demonstrated excellent performances of 6×10^{-11} at 1 s and 3×10^{-11} at 1 day integration [20].

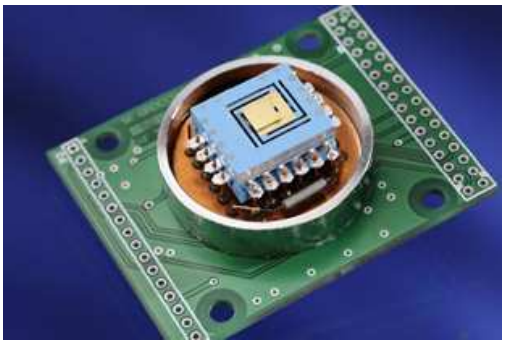

Figure 37: *MAC-TFC clock prototype.*

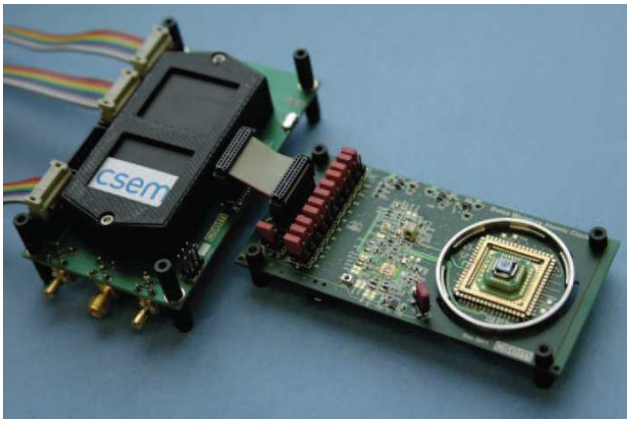

Figure 38: *CSEM clock prototype, named SMAC.*

2.5.4 Cold atom compact clocks

Laser cooling atoms is a useful method to increase atom-light interaction time and to reduce the resonance linewidth. Many applications based on laser cooling atoms have been demonstrated [60] [61] [62] [63]. The world's most accurate atomic clocks are based on ultra-cold atoms because the interrogation time is very long and the perturbations are greatly reduced compared to traditional atomic clocks [64].

HOrloge à Refroidissement d'Atomes en CEllue HOrloge à Refroidissement d'Atomes en CEllule (HORACE) is a compact cold cesium atom clock developed in LNE-SYRTE for space applications and onboard systems. The operation of this clock is different from fountains since the laser cooling; the microwave interrogation and the detection are sequentially performed inside a spherical microwave cavity. This allows a high potential for compacity.

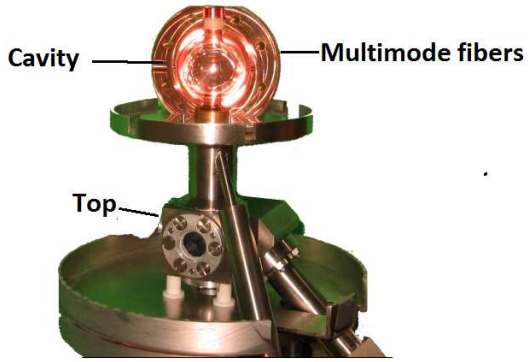

Figure 39: Heart of HORACE clock.

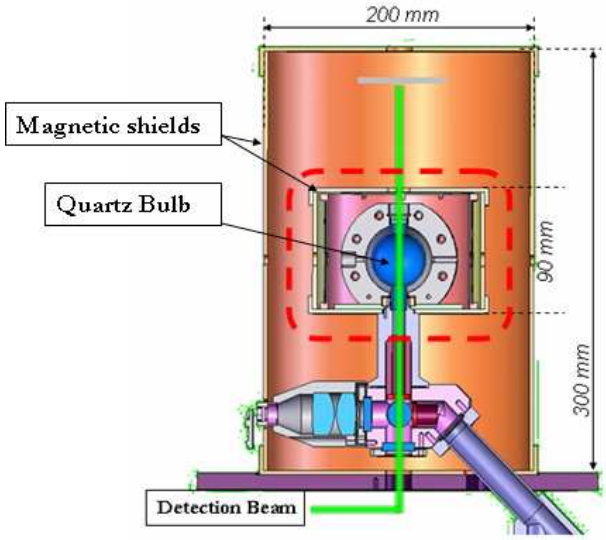

Figure 40: Architecture of HORACE clock.

What is specific about the HORACE clock is that all interactions (laser cooling, microwave spectroscopy and detection) are performed at the same place, directly inside a spherical OFHC copper microwave cavity.

In order to perform laser cooling, this cavity is fed with 6 multimode optical fibers in the (1,1,1) configuration. Its wall are optically polished so as to reflect and scatter the 852 nm cooling light. A nearly isotropic light field is created inside leading to an optical molasscs cooling scheme. The microwave cavity acts here as a reflecting sphere for the laser field and averages power imbalances between multimode fibers. Two slits (1×4 mm) provide symmetrical microwave coupling. The cavity operates a TEM_{011} mode with a quality factor of about 5000. This cavity is surrounded by a solenoid creating a 5 mG vertical static magnetic field to raise the Zeeman degeneracy. For experimental reasons and convenience a blown quartz bulb is used to prevent interaction between Cs atoms and copper cavity walls. As it shifts cavity resonance by several 100 MHz, each cavity has to be made, polished and tuned for a given bulb. This bulb is glued to a laser soldered Titanium apparatus. An ion pump maintain a residual pressure below 7.5×10^{-9} Torr in the vacuum chamber and in the bulb. A glass cell containing liquid Cs acts as a reservoir which can be heated up to increase Cs pressure in the bulb. A time-off light detection zone, located 9 cm below the cavity, allows to perform atomic velocity diagnostics.

The typical operation sequence of the HORACE clock that consists of laser cooling, atom preparation, clock transition interrogation and detection is shown on figure 41.

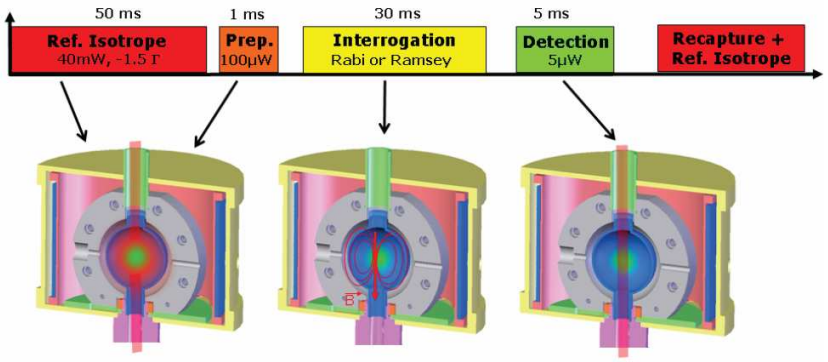

Figure 41: Sequence of HORACE clock.

Atoms are first laser-cooled isotropically. About 4×10^7 atoms are captured in $T_{cool} \sim 40$ ms. Although parameters are set for Doppler cooling, atomic temperatures of 35 μK, much below the Doppler limit, are observed. Atoms are then optically pumped in the $|F{=}3\rangle$ state among all Zeeman sublevels thanks to a 0.5 ms and 100 μW light pulse. The fraction of atoms in the useful sublevel is about 20% of the total number. During atomic free fall (limited by gravity to 50 ms), the clock transition is probed by applying either Rabi or Ramsey sequence. The typical result linewidth is about 20 Hz. The interrogation microwave field is derived from a 100 MHz reference signal. The probability of transition is derived by measuring the atomic population of the $|F{=}4\rangle$ state only. The goal of the cooling stage is to produce the largest number of cold atoms in the shortest time in order to improve the following trade-off. On the one hand, a large number of atoms contributing to the clock signal improves the signal to noise ratio and the clock stability. On the other hand, one cannot perform a too long cooling sequence so as not to increase sensitivity to the local oscillator phase noise. A recapture technique was implemented to recapture atoms from one clock cycle to the next one in that sense to optimize the clock performances [65]. Figure 42 shows Allan deviation of Horace clock. A short term relative frequency stability of $2.2 \times 10^{-13}\ \tau^{-1/2}$ is achieved. Results on mid term show that a level of 4×10^{-15} is reached after 5000 s of integration. The main contribution comes from the atomic shot

noise.

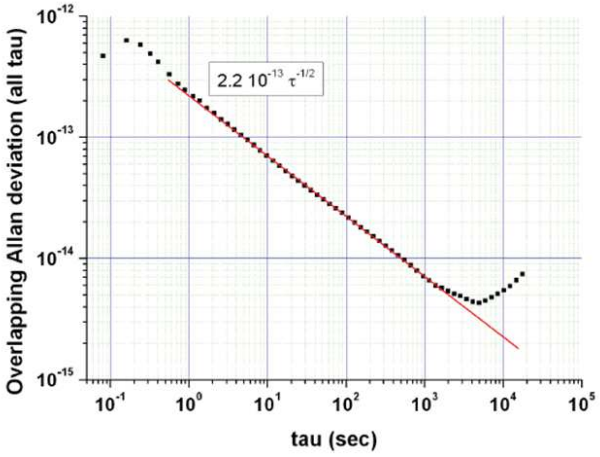

Figure 42: Allan deviation of HORACE clock.

Miniature cold-atom clock V. Shah *et al.* developed a miniature cold atom physics package with volume < 75 cm^3 [70]. The device is demonstrated as a miniature cold atom frequency standard (MCAFS). Figure 43 shows a 3D cross-sectional view of the MCAFS. A frequency stabilized distributed bragg reflector (DBR) laser pass though an optical shutter, which is a stack of four liquid crystal display (LCD) polarization rotators. At the output of the optical shutter, a 1.6×1.8 cm^2 circularly polarized laser beam is generated by a pair of beam expansions lenses and a quarter wave plate. The beam is divided into three pairs of opposing circularly polarized beams by a conical mirror. The three pairs of beams are used to cooling atoms in a MOT. The MOT contains an electrically heated Cs metal dispenser (AMD) and a non-evaporable getter (NEG) pump.

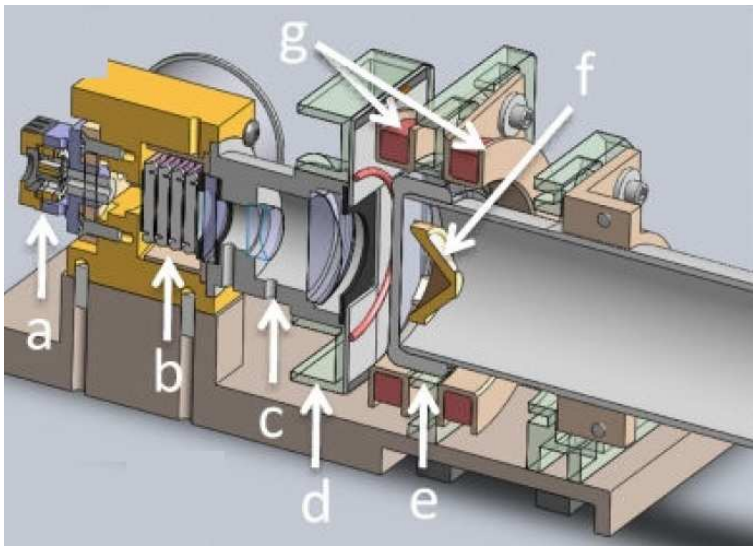

Figure 43: 3D cross-sectional view of the MCAF. (a): packaged diode laser. (b): optical shutter. (c): expansions lenses and quarter wave plate. (d): photodiodes for fluorescence collection. (e): ultra high vacuum chamber. (f): copper cone. (g): magnetic field coil for MOT. The figure is extracted from [70].

Figure 44 shows the detected Cs resonance signal interrogated with the Ramsey and Rabi techniques, respectively. Figure 45 shows the typical frequency stability of the MCAFS. The short term frequency stability is better than 2×10^{-11} at 1 second integration time.

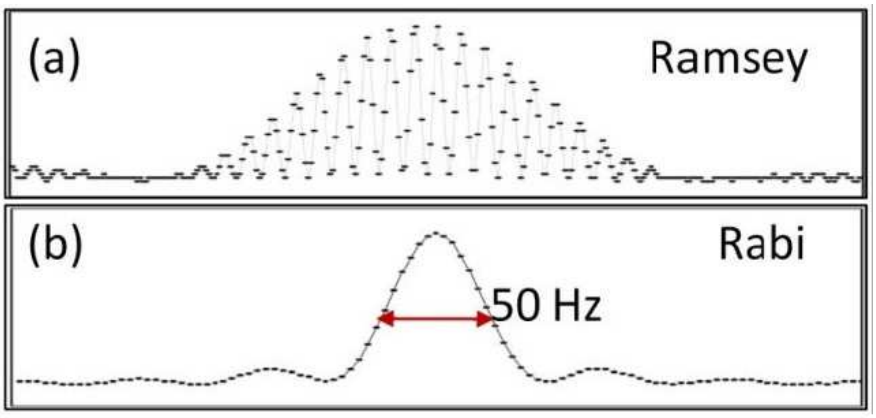

Figure 44: Microwave resonance seen by sweeping the LO frequency. (a) : Two pulse microwave Ramsey interrogation, frequency sweep=3 kHz. (b): Rabi interrogation with one 16 ms microwave pulse, frequency sweep=500 Hz. The figure is extracted from [70].

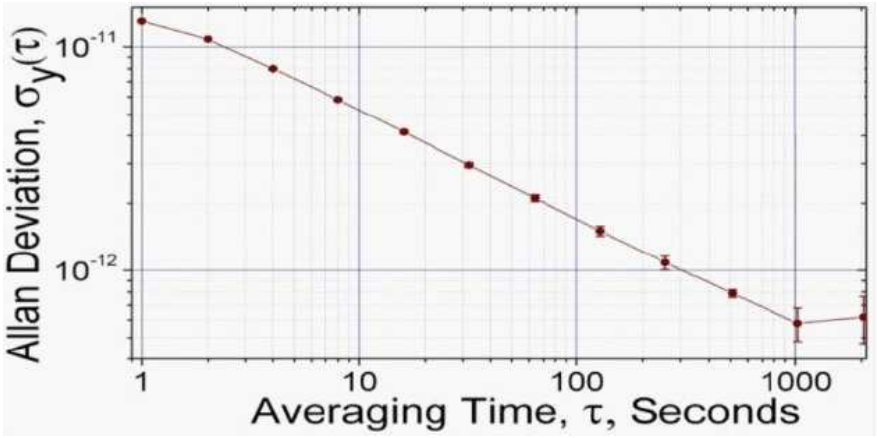

Figure 45: Frequency stability of the MCAFS. The figure is extracted from [70].

CPT cold atom clock Recently, a compact cold atom frequency standard based on CPT was proposed in NIST [71]. The cold atom clock developed by F.-X. Esnault *et al.* [71] is based on a compact source of laser cooling Rb atoms. The vacuum system has two chambers, which allows a $2D^+$ magneto-optical trap (MOT) beams loads to a 3D MOT in different pumping configurations. A laser system with a relatively pure spectrum based on an optical phase lock loop with two commsercial DFB/DBR laser diodes [72] is used. The clock uses *lin* ∥ *lin* pumping scheme [29] to pump atoms in order to produce high contrast CPT resonance. Ramsey interrogation is applied in the clock to reduce the average intensity of the CPT light. The interrogation time is limited to less than 10 ms, because a short interrogation time allows the atoms being recaptured from cycle to cycle with the MOT beams. Figure 46 shows an Allan deviation of the frequency steers of this cold atom clock. The short term frequency stability is limited by laser frequency noise to 4×10^{-11}. The mid-long term frequency stability is limited by magnetic field drift.

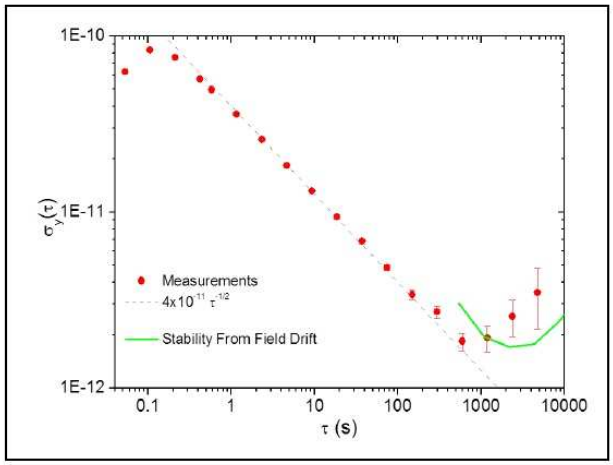

Figure 46: Allan deviation of the CPT cold atom clock. The figure is extracted from [71].

2.5.5 Trapped ion clocks

In the previous section, we presented that the buffer gas in alkali vapor cell is used to increase the interaction time between alkali atoms and light fields in Lamb-Dicke regime. A potential well can also realize this purpose. The potential well in an atomic clock is used to trap ions in a small space without extra wall for a long period. The type of potential well can be magnetic, electric and dipolar. The confinement regime of the clock permits to achieve an appropriate Lamb-Dicke regime to reduce the systematic effects, which leads to great increase of atomic quality factor and interaction time, some seconds in a Hg^+ ion trapped clock for example. Compared to atomic clocks based on vapor cells, the needless of external wall of this clock also prevents the atoms-wall collisions. Nevertheless, potential well also disturbs the clock transition due to Zeeman or AC Stark effect. To reduce this disturbance, a confinement regime that traps the atoms around zero potential well is expected, in such a confinement regime, the frequency shift is reduced to minimum. For magnetic and dipolar potential wells, there are also certain "magic" value that shift the two hyperfine energy levels identically, where the atomic transitions are not affected. Since ions are trapped in a certain space in this clock, the performance of ion trapped clock is no longer limited by its physical dimension as alkali atoms beam clock does.

Hg^+ trapped ion clock Jet Propulsion Laboratory (JPL) developed a $^{199}Hg^+$ ion trapped clock called Linear Ion Trap (LITE) to be applied on DSN of NASA [37]. The frequency stability of LITE is 2×10^{-13} $\tau^{-1/2}$ without flicker floor. The volume of LITE is 3 liters. Figure 47 shows a principle scheme of LITE.

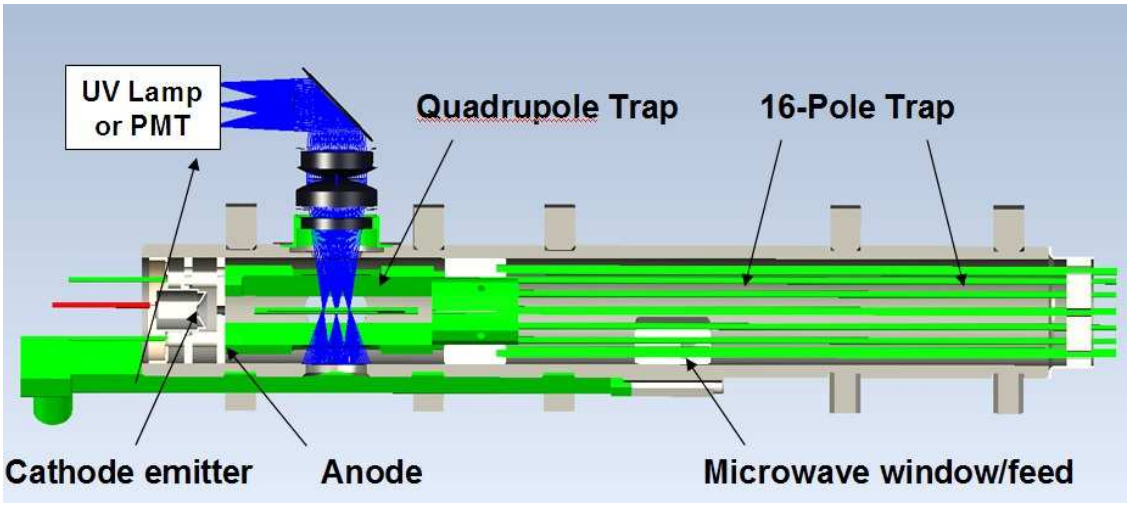

Figure 47: Principle scheme of LITE. The figure is extracted from [37].

In the LITE, some HgO is heated into Hg vapor. The Hg vapor is ionized to $^{199}Hg^+$ by collisions with electrons emitted from a canon. The $^{199}Hg^+$ ions are trapped in a quadrupole potential well. A spectral lamp that contains ^{202}Hg can pump the $^{199}Hg^+$ ions to the energy level $|F = 0, m_F = 0\rangle$, because the emission spectrum of ^{202}Hg overlaps with the absorption spectrum of $^{199}Hg^+$. The ions are sent to a interrogation zone and trapped by buffer gas and 16 poles potential well after the optical pumping finished. The linear zone of 16 poles potential well of clock can confine a large number of ions (10^6 to 10^7). This greatly improves the signal to noise ratio. Meanwhile, the systematic effects are reduced by coulomb repulsion between ions.

The ions trapped in the confinement are then interacted with a 40.5 GHz light field in continue wave regime (Rabi) or pulsed regime (Ramsey). The interaction time can last up to ten seconds. After the interaction, the ions are sent back to the quadrupole trap in order to turn on the spectral light again. Then the ions return to the energy level $|F = 1\rangle$ by microwave, and a fluorescence signal is detected by a photomultiplier tube (Figure 48).

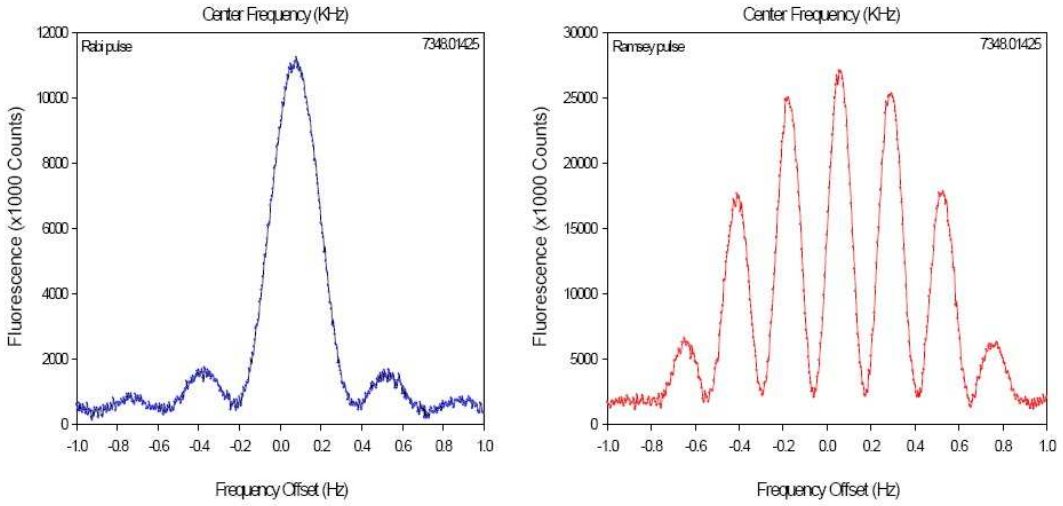

Figure 48: LITE resonance signal in continue wave regime for 3 s (left) and in pulsed regime for 0.5+5+0.5 s (right). The figure is extracted from [66].

Figure 49 shows a typical measurement of Hg^+ ions trapped clock frequency stability. The short term frequency stability is 2×10^{-13} at 1 second integration time, and averaging to 10^{-15} at 1 day.

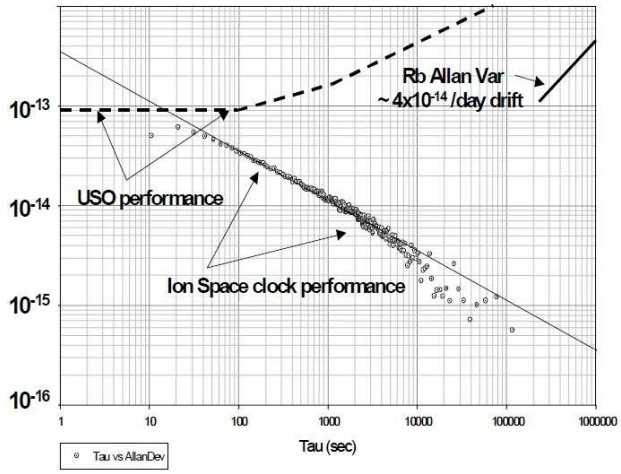

Figure 49: Typical frequency stability of Hg^+ ions trapped clock. The figure is extracted from [67].

Yb^+ trapped ion clock Recently, Sandia National Laboratory and JPL proposed a low power miniature $^{171}Yb^+$ ion clock [68]. The hyperfine ground state splitting of $^{171}Yb^+$ is 12.6 GHz. The atomic transition for

optical pumping and detection of Yb is at 369 nm. This allows to use low volume and low power consumption frequency-doubled laser diode. The laser source in Yb^+ ions clock can scatter thousands of photons per ion. The $^{171}Yb^+$ ions are trapped in a miniature, completely sealed-off 3 cm^3 ion-trap vacuum package. Figure 50 shows energy level structure of $^{171}Yb^+$ ion and the system level schematic of the frequency control loop.

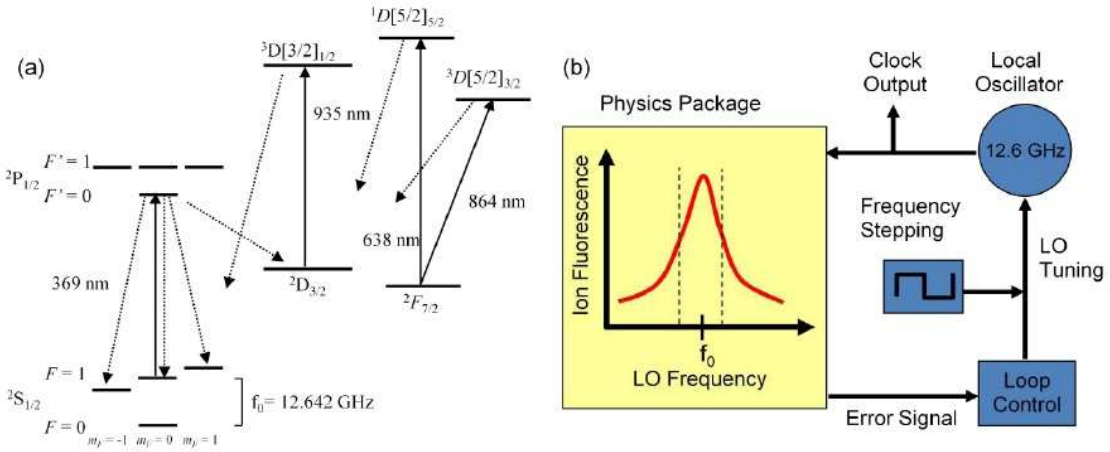

Figure 50: a: Energy level structure of $^{171}Yb^+$ ion with the 12.6 GHz clock transition, the optical transition. b: System level schematic of the frequency control loop of the clock. The figure is extracted from [69].

As shown in Figure 50, $^{171}Yb^+$ ion has low-lying $D_{3/2}$ and $F_{7/2}$ states. To improve detection and optical pumping, these two states must be cleared out. For the $D_{3/2}$, a 935 nm laser is applied, and for the $F_{7/2}$, different strategies were proposed, including optical pumping transitions at 638 nm or 864 nm, back filling with buffer gas, and dumping and reloading the trap. A 12.6 GHz microwave impulse is used to interact with $^{171}Yb^+$ ions, and the 369 nm and the 935 nm light fields are used to illuminate the ions to determine the number of ions that participate in the transition. The ion fluorescence from the $F = 1$ to the $F' = 0$ transition is detected by a detector. The fluorescence signal is used to generate a control signal to lock the local oscillator on the ions hyperfine ground state transition. Figure 51 shows the key part of Yb^+ ions trapped clock miniature vacuum package. A Yb source was constructed form a micromachined silicon hotplate that has Yb evaporated onto the surface. The getter pump was used to contain required vacuum of the package, which is 10^{-6} Torrs of He or Ne buffer gas with the partial pressures of other gases a few orders of magnitude lower. The buffer gas introduced was used to cooling the trapped ions. The ion trap of this clock is a linear RF Paul trap with octupole configuration, because the octupole configuration can balance good optical access and large trap depth to reduce the second order Doppler shift.

Figure 52 shows the typical frequency stability of the miniature $^{171}Yb^+$ ion clock. The short term frequency stability is 3.5×10^{-11} at 1 second and reaches the 10^{-14} range after a few days.

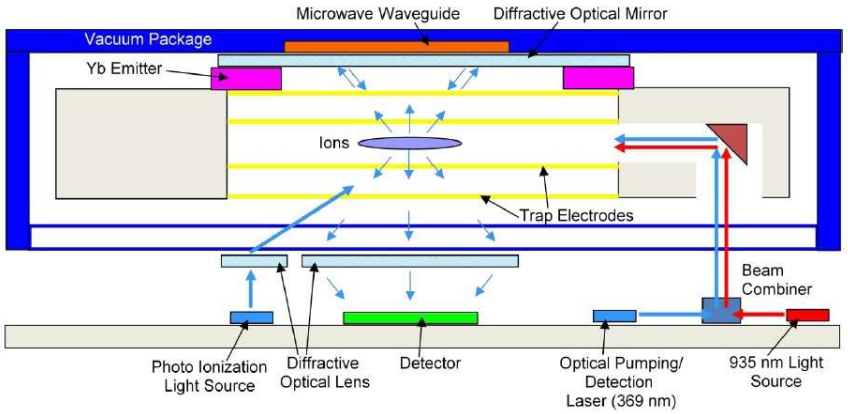

Figure 51: Vacuum package and octupole ion trap of Yb^+ Ions Trapped Clock. The figure is extracted from [69].

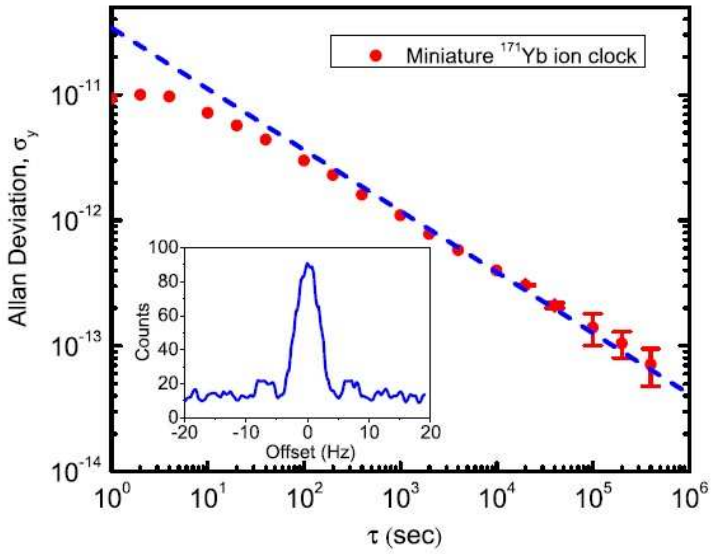

Figure 52: Frequency stability of the miniature $^{171}Yb^+$ ion clock. The blue dashed line represents 3.5×10^{-11} $\tau^{-1/2}$. The inset shows the typical signal of the clock resonance (Rabi fringes) with the microwave pulse length is 200 ms. The figure is extracted from [68].

2.5.6 Resume of compact atomic clocks

Table 4 resumes typical performances of best laboratory-prototype vapour cell clocks. We clearly identify some prototypes with best frequency stability performances in the range of a few 10^{-13} $\tau^{-1/2}$: the CW Rb clock (UNINE), the POP clock with optical detection (INRIM), the pulsed Cs CPT clock (LNE-SYRTE) and the cold atom HORACE clock (LNE-SYRTE). These frequency standards present a high potential for high performance and compacity. Among them, current performances of the POP clock with optical detection (INRIM) and the pulsed Cs CPT clock (LNE-SYRTE) remain far from being at the shot noise level.
It is thought that the Cs CPT clock has a great potential for improvement of performances and further compacity. In that sense, the main goal of my PhD thesis was to develop a simple-architecture laser system at 895 nm to demonstrate the detection of high-contast CPT resonances in Cs vapour cells. This study will be a basis for the development of a future high-performance and compact Cs CPT clock. Obviously, some studies in this thesis were done in close collaboration with researchers from LNE-SYRTE of Paris Observatory.

Table 4: Resume of best laboratory-prototype vapour cell clocks typical performances. FWHM: clock signal linewidth; SNR: signal-to-noise ratio of the clock resonance in a 1 Hz bandwidth; C: contrast of the resonance = ratio between the signal height and the dc background; FL: fundamental limit (shot noise or thermal noise, best achievable frequency stability at 1 s; x: not known or not measured.)

Atomic clock	FWHM (Hz)	SNR	C (%)	σ_y(1s)	σ_y(1000s)	FL (1s)
CW Rb clock (UNINE)	361	2.2×10^5	25	2.4×10^{-13}	7×10^{-15}	5.5×10^{-14}
POP μ (INRIM)	54	x	x	1.2×10^{-12}	3×10^{-14}	1×10^{-12}
POP opt (INRIM)	150	x	33	1.7×10^{-13}	6×10^{-15}	2×10^{-14}
POP opt (China)	125	840	90	2×10^{-12}	2.5×10^{-14}	¡1 $\times 10^{-13}$
CPT maser (INRIM)	210	21×10^3	x	3×10^{-12}	4×10^{-12}	7×10^{-13}
CW CPT (Zhu)	218	2.6×10^4	22	1.5×10^{-12}	2×10^{-13}	x
CW CPT (Knappe)	100	1100	x	1×10^{-11}	2×10^{-12}	x
Pulsed CPT (LNE-SYRTE)	125	4×10^4	12	3.2×10^{-13}	3×10^{-14}	2×10^{-14}
MCAFS (Shah)	50	x	x	2×10^{-11}	x	1×10^{-12}
Horace (LNE-SYRTE)	20	900	x	2.2×10^{-13}	5×10^{-15}	1×10^{-13}

3 CPT Physics

3.1 Three energy level Λ-system

CPT resonance [52] [53] is a type of quantum interference process that can be most of the time described by a simple three energy level Λ-system which can be easily found in the D lines of alkali atoms (Cs, Rb, K etc.). It occurs when two phase coherent optical lines couple two ground states of an atomic specie to a common excited state and an excited state of alkali atoms (Cs, Rb, K etc.). When the frequency difference between these two optical lines is exactly equal the ground state hyperfine splitting atoms do not absorb photons anymore. In this case, the atoms are trapped in a so-called dark state. Under ideal conditions (isolated Λ-system, no ground-state decoherence), all the atoms involved into the CPT interaction can be trapped into the dark state, which is fully decoupled from the excited state. In this particular state, a narrow peak CPT resonance signal is observed through EIT [73]. CPT resonance signal has been widely investigated for precision sensing in view of applications in high resolution spectroscopy, magnetometers [74], laser cooling [9], slow light [75] or quantum frequency standards [76].

The three energy level Λ-system is composed by two frequency-separated long-lived ground states $|1\rangle$ and $|2\rangle$ at energies $\hbar\Omega_1$ and $\hbar\Omega_2$ respectively, where $\hbar = \frac{h}{2\pi}$ and Ω is angular frequency. These two states are splitted by a frequency $\Delta_{HFS} = \Omega_2 - \Omega_1$ as well as a common excited state $|3\rangle$. In our case, Δ_{HFS}=9 192 631 770 Hz for Cs atoms (Figure 53). We consider a bichromatic light field with frequencies ω_1 and ω_2 that couples each ground state to the excited state.

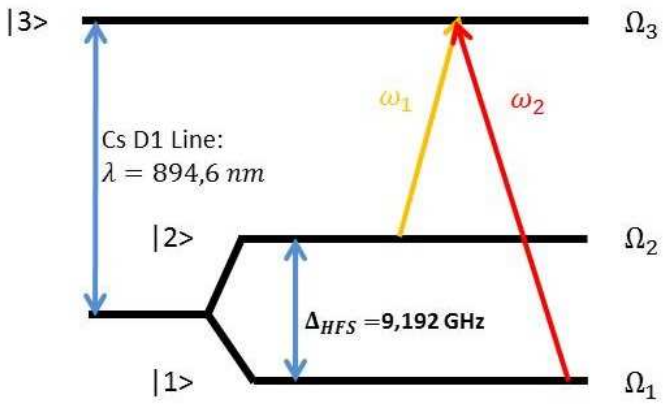

Figure 53: Cs three energy level Λ-system for CPT interaction.

The total light field $E(t)$ can be described by:

$$E(t) = E_1 exp(-i\omega_1 t + i\varphi_1) + E_2 exp(-i\omega_2 t + i\varphi_2) \tag{23}$$

where ω_1 and ω_2 are angular frequencies of the light field, φ_1 and φ_2 are phases of the light field.

The interaction between atoms and bichromatic light field can be described by the Hamiltonian:

$$\widehat{H}_{int} = \frac{\hbar g_1}{2} e^{-i\omega_1 t + i\varphi_1} \mid 3\rangle\langle 1 \mid + \frac{\hbar g_2}{2} e^{-i\omega_2 t + i\varphi_2} \mid 3\rangle\langle 2 \mid + h.c. \tag{24}$$

The interaction strength is included in the Rabi frequencies:

$$g_j = -\frac{\langle 3 \mid e\widehat{r} \mid j\rangle}{\hbar} E_j, \qquad j \in \{1, 2\}. \tag{25}$$

In the three energy levels Λ-system, the coupled state and the non-coupled state are defined as: $\mid C\rangle$ and $\mid NC\rangle$. They are described in Equation 26.

$$\begin{aligned} \mid C\rangle(t) &= \frac{1}{\sqrt{|g_1|^2 + |g_2|^2}} (g_1 e^{-i\Omega_1 t} \mid 1\rangle + g_2 e^{-i\Omega_2 t + i(\varphi_2 - \varphi_1)} \mid 2\rangle) \\ \mid NC\rangle(t) &= \frac{1}{\sqrt{|g_1|^2 + |g_2|^2}} (g_2 e^{-i\Omega_1 t} \mid 1\rangle - g_1 e^{-i\Omega_2 t + i(\varphi_2 - \varphi_1)} \mid 2\rangle) \end{aligned} \tag{26}$$

The non coupled state $\mid NC\rangle$ is an eigenstate of the interaction Hamiltonian $\widehat{H}_{int}$. The excitation amplitudes of the coupled state $\mid C\rangle$ and the non coupled state $\mid NC\rangle$ are given by Equation 27.

$$\begin{aligned} \langle 3 \mid \widehat{H}_{int} \mid C\rangle(t) &= \frac{\hbar}{2\sqrt{|g_1|^2 + |g_2|^2}} e^{-i(\Omega_1 + \omega_1)t + i\varphi_1} (g_1^2 + g_2^2 e^{i\delta_R t + i(\varphi_2 - \varphi_1)}) \\ \langle 3 \mid \widehat{H}_{int} \mid NC\rangle(t) &= \frac{\hbar g_1 g_2}{2\sqrt{|g_1|^2 + |g_2|^2}} e^{-i(\Omega_1 + \omega_1)t - i\varphi_1} (1 - e^{i\delta_R t - i(\varphi_2 - \varphi_1)}) \end{aligned} \tag{27}$$

where δ_R is the Raman detuning which equals $\omega_1 - \omega_2 - \Delta_{HFS}$. From these equations, we can see that the excitation is impossible in the non coupled state when the Raman detuning $\delta_R = 0$ and the phase differences $\varphi_2 - \varphi_1 = 2n\pi$, so the non coupled state is called dark state. The excited conditions indicate that if the frequencies or phases of the bichromatic light field fluctuate, the atoms will be excited to the excited state again.

3.2 Frequency stability performances: a first approach

Figure 54 shows a typical normalized CPT resonance.

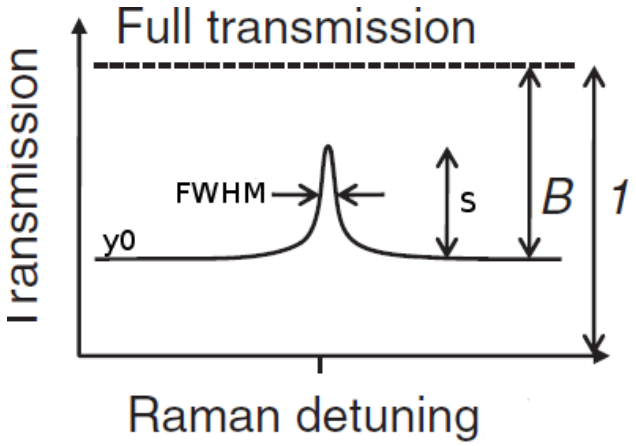

Figure 54: Normalized CPT resonance.

Let's define the full width at half maximum (FWHM) of the resonance (FWHM = $\Delta\nu$) and S the peak-peak height of the resonance. The resonance contrast C is defined as the ratio between the height S and the dc background y_0 (see figure 54)

$$C = \frac{S}{1-B} = \frac{S}{y_0} \tag{28}$$

The absorption contrast C_A (assuming $B << 1$) is:

$$C_A = \frac{S}{B} \tag{29}$$

The condition $B << 1$ stands when the cell temperature and the cell length are such that the vapor is optically thin. If $B << 1$, the signal S is associated to the transmitted optical power change when the local oscillator frequency is swept around the CPT resonance. The out-of-CPT-resonance absorption can be written:

$$B = 1 - \exp[-\alpha L] = 1 - \exp[-n\sigma L] \sim n\sigma L \tag{30}$$

with n the alkali density, L the cell length, σ the optical cross-section and α the absorption coefficient (later defined). The amplitude maximum of the signal A is then:

$$A = SP_{in} = C_A n\sigma L P_{in} \tag{31}$$

with P_{in} the incident optical power in the cell. We observe that the signal is proportional to the alkali density, the incident power and the absorption contrast C_A. In practice, the typical value of C_A is 0.1 - 10%. Experimentally, it has been demonstrated for cm-scale cells that the optimum CPT signal is typically obtained for $C_A = 0.5$.

The noise on the signal comes from different sources such as the laser relative intensity noise, the laser frequency noise, the local oscillator noise, the detector noise. The fundamental and ultimate noise is the photon shot noise. The power spectral density function of this (optical power) noise is given by [77]:

$$S_{\Delta P} \equiv N^2 = 2h\nu_{opt}(1-B)P_{in} = 2h\nu_{opt}(1-\sigma nL)P_{in} \tag{32}$$

with N the noise and $h\nu_{opt}$ the energy of a single photon.
The signal-to-noise ratio can be expressed in terms of the CPT resonance parameters above as:

$$\frac{S}{N} = SNR = C_A n\sigma L\sqrt{\frac{(1-n\sigma L)P_{in}}{2h\nu}} \tag{33}$$

Expressed in this way, the signal-to-noise ratio is proportional to the optical absorption contrast and the square root of the input power, but has a somewhat complicated dependence on the alkali atom density and cell length. To simplify this problem, the signal-to-noise ratio can be expressed instead in terms of the transmission contrast C and the output power $P_{out} = y_0 P_{in}$:

$$\frac{S}{N} = SNR = C\sqrt{\frac{P_{out}}{2h\nu_{opt}}} \tag{34}$$

In this expression, all of the effects of the alkali density are contained within the parameters P_{out} and C, which can be measured experimentally in a direct manner. We see therefore that the characterization of the CPT resonance in terms of the absorption contrast C_A allows for a density- independent measure of the CPT resonance parameters, while the characterization in terms of the transmission contrast C allows for a simple evaluation of the signal-to-noise ratio and clock stability. In the following, we study the impact of main experimental parameters on the CPT resonance.

3.3 CPT resonance linewidth

The full width at half maximum (FWHM) of a CPT resonance signal in an optically thin medium and low laser intensity regime can be described by [76]:

$$\text{FWHM} = \frac{1}{\pi}(\gamma_2 + \frac{\omega_R^2}{\Gamma^\star}) \tag{35}$$

where γ_2 is the hyperfine ground state coherence relaxation rate, Γ^* is the excited state decay rate or linewidth of the optical resonance and ω_R is the optical Rabi pulse related to the laser intensity I as:

$$\omega_R^2 \propto I \tag{36}$$

The optical pumping rate Γ_p is defined as:

$$\Gamma_p = \frac{\omega_R^2}{\Gamma^\star} \tag{37}$$

The CPT resonance FWHM increases with increased laser intensity. Figure 55 shows an example FWHM of resonance signal measured as a function of laser intensity with a Cs-Ne cell (Diameter = 2 cm, length = 2.5 cm, Ne pressure = 9.7 kPa) [78].

When the laser intensity equals zero, the FWHM is only limited by the hyperfine ground state coherence relaxation rate γ_2. Different relaxation mechanisms can affect the ground state coherence. The CPT resonance FWHM is mainly limited by collisions between the Cs atoms and the cell walls in low density regime, and spin exchange collisions of Cs atoms themselves play a more important role in high density regime. In general, a buffer gas is introduced in the alkali atoms vapor cell in order to reduce the FWHM. With the presence of buffer gas, the diffusive motion of the Cs atoms in the cell reduces the residual Doppler broadening through the Lamb-Dicke effect [34] [79]. The buffer gas can also slow down the atoms to reach the cell

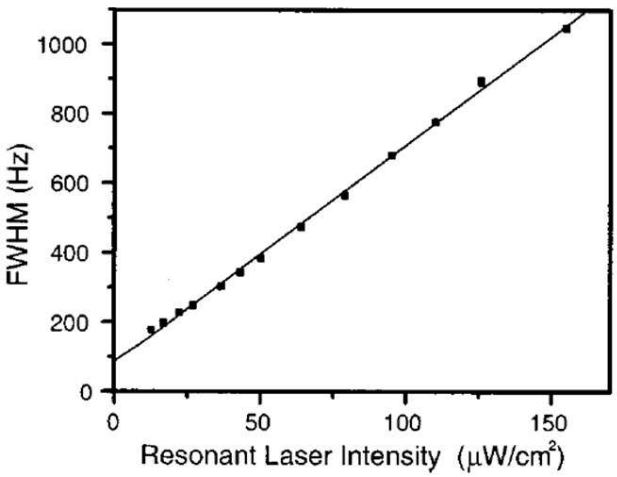

Figure 55: FHWM of resonance signal measured as a function of laser intensity with a Cs-Ne cell (Diameter=2 cm, length=2.5 cm, Ne pressure=9.7 kPa). The figure is extracted from [78].

walls. However, the buffer gas also brings a new relaxation mechanism caused by Cs-buffer gas collisions. The hyperfine ground state coherence relaxation rate γ_2 is given by:

$$\gamma_2 = \gamma_w + \gamma_{se} + \gamma_{csbg} \tag{38}$$

The first term γ_w in the equation (38) presents the collisions between the Cs atoms and the cell walls. It can be described as:

$$\gamma_w = [(\frac{2.405}{R})^2 + (\frac{\pi}{L})^2]D_0\frac{P_0}{P} \tag{39}$$

where L and R present respectively the length and the radius of the vapor cell, D_0 is the diffusion constant of Cs atoms in buffer gas with pressure $P_0 = 101.3\,\text{kPa}$ (for $Cs - Ne$, $D_0 = 0.153 \pm 0.014\text{cm}^2/s$; for $Cs - N_2$, $D_0 = 0.087 \pm 0.015\text{cm}^2/s$; for $Cs - Ar$, $D_0 = 0.134 \pm 0.02\text{cm}^2/\text{s}$ [59]), and P is the buffer gas pressure. This equation shows that γ_w is inversely proportional to the buffer gas pressure P for given cell dimensions. This CPT linewidth contribution is increased when the buffer gas pressure is increased.

The second term γ_{se} represents the contribution to the ground state coherence of the Cs spin exchange collisions, which is given by:

$$\gamma_{se} = \frac{6I+1}{8I+4}\overline{v_r}n_{cs}\sigma_{se} \tag{40}$$

with I is the nuclear spin quantum number ($I = 7/2$ for Cs), $\sigma_{se} = (2.18 \pm 0.12) \times 10^{-14}$ cm^2 the Cs spin exchange cross-section [80] and n_{cs} presents the density of Cs atoms. $\overline{v_r}$ is the average velocity of Cs atoms which relates to the cell temperature T:

$$\overline{v_r} = \sqrt{\frac{8k_BT}{\pi\mu_{cs}}} \tag{41}$$

where $k_B = 1.38 \times 10^{-23}$ JK^{-1} is the Boltzmann constant and $\mu_{cs} = 66.5$ stands for the Cs reduced mass.

The last term γ_{csbg} presents the alkali-buffer gas collisions, which is described by:

$$\gamma_{csbg} = L_0\overline{v}_{rel}\sigma_{csbg}\frac{P}{P_0} \tag{42}$$

where $L_0 \simeq 2.69 \times 10^{25}$ m^{-3} is the Loschimdt constant, $\overline{v}_{rel}$ is the relative velocity of Cs atoms with respect to buffer gas, and σ_{csbg} is the collisional cross-section between Cs and buffer gas (for $Cs - Ne$, $\sigma_{csbg} = 9.3 \pm 0.9 \times 10^{-23}$cm^2; for $Cs - N_2$, $\sigma_{csbg} = 60 \pm 4.4 \times 10^{-23}$cm^2; for $Cs - Ar$, $\sigma_{csbg} = 104 \pm 10 \times 10^{-23}$cm^2 [59]). This type of collisionally broadened width is proportional linearly to the buffer gas pressure P.

As an example, figures 56(a), 56(b), 56(c) and 56(d) show the linewidth contribution for each process described above for a Cs vapor microcell filled with a Ne buffer gas pressure. Experimental data are $L =$ 1.4 mm, $D = 2$ mm and $T = 80$ °C.

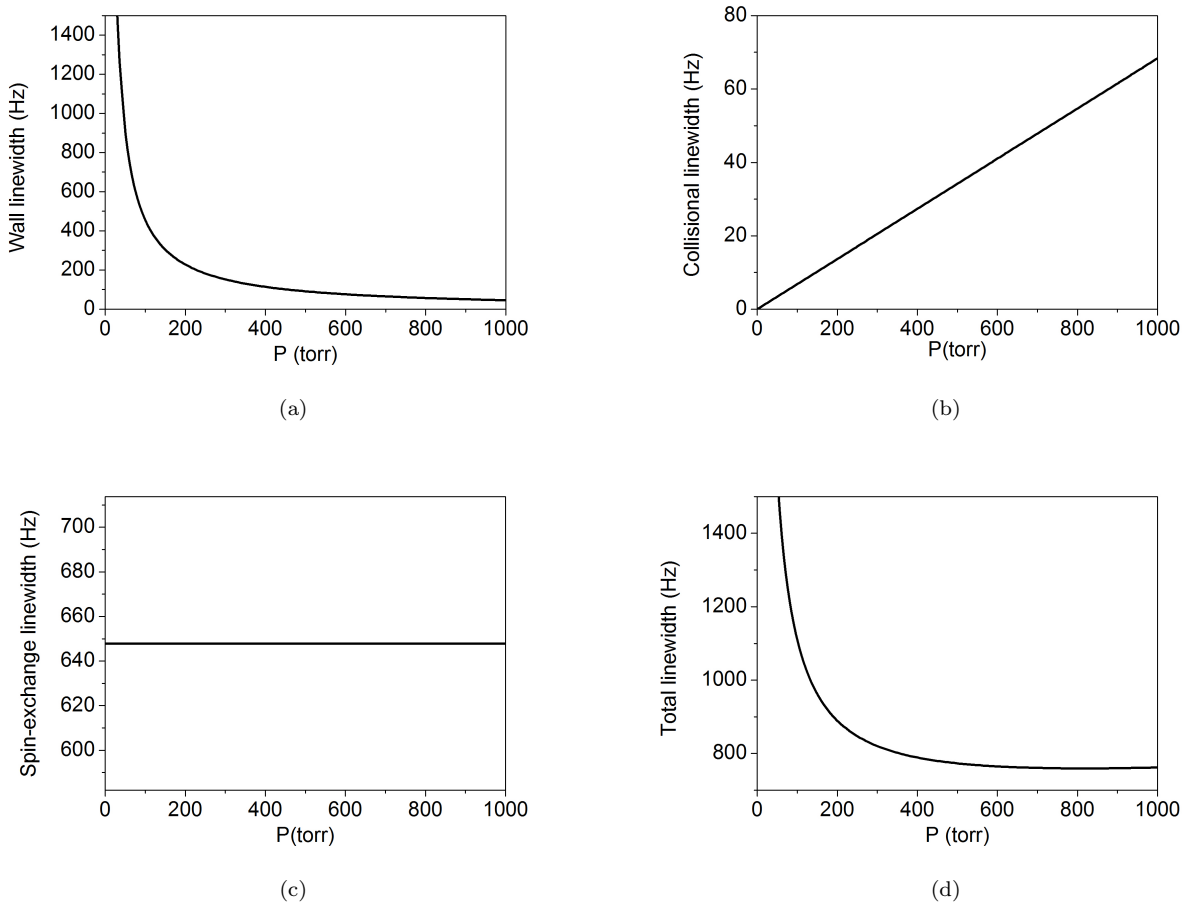

Figure 56: Contributions of collisions on the CPT linewidth in a Cs-Ne microcell (L=1.4mm, D=2mm, T=80°C) versus the Ne pressure.(a): atoms-walls; (b): atoms-buffer gas; (c):Cs-Cs; (d): total linewidth

The CPT linewidth due to atom-wall collisions is decreased when the buffer gas pressure is increased because the time for the atoms to reach the cell walls is increased. At the contrary, the increase of buffer gas pressure increases the linewidth contribution due to atom-buffer gas collisions. The spin-exchange linewidth contribution essentially depends on the Cs denstiy, i. e the cell temperature. For such a mm-scale cell, the total CPT resonance is minimized for a Ne buffer gas pressure of about 750 Torr. This optimum is found to be of a few tens of Torr in a cm-scale cell.

3.4 CPT resonance signal height

The CPT resonance signal height H can be derived by the population difference in excited state in resonance and off resonance, which is given by:

$$H \propto n_{cs} \frac{\omega_R^4}{\Gamma^\star} \frac{1}{2\gamma_2 + \omega_R^2/\Gamma^\star} \tag{43}$$

where n_{cs} is the number density of Cs, ω_R is the optical Rabi pulse, $\Gamma^\star$ is the exited state decay rate or linewidth of the optical resonance and γ_2 is the hyperfine coherence relaxation rate.

Figure 57 shows an example of height of resonance signal measured in a Cs-Ne cell (Diameter = 2 cm, length = 2.5 cm, Ne pressure = 5.1 kPa) as a function of laser intensity [78]. The signal height increases quadratically with increased laser intensity in low intensity regime and linearly in high intensity regime.

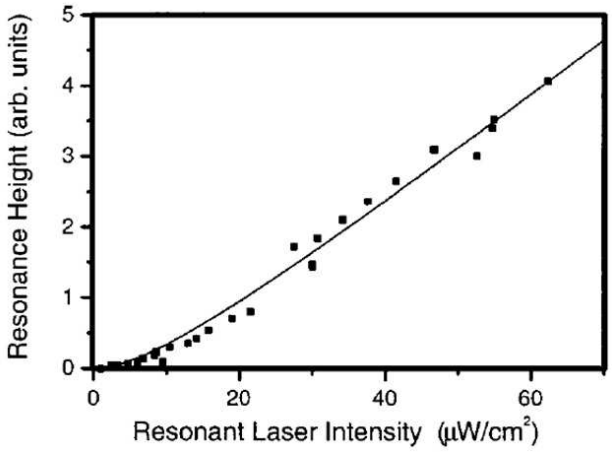

Figure 57: Height of resonance signal measured in a Cs-Ne cell (Diameter = 2 cm, length = 2.5 cm, Ne pressure = 5.1 kPa) as a function of laser intensity. The figure is extracted from [78].

Since γ_2 is related to the contribution of alkali-buffer gas collisions γ_{csbg}, the CPT resonance signal height is influenced by the buffer gas pressure. Indeed, optical atomic transitions of alkali atoms can be broadened and shifted by alkali atoms-buffer gas collisions [81]. For illustration, examples of pure Cs and Cs-Ne (buffer gas pressure = 90 Torr) absorption spectra on Cs D_1 line are shown in the figure 58 [59]. The comparison between the atomic transition of pure Cs and Cs + 90 Torr Ne shows the optical broadening and shift of optical transitions. The Cs-Ne collisional relaxation decreases the optical pumping rate and reduces the CPT signal height H. Figure 59 shows the height of a CPT signal generated with a microfabricated Cs-Ne cell (D = 2 mm, L = 1.4 mm) in a temperature of 80 °C as a function of the Ne pressure under different laser intensities. The signal height H is decreased when Ne pressure is increased. The CPT resonance signal height is proportional to the number density n_{cs}, which increases with the vapor temperature. At the same time, the Cs vapor becomes optically thick at high temperature. The output laser power P_{out} of the alkali atoms vapor cell depends on the input laser power P_{in} and the absorption coefficient α:

$$P_{out} = P_{in} e^{-\alpha L} \tag{44}$$

where

$$\alpha = \frac{\Gamma^{\star}\lambda^3 n_{cs}}{8\pi}\sqrt{\frac{m_{cs}}{2\pi k_B T}} \tag{45}$$

where λ is the wavelength of the laser and m_{cs} is the Cs atom mass.

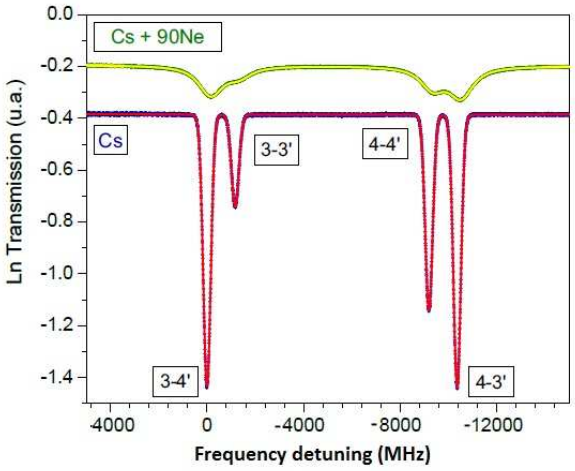

Figure 58: Examples of pure Cs and Cs + 90 Torrs Ne absorption spectra on Cs D_1 line.

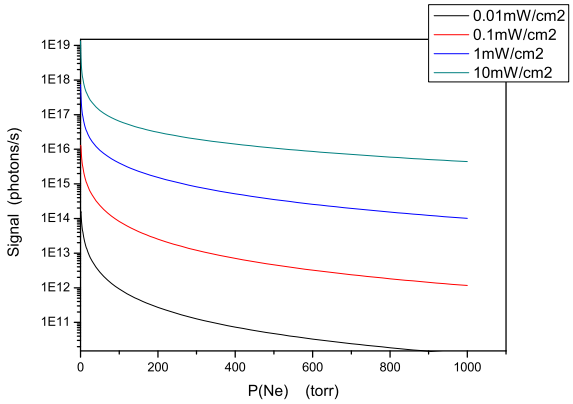

Figure 59: CPT signal height as a function of Ne pressure under different laser intensities with a microfabricated Cs-Ne cell (D = 2 mm, L = 1.4 mm) at 80 °C.

By considering the equation 44 and the equation 45 together, the output laser power P_{out} decreases with the increase of alkali atoms vapor temperature T, which causes the reduction of the CPT resonance height. The competition between the n_{cs} and the α coefficient determines that an optimal vapor temperature exists for a maximal CPT signal height. S. Knappe *et al.* measured the properties of CPT resonance in Cs vapor cm scale cells as a function of the cell temperature [82]. R. Boudot *et al.* [83] reported a similar study for Cs-Ne microcells with different Ne pressure. In the figure 60, the CPT resonance signal increases with the Cs density n_{cs} in the low cell temperature regime. When the cell temperature rises to around 50 - 60 °C, the Cs vapor becomes optically thick and the CPT resonance signal starts to decrease. For the even higher cell temperature, the CPT resonance signal drops rapidly and nearly vanishes completely at about 85 °C. The measured curves agree well with the theoretical explanations above. Meanwhile, by comparing

these three different curves, we can see that the CPT signal height is also decreased with higher buffer gas pressure. This phenomenon can be explained by the expression of γ_{csbg} (Equation 42). The γ_{csbg} term is linearly proportional to the buffer gas pressure, which means it is inversely proportional to CPT signal height (Equation 43). In this Cs-Ne microfabricated cell, the optimal temperature for a maximal CPT signal height is around 55 °C. This optimal temperature is shifted to higher temperatures for higher Ne pressure.

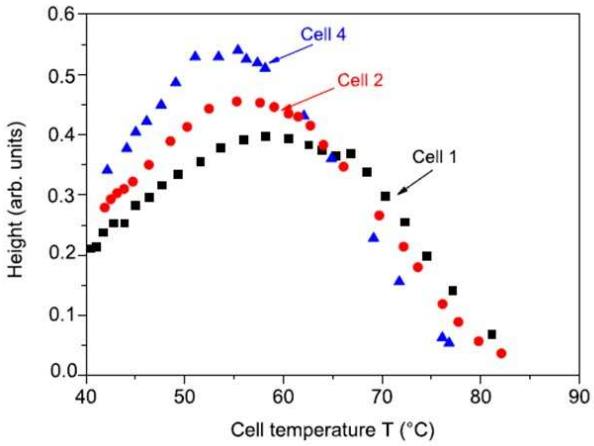

Figure 60: CPT resonance signal height as a function of the cell temperature for three Cs-Ne cells with different Ne pressure (8.1 kPa for cell 1, 6.7 kPa for cell 2 and 4.4 kPa for cell 4). Experimental parameters are: $I = 500\ \mu\text{W/cm}^2$, $P_\mu = 2.5$ dBm. The data are extracted from [83].

3.5 Frequency shifts

Mid-long term frequency stability of an atomic clock is mainly limited by fluctuations of experimental parameters such as temperature variations, laser intensity and frequency variation, magnetic field variation and cell aging. The clock frequency can be shifted by different mechanisms. Main shifts are the Zeeman shift, the collisional shift and the light shift. Basic analysis of each frequency shift is presented in this section.

3.5.1 Zeeman shift

The energy levels of atoms are divided into a number of Zeeman sublevels with the presence of a static magnetic field. Figure 61 shows the evolution of the m_F Zeeman sublevels as a function of the static magnetic field for the Cs atom ground state.

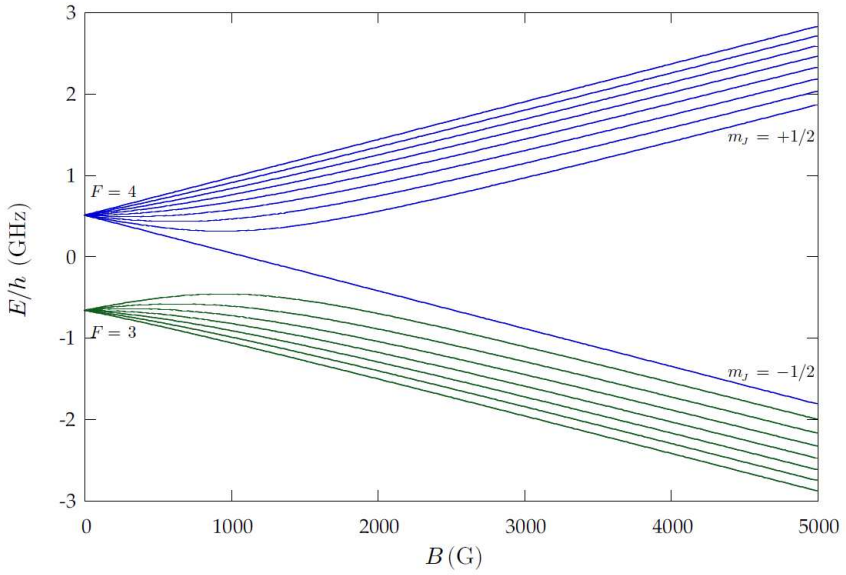

Figure 61: Evolution of the m_F Zeeman energy sublevels as a function of the static magnetic field for the Cs atom ground state (D_1 line). The figure is extracted from [84]

The dependence of the 0-0 clock transition frequency is quadratic to the magnetic field for low B values. The shift of the Cs clock frequency $\Delta\nu_z$ as a function of the magnetic field B is given by:

$$\Delta\nu_z = 427.45B^2 \tag{46}$$

where B is expressed in Gauss.
A variation dB of the static magnetic field produces a change $d(\Delta\nu_z)$ of the Zeeman shift. The clock frequency sensitivity to the static magnetic field is for $B = 60$ mG:

$$\frac{1}{\nu}\frac{d(\Delta\nu_Z)}{dB} = 5.58 \times 10^{-9} \text{per Gauss} \tag{47}$$

A complete reversal of the clock in the earth magnetic field induces a change of 1 Gauss in the magnetic field induction. To get a relative stability objective of 1×10^{-12}, we need to attenuate by a factor of at least

1 000 the magnetic field variations. This is difficult to obtain with a single layer magnetic shield.
The dc magnetic induction B is generated by a current I circulating in a solenoïd or Heltmoltz coils. Rewritting the previous formula for a mean magnetic induction $B = 60$ mG, we get that the relative frequency stability is related to the current source stability by:

$$\frac{d\nu}{\nu} \approx 3.4 \times 10^{-10} \frac{dB}{B} = 3.4 \times 10^{-10} \frac{dI}{I} \tag{48}$$

A relative frequency stability of 1×10^{-12} imposes a relative current stability of 3×10^{-3} with a small sensitivity to temperature changes.

3.5.2 Buffer gas collisional shift

In order to reduce the CPT resonance linewidth, we introduce a pressure of buffer gas into the alkali vapor cell. The presence of buffer gas causes a frequency shift of the hyperfine transition of alkali atoms [85] [86]. When buffer gas atoms are introduced, collisions between alkali atoms and buffer gas atoms cause a distortion of electron clouds of the alkali atom. On the one hand, the Van der Walls force attracts the electrons, and the electrons density is reduced to nucleus, then the hyperfine ground states coherence interaction is decreased. On the other hand, the electron clouds are repush and recover when the alkali atoms approaching the buffer gas atoms, and this approaching rises the electrons density to nucleus. Consequently, the hyperfine ground states coherence interaction increases in this case. The unbalance of these two opposite effects shifts the CPT resonance frequency to positive or negative. For the light buffer gas atoms, such as Ne, He, N_2, the exclusion force is dominant, and the CPT resonance frequency is blueshifted. For heavier buffer gas atoms as Ar, Kr and Xe, the frequency is redshifted, because the Van der Walls force is dominant. Consequently, a classical method to reduce the buffer gas frequency shift is to fill the alkali atoms cell with two buffer gas shifting the clock frequency in opposite directions [87]. In the case of a single buffer gas, the collisional frequency shift $\Delta\nu_{coll}$ can be described by:

$$\Delta\nu_{coll} = P[\beta + \delta(T - T_0) + \gamma(T - T_0)^2] \tag{49}$$

where P presents the buffer gas pressure at the reference temperature $T_0 = 273$ K, and β, δ and γ are pressure and temperature shift coefficients [85] [86]. In the case of a buffer gas mixture, the collisional frequency shift $\Delta\nu_{coll}$ is given by:

$$\Delta\nu_{coll} = P[(r_1\beta_1 + r_2\beta_2) + (r_1\delta_1 + r_2\delta_2)(T - T_0) + (r_1\gamma_1 + r_2\gamma_2)(T - T_0)^2] \tag{50}$$

where β_i, δ_i and γ_i with $i = 1, 2$ are pressure and temperature coefficients for buffer gas 1 and 2 respectively. r_i with $i = 1, 2$ are the ratio between the buffer gas i pressure and the total buffer gas pressure respectively, so $r_1 + r_2 = 1$. The value of β, δ and γ for different buffer gas were measured by different groups [85] [88] [89] [90] [91] [92] [93] . Table 5 shows these pressure and temperature shift coefficient values for Ne, N_2 and Ar of Cs clock transition measured by Kozlova *et al.* [88]. Frequency shift of alkali atoms mixed with different types of buffer gas can be calculated thanks to these shift coefficients.

Figures 62(a), 62(b) and 62(c) show the expected CPT resonance frequency shift versus the cell temperature in different Cs-buffer gas cells (Ne, N_2 and Ar).

In the case of the Cs-Ne cell, the quadratic relation between frequency shift and the cell temperature exists at about 79 °C. In a Cs-N_2 cell, a quadratic relation should exist at about 160 °C. This indicates that

Table 5: Pressure and temperature shift coefficients of the Cs clock transition in presence of Ne, N_2 and Ar (D_1 line).

Buffer gas	β (Hz/Torr)	δ (Hz/(Torr.K))	γ (mHz/(Torr.K^2))
Ne	686 ± 14	0.266 ± 0.006	−1.68 ± 0.05
N_2	922.5 ± 4.8	0.824 ± 0.006	−2.51 ± 0.03
Ar	−194.4 ± 1.6	−1.138 ± 0.010	0.0 ± 0.3

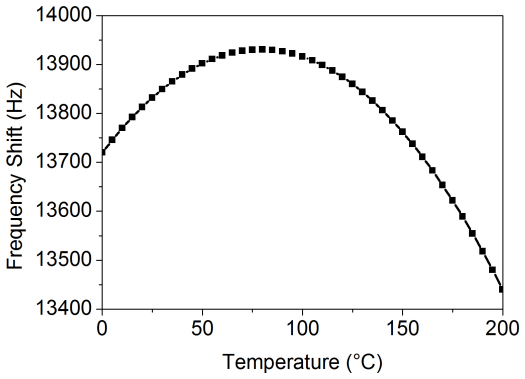

(a)

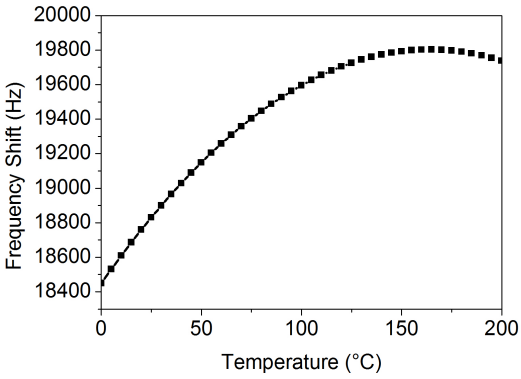

(b)

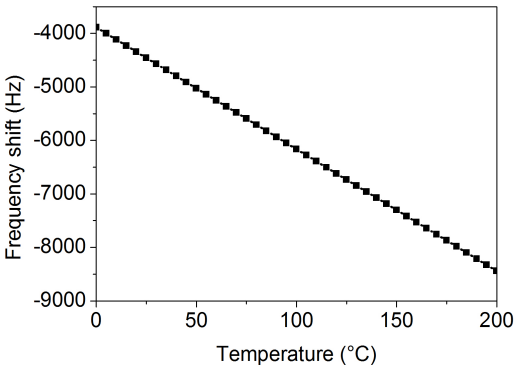

(c)

Figure 62: CPT resonance frequency shift versus the cell temperature. (a): Cs-Ne with a pressure of 20 Torr. (b): Cs-N_2 with a pressure of 20 Torr. (c): Cs-Ar with a pressure of 20 Torr. Coefficients of table 5 are used.

the temperature dependence of the Cs clock frequency is canceled at this so-called inversion temperature. This result is meaningful for developing miniature atomic clocks operating in this temperature range because it avoids to use another suitable buffer gas to compensate the frequency shift [88] [94]. In the Cs-Ar cell, the frequency shift is found to decrease linearly with increased cell temperature.

3.5.3 Light shift

Introduction The light-shift (AC-Stark shift) is the shift of atomic energy levels due to the interaction of the induced atomic dipole moment with the oscillating electric field of the light [95]. The light-shift $\delta\nu_i$ of an atomic level i can be approximated by a sum of dispersive Lorentzians (as a function of a single laser of frequency f_L and intensity $I \sim |\Omega_R^2|$) of width Γ_{ik} centered at the optical atomic transition frequency f_{ik} [96]:

$$\delta\nu_i(f_L, I) = \frac{1}{4}\sum_{k=3}^{4} |\Omega_{Rk}|^2 \frac{(f_L - f_{ik})}{(f_L - f_{ik})^2 + \Gamma_{ik}^2/4} \tag{51}$$

The total light shift $\delta\nu_{00}$ of the microwave atomic clock transition is the difference of the involved ground-state level shifts (including the contribution from the off-resonant excited state by summation over k in Eq. 51:

$$\delta\nu_{00}(f_L, I) = \delta\nu_4(f_L, I) - \delta\nu_3(f_L, I) \tag{52}$$

The light-shift $\delta\nu_{00}$ of the clock transition is shown schematically in Fig. 63 b, as a function of the frequency f_L for a monochromatic laser field varied around the Cs D_1 transition. In the case of a multi-frequency laser spectrum, e.g. for CPT induced with a frequency-modulated laser, the total light-shift is obtained as the sum over the contributions from all existing laser frequency components f_j with their respective intensities I_j:

$$\delta\nu_{00}(f_L, I) = \sum_j [\delta\nu_4(f_j, I_j) - \delta\nu_3(f_j, I_j)] \tag{53}$$

where f_L is the laser carrier frequency (j=0) here and $j \neq 0$ numbers the modulation sidebands. A typical case of a multi-frequency laser spectrum used for CPT excitation is depicted in Fig. 63 c.

In an atomic clock application, the light-shift can be expressed locally (i.e. at a given laser frequency and laser intensity) by coefficients known as the intensity light-shift coefficient α_i and the frequency light-shift coefficient β_i, by partial derivation of Equation 52 and 53:

$$\alpha_i(f_L, I) = \frac{d\nu_{00}}{dI} \tag{54}$$

$$\beta_i(f_L, I) = \frac{d\nu_{00}}{df_L} \tag{55}$$

Calculation of light shifts is complicated. Results are highly dependent on the experimental conditions and laser field characteristics. With modulated laser sources, light shift slopes can be nulled or at least greatly reduced by adjusting the RF modulation power [83] or the cell temperature [97]. Active light shift cancelation techniques can be implemented [98] [99]. We report in Table 6 typical reported values of α_i and β_i.

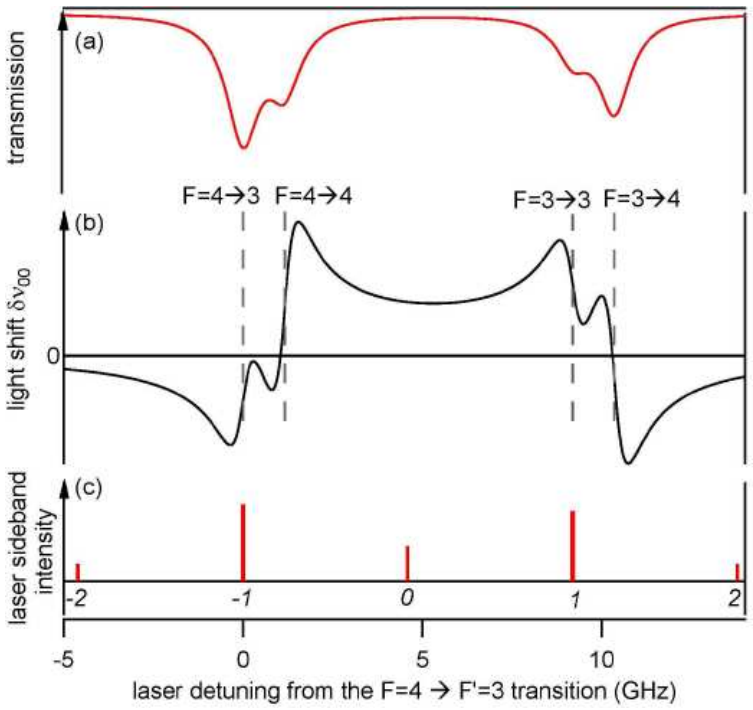

Figure 63: Schematic view of light-shift in the case of CPT on the Cs D1 line. a) example of an optical transmission spectrum for a thermal Cs vapour, showing line broadening by a buffer-gas. b) frequency-dependence of the light-shift $\delta\nu_{00}$ of the clock transition in presence of one single light frequency f_L only. The dashed vertical lines indicate the positions of the optical transitions. c) typical example of a multi-frequency laser spectrum, for CPT excitation by the positive and negative first-order sidebands. Italic numbers give the order j of each sideband.

Table 6: Reported values of α and β in different configurations. The values for β are normalized to the resonant laser intensity of $I = 45\mu\mathrm{W/cm}^2$ used in [78]. The line labelled "I_{-1} / I_0 / I_{+1}" gives the percentage of total light intensity contained in the -1^{st}-order sideband, the carrier, and the +1^{st}-order sideband in the respective studies (CPT is induced using the two first-order sidebands in all cases).

Reference	Nagel *et al.* [100]	Knappe *et al.* [78]	Lutwak *et al.* [101]	Boudot *et al.* [83]	Miletic *et al.* [97]
Transition	D_2	D_2	D_2	D_2	D_1
Buffer gas	Ne	Ne	N_2-Ar	Ne	Ne
Laser	PLL ECLD	VCSEL	VCSEL	VCSEL	DFB+EOM
$\mathrm{I}_{-1}/\mathrm{I}_0/\mathrm{I}_{+1}$ [%]	60/0/40	19/8/47	no data	14/14/33	32/16/35
α_i $[\mu\mathrm{W/cm}^2)^{-1}]$	8.7×10^{-10}	1.08×10^{-10}	1.6×10^{-10}	-3.2×10^{-12}	-1.7×10^{-13}
β_i [mHz/MHz]	no data	-20	no data	no data	-11

As an example, for laser frequency fluctuations, assuming a value of -20 mHz/MHz, we get:

$$\frac{1}{\Delta f_L}\frac{\Delta\nu_0}{\nu_0} = 2.2 \times 10^{-12}/MHz \tag{56}$$

Models J. Vanier *et al.* [102] and T. Zanon *et al.* [103] proposed different models to describe the light shift. Both models are briefly described in the following.

J. Vanier model

The light shift in CPT resonance is considered to be a sum of light shift caused by a single optical field. Then, the light shift Δ_{LS} of the hyperfine sublevels transition frequency Δ_{HFS} is given by:

$$\Delta_{LS} \sim \frac{-\Delta_0}{\Delta_0^2 + (\Gamma^\star/2)^2}(\omega_1^2 - \omega_2^2) \tag{57}$$

where ω_1 and ω_2 are the Rabi frequencies, and $\Gamma^\star = \Gamma_{31} + \Gamma_{32}$ is the excited decay rate.
In the low laser power regime, the relation between light shift and total laser power is linear with a coefficient $\alpha = \Delta_{LS}/\delta P_L$. The light shift also depends on the power difference between two optical fields $(\omega_1^2 - \omega_2^2)$. In this case, the coefficient between light shift and light power can be rewritten as $\alpha_{1,2} = \Delta_{LS}/\delta P_{L1,L2}$, where $P_L = P_{L1} + P_{L2}$. According to Equation 57, the lightshifts in the two hyperfine levels are equivalent when two optical fields powers are the same, and the light shift as a function of input laser power has a Lorentzienne lineshape. In the paper of J. Vanier *et al.,* [102], the linear dependence of light shift on the light field detuning Δ_0 is canceled, but a quadratic dependence on the light field is observed, which is not explicated in the paper.

T. Zanon model

The J. Vanier model indicates that light shift relates to hyperfine ground state coherence, but the Equation 57 does not include the term correspond to this coherence. T. Zanon *et al.,* proposed a light shift equation that contains the hyperfine ground state coherence (Equation 58) [103].

$$\Delta_{maximum} \simeq \Delta_0 \frac{\gamma_2}{2\gamma_{opt}} \frac{2\gamma_2\Gamma^\star S - (\omega_1^2 - \omega_2^2)}{2\gamma_{opt}\gamma^* + \Gamma^\star\gamma_2 S} \tag{58}$$

where $\Gamma^\star = \Gamma_{31} + \Gamma_{32}$ is the excited decay rate, and $\Gamma_{31} = \Gamma_{32}$ for alkali atoms, γ_2 is the hyperfine coherence relaxation rate, γ_{opt} is the optical coherence relaxation rate and we assume the relaxation rates to $|1\rangle$ and $|2\rangle$ are the same, $\gamma^* = \frac{\omega_1^2+\omega_2^2}{4\gamma_{opt}}$ is a power enlargement, and $S = \frac{\omega_1^2\omega_2^2}{\gamma_{opt}\Gamma^\star(\omega_1^2+\omega_1^2)}$. Then we have:

$$\Delta_{maximum} \simeq \Delta_0 \frac{\gamma_2}{\gamma_{opt}} \frac{2\gamma_2\omega_1^2\omega_2^2 - \gamma_{opt}(\omega_1^4 - \omega_2^4)}{2\gamma_2\omega_1^2\omega_2^2 + \gamma_{opt}(\omega_1 + \omega_2)^2} \tag{59}$$

When $\gamma_2 = 0$, the light shift is zero, which means the atoms are completely decoupled with light fields. The light shift increases linearly with the light field detuning increases. If two light fields powers are equivalent, the light shift is low, otherwise, the variation of light shift is very complicate when two light fields powers are different.

3.6 Optimized CPT pumping schemes

3.6.1 Overview

In a simple approach, the CPT phenomenon can be well represented by a simple three energy level Λ-system. Nevertheless, the actual energy structure of atoms is much more complex. Each energy level is splitted into several Zeeman sublevels in the presence of a static magnetic field. Among the atomic transitions between the different Zeeman sublevels, the ground state transition between $m_F = 0$ Zeeman sublevels is the clock transition.

A promising technique to improve the frequency stability performances of CPT atomic clocks is to increase the resonance contrast. In that sense, let us first remind that the D_1 line of alkali atoms is the best candidate for the development of CPT atomic clocks [104]. Compared to the D_2 line, the D_1 line allows the detection of narrower resonances with higher contrast, i.e. to increase the number of atoms participating to the $0 - 0$ clock transition. Figure 64 shows a CPT resonance in similar experimental conditions using the D_1 or D_2 line.

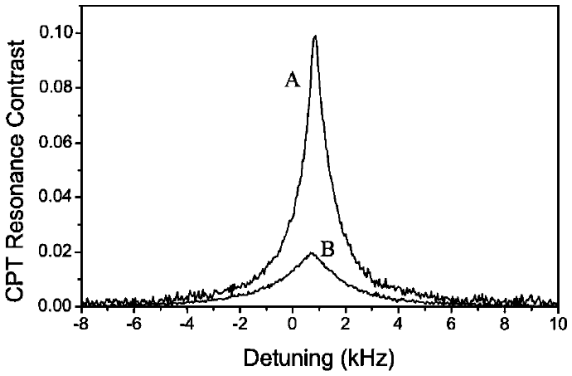

Figure 64: CPT resonance in similar experimental conditions using the D_1 (A) or D_2 line (B) (Rb atom). From [104].

The advantage of the D_1 line is simply due to the fact that there is a smaller number of energy levels in the hyperfine structure. The distribution of atoms among a multiple number of Zeeman sublevels is then reduced. Moreover, frequency splitting between both excited states is higher on the D_1 line (1.16 GHz for the Cs atom D_1 line instead of about 250 MHz on the Cs D_2 line). On the Cs D_2 line, excited states $F' = 2$ and $F' = 5$ act as loss-channels because each of them is coupled to one of the ground states only. Atoms in the superposition state can then be excited through one-photon transitions to these states, increasing the width of the resonance and reducing the CPT signal. In classical CPT atomic clocks, atoms interact with circularly polarized bichromatic optical field. Figure 65 shows an interaction scheme of a right circular polarized bichromatic light with Cs atoms on the D_1 line. Figure 66 shows an example of Zeeman sublevels transitions signals generated by left and right circular bichromatic light fields with a microfabricated Cs-Ne cell we measured. With use of circular polarization, it is observed that numerous atoms are concentrated in the extreme Zeeman magnetic sublevels with the highest angular momentum m_F. Consequently, only a small fraction of atoms participates to the magnetic-field-insensitive clock transition, resulting in CPT resonances with very low contrast of about 1 or a few %. Higher CPT resonance contrast can be achieved by increased laser intensity but at the expense of the CPT linewidth power broadening. Consequently, classical

CPT atomic clocks operate with low laser intensity in order to minimize the ratio between linewidth and contrast, to optimize the short term frequency stability of the clock.

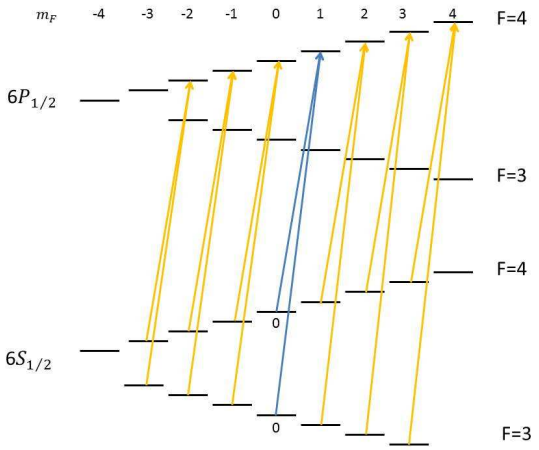

Figure 65: The interaction scheme of right circular bichromatic light field-Cs atoms.

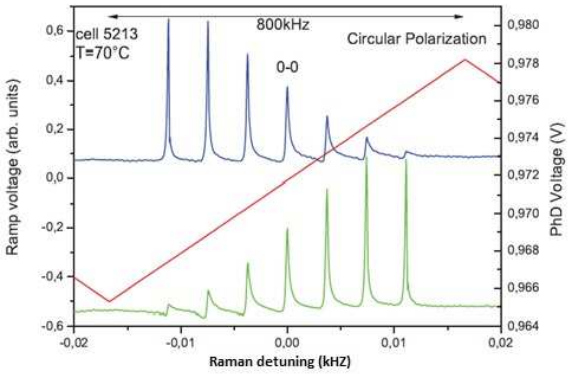

Figure 66: Example of Zeeman sublevels transitions signals generated by left (blue) and right (green) circular polarized bichromatic light fields.

In order to optically pump the maximum number of atoms into the dark state out of any other trap state, different optimized CPT pumping schemes were proposed in the literature. Jau *et al.* proposed the so-called Push Pull Optical Pumping (PPOP) technique. In this method, alkali atoms interact with a D_1 line resonant bichromatic optical field separated into left and right circular polarized sub-optical fields, with one sub-optical field delayed with respect to the other by a half period of the ground state hyperfine transition [28] (Figure 67 (a)). The resulting optical field can be thought as alternating between the states of left and right circular polarization. A CPT resonance with contrast of 30 % was achieved in a Rb vapor cell using this pumping scheme. PPOP was used in an elegant mode-locked laser atomic oscillator where a K-vapor cell, inserted in the external cavity of a semiconductor diode laser, acts as an optical modulator and causes the laser to be self-modulated at the clock transition frequency of the atoms [105]. Later, different research groups have realized the PPOP scheme with different architectures [106] [107].

T. Zanon *et al.* demonstrated another optimized pumping scheme: the *lin* $\perp$ *lin* double-Λ interaction scheme using two orthogonally polarized light fields [26] (Figure 67 (b)). CPT resonance contrasts higher than 50% were observed using this technique [27] in Cs vapor cells. A Ramsey-type pulsed sequence was also combined with such a CPT resonance signal to obtain a CPT frequency stability better than 7×10^{-13} $\tau^{-1/2}$ at 1 second [25]. Recently, efforts have been made in different laboratories to realize the *lin* $\perp$ *lin* interaction scheme with only one single laser source and a simple architecture laser system [108] [109] [110]. We demonstrated during my thesis that *lin* $\perp$ *lin* and PPOP are strictly identical under given conditions (see section 3.6.2).

A. V. Taichenachev *et al.,* developed a CPT optimized pumping method based on the use of a $\sigma_+ - \sigma_-$ configuration of polarized counterpropagating wave resonant with alkali atoms D_1 line in small size cells [111]. Essentially, this pumping scheme is equivalent to the PPOP, except that this pumping scheme requires a particular place of the alkali atoms vapor cell along the optical beams and a small cell length comparing to the microwave length. A so-called *lin* $\parallel$ *lin* pumping scheme was also proposed by A. V. Taichenachev *et al.,* (Figure 67 (c)). This pumping scheme uses bichromatic linearly polarized light field to increase significantly the contrast of of CPT resonances on the alkali atoms D_1 line with nuclear spin $I = 3/2$ [112]. A Rb CPT atomic clock prototype was developed based on this interaction scheme [113] [114]. This configuration was also implemented with alkali atoms of large nuclear spin, such as Cs [115]. Nevertheless, the *lin* $\parallel$ *lin* pumping scheme creates a dark state between $m_F = \pm 1$ Zeeman sublevels of both hyperfine levels instead of 0-0 Zeeman sublevels, which means the dark state of *lin* $\parallel$ *lin* is more sensitive to fluctuations of magnetic field.

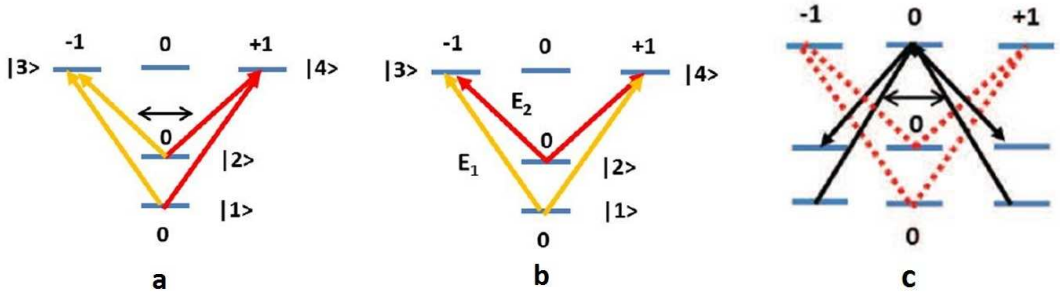

Figure 67: Optimized CPT pumping schemes.a: Push Pull Optical Pumping; b: *lin* $\perp$ *lin*; c: *lin* $\parallel$ *lin*.

3.6.2 Theoretical analysis of push-pull optical pumping

In the frame of my PhD thesis, we developed a theoretical model to analyze the push-pull optical pumping (PPOP) interaction scheme. This scheme is used in the experimental setup we developed and is presented in chapiter 4. This work was conducted and concluded thanks to the precious help of Emeric De Clercq (LNE-SYRTE). We point out that the push-pull interaction scheme is identical to the so-called *lin*$\perp$*lin* polarization scheme. Expressions of the relevant dark states, as well as of absorption, are reported. This model is in correct agreement with experimental observations led in section 5.

Pumping waves The push-pull interaction scheme uses two sets of circularly polarized fields, rotating in opposite directions, propagating along the z axis. Each set contains two frequencies ω_1 and ω_2; one set

is phase delayed with respect to the other one. The right-handed circularly polarized beam, $\overrightarrow{E_r}$, and the left-handed circularly polarized one $\overrightarrow{E_l}$, can be written using the Jones vectors:

$$\begin{cases} \overrightarrow{E_r}(t) = \begin{pmatrix} E_{rx}(t) \\ E_{ry}(t) \end{pmatrix} = \frac{E_1}{2} e^{i(k_1 z - \omega_1 t)} \begin{pmatrix} 1 \\ -i \end{pmatrix} + \frac{E_2}{2} e^{i(k_2 z - \omega_2 t + \eta)} \begin{pmatrix} 1 \\ -i \end{pmatrix}, \\ \overrightarrow{E_l}(t) = \frac{E_1}{2} e^{i(k_1 z - \omega_1 t + \varphi)} \begin{pmatrix} 1 \\ +i \end{pmatrix} + \frac{E_2}{2} e^{i(k_2 z - \omega_2 t + \eta + \varphi')} \begin{pmatrix} 1 \\ +i \end{pmatrix}, \end{cases} \tag{60}$$

where E_1, E_2 are the amplitudes of the rotating fields, k_1 (k_2) is the wave number of the field E_1 (E_2) and η is the phase difference between the two fields. φ, φ' are the phase shifts due to the optical path difference Δz between the E_l and the E_r fields such as:

$$\varphi = k_1 \Delta z, \qquad \varphi' = k_2 \Delta z. \tag{61}$$

As the two optical frequencies ω_1, ω_2 are very close, a beat-note occurs for each beam. For the sake of simplicity the calculation is performed in the case of equal amplitudes $E_2 = E_1$. Equations (60),(61) can be rewritten as :

$$\begin{cases} \overrightarrow{E_r}(t) = E_1 e^{\frac{i}{2}[(k_1+k_2)z - (\omega_1+\omega_2)t + \eta])} \cos\left[\frac{(k_1-k_2)z - (\omega_1-\omega_2)t - \eta}{2}\right] \begin{pmatrix} 1 \\ -i \end{pmatrix}, \\ \overrightarrow{E_l}(t) = E_1 e^{\frac{i}{2}\left[(k_1+k_2)z - (\omega_1+\omega_2)t + \eta + \varphi + \varphi']\right)} \cos\left[\frac{(k_1-k_2)z - (\omega_1-\omega_2)t - \eta + \varphi - \varphi'}{2}\right] \begin{pmatrix} 1 \\ +i \end{pmatrix}. \end{cases} \tag{62}$$

The two sets of circularly polarized waves exhibit a beat note at the angular frequency $(\omega_1 - \omega_2)/2$, phase shifted relative to each-other by:

$$\theta = \frac{\varphi - \varphi'}{2} = \frac{(k_1 - k_2)\Delta z}{2} = \pi \frac{\Delta z}{\lambda_{mw}}, \tag{63}$$

with λ_{mw} the wavelength of the microwave wave of angular frequency $(\omega_1 - \omega_2)$.

When the terms of same frequency are grouped together, we get:

$$\begin{cases} \overrightarrow{E_1} = \frac{E_1}{2} e^{i(k_1 z - \omega_1 t)} \left[\begin{pmatrix} 1 \\ -i \end{pmatrix} + e^{i\varphi} \begin{pmatrix} 1 \\ +i \end{pmatrix} \right] = E_1 e^{i(k_1 z - \omega_1 t + \frac{\varphi}{2})} \begin{pmatrix} \cos(\frac{\varphi}{2}) \\ -\sin(\frac{\varphi}{2}) \end{pmatrix}, \\ \overrightarrow{E_2} = \frac{E_2}{2} e^{i(k_2 z - \omega_2 t + \eta)} \left[\begin{pmatrix} 1 \\ -i \end{pmatrix} + e^{+i\varphi'} \begin{pmatrix} 1 \\ +i \end{pmatrix} \right] = E_2 e^{i(k_2 z - \omega_2 t + \eta + \frac{\varphi'}{2})} \begin{pmatrix} \cos(\frac{\varphi'}{2}) \\ -\sin(\frac{\varphi'}{2}) \end{pmatrix}. \end{cases} \tag{64}$$

Equations (64) represent linearly polarized waves of angle $-\varphi/2$ and $-\varphi'/2$, respectively, with the x axis. The angle between both polarization vectors is:

$$\theta = \frac{-\varphi' + \varphi}{2} = (k_1 - k_2)\frac{\Delta z}{2}. \tag{65}$$

Then

$$\begin{cases} \theta = 0 \ \text{ when } \Delta z = 2p\lambda_{mw}, \\ \theta = \dfrac{\pi}{2} \ \text{ when } \Delta z = \left(2p + \dfrac{1}{2}\right)\lambda_{mw}, \end{cases} \tag{66}$$

with p an integer.

Here, we demonstrate that the push-pull scheme is identical to two linearly polarized waves of angular frequencies ω_1 and ω_2 respectively. Their polarization vectors form an angle $\theta = \pi\Delta z/\lambda_{mw}$, depending on the path difference Δz. If the path difference is realized in a Michelson interferometer like in [28], it is worth to note that a displacement δz of a mirror in one arm of the interferometer yields a path difference $2\delta z$. Then, the angle between polarization vectors increases from 0 to $\pi/2$ for a displacement $\delta z = \lambda_{mw}/4$. This angle is equal to the phase shift between the two beat-notes of equation (62), which are in phase and in quadrature when $\theta = 0$ and $\theta = \pi/2$, respectively. Finally, we point out that the push-pull scheme is identical to the *lin⊥lin* scheme of [26] when $\theta = \pi/2$.

Dark states

Interaction Hamiltonian As the push-pull scheme is equivalent to two linear polarized fields with an angle θ between them, we consider now this last case. The same calculation can be performed with circular polarizations. Let's assume two waves copropagating along the z axis, $\overrightarrow{E_1}$ parallel to x axis, and $\overrightarrow{E_2}$ forming an angle θ with the x axis.

$$\begin{cases} \overrightarrow{E_1}(t) = \mathcal{E}_1(t)\hat{e}_x = \dfrac{\mathcal{E}_1(t)}{\sqrt{2}}(\hat{e}_- - \hat{e}_+), \\ \overrightarrow{E_2}(t) = \mathcal{E}_2(t)\left(\cos(\theta)\hat{e}_x + \sin(\theta)\hat{e}_y\right) = \dfrac{\mathcal{E}_2(t)}{\sqrt{2}}\left[e^{i\theta}\hat{e}_- - e^{-i\theta}\hat{e}_+\right], \end{cases} \tag{67}$$

with $\mathcal{E}_1(t) = E_1(e^{-i\omega_1 t} + e^{i\omega_1 t})/2$, $\mathcal{E}_2(t) = E_2(e^{-i(\omega_2 t-\eta)} + e^{i(\omega_2 t-\eta)})/2$. We used the standard basis, defined as: $\hat{e}_\pm = \mp(\hat{e}_x \pm i\hat{e}_y)/\sqrt{2}$, $\hat{e}_0 = \hat{e}_z$. The interaction Hamiltonian between the atoms and the electromagnetic fields is the dipole interaction Hamiltonian:

$$V = -\overrightarrow{D} \cdot \left(\overrightarrow{E_1}(t) + \overrightarrow{E_2}(t)\right) = V_1 + V_2, \tag{68}$$

where $\overrightarrow{D}$ is the electric dipole operator. The operators V_1, V_2 are equal to:

$$\begin{cases} V_1 = \dfrac{\mathcal{E}_1(t)}{\sqrt{2}}\left(D_+ - D_-\right), \\ V_2 = \dfrac{\mathcal{E}_2(t)}{\sqrt{2}}\left(D_+ e^{-i\theta} - D_- e^{i\theta}\right). \end{cases} \tag{69}$$

where D_+ and D_- are the standard components of D such as: $D_+ = -(D_x + iD_y)/\sqrt{2}$, $D_- = (D_x - iD_y)/\sqrt{2}$.

We consider a four-level atom, two hyperfine levels of the ground state with quantum magnetic number $m = 0$, $|1\rangle$ and $|2\rangle$, and two Zeeman sublevels $|3\rangle$ and $|4\rangle$ in the excited state, with $m = -1$ and $m = +1$ respectively (see Fig.67(b)). The field $\overrightarrow{E_1}(t)$ is resonant with the transitions $|1\rangle - |3\rangle$ and $|1\rangle - |4\rangle$, $\overrightarrow{E_2}(t)$ with the transitions $|2\rangle - |3\rangle$ and $|2\rangle - |4\rangle$. The V_2 term can be written:

$$V_2 = \frac{d\mathcal{E}_2(t)}{\sqrt{2}} \left[e^{-i\theta} \left(c_{42}|4\rangle\langle 2| - c_{32}|2\rangle\langle 3| \right) - e^{i\theta} \left(c_{32}|3\rangle\langle 2| - c_{42}|2\rangle\langle 4| \right) \right], \tag{70}$$

with $d = \langle J_e||D||J_g\rangle/\sqrt{2J_e+1}$, J_e, J_g the total electronic angular momentum quantum numbers of the excited and ground states, respectively. The c_{ij} coefficients are the Clebsch-Gordan coefficients such that $\langle i|D|j\rangle = d_{ij} = c_{ij}d$; their values for alkali-metal atoms are given in appendix 4E of [79]. In the rotating frame V_2 becomes $\widetilde{V}_2$ [116] :

$$\widetilde{V}_2 = T(t)V_2T^\dagger(t), \tag{71}$$

with:

$$\begin{cases} T(t) = e^{-iS(t)}, \\ S(t) = \omega_2 t|2\rangle\langle 2|. \end{cases} \tag{72}$$

In the rotating wave approximation we get:

$$\widetilde{V}_2 = \frac{dE_2}{2\sqrt{2}} \left\{ e^{i(\eta-\theta)}c_{42}|4\rangle\langle 2| - e^{i(\eta+\theta)}c_{32}|3\rangle\langle 2| + e^{-i(\eta-\theta)}c_{42}|2\rangle\langle 4| - e^{-i(\eta+\theta)}c_{32}|2\rangle\langle 3| \right\}. \tag{73}$$

The same calculation leads to:

$$\widetilde{V}_1 = \frac{dE_1}{2\sqrt{2}} \left\{ c_{41}|4\rangle\langle 1| - c_{31}|3\rangle\langle 1| + c_{41}|1\rangle\langle 4| - c_{31}|1\rangle\langle 3| \right\}. \tag{74}$$

Dark states The dark state, when it exists, is a linear superposition of the two ground states: $|dark\rangle = a|1\rangle + b|2\rangle$. It must satisfy:

$$(\widetilde{V}_1 + \widetilde{V}_2)|dark\rangle = 0. \tag{75}$$

Substituting $\widetilde{V}_1$ and $\widetilde{V}_2$ by their expression in (74), (73), it comes:

$$\begin{cases} \dfrac{b}{a} = -\dfrac{c_{31}}{c_{32}}\dfrac{E_1}{E_2}e^{-i(\eta+\theta)}, \\ \dfrac{b}{a} = -\dfrac{c_{41}}{c_{42}}\dfrac{E_1}{E_2}e^{-i(\eta-\theta)}, \end{cases} \tag{76}$$

where the first (second) equation holds for coupling with the $|3\rangle$ ($|4\rangle$) excited state, respectively. A dark state common to the two Λ schemes exists when the following condition is satisfied:

$$e^{i2\theta} = \frac{c_{42}}{c_{41}}\frac{c_{31}}{c_{32}}. \tag{77}$$

We consider the Cs D_1 line. The $|1\rangle$ and $|2\rangle$ states are the ground states $|F = 3, m = 0\rangle$ and $|F = 4, m = 0\rangle$, respectively, with F the hyperfine quantum number. The states $|3\rangle$ and $|4\rangle$ are the states $|F', m = -1\rangle$ and $|F', m = +1\rangle$, respectively of the $6^2P_{1/2}$ excited state hyperfine level F' ($F' = 3$ or $F' = 4$). The Clebsch-Gordan coefficients are such that:

$$\begin{cases} F'=4: & c_{42}=-c_{41} \quad c_{32}=c_{31}=c_{41} \\ F'=3: & c_{42}=-c_{41} \quad c_{32}=c_{31}=-c_{41}. \end{cases} \tag{78}$$

These relations are valid for the D_1 line of all alkali-metal atoms, but not for the D_2 line. The dark states corresponding to the transitions towards $|3\rangle$ and towards $|4\rangle$ are:

$$\begin{cases} |dark_3\rangle = \dfrac{1}{\sqrt{E_1^2+E_2^2}}(E_2|1\rangle - E_1 e^{-i(\eta+\theta)}|2\rangle) \\ |dark_4\rangle = \dfrac{1}{\sqrt{E_1^2+E_2^2}}(E_2|1\rangle + E_1 e^{-i(\eta-\theta)}|2\rangle). \end{cases} \tag{79}$$

Note that when $\theta = 0$ and $E_1 = E_2$ the dark state $|dark_3\rangle$ for the transitions with $|3\rangle$ is the bright state for the transitions with $|4\rangle$, and vice-versa. In this case, no CPT effect occurs. According to (77) and (78) a common dark state exists when $e^{i2\theta} = -1$, *i. e.*:

$$\theta = \frac{\pi}{2} + k\pi, \tag{80}$$

where k is an integer. The common dark state is then:

$$\begin{cases} |dark_+\rangle = \dfrac{1}{\sqrt{E_1^2+E_2^2}}(E_2|1\rangle + iE_1 e^{-i\eta}|2\rangle) \quad when \quad \theta = \dfrac{\pi}{2} + 2k\pi, \\ |dark_-\rangle = \dfrac{1}{\sqrt{E_1^2+E_2^2}}(E_2|1\rangle - iE_1 e^{-i\eta}|2\rangle) \quad when \quad \theta = -\dfrac{\pi}{2} + 2k\pi, \\ i.e., \\ |dark\rangle = \dfrac{1}{\sqrt{E_1^2+E_2^2}}(E_2|1\rangle + E_1 e^{i\theta} e^{-i\eta}|2\rangle) \quad when \quad \theta = \dfrac{\pi}{2} + k\pi. \end{cases} \tag{81}$$

It is worth to note that, according to relations (78), this dark state is also common to transitions involving the two excited levels of the D_1 line of alkali-metal atoms, of hyperfine number ($F' = I - 1/2$) and ($F' = I + 1/2$) with I the nuclear spin quantum number, as already reported in [104]. This means that in a vapor cell where the optical transitions are broadened by Doppler effect and buffer gas collisions, the dark state built with an optical transition is not destroyed by the coupling with the other hyperfine excited level.

$\Delta m = 2$ transitions Double Λ schemes as PPOP or $lin\perp lin$ induce two single Λ transitions corresponding to $\Delta m = 2$ [25]. These transitions are enabled by the coexistence of σ^+ and σ^- polarized light. They are those created in $lin||lin$ configuration [112]. One transition couples the states $|F = I - 1/2, m - 1\rangle$ and $|F = I + 1/2, m + 1\rangle$, and the other one the states $|F = I + 1/2, m - 1\rangle$ and $|F = I - 1/2, m + 1\rangle$. For simplification, these states are labeled $|1'\rangle$, $|2''\rangle$, $|2'\rangle$, $|1''\rangle$, respectively. Calculations lead to the dark states expressions:

$$\begin{cases} |dark_{1'2''}\rangle = \dfrac{1}{\sqrt{c_{01'}^2 E_1^2 + c_{02''}^2 E_2^2}}(c_{02''}E_2|1'\rangle + c_{01'}E_1 e^{-i(\eta+\theta)}|2''\rangle) \\ |dark_{2'1''}\rangle = \dfrac{1}{\sqrt{c_{02'}^2 E_1^2 + c_{01''}^2 E_2^2}}(c_{01''}E_1|2'\rangle + c_{02'}E_2 e^{-i(\eta-\theta)}|1''\rangle), \end{cases} \tag{82}$$

where the c_{ij} coefficients are the Clebsch-Gordan coefficients defined above. These dark states are independent and exist whatever the value of θ. The corresponding CPT resonances split by increasing the magnetic field value. Unlike previous dark states, these dark states are not common to both excited hyperfine levels of the D_1 line. Cs atoms in these states are not fully uncoupled from the laser field because the transitions towards other excited Zeeman sublevels remain.

3.6.3 Absorption

An analytical calculation of the light propagation in a medium of four-level atoms in a double Λ configuration has been performed by Korsunsky and Kosachiov [117]. This was realized in the particular case corresponding to the D_1 line of an alkali-metal atom with $E_1 = E_2$, at resonance. Following their calculation it is more convenient to use Rabi frequencies rather than field amplitudes, with $\Omega_{ij} = |d_{ij}E_{ij}|/\hbar$, where E_{ij} is the amplitude of the field component coupling the atomic states $|i\rangle$ and $|j\rangle$. At the steady-state the absorption of the Rabi frequency along the cell length z is governed by:

$$\frac{d\Omega_{ij}}{dz} = -\frac{n_d}{\varepsilon_0 c\hbar}\omega_{ij}|d_{ij}|^2\mathrm{Im}(\widetilde{\rho}_{ij}), \tag{83}$$

where n_d is the density of involved atoms, ω_{ij} is the Bohr angular frequency between $|i\rangle$ and $|j\rangle$, $\widetilde{\rho}_{ij}$ is the optical coherence in the rotating frame, ε_0 is the vacuum permittivity, c the speed of light and $\hbar$ the Plank constant divided by 2π.

From the expression of the steady-state optical coherence density matrix elements imaginary part established in [117], it can be shown that the absorption phenomenon along z can be described at low saturation $\Omega_{ij} \ll \Gamma ij$ by:

$$\frac{d\Omega_{ij}}{dz} \simeq -\frac{n_d}{8\varepsilon_0 c\hbar}\omega_{ij}|d_{ij}|^2\frac{\Omega_{ij}^2\left(1-\cos(\Phi)\right)+2\Gamma_{ij}\gamma_2}{\Omega_{ij}\Gamma_{ij}}, \tag{84}$$

with Γ_{ij} the relaxation rate of the population $|i\rangle$ towards $|j\rangle$, γ_2 the hyperfine coherence decay rate and $d_{ij} = |d_{ij}|e^{i\eta_{ij}}$. Φ is a relative phase given by:

$$\Phi = (\beta_{31} - \beta_{32}) - (\beta_{41} - \beta_{42}), \tag{85}$$

with $\beta_{ij} = \varphi_{ij} + \eta_{ij}$ the sum of the laser phase φ_{ij} and the phase of the atomic dipole moment η_{ij}. Using Eq. (60), (61), and (85) it comes:

$$(\varphi_{31} - \varphi_{32}) - (\varphi_{41} - \varphi_{42}) = (k_1 - k_2)\Delta z. \tag{86}$$

According to (78) the phases η_{ij} are equal to 0 or π, so that $(\eta_{31} - \eta_{32}) - (\eta_{41} - \eta_{42}) = \pi$. From (85) and (65) we get:

$$\Phi = (k_1 - k_2)\Delta z + \pi = 2\pi\frac{\Delta z}{\lambda_{mw}} + \pi = 2\theta + \pi, \tag{87}$$

$$\frac{d\Omega_{ij}}{dz} \simeq -\frac{n_d}{4\varepsilon_0 c\hbar}\omega_{ij}|d_{ij}|^2\frac{\Omega_{ij}^2\cos^2(\theta)+\Gamma_{ij}\gamma_2}{\Omega_{ij}\Gamma_{ij}}. \tag{88}$$

For the D_1 line of alkali-metal atoms, the $|d_{ij}|$ (and the Γ_{ij}) coefficients are equal for the different involved atomic states. We note $\Gamma_1 = \Gamma_{ij}$. With a good approximation, we consider that $\omega_{31} = \omega_{41} = \omega_{32} = \omega_{42} = \omega_{eg}$ because the optical angular frequencies ω_{ij} are very close. Consequently, we define the same absorption coefficient α_d for the four laser fields such as:

$$\alpha_d = \frac{n_d}{2\varepsilon_0 c\hbar}\frac{\omega_{eg}|d_{ij}|^2}{\Gamma_1}. \tag{89}$$

In a Cs vapor cell, most atoms are not involved in the CPT resonance because of the presence of other Zeeman sublevels for which the Raman detuning is too large. However, these atoms contribute to the laser light absorption because the related optical transitions remain at resonance. In order to take into account

this additional absorption we add an absorption coefficient α_{ij}, corresponding to the absorption of the laser beam of intensity I_{ij}, related to Ω_{ij} by $I_{ij} = \epsilon_0 c\hbar^2\Omega_{ij}^2/2d^2$. I_{ij} corresponds to an angular frequency ω_1 or ω_2 and a polarization σ^- or σ^+. Using I_{ij}, α_d, α_{ij} the equation (88) becomes:

$$\frac{dI_{ij}}{dz} \simeq -\left(\alpha_d \cos^2(\theta) + \alpha_{ij}\right) I_{ij} - \frac{n_d}{4}\hbar\omega_{eg}\gamma_2. \tag{90}$$

The last term of (90) is the linear absorption expected for a closed system in a dark state ($\alpha_{ij} = 0$, $\cos(\theta) = 0$) [117] [118]. The solution of (90) is:

$$I_{ij}(z) \simeq \left(I_{ij}(0) + \frac{(n_d/4)\hbar\omega_{eg}\gamma_2}{\alpha_{ij} + \alpha_d\cos^2(\theta)}\right) e^{-(\alpha_{ij}+\alpha_d\cos^2(\theta))z} - \frac{(n_d/4)\hbar\omega_{eg}\gamma_2}{\alpha_{ij} + \alpha_d\cos^2(\theta)}, \tag{91}$$

where $I_{ij}(0)$ is the beam intensity at the cell input ($z = 0$), we recall that we have assumed that all the partial intensities are equal, $I_{ij}(0) = I_0/4$ with I_0 the full laser intensity at the cell input.
For reasons of symmetry the absorption coefficients α_{ij} of the beams σ^+ and σ^+ are equal. However, the absorption coefficients are different for the beams of angular frequencies ω_1 and ω_2, depending on the ground state hyperfine level involved. The full transmitted laser intensity is given by the sum of the four intensities: $I_t = \sum I_{ij}$. In the usual conditions of an alkali-metal vapour cell filled with buffer gas and for usual laser intensities, we assume that γ_2 is sufficiently weak ($\Omega_{ij}^2 \gg \Gamma_{ij}\gamma 2$) and the transmitted total laser intensity can be simplified as follows:

$$I_t(z) \simeq \frac{I_0}{2} e^{-\alpha_d\cos^2(\theta)z}\left(e^{-\alpha_1 z} + e^{-\alpha_2 z}\right), \tag{92}$$

where the subscript 1, 2 holds for the angular frequencies ω_1, ω_2. When $\cos(\theta) = 0$, atoms involved in the dark state become fully transparent and eq. (92) reduces to the well-known Beer-Lambert law.
Note that the model of [117] is valid for a four-level atom and equal laser intensities. Here we have many levels and, even if the laser intensities are equal at the input of the cell, as the absorption coefficients due to other levels are different for the two frequencies, the laser intensities equality will not be valid after propagation inside the cell.

3.7 Ramsey interference

A well-known technique to reduce the linewidth of atomic resonance is the Ramsey interference scheme using two separated oscillating fields [7]. Ramsey interrogation is realized by using a sequence of microwave pulses to interact with alkali atoms. Figure 68 shows the Ramsey interference scheme. To simplify the analysis, we only consider two energy levels of atoms $|1\rangle$ and $|2\rangle$ here.

In this scheme, two energy levels atoms interact with successive microwave pulses for a pumping time of τ_p. The pulses are separated by a dark time T and the atoms evolve freely in the time T without interacting with microwave field. In the free evolution time T, alkali atoms aren't disturbed. The evolution of atoms $|\Psi(t)\rangle = c_1(t)|1\rangle + c_2(t)|2\rangle$ in every impulse is given by:

$$\begin{aligned}|\Psi(t)\rangle = &[c_1(0)\cos(\frac{\omega_R}{2}t) + i(\frac{-\delta_R c_1(0) + 2\omega c_2(0)}{\omega_R})\sin(\frac{\omega_R}{2}t)]|1\rangle \\ &+[c_2(0)\cos(\frac{\omega_R}{2}t) + i(\frac{\delta_R c_2(0) + 2\omega c_1(0)}{\omega_R})\sin(\frac{\omega_R}{2}t)]|2\rangle\end{aligned} \tag{93}$$

with the initial conditions $c_1(0)$ and $c_2(0)$ at $t = 0$ and the Rabi pulse frequency $\omega_R = \sqrt{\delta_R^2 + 4\omega^2}$, δ_R is the Raman detuning between the microwave impulse frequency and the atomic transition frequency. The

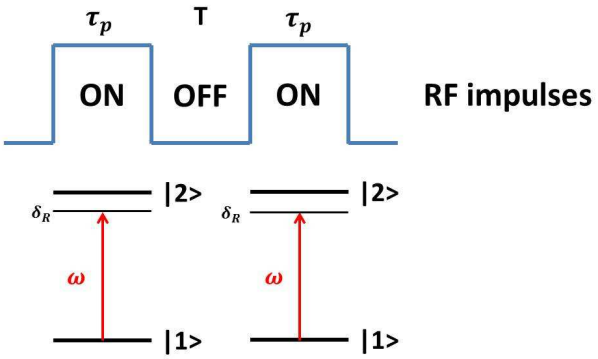

Figure 68: Ramsey interference scheme. T is free evolution time, τ_p is pumping time, ω is frequency of microwave field. Atomic transition probability between two states is measured after the second impulse, the probability will reach maximum if $\tau_p \cdot 2\omega = \pi/2$.

Rabi pulse frequency ω_R describes the coupling between the dipolar momentum of atomic transition and the exciting field. We introduce an electromagnetic field along the z axis, and the 3 dimensions Pauli vector σ relate to $|1\rangle$ and $|2\rangle$, then the evolution $|\Psi(t)\rangle$ is rewritten:

$$|\Psi(t)\rangle = [\cos(\frac{\omega_R}{2}t) + i\sigma \cdot (\frac{-\delta_R\widehat{z} + 2\omega\widehat{x}}{\omega_R})\sin(\frac{\omega_R}{2}t)]|\Psi(0)\rangle \tag{94}$$

During each step of Ramsey interrogation, the temporal evolution is given:

$$\begin{aligned} U_{\tau_p} &= \cos(\frac{\omega_R}{2}\tau_p) + i\sigma \cdot (\frac{-\delta_R\widehat{z} + 2\omega\widehat{x}}{\omega_R})\sin(\frac{\omega_R}{2}\tau_p) \text{ during the pumping time } \tau_\mathrm{p}, \\ U_T &= \cos(\frac{\delta_R}{2}T) - i\sigma \cdot \widehat{z}\sin(\frac{\delta_R}{2}T) \text{ during the free evolution time T} \\ U_{\tau_p} &= \cos(\frac{\omega_R}{2}\tau_p) + i\sigma \cdot (\frac{-\delta_R\widehat{z} + 2\omega\widehat{x}}{\omega_R})\sin(\frac{\omega_R}{2}\tau_p) \text{ during the pumping time } \tau_\mathrm{p}, \end{aligned} \tag{95}$$

Then the atomic transition probability in a final state $|f\rangle$ after a sequence of interrogation can be described as:

$$P(2\tau_p + T) = |\langle f|\Psi\rangle|^2 = |\langle f|U_{\tau_p}U_T U_{\tau_p}|\Psi(0)\rangle|^2 \tag{96}$$

We assume the initial conditions $c_1(0) = 1$ and $c_2(0) = 0$ when the atoms in the $|1\rangle$. Then by Equation 96, we have the probability of atoms exist in the $|2\rangle$:

$$P_2(t) = 16\frac{\omega^2}{\omega}\sin^2(\frac{\omega_R\tau_p}{1})[\cos(\frac{\omega_R\tau_p}{2})\cos(\frac{\delta_R T}{2}) - \frac{\delta_R}{\omega_R}\sin(\frac{\omega_R\tau_p}{2})\sin(\frac{\delta_R T}{2})]^2 \tag{97}$$

If we consider the detuning between the excitation impulse ω and the Rabi pulse frequency ω_R is very weak, we can simplify the probability of atoms exist in each states:

$$\begin{aligned} P_1(t) &= \frac{1}{2}(1 - \cos[\delta_R T]) \\ P_1(t) &= \frac{1}{2}(1 + \cos[\delta_R T]) \end{aligned} \tag{98}$$

with central Ramsey fringes linewidth $\Delta\nu = 1/2T$ when $\tau_p \ll T$. From equation 98, we can measure the phase shift between atoms and the microwave field caused by possible disturbances [7].

4 Experimental Setup

We developed an experimental set-up to detect high-contrast CPT resonances in Cs vapor cells using the push-pull optical pumping technique. This section is devoted to describe in detail the experimental set-up and its main components. The philosophy of this work was to develop a simple-architecture, compact and high-performance laser system compatible with the future development of a high-performance Cs CPT clock. The typical frequency objective is in the first step $10^{-12}\ \tau^{-1/2}$. To be compatible with industrial requirements, a choice was to use as many commercially-available components as possible. Even if not realized in the frame of this PhD thesis, we're confident that this laser system can be integrated in a A3-format elegant optical breadboard. Different noise reduction techniques were implemented for proper operation of the future Cs CPT clock.

4.1 System architecture

Figure 69 shows the experimental set-up used to detect high-contrast CPT resonances in Cs vapor cells using PPOP. The setup is divided in four main basic blocks defined as the laser source, the optical sidebands generation using an electro-optic modulator (EOM), a Michelson delay-line system to produce PPOP [28] and the Cs vapor cell physics package. These blocks will be described in detail in the following.

The laser source is a 1 MHz-linewidth DFB diode laser tuned on the Cs D_1 line at 894.6 nm. The laser frequency is shifted from Cs atom resonance by about 4.596 GHz. The laser light is injected into a 20 GHz bandwidth polarization maintaining (PM) pigtailed intensity Mach-Zehnder electro-optic modulator (MZ EOM, Photline NIR-MX800-LN). CPT sidebands are created by driving the EOM with a low noise 4.596 GHz microwave signal generated by frequency division from a 9.192 GHz frequency synthesizer. At the output of the EOM, the modulated light beam of fixed linear polarization passes through a half-wave plate. The incident beam is divided in two sub-beams in the two arms of a Michelson interferometer. A quarter-wave plate is placed in each arm. A fine adjustment of both quarter-wave plates and the half-wave plate allows to obtain at the output of the polarizing cube two superimposed beams of equal intensity, linearly polarized at right angle, and differing by a phase delay. A mirror, mounted on a micrometric translation stage, allows to tune the time-delay. A displacement of the mirror of $\lambda_0/4$, one quarter of the clock transition wavelength, induces a differential optical path $\Delta\ell = \lambda_0/2$, and shifts the intensity peaks of the beat-note on one beam by half a hyperfine period with respect to the peaks of the other beam. A last quarter-wave plate ensures that the output beams are circularly polarized, rotating in opposite directions. The laser beam passes through a Cs vapor cell. The cell is temperature-stabilized at the mK level and surrounded by a static magnetic field parallel to the laser beam direction in order to lift the Zeeman degeneracy. The cell is isolated from external electromagnetic perturbations with a double-layer μ-metal shield. The transmitted optical power through the cell is detected by a low noise photodiode.

4.2 894.6 nm frequency-stabilized DFB laser

A frequency-stabilized laser source is required in atomic clock applications because frequency fluctuations of the laser source can degrade the frequency stability of the atomic clock. Numbers of frequency stabilization techniques were described and proposed in the literature [119]. For short term integration times,

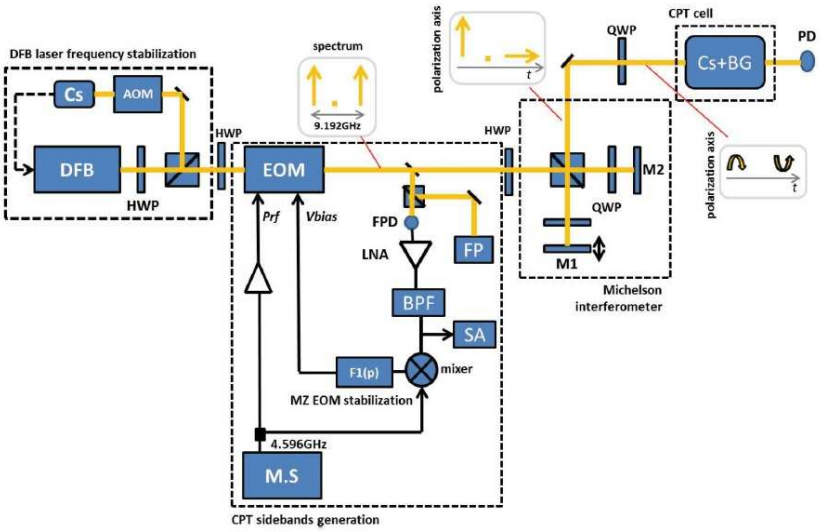

Figure 69: Experimental setup used to detect high-contrast CPT resonances in Cs vapor cells with push-pull optical pumping. A MZ EOM is used to generate optical sidebands with linear and parallel polarizations, frequency-separated by the clock transition (9.192 GHz). A microwave-based stabilization technique of the transfer function operating point is implemented to stabilize the optical carrier rejection. The Michelson interferometer is used to obtain at the output of the cube C1 two time-delayed optical components with orthogonal linear polarizations. The last quarter wave plate before the cell creates alternating right and left circular polarizations for push-pull interaction. The photodiode PD detects the transmitted optical power through the vapor cell. MS: microwave synthesizer, PD: photodiode, EOM: electro-optic modulator, FPD: fast photodiode, Cs+BG: Cs + buffer gas, QWP: quarter-wave plate, HWP: half-wave plate, BPF: bandpass filter, M1 and M2: mirrors, LNA: low-noise amplifier, SA: microwave spectrum analyzer, FP: Fabry-Perot interferometer.

the frequency of the laser source can be stabilized by locking to the transmission peak of a ultra stable Fabry-Perot cavity with the Pound-Drever-Hall technique [120]. The frequency stability of such a laser can reach exceptional frequency stability level at the order of a few 10^{-16} for averaging times of $1-10$ seconds [121] [122] [123] [124]. A compact alternative method to cavity stabilization for fast Fourier frequencies noise reduction consists to use an optical fiber delay line interferometer with arm imbalance to measure the laser frequency fluctuations during a fixed time delay [125] [126] [127]. For atomic clocks, the long term frequency stability is required. In this case, we can use absorption line of atoms or molecules as frequency references to lock the frequency of the laser source. Narrow linewidth ($\sim$ 100 kHz) external cavity diode laser (ECDL) can achieve high frequency stability by using saturated absorption technique [128] [129] [130]. However, ECDLs usually have strict requirements of environmental vibrations, optical alignment of the optical feedback path and accurate cavity length. Since our aim is to simplify our experimental setup as much as possible, ECDL is not a good candidate for us. A narrow linewidth Distributed Feedback (DFB) laser diode is a potential cost-effective alternative for atomic clock because of its more compact volume and less strict requirements. DFB with linewidth lower than 1 MHz was demonstrated by F. J. Vermersch *et al.,* [131], and even as narrow as 350 kHz on Cs D_1 line (895 nm) [132]. We built a DFB laser diode source tuned on Cs D_1 line that can be frequency-stabilized by the standard saturated absorption technique.

4.2.1 Saturated absorption setup

The laser source is a 1 MHz linewidth DFB diode laser resonant on the Cs D_1 line at 894.6 nm. The laser source is a commercially available GaAs semiconductor DFB laser diode with integrated grating structure emitting in a single mode at 895 nm (Eagleyard EYP-DFB-0895). It is housed in a hermetic TO-3 package with thermistance and thermoelectric cooler. The maximum output optical power is about 50 mW while its threshold current is about 50 mA. The temperature coefficient of wavelength is about 0.06 nm/K while the dependence of wavelength on injection current is $\sim$ 1 GHz/mA. The diode laser is driven by a low noise current controller inspired by [133] exhibiting a current noise power spectral density lower than $50\,\mathrm{pA}/\sqrt{\mathrm{Hz}}$. The diode laser temperature is stabilized within to the mK level with a high precision temperature controller using the internal Peltier. The laser diode is frequency-stabilized by saturated absorption technique with a 2 cm diameter and 2.5 cm long anti-reflection coated auxiliary Cs cell. Figure 70 shows the DFB laser diode combined with the saturated absorption scheme.

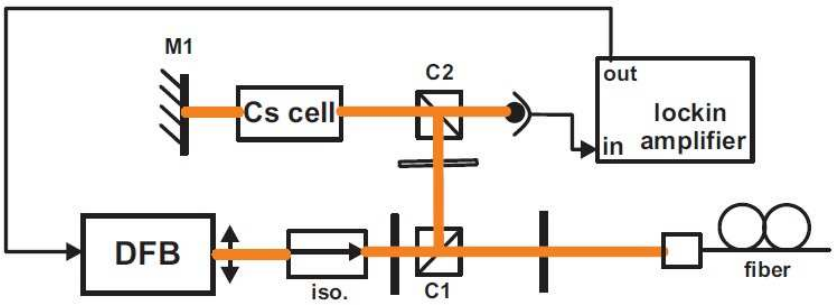

Figure 70: DFB laser diode optical setup for saturated absorption spectroscopy. C1, C2: Polarizing beam splitter cube; Plates: half-wave plate.

The DFB diode laser beam is collimated by an anti-reflection coated aspheric lens with a focal length of 2.5 mm and a numerical aperture of 0.55. The output of the DFB laser is passed through an optical Faraday isolator with isolation of 45 dB in order to avoid optical feedback. A half wave plate is used to rotate the polarization of the laser beam. The isolated and oriented laser beam is splitted in two directions by the PBS $C1$ in free space. Figure 71 shows a 3D graphic model of the optical structure of the laser system. The first beam is sent to the saturated absorption setup used to stabilize the laser frequency. In the first sense, the 3 mm diameter beam is used as the pump beam to saturate Cs vapor contained in the auxiliary cell. There are four optical transitions on the Cs D_1 line: $F = 3 \rightarrow F = 3'$, $F = 3 \rightarrow F = 4'$, $F = 4 \rightarrow F = 3'$ and $F = 4 \rightarrow F = 4'$. We do not directly use the linear absorption peak as a frequency reference for the laser diode, because these signals have a large linewidth of about 350 MHz due to the Doppler effect. In order to generate narrow resonance signal, the laser beam is retroreflected by a silver coated mirror at the output of the cell and detected by a low noise photodiode at the output of the PBS C2. The reflected beam is used as the probe beam. This technique is so-called saturated absorption technique. The linewidth of this saturated absorption peak signal is close to the Cs D_1 line natural linewidth (about 5 MHz). Figure 72 shows the saturated absorptions spectrum on the Cs D_1 line. We usually use the saturated absorption signal of the $F = 4 \rightarrow F = 3'$ or the $F = 4 \rightarrow F = 4'$ as a reference signal for the laser system.

The auxiliary cell is surrounded by a single layer μ metal magnetic shield in order to avoid perturbations

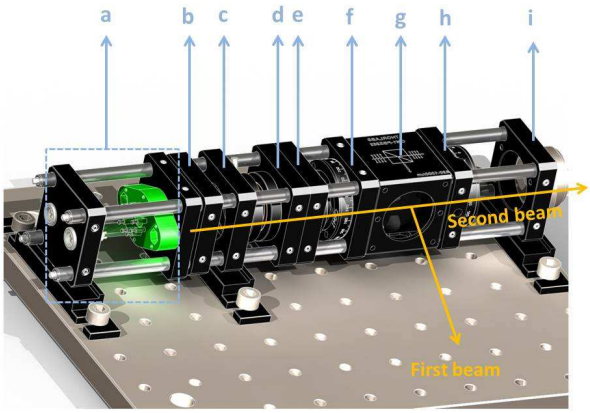

Figure 71: 3D graphic model of the optical structure of the laser system. (a): DFB diode. (b): Reflection coated aspheric lens. (c): Optical Faraday isolator. (d): Polarizer. (e): Diaphragm. (f): Half wave plate. (g): Polarization beam splitter. (h): Half wave plate. (i): Fiber port collimator.

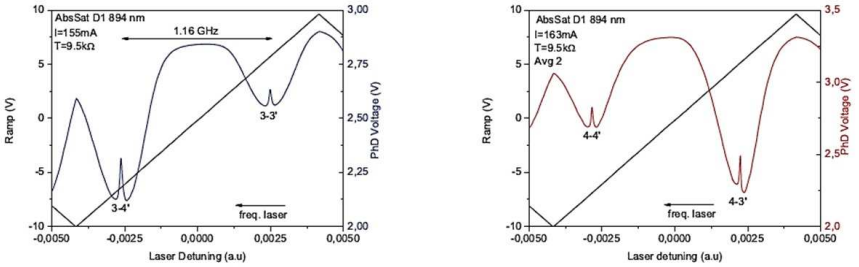

Figure 72: Saturated absorption spectrum on the Cs D_1 line with our DFB laser. Dips in the bottom of the absorption line are due to saturated absorption spectroscopy.

from external magnetic fields. For optimized mid-long term operation and frequency stability, the cell is placed in an oven temperature-stabilized using an improved analog-digital version of the electronic temperature controller presented in [134]. The cell temperature sensor is controlled below the mK level at 1 second integration time and better than 10^{-5} K level at 4000 seconds. The laser frequency is stabilized by applying a low frequency sinusoidal modulation of 60 kHz added to the DFB laser injection current. The saturated absorption signal is amplified, filtered and synchronously demodulated by a laboratory prototype lockin amplifier. The lockin amplifier generates a dispersive error signal used to correct the laser frequency by adjusting the injection current through a PI controller. The second beam is sent to the EOM for sidebands generation. A half wave plate is used adjust the laser polarization before entering the EOM.

4.2.2 Characterization of the laser system

Figure 73 shows the voltage noise of the laser frequency servo lockin amplifier output in free running and locked conditions. Optimal conditions result from a trade-off between loop noise reduction for long term operation and control bandwidth. In this case, the laser frequency servo bandwidth is about 300 Hz while the noise level at 1 Hz offset frequency is reduced by about 50 dB.

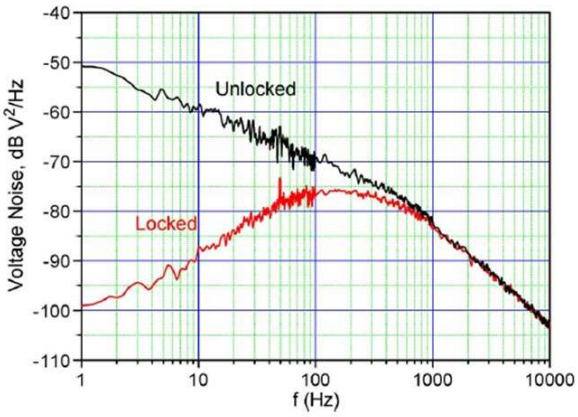

Figure 73: Voltage noise of the laser frequency servo lockin amplifier output (servo ON or servo OFF)

Figure 74 shows the frequency noise of the laser $S_{\Delta\nu}$ in free running regime. The frequency noise spectrum presents a f^{-1} slope from 1 Hz to 100 kHz. The f^{-1} slope indicates that the principal type of noise flicker frequency noise. The frequency stability of the laser can be calculated from its frequency noise. The frequency noise at 1 Hz is measured to be 2.5×10^5 Hz/$\sqrt{\text{Hz}}$. From the equation 10, we calculate that $h_{-1} = 1.488 \times 10^{-18}$. From the Table 1, we deduce $\sigma_y(\tau)$ at 1 s by:

$$\sigma_y(\tau) = \sqrt{2 \ln 2 h_{-1}} = \sqrt{2 \ln 2 \times 1.488 \times 10^{-18}} = 2 \times 10^{-9} \tag{99}$$

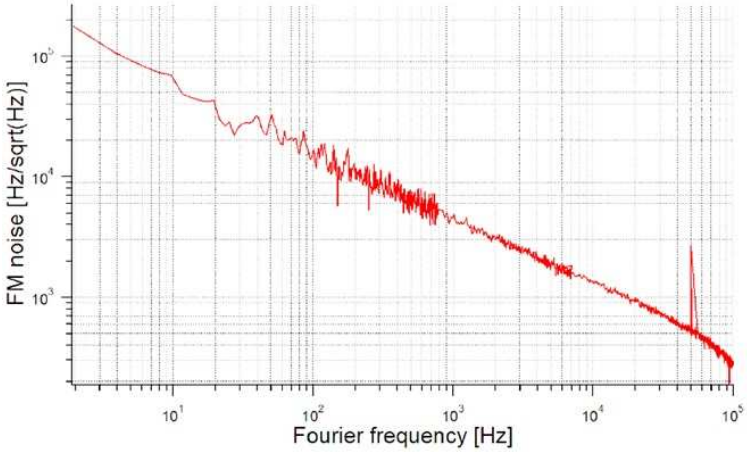

Figure 74: Frequency noise of the laser in free running regime.

Since the frequency noise has the same f^{-1} slope from 1 Hz to 100 kHz, we can expect that there is a flicker floor at the level of 2×10^{-9} from $\tau = 10^{-5}$ s to $\tau = 1$ s in free running regime. This corresponds to typical laser frequency fluctuations of about 670 kHz for such integration times. In order to measure experimentally the frequency stability of our laser system, we built another similar laser system to measure the beatnote signal. Figure 75 shows the experimental setup.

Both lasers are locked to independent Cs vapor cells onto the different optical transitions: $F = 4 \rightarrow F = 3'$ and $F = 4 \rightarrow F = 4'$. The frequency difference between these two optical transitions is about 1.16 GHz. Both laser beams are injected into a 50-50 splitting ratio optical polarization maintaining fiber coupler.

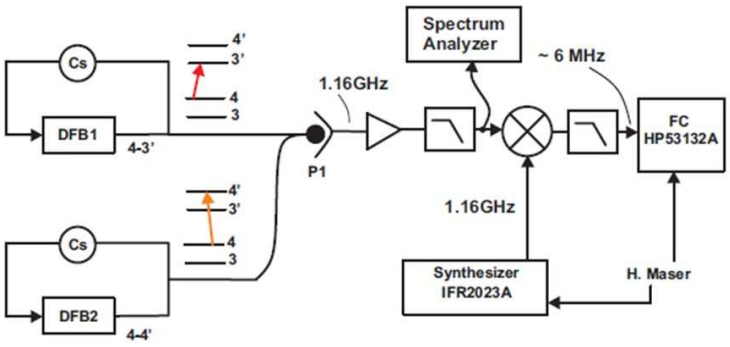

Figure 75: Measurement of the optical beatnote at 1.16 GHz between both DFB lasers.

The coupler is used to mix the two beams and to generate the beatnote signal. FC-APC connectors are used to avoid optical feedback. The beatnote signal is detected by a fast photodiode, low-pass filtered, amplified by 23 dB with a low noise amplifier and analyzed with a microwave spectrum analyzer. Figure 76 shows the spectrum of the beatnote signal at 1.16 GHz from these two similar DFB laser systems in locked configuration. The linewidth of the beatnote signal is 1.95 MHz and 1.47 MHz in free running regime and locked regime, respectively. The linewidth of a single laser signal is about 975 kHz in free running regime.

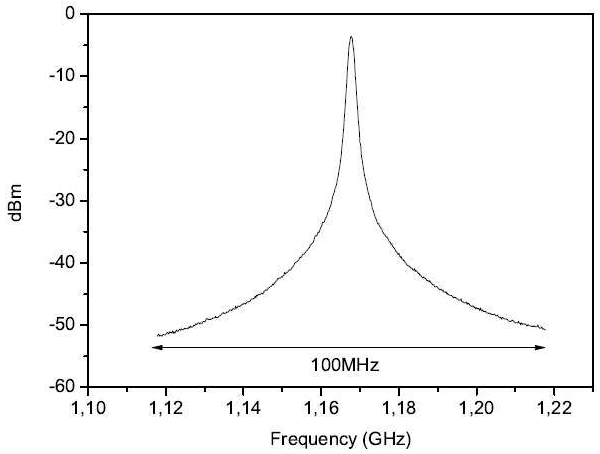

Figure 76: DFB beatnote spectrum in locked configuration.

The 1.16 GHz beatnote signal is compared to a 1.16 GHz + 6 MHz signal generated by a IFR2023A synthesizer driven by a hydrogen maser. The final beatnote signal at 6 MHz is low pass filtered, amplified and counted using a high resolution frequency counter. This frequency down-conversion to 6 MHz was done because no microwave counter was available in the laboratory but also to improve the frequency counting resolution. Figure 77 shows the Allan deviation versus the integration time of the beatnote signal frequency under free running or locked conditions.

In the free running regime, the short term frequency stability is measured to be 1.5×10^{-9} at 1 second integration time, increasing to reach about 8×10^{-9} at 100 s integration time. The resulting frequency stability at 1 second is in good agreement with the 2×10^{-9} level flicker floor derived from the frequency

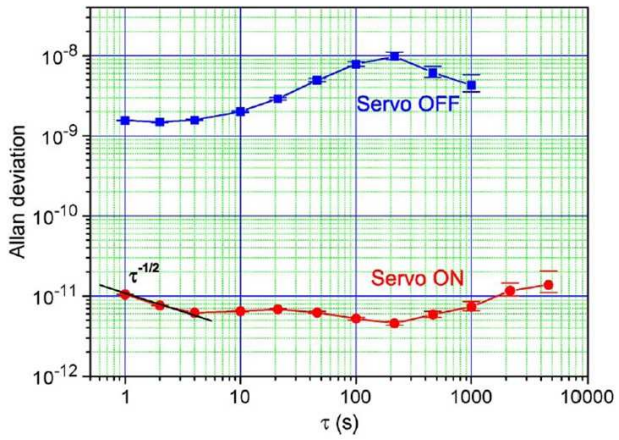

Figure 77: Relative frequency stability of a single laser in locked configuration and free-running regime.

noise. In the stabilization regime, the laser beatnote exhibits a frequency instability of 1×10^{-11} at 1 s integration time and decreases with a $\sqrt{\tau}$ slope until 4 s before reaching a wide flat flicker floor at the level of about $5 - 6 \times 10^{-12}$. For averaging times longer than 200 seconds, the deviation increases again without showing a clear τ slope drift. These results are reported in IEEE Trans. Instr. Meas. [135] and compare favorably with those presented on Cs D_2 line [136] [137].

Laser frequency fluctuations can induce a clock frequency fluctuations though the lightshift. Typically, frequency of atomic clock varies about -20 mHz for a 1 MHz laser frequency change [78]. In our laser system, the DFB laser frequency instability of 1×10^{-11} in locked regime corresponds to a frequency variation of 3.5 kHz at 1 second. This frequency variation induces an atomic clock frequency variation of 3.5 kHz $\times \frac{-20\,mHz}{1000\,kHz} = 0.07$ mHz. CPT based Cs vapor cell clock frequency stability limitation due to laser frequency changes could be consequently reduced to a level of $\frac{0.07\,mHz}{9.192\,GHz} = 7 \times 10^{-15}$, which is several orders of magnitude lower than frequency stability performances obtained with state-of-the-art CPT based Cs vapor cell atomic frequency references [25]. Consequently, frequency stability performances of our DFB laser system seems satisfying for a CPT Cs vapor cell clock application.

4.3 Electro-optic modulator (EOM)

A key element of our system is the electro-optic modulator for sidebands generation. We worked with 20 GHz-bandwidth pigtailed $LiNbO_3$ electro-optical modulators (EOM). Pigtailed EOMs were prefered to bulk modulators for their compacity and low driving voltages. We tested commercially-available phase modulator Photline NIR-MPX800 and intensity Mach-Zehnder modulator Photline NIR-MX800. These EOMs integrate a 10 kΩ thermistance for temperature control. No integrated photodiode is available at 894 nm. The modulators are connected with polarization maintaining fibers with FC-APC connectors. Figure 78 shows photographs of the EOMs.

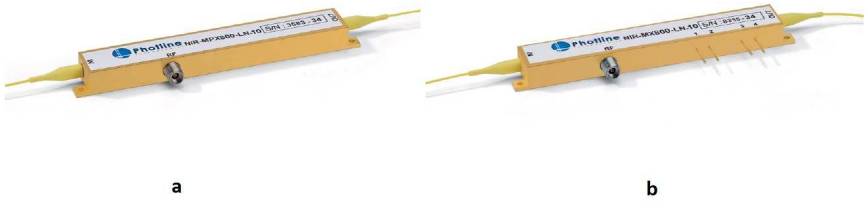

Figure 78: Photographs of the phase modulator Photline NIR-MPX800(a) and the intensity modulator Photline NIR-MX800 (b). The figure is extracted from [138].

4.3.1 Phase modulator

The phase modulator is constituted by a simple light guide where the electrical length or optical path length can be adjusted by the electro-optic Pockels effect. Optical sidebands are generated by driving the phase modulator with a low noise microwave signal.
We assume that the input optical signal is $E_{in}(t) = E_0 e^{i\omega_0 t}$. The microwave signal is $s(t) = V_s \sin(\Omega t)$, where V_s represents the amplitude of the microwave signal. The output signal of the phase modulator is given by:

$$E_{out}(t) = E_0 e^{i\omega_0 t + iV_m \sin(\Omega t)} \tag{100}$$

where $V_m = mV_s$, m is the modulation index.

We can use the Taylor expansion to rewrite Equation 100:

$$\begin{aligned} E_{out}(t) = E_0 e^{i\omega_0 t}(1 + iV_m \sin(\Omega t)) = E_0 e^{i\omega_0 t}(1 + \frac{V_m}{2}(e^{i\Omega t} - e^{-i\Omega t})) \\ = E_0(e^{i\omega_0 t} + \frac{V_m}{2} e^{i(\omega_0+\Omega)t} - \frac{V_m}{2} e^{i(\omega_0-\Omega)t}) \end{aligned} \tag{101}$$

Equation 101 indicates that the output signal of the phase modulator consists of the carrier signal and two optical sidebands at $\omega_0 + \Omega$ and $\omega_0 - \Omega$, respectively. One of the optical sidebands is phase opposite to the carrier signal and the other sideband. However, this equation is obtained by using only the first term in the Taylor expansion. In order to describe the actual phase modulation, we use the Jacobi-Anger expansion

to get:

$$E_{out}(t) = E_0 e^{i\omega_0 t + iV_m \sin(\Omega t)} = E_0 e^{i\omega_0 t}(J_0(V_m) + \sum_{k=1}^{\infty} J_k(V_m) e^{ik\Omega t} + \sum_{k=1}^{\infty}(-1)^k J_k(V_m) e^{-ik\Omega t}) \quad (102)$$

Equation 102 indicates that there are an infinite number of sidebands besides the carrier signal and the two first order sidebands. The frequency difference between two neighboring sidebands is Ω. Figure 79 shows the output power of the carrier signal and both first-order sidebands generated by our phase modulator versus the microwave signal power. The frequency of the modulation is 4.596 GHz. We measured that the CPT signal reaches a maximum when the optical power of both first-order optical sidebands is maximized.

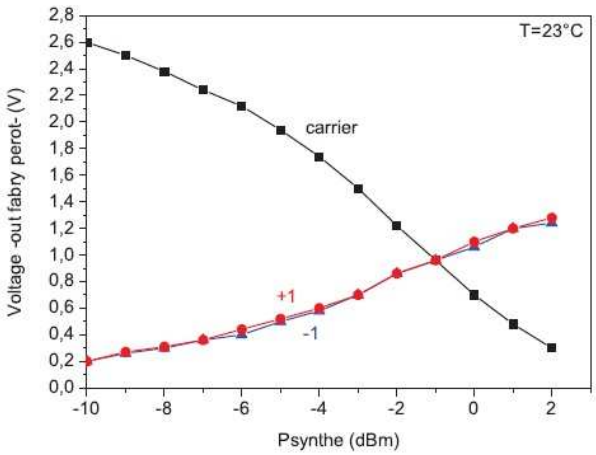

Figure 79: Powers of the carrier signal and the two first order sidebands generated by a phase modulator versus the microwave signal power at 4.596 GHz. The RF powers are amplified by an amplifier with gain = 22 dB.

4.3.2 Intensity Mach-Zehnder modulator

The intensity EOM is constituted by an integrated Mach-Zehnder interferometer (MZ EOM). The modulation is realized by adjusting optical path difference between two optical arms of the interferometer by electro-optic effect. The MZ EOM has a RF connector to generate two phase coherent optical bands and a dc bias voltage connector to control the optical path difference of the interferometer. The carrier signal at the output of the MZ EOM can be rejected by adjusting the bias voltage V_{dc}. Figure 80 shows a simplified scheme of a pigtailed MZ EOM.

We assume that the input signal is $E_{in} = E_0 e^{i\omega_0 t}$. The microwave signal $s(t) = V_m \cos(\Omega t)$. The output signal $E_{out}(t)$ is given by:

$$\begin{aligned} E_{out}(t) = E_0 \cos(\omega_0 t)\{J_0(C_m)\cos(\phi_{dc}+\phi_0) + 2\sum_{n=1}^{\infty}(-1)^n J_{2n}(C_m)\cos(\phi_{dc}+\phi_0)\cos(2n\Omega) \\ +2\sum_{n=1}^{\infty}(-1)^n J_{2n-1}(C_m)\sin(\phi_{dc}+\phi_0)\cos((2n-1)\Omega)\} \end{aligned} \quad (103)$$

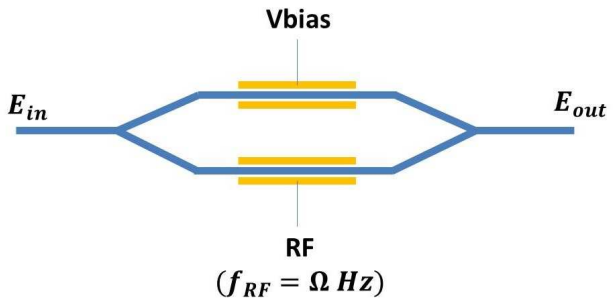

Figure 80: Simplified scheme of pigtailed MZ EOM. Vbias: voltage bias; RF: microwave; E_{in} and E_{out}: Amplitude of input and output signal.

with $\phi_{dc} = \pi V_{dc}/V_{\pi dc}$ and $C_m = \pi V_m/V_{\pi m}$ is the modulation index of the MZ EOM, where $V_{\pi dc}$ and $V_{\pi m}$ are half wave voltages at the RF and dc of the MZ EOM. The amplitude of each sideband depends on the microwave signal power and the dc voltage bias.
In order to optimize the configuration of the MZ EOM, we measured the transfer function of the MZ EOM as a function of microwave power and bias voltage, respectively. Figure 81 reports the transfer function of the MZ EOM as a function of microwave power when the bias voltage is fixed. The power of the three sidebands is equivalent when the microwave power is slightly lower than 0 dBm.

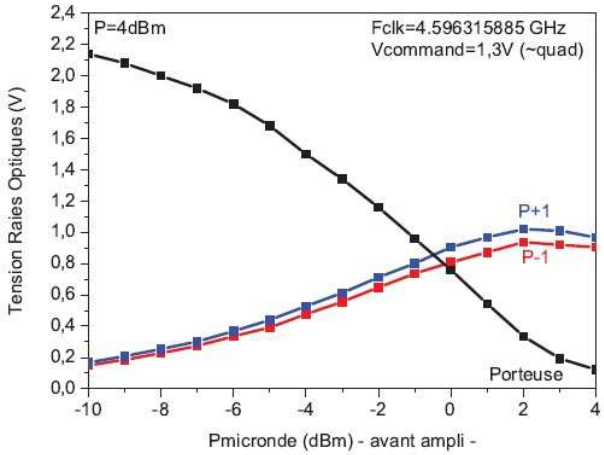

Figure 81: Transfer function of the MZ EOM as a function of microwave power with a bias voltage of 1.3 V. The RF powers are amplified by an amplifier with gain = 22 dB.

Figure 82(a) shows the transfer function of the MZ EOM as a function of bias voltage when the RF is on. We also report the CPT signal amplitude at the output of the cell for each case.

The CPT signal resonance height is found to be optimized when the carrier signal power is minimized and the sidebands powers maximized (see Figure 82(b)). This operation point is called dark point.

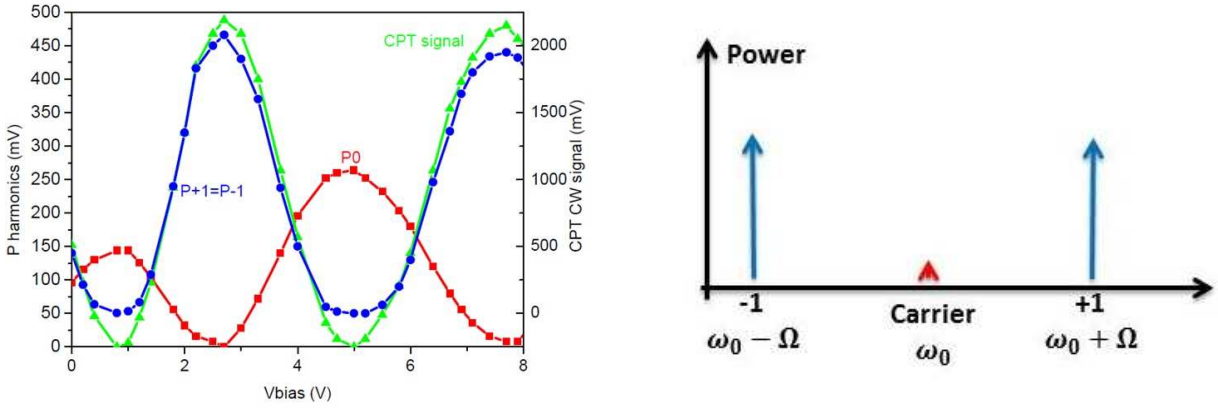

(a) (b)

Figure 82: (a): Transfer function of MZ EOM as a function of bias voltage. Red curve: carrier signal power. Blue curve: sidebands power. Green curve: CPT resonance signal detected by the experimental setup using the MZ EOM. (b): Typical spectrum of the MZ EOM output signal at the carrier suppression point.

4.3.3 Choice of the EOM

We tested the CPT spectroscopy with the phase EOM and the intensity MZ EOM at different frequencies (4.596 or 9.192 GHz). The bias voltage of the MZ EOM is adjusted to reject the carrier by 28 dB. Figure 83(a), 83(b), 83(c) show the optical sidebands generated by the different EOMs that participate into CPT interaction, respectively.

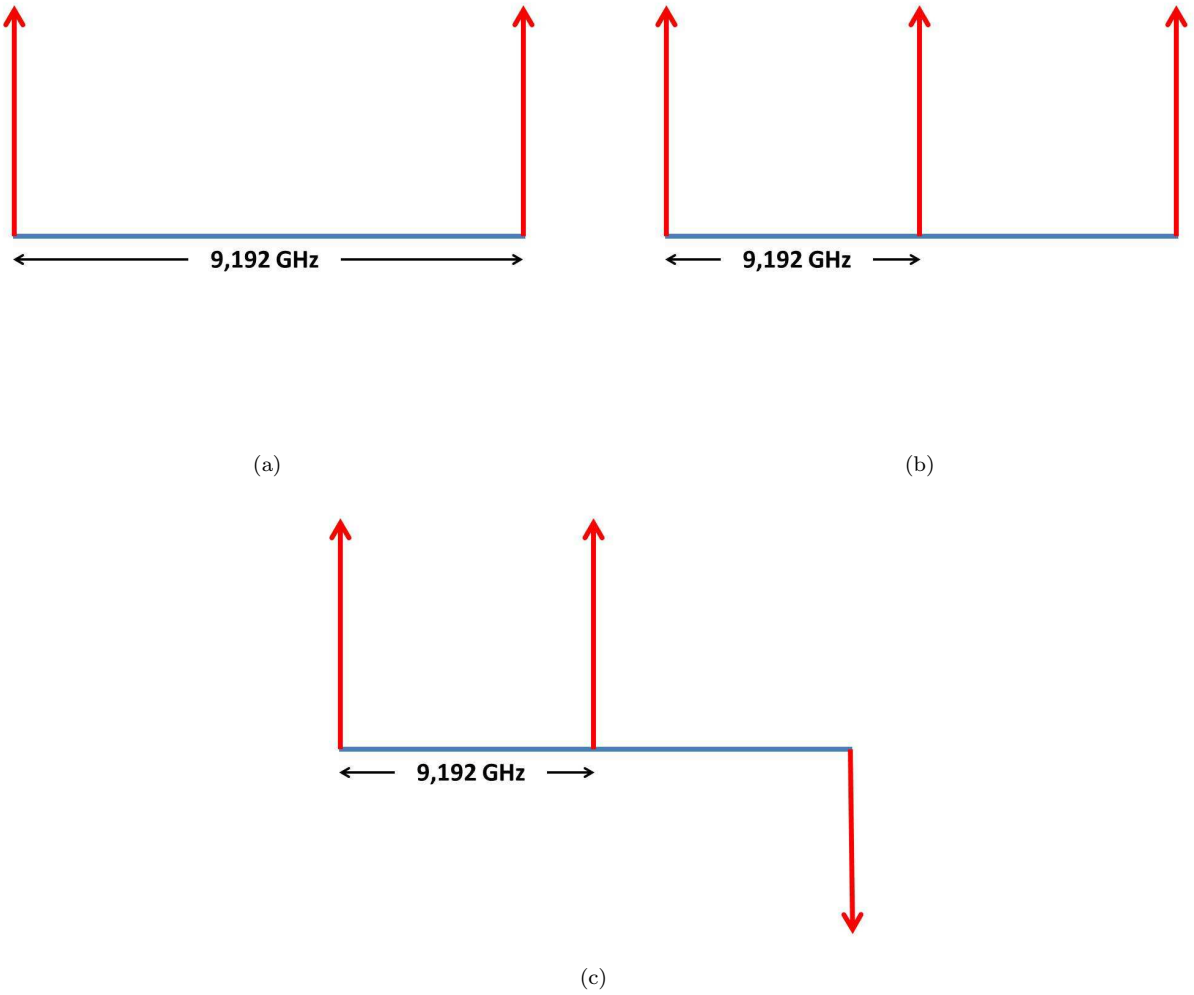

(a) (b)

(c)

Figure 83: Different optical sidebands that participate into the CPT interaction. (a): MZ EOM modulated at 4.596 GHz. (b): MZ EOM modulated at 9.192 GHz. (c): Phase modulator modulated at 9.192 GHz.

We measured the CPT resonance parameters as a function of the laser intensity for different excitations with MZ EOM (AM) and phase modulator (PM) in a given Cs vapor cell (N_2-Ar buffer gas mixture, L = 5 cm, D = 2 cm). Figure 84(a), 84(b) and 84(c) show the CPT resonance contrast, the FWHM and the FWHM/Contrast as a function of the laser intensity for different excitations. The laser is locked at the 4-4' optical transition. The cell temperature is stabilized at 33°C. The laser beam diameter is 6 mm.

These results indicate that the CPT resonance contrast and the FWHM are optimized in the case of the MZ EOM modulated at 4.596 GHz. The FWHM/Contrast ratio for the AM 4.596 GHz case is the lowest

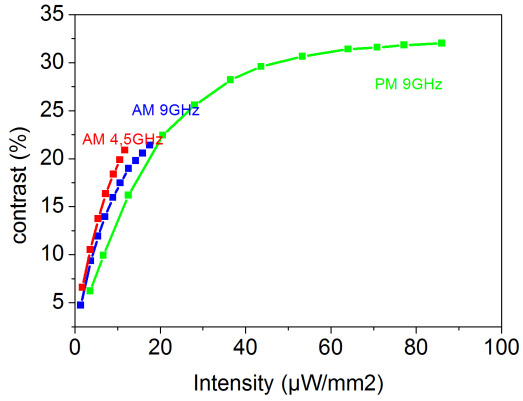

(a)

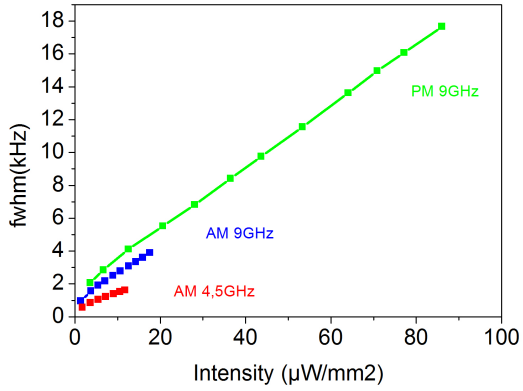

(b)

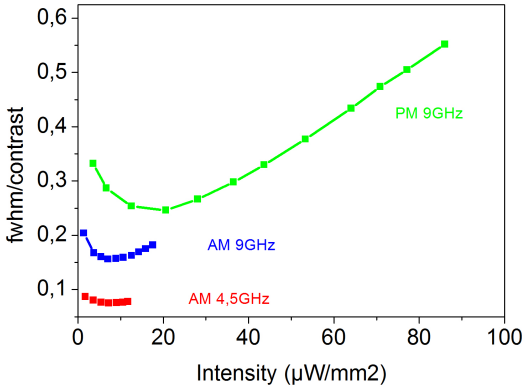

(c)

Figure 84: CPT resonance contrast (a), FWHM (b) and FWHM/Contrast (c) as a function of the laser intensity for AM modulated at 4.596 GHz (red), AM modulated at 9.192 GHz (Blue) and PM modulated at 9.192 GHz (Green). The cell temperature is 33°C. The laser beam diameter is 6 mm.

among the three configurations. Consequently, we decided to develop our system in this configuration. In the case of the AM modulation at 4.596 GHz, CPT interaction is realized by both first-order sidebands. The optical carrier must be rejected as much as possible to reduce light shift effects and perturbations of the signal. This carrier rejection is limited by the EOM extinction ratio of the EOM, measured to be 28 dB with our device. Higher-order harmonics were measured to be in power about 30 dB lower than first-order sidebands. Moreover, these optical lines are 4.596 GHz out of CPT resonance and should not participate to CPT interaction.

4.3.4 MZ EOM Stabilization

The transfer function operating point of a MZ EOM is known to drift due to the temperature variations, photorefractive effects and aging [139] [140]. The stabilization of the MZ EOM transfer function operation point is required in our experiment. In our case, we want to make it operate at the so-called dark point where the optical carrier is suppressed. We developed several advanced techniques to make the EOM operate properly. At the first, the EOM is temperature stabilized. A carrier suppression stabilization technique was implemented. The microwave power of the microwave synthesizer that drives the EOM is actively stabilized. Eventually, the optical power at the output of the EOM is stabilized using a voltage-controlled liquid crystal device (LCD) attenuator to ensure that the optical power contained in both first-order sidebands realizing the CPT interaction is stable. These techniques are described in the following parts.

EOM temperature stabilization The EOM is actively temperature controlled. For this purpose, the EOM is inserted in a mechanical duralumin box on which a high-precision electronic temperature controller inspired from [134] is embedded. The ensemble is placed in a box containing a 5 cm-thick insulating foam to isolate the system from ambient temperature variations. The integrated EOM thermistance is used for temperature control while a second thermistance is placed close to the EOM in the duralumin box to monitor the EOM temperature. The duralumin box is heated with 2 IRF840 transistors symmetrically fixed on each side of the duralumin box. Figure 85 shows the temperature fluctuations of the laboratory room, the CPT experiment optical table that is passively temperature stabilized with an insulating foam box and the EOM temperature. The EOM set temperature is 41.7 °C. The temperature fluctuations in the servo regime achieves 2×10^{-4} °C at 1 second integration time and remain well below 1×10^{-3} °C up to 50 000 s.

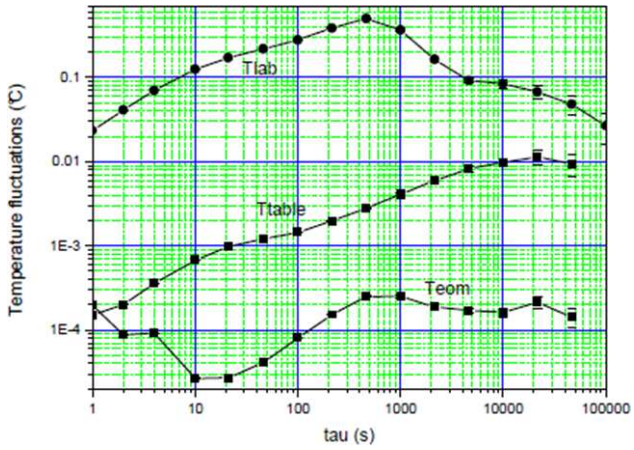

Figure 85: Temperature fluctuations of the laboratory room, the CPT experiment optical table and the EOM temperature. Temperatures of the laboratory room and optical table are about 24°C.

Microwave power stabilization Figure 86 shows the microwave power stabilization loop system. The 4.596 GHz microwave power is detected by a Schottky diode detector. The resulting output voltage is compared with an ultrastable voltage reference (LM399). An error signal is generated at the output to be amplified and processed in a PI controller to send a correction voltage to a voltage-controlled attenuator at

the output of the synthesizer. In the locked regime, microwave power fractional fluctuations are measured to be 1×10^{-3} at 1 second integration time and better than 1×10^{-5} at 10000 s.

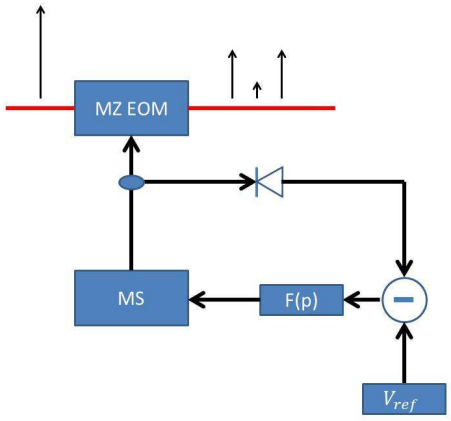

Figure 86: Microwave power stabilization loop. MS: microwave synthesizer. F(p): low pass filter. V_{ref}: LM399 voltage reference.

Carrier suppression stabilization We have already seen that the optimal CPT resonance signal height is detected when the carrier signal at the output of the MZ EOM is suppressed. A microwave technique to stabilize the operating point of the MZ EOM at the exact dark point is then required. A classical technique to stabilize the operating point of a MZ EOM is the low frequency synchronous modulation-demodulation technique [141] [142] [143]. The operating point voltage is slightly modulated at low frequency (typically 1 kHz) and the optical power at the output of the EOM is detected with a photodiode. The detected signal is synchronously demodulated and a correction signal is applied on the dc electrode of the MZ EOM. However, this technique was not appreciated for our application because it adds noise at Fourier frequency of 1 or a few kHz. This additional noise could disturb the clock performance through the Dick effect [144]. Consequently, we developed a carrier signal suppression microwave stabilization technique inspired by [145].

Let first explain the basic concept of this servo loop. Owing to the interference mechanism, the power P at the output of a MZ EOM for a given input power P_0 is given by:

$$P = P_0 \cos^2\left(\frac{\phi_0}{2} - \frac{\pi}{2}\frac{V}{V_\pi}\right) = \frac{P_0}{2}\left[1 - \cos\left(\phi_0 - \pi\frac{V}{V_\pi}\right)\right] \tag{104}$$

where ϕ_0 is a phase that results from actual length of the arms and ultimately from the manufacturing process, V is the control voltage, and V_π is the value of V needed to shift the differential phase by π. Intensity mismatch between the two arms results in a residual power at the output not included in Eq. (104), and expressed by the 'extinction ratio' parameter for the modulator. In general, the so-called dark point, shown in figure 87, is of a great interest. We propose here an original measurement technique to identify and stabilize the dark point.

At the exact dark point, the transparency (power) is an even function of the control voltage. The modulator acts as a maximally-efficient frequency doubler for the microwave modulation frequency ω_0.

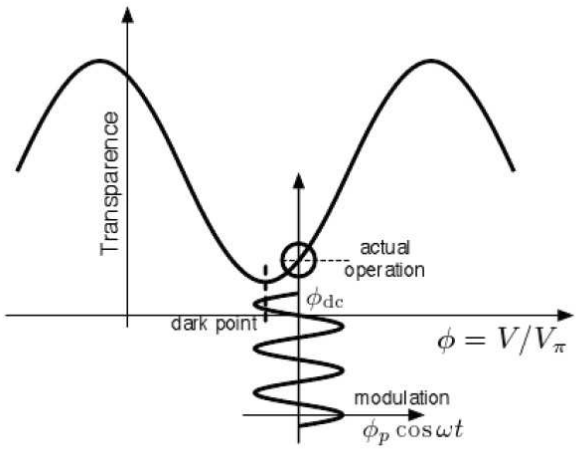

Figure 87: Transparency of the MZ EOM as a function of the ration between V and V_π.

Consequently, the fundamental frequency ω_0 is ideally absent in the microwave modulation. In this case, we note and replace in equation (104) $\phi_0 \to \phi_{dc}$ for the dc point and $-\pi V/V_\pi \to \phi_p \cos(\omega_0 t)$ for the microwave modulation. Since the operation is ideally kept at the exact dark point, it is legitimate to assume that ϕ_{dc} is a small quantity, hence to approximate $\sin \phi_{dc} \simeq \phi_{dc}$ and $\cos \phi_{dc} \simeq 1$.
Accordingly, Eq. (104) rewrites as:

$$P(t) = \frac{P_0}{2}\Big\{1 - \cos\big[\phi_{dc} + \phi_p \cos(\omega_0 t)\big]\Big\} \tag{105}$$

$$P(t) \simeq \frac{P_0}{2}\Big\{1 - \cos\big[\phi_p \cos(\omega_0 t)\big] + \phi_{dc} \sin\big[\phi_p \cos(\omega_0 t)\big]\Big\} \tag{106}$$

Further, we use the following expansions derived from the Jacobi-Anger identity:

$$\cos(z\cos\theta) = J_0(z) - 2J_2(z)\cos(2\theta) + \ldots \quad (n\omega_o \; terms, even \; n) \tag{107}$$

$$\sin(z\cos\theta) = 2J_1(z)\cos(\theta) + \ldots \quad (n\omega_o \; terms, odd \; n) \tag{108}$$

The power at the modulator output is given by:

$$P(t) = \frac{P_0}{2}\Big[1 - J_0(\phi_p) + 2\phi_{dc} J_1(\phi_p)\cos(\omega_0 t) + 2J_2(\phi_p)\cos(2\omega_0 t) + \ldots\Big] \tag{109}$$

Figure 88 reports the experimental setup able to detect the '$\cos(\omega_0 t)$' term of $P(t)$, which is proportional to ϕ_{dc}. The mixer is saturated at the LO input, and receives a small signal $V_{RF}\cos\omega_0 t$ at the RF input. In this condition, it operates as a synchronous detector. The output signal is $V_{IF} = \frac{2}{\ell_m} V_{RF}$, where ℓ_m is the SSB loss of the mixer, and the factor 2 is due to the overlapping of the lower and upper sidebands in the synchronous conversion.

In the end, the output voltage is

$$V_0 = K\phi_{dc}, \tag{110}$$

where

$$K = \frac{2}{\ell_m} A\, J_1(\phi_p)\, \rho P_0 R_0 \qquad (V/rad) \tag{111}$$

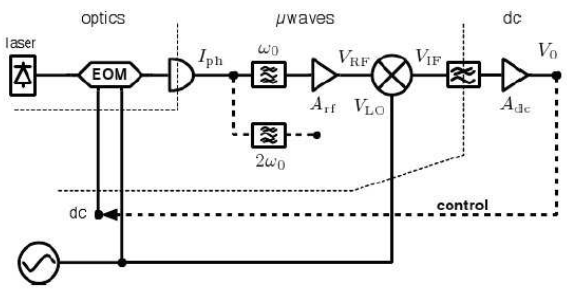

Figure 88: Basic scheme for carrier signal suppression stabilization.

Here A is the total voltage amplification (rf and dc), ρ is the photodetector responsivity, ρP_0 is the photocurrent at the frequency ω_0, and R_0 is the resistance seen by the photodetector.

We implemented this technique in our setup. A fast photodiode at the output of the MZ EOM detects the optically carried 4.596 GHz microwave signal. The 4.596 GHz detected signal is amplified by a low noise amplifier with a gain of 52 dB and filtered by a band-pass filter with bandwidth about 50 MHz. This signal is sent to a microwave mixer to be compared with the 4.596 GHz signal generated by the synthesizer. An error signal is generated at the output of the mixer and active feedback control is applied to the MZ EOM dc electrode bias voltage V_{bias}. Figure 89 shows as a function of the bias voltage V_{bias} the power of the first-order optical sidebands (measured with a Fabry-Perot interferometer), the power of the 4.596 GHz optically carried signal detected with a fast photodiode, the dc voltage V_m at the output of the mixer and the CPT signal height. When $V_{bias} \simeq 3.1\,V$, the first order optical sidebands power is maximized and the optical carrier power is minimized. It is then clearly observed that the mixer output voltage exhibits a sharp zero-crossing point that can be used for keeping the carrier signal suppressed. In our experiment, a microwave mixer with an ultralow intrinsic offset output voltage is finely selected to prevent being slightly shifted from the exact dark point. For $V_{bias} \simeq 3.1\,V$, the CPT signal height is maximized while the CPT signal dc background is minimized, maximizing the CPT resonance contrast. In figure 89, the mixer output is also nulled where the optical sidebands power is minimum while the optical carrier signal is maximized when $V_{bias} \simeq 6\,V$. In this configuration, the CPT signal and contrast is greatly reduced. This result indicates the importance to stabilize actively the MZ EOM operating point to the exact dark point for CPT atomic clock.

Figure 90 shows the 4.596 GHz optical beatnote signal power versus time in free running regime and stabilized regime. In the free running regime, the carrier suppression is degraded by about 17 dB in 3000 s. In the stabilized regime, the relative carrier power fluctuations are less than 5×10^{-3} after 1000 s integration time. Relative power fluctuations at the output of the MZ EOM are reduced by a factor 100 in the stabilized regime.

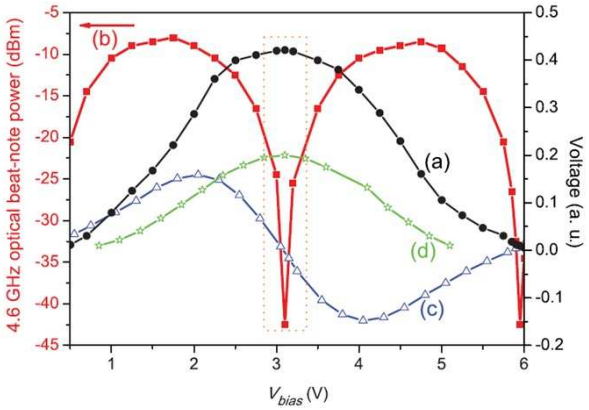

Figure 89: Impact of the MZ EOM bias voltage V_{bias} on experimental signals. The laser beam diameter is 2 cm. The cm scale Cs vapor cell (Diameter=2 cm, length=5 cm) is used. (a) Optical sidebands power. (b) Power of the optically carried 4.596 GHz signal at the output of the MZ EOM. (c) dc signal at the output of the microwave mixer. (d) CPT resonance signal height.

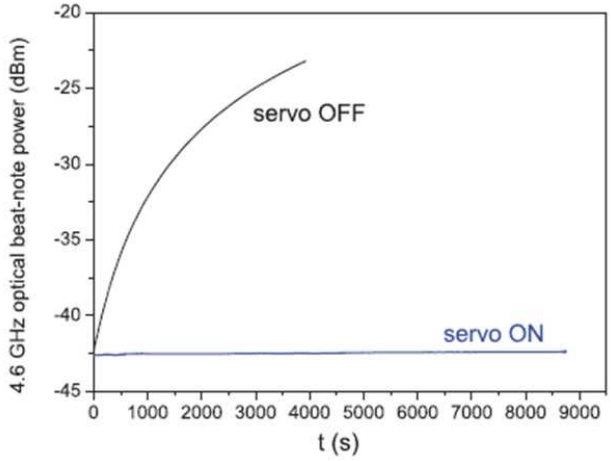

Figure 90: Power of the 4.596 GHz optically carried signal at the MZ EOM output versus measuring time: servo loop ON or OFF.

4.3.5 Laser Power Stabilization

After the carrier suppression is stabilized, the power of optical sidebands for CPT signal generation needs to be stabilized. The fluctuations of the optical sidebands power could increase the intensity noise. Our system uses a voltage-controlled liquid crystal device (LCD) attenuator. Figure 91 shows the laser power stabilization servo loop implemented at the output of the MZ EOM. The LCD consists of a voltage-controlled half wave plate (HWP) placed between two crossed linear polarizers (Figure 92). Since the HWP rotation can change polarization direction of the input laser beam, the transmitted laser power can be adjusted by the voltage applied on the HWP. The LCD is driven by a 2 kHz square signal. Changing the peak to peak voltage of this signal allows to change the transmitted laser power. A polarizer is placed at the output of the LCD to control the polarization direction of the laser beam before entering the Michelson interferometer. The laser power is detected by a low noise photodiode. The detected signal is sent to a DAQ card connected to a computer. The DAQ card detects 20 samples per second. The detected signal is compared with a digital reference signal in a LabVIEW program to generate an error signal. The error signal is sent to a PI controller in the programme. Subsequently, the programme generates a correction signal to adjust the output square signal amplitude of the Agilent 33220A by GBIP link.

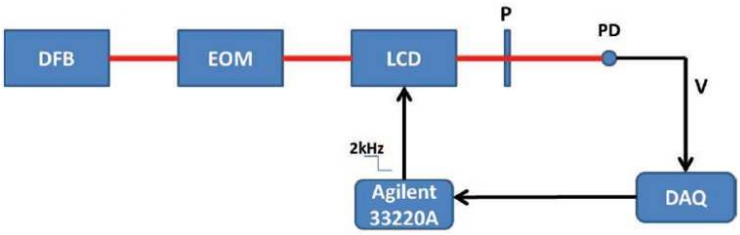

Figure 91: Laser power stabilization servo loop. LCD: liquid crystal device. DAQ: National Instruments data acquisition card. Agilent 33220A: 20 MHz function arbitrary waveform generator.

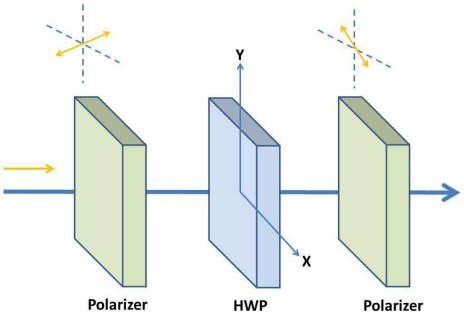

Figure 92: Basic scheme of a liquid crystal device. HWP: half wave plate.

Figure 93 shows the LCD output power as a function of the 2 kHz square signal amplitude. This transfer function presents two linear zones. We set the operating point at the center of the linear zone to build the laser power stabilization servo loop. Figure 94 shows the laser power detected by the photodiode as a function of measuring time in free running regime (a) and stabilized regime (b).

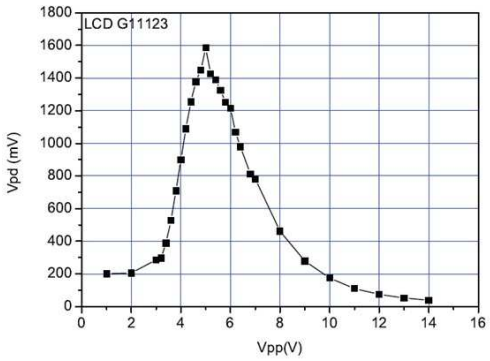

Figure 93: LCD output laser power as a function of the 2 kHz square signal amplitude.

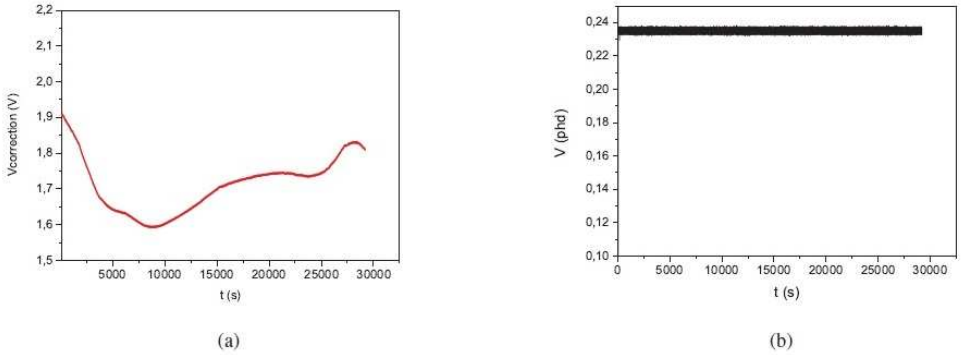

(a) (b)

Figure 94: Laser power detected by the photodiode as a function of measuring time. (a): free running regime. (b): stabilized regime.

Figure 95 shows the relative laser power fluctuations at the output of the LCD in free running regime (black) and stabilized regime (red). The relative laser power fluctuations in stabilized regime are 2×10^{-6} at 500 seconds integration time, which is almost 4 orders of magnitude lower than power fluctuations in the free running regime.

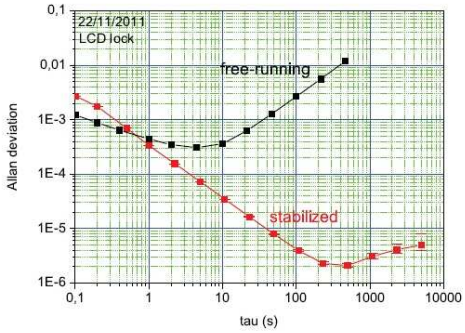

Figure 95: Relative laser power fluctuations at the output of the LCD in free running regime (black) and stabilized regime (red).

4.4 4.596 GHz Frequency Synthesizers

The short term frequency stability of an atomic clock can be degraded by the local oscillator noise [144] [146]. In a continuous wave (CW) regime atomic clock with resonance frequency ν_0, operating at a LO modulation frequency f_m, the frequency stability limitation $\sigma_y(\tau)$ due to this aliasing effect is given by:

$$\sigma_y(\tau) \sim \frac{f_m}{\nu_0}\sqrt{S_\varphi(2f_m)} \tag{112}$$

where $S_\varphi(2f_m)$ is the LO phase noise at Fourier frequency $2f$.
This relation indicates that an atomic clock with a relative frequency stability of 10^{-12} at 1 s, operating at a LO modulation frequency of 100 Hz requires a LO with a phase noise at 200 Hz lower than about -80 dBrad^2/Hz. For the Cs CPT clock under development, Rodolphe Boudot, my thesis tutor, developed a frequency-multiplied quartz oscillator-based low phase noise microwave synthesizer used to drive the MZ EOM.
Figure 96 shows the basic scheme of the microwave frequency synthesizer architecture. The architecture is inspired from [25] with additional functions.

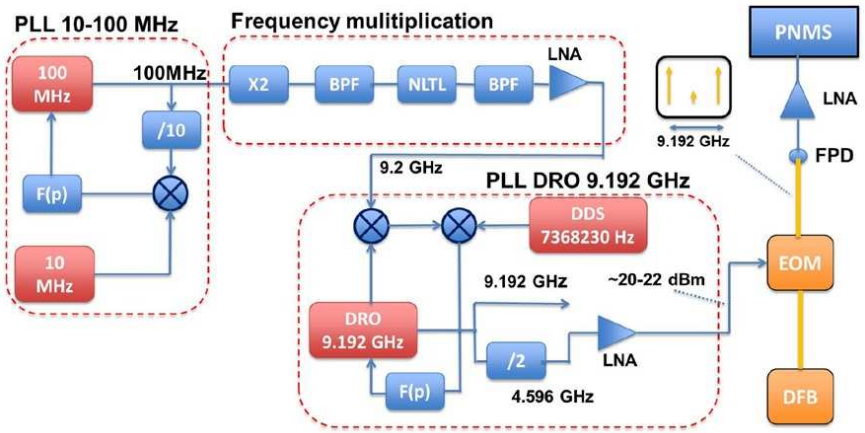

Figure 96: Basic scheme of the microwave synthesizer linked to the optical setup. BPF: bandpass filter. FPD: fast photodiode. PNMS: phase noise measurement system. LNA: low noise amplifier.

A high spectral purity 100 MHz quartz oscillator is phase locked through a SP8401 digital frequency divider by 10 to a high stability frequency-doubled 5 MHz quartz oscillator with a bandwidth of about 60 Hz. At the output of this chain, the 100 MHz signal is frequency doubled to 200 MHz using a Minicircuits RK3 frequency-doubler and amplified to a power of about 21 dBm with a low noise amplifier (Minicircuits Gali-84+). After bandpass filtering, the 200 MHz signal is used to drive a Non-Linear Transmission Line (NLTL) device that generates harmonics up to 20 GHz. The 9.2 GHz harmonics generated by the NLTL is bandpass filtered with a 50 MHz bandwidth bandpass filter and amplified to a power of about 8 dBm with a low noise microwave amplifier (AML612L2201). Microwave isolators are added for 50 Ω impedance matching and to prevent undesired feedback. The 9.2 GHz is sent to a mixer to be compared with a 9.192 GHz signal from a dielectric resonator oscillator (DRO). The resulting 7.368 MHz beatnote signal is low-pass filtered and compared to the 7.368 MHz from a direct digital synthesis (DDS) to generate an error signal. The error signal is filtered, processed in a PI controller and used to phase lock the DRO to the frequency-multiplied 100 MHz signal with a bandwidth of 200 kHz. A low phase noise 9.192 GHz signal with a microwave power of about

13 dBm is then obtained at the output of the DRO. The signal is splitted into two different arms to generate 9.192 GHz or 4.596 GHz frequency outputs. A low noise frequency divider is used to frequency divide the 9.192 GHz signal into the 4.596 GHz signal. The output microwave signal is isolated, bandpass filtered and amplified with a 4-12 GHz bandwidth high power amplifier to drive the MZ EOM with a microwave power of about 23-24 dBm. Figure 97 shows a photograph of the microwave synthesizer. All the components of the synthesizer, except the 10 MHz quartz oscillator source and the DDS, are inserted and mechanically fixed in a 12 dm^3 rack. The total power consumption of this rack is 12.9 W.

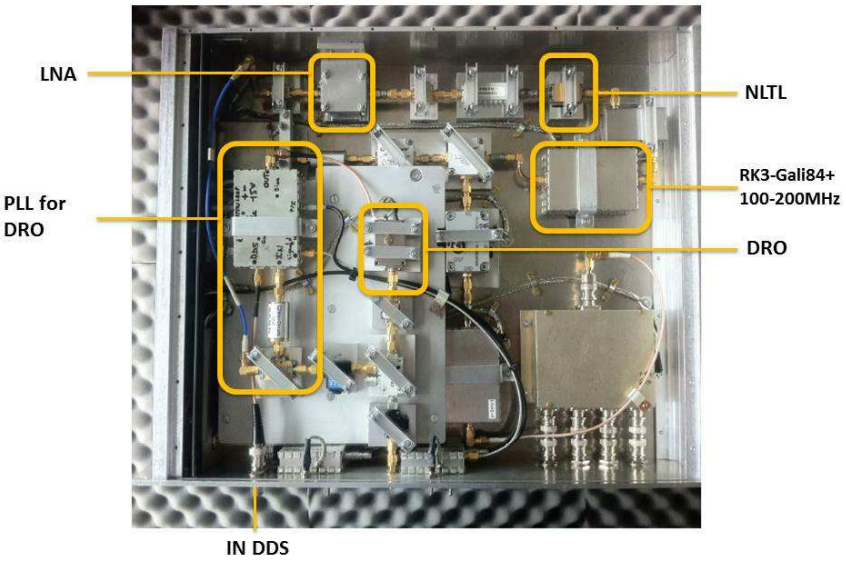

Figure 97: Photograph of the microwave frequency synthesizer. The 10 MHz quartz oscillator and the DDS are not included here.

Figure 98 plots absolute phase noise performances of the key signals of the system. The phase noise spectrum $L(f) = \frac{1}{2}S_\varphi(f)$ of the free running 10 MHz quartz oscillator pilot is given in dBc/Hz by the power law $(-145)f^0 + (-127)f^{-1} + (-121)f^{-3}$. The phase noise spectrum $L(f)$ of the free running 100 MHz crystal oscillator is given in dBc/Hz by the power law $(-128)f^0 + (-121)f^{-1} + (-70)f^{-3}$. The free running DRO phase noise spectrum exhibits from $f = 1$ Hz to 10 MHz a f^{-3} slope with +12 dBc/Hz at 1 Hz offset frequency. Its phase noise floor for $f > 10$ MHz is about -175 dBc/Hz. The 9.192 GHz output signal from the synthesizer presents phase noise performances of -170, -120 and -61 dBc/Hz at $f = 10$ MHz, 10 kHz and 1 Hz respectively. The peak at 200 kHz is attributed to the DRO PLL gain while the slope change at 55 Hz is due to the bandwidth of the 100 MHz oscillator PLL. At the output of the frequency divider by 2, the 4.596 GHz signal phase noise performances are as expected 6 dB lower than those of the 9.192 GHz signal. The phase noise floor of the 4.596 GHz signal is limited by the frequency divider residual noise at a level of -149 dBc/Hz. No phase noise degradation is observed between the 9.192 GHz optical beatnote signal at the output of the EOM and the direct synthesis output for $f < 1$ kHz. For higher Fourier frequencies, the phase noise floor is limited by the low input power (about -51 dBm) of the microwave amplifier placed at the output of the fast photodiode used to detect the optical beatnote. With equation 112, the phase noise performances of the optical beatnote should be compatible with the development of a CPT atomic clock

with frequency stability better than 2×10^{-13} at 1 second integration time.

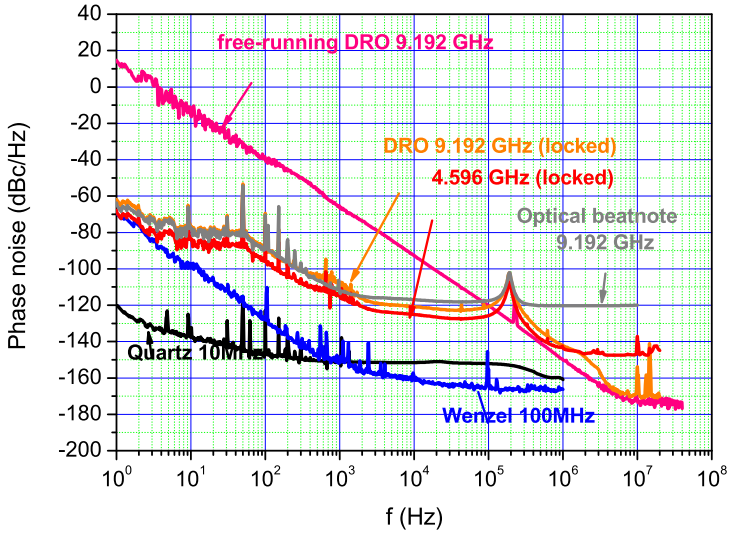

Figure 98: Absolute phase noise performances of key signals of the frequency synthesizer.

4.5 Michelson system

A key part of our laser system is the Michelson delay-line system placed at the output of the EOM. This system is shown in Figure 99.

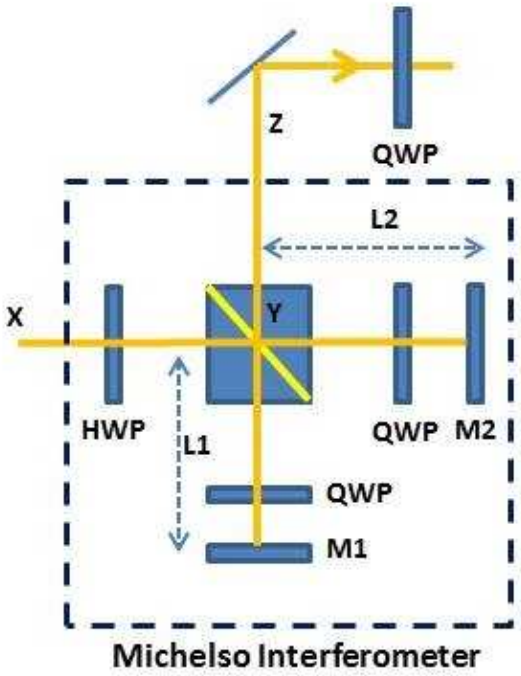

Figure 99: Michelson delay-line and orthogonalizer system. M1, M2: mirrors. QWP: quarter wave plate. HWP: half-wave plate.

At the output of the MZ EOM, both optical lines of fixed linear polarization pass through a polarization-beam splitter cube (PBSC) to be divided into two sub-beams in the two arms of a Michelson interferometer. A half wave plate is placed before the input of the Michelson system in order to balance the laser intensity in both arms. A quarter wave plate is placed in each arm to rotate as desired the polarization of each sub-beam and to ensure that no optical power is sent back to the system input. The splitted laser beams traverse $X \rightarrow Y \rightarrow M1 \rightarrow Z$ and $X \rightarrow Y \rightarrow M2 \rightarrow Z$ paths respectively.
Let's assume that the polarizations of both sub-beams beams are along the x and z axes respectively and that the frequencies of the two optical lines in each arm are ω_1 and ω_2. The polarizations of the optical lines ω_1 and ω_2 at the output of the Michelson interferometer are presented by a unit vector:

$$\begin{aligned} \hat{\epsilon}(\omega_1) &= \frac{1}{\sqrt{2}}(\hat{x} + e^{2ik_1\Delta L}\hat{y}) \\ \hat{\epsilon}(\omega_2) &= \frac{1}{\sqrt{2}}(\hat{x} + e^{2ik_2\Delta L}\hat{y}) \end{aligned} \tag{113}$$

where k_1 and k_2 are the wavevector for the ω_1 and ω_2 fields respectively, $2\Delta L$ is the optical path difference between the two paths.
The two optical lines are orthogonally polarized to each other when the following conditions are satisfied

[108].

$$\begin{aligned} 2k_1\Delta L &= 2m\pi \\ 2k_2\Delta L &= (2n+1)\pi \end{aligned} \tag{114}$$

with m and n present integers.
A fine adjustment of both quarter wave plates makes possible to obtain at the output of the polarizing cube two superimposed beams linearly polarized with perpendicular angle and differing by a phase delay. The optical path difference of the Michelson system induced a time-delay between both orthogonally polarized optical lines. A displacement of the mirror of $\lambda_0/2$ shifts the intensity peaks of the beatnote on one beam by half a hyperfine period with respect to the peaks of the other beam. A quarter wave plate at the output of the Michelson interferometer allows to create two time-delayed sets of bichromatic circularly polarized optical fields rotating in opposite directions. This is the basic principle of the PPOP scheme.
The evolution of the polarizations of the two optical lines is analyzed using a linear polarizer at the output of the system. The results are shown in Figure 100. The distance between two peaks is about 16 mm, corresponding to half the wavelength of the clock transition. The optical path difference between both arms of the interferometer can be written:

$$\Delta L = 2(x - x_0) \tag{115}$$

where x is the mirror position and x_0 is the position where the optical path differences is null or a multiple of $\lambda_0 = 32.6\,mm$.

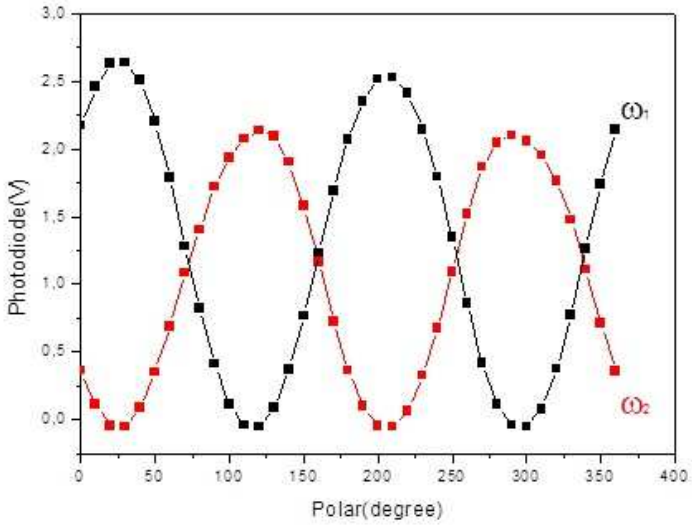

Figure 100: Polarization analysis for the output beams. Black curve: the field at ω_1. Red curve: the field at ω_2.

The theoretical laser transmitted power, described in section 3, with $\theta = 2\pi(x - x_0)/\lambda_0$, can be written:

$$S = S_{max} e^{-\alpha_d \cos^2(2\pi \frac{x-x_0}{\lambda_0})L} \tag{116}$$

where S is the transmitted power, S_{max} the signal at CPT resonance maximum, α_d the absorption coefficient

and L the cell length.

In our experimental setup, the actual Michelson system is not stabilized. For further studies, Hugo Dzuira (along a training period) developed a compact box that will contain all components of the Michelson system (Figure 101(a) and 101(b)). One arm of the system will be fixed with mirrors, QWP and cube glued. The length of the other arm will be certainly actively controlled using a PZT actuator. Nevertheless, additional measurements are to be done to fix specifications of the system. Eventually, the whole box will be actively temperature controlled.

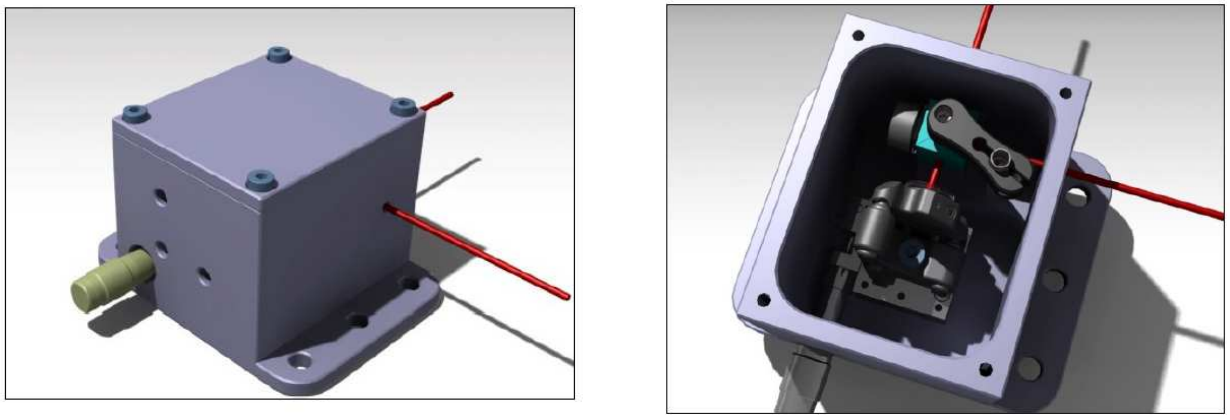

(a) (b)

Figure 101: 3D model of Michelson system rack.

4.6 Physics Package

The physics package is made of a Cs-buffer gas cell, an oven to control the temperature of the cell, a solenoid to apply a static magnetic field and a double-layer mu-metal shield to protect the atoms from ambient electromagnetic perturbations. The package is suitable for different cell dimensions. We tested three different Cs vapor-buffer gas cells. Figure 102 shows the photographs of cells 1, 2 and 3. Their main characteristics are reported in Table 7. Cell 1 is a microfabricated cell realized according to the process described in [147] and studied in [83], whereas cell 2 and cell 3 are glass-blown cm-scale pyrex vapor cells. We thank Stéphane Guérandel from LNE-SYRTE, Observatoire de Paris, for lending us cells 2 and 3.

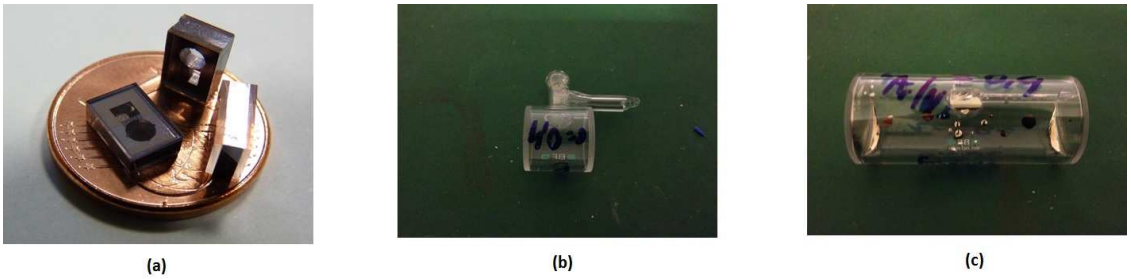

Figure 102: Tested Cs vapor-buffer gas cells. (a): cell 1. (b): cell 2. (c): cell 3.

Figure 103 shows the cell oven. The oven is heated by a coaxial wire. Amagnetic thermistance and heater are used. The cell temperature is stabilized using a home-made external high-precision temperature controller. Figure 104 shows typical relative temperature fluctuations of the cell at a set point of 38°C. These results correspond to a typical temperature variation of 0.9 mK and 100 μK at 1 s and 1000 s respectively.

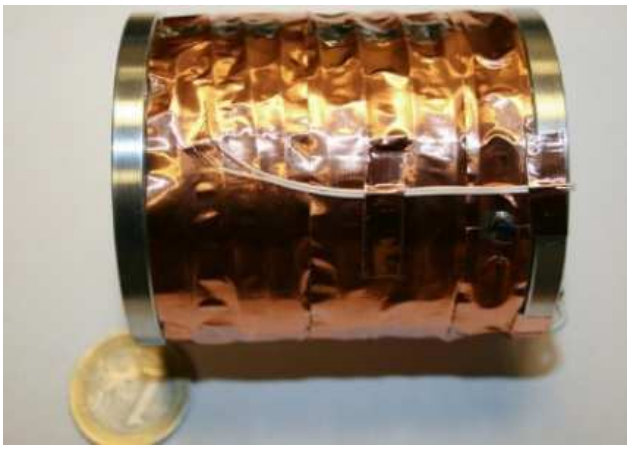

Figure 103: Oven used to control the cell temperature.

In order to split the Zeeman sublevels and to control the static magnetic field, the oven is placed into a mechanical tube surrounded by a solenoid as figure 105 shows. The coil is connected to a Thorlabs LDC 201 C ULN laser diode current driver to generate the magnetic field. Measuring the frequency splitting between the transitions $|F = 3, m_F = -1\rangle \rightarrow |F = 4, m_F = -1\rangle$ and $|F = 3, m_F = -1\rangle \rightarrow |F = 4, m_F = -1\rangle$ versus the solenoid current, the relation between the magnetic field B and the current I such as $B = \alpha I$ was

Table 7: Characteristics of tested buffer gas filled cells and relevant parameters. For buffer gas mixtures, r is defined as the ratio P_{Ar}/P_{N_2} between Ar and N_2 partial pressures. The experimental data are the features of the cell, the buffer gases, the laser beam, the contrast and the CPT linewidth. All other data are calculated values.

Cell	1	2	3
Buffer gas	Ne	N_2-Ar	N_2-Ar
Buffer gas total pressure P (Torr)	75	15	15
Buffer gas ratio r	-	0.4	0.4
Cell length L (cm)	0.14	1	5
Cell diameter D (cm)	0.2	1	2
Cell temperature T_{cell} (°C)	80	38	32
Cs atomic density n_{Cs} (at/cm^3)	4.0×10^{12}	1.6×10^{11}	9.0×10^{10}
Cs-wall collisions relaxation rate γ_w (rad/s)	2470	442	374
Cs-Buffer gas relaxation rate γ_{bg} (rad/s)	16	19.4	19.2
Spin-exchange relaxation rate γ_{se} (rad/s)	2040	73	42
Ground-state relaxation rate γ_2 (rad/s)	4520	534	435
CPT linewidth FWHM (kHz)	1.4	0.17	0.14
Laser power P_L (mW)	0.5	0.5	0.5
Laser diameter (cm)	0.2	0.6	0.6
Rabi Frequency Ω (rad/s)	2.9×10^7	9.5×10^6	9.5×10^6
Excited level relaxation rate $\Gamma^\star$ (rad/s)	5.9×10^9	1.8×10^9	1.8×10^9
Optical transition width $\Gamma^\star/2\pi$ (MHz)	937	292	292
Optical transition shift (MHz)	-155	-136	-131
Number of Cs atoms in the laser beam	1.8×10^{10}	4.5×10^{10}	13×10^{10}
Experimental contrast (%)	6	10.5	50
Experimental CPT linewidth (kHz)	1.32	0.59	0.42

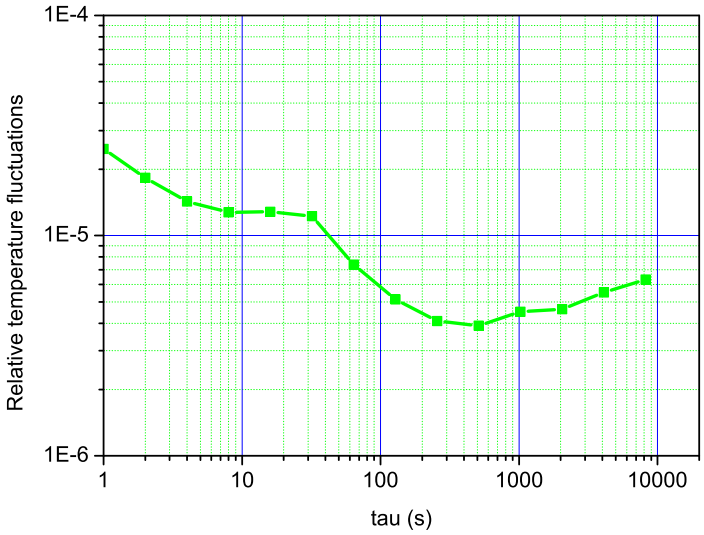

Figure 104: Relative temperature fluctuations of the cell at a set point of 38 °C.

measured to be $\alpha = 44.52$ mG/mA.

Figure 105: Mechanical tube with the solenoid to generate the static magnetic field.

Figure 106 shows the relative fluctuations of the current source when $I = 3.5$ mA. They are measured to be 6×10^{-4} and 3×10^{-5} at 1 s and 10000 s respectively. From these performances, we evaluate the expected clock frequency stability limitation due to the variations of the magnetic field (induced by variations of the solenoid current). For a current $I = 3.5$ mA, we have $B = \alpha I = 155.75$ mG. The current stability is about 3×10^{-5} at 10000 s. This means that current fluctuations don't exceed 0.1 μA at 10000 seconds. For the magnetic field, the fluctuations dB is limited to 1×10^{-4} mA $\cdot$ 44.5 mG/mA $= 4.45 \times 10^{-3}$ mG$= 4.45 \times 10^{-6}$ G. The frequency shift of the 0-0 transition $\Delta\nu_{cs}$ caused by the magnetic field variations is:

$$\Delta\nu_{cs} = 2 \cdot B \cdot dB \cdot 427(\mathrm{Hz/G^2}) \approx 0.6 \quad \mathrm{mHz} \tag{117}$$

This limits the clock frequency stability to a level of 6.5×10^{-14} at 10 000s. This result can be improved by re-

ducing the ratio between magnetic field and current, this ratio equals 44.5 mG/mA in our case. Modifications will be realized in a near future to reduce this limitation.

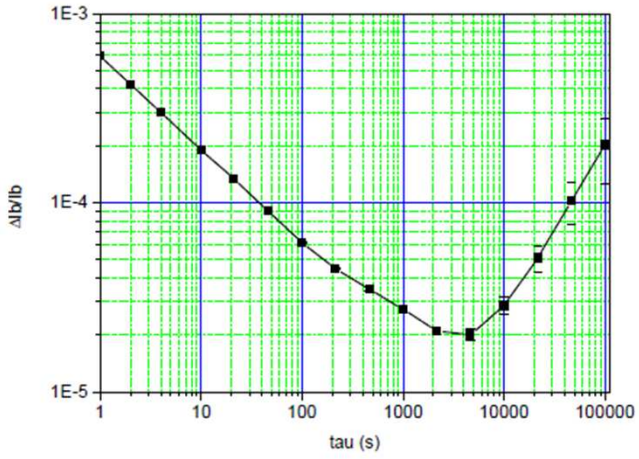

Figure 106: Relative fluctuations of the current source when $I = 3.5$ mA.

Figure 107 shows a photograph of the total physics package.

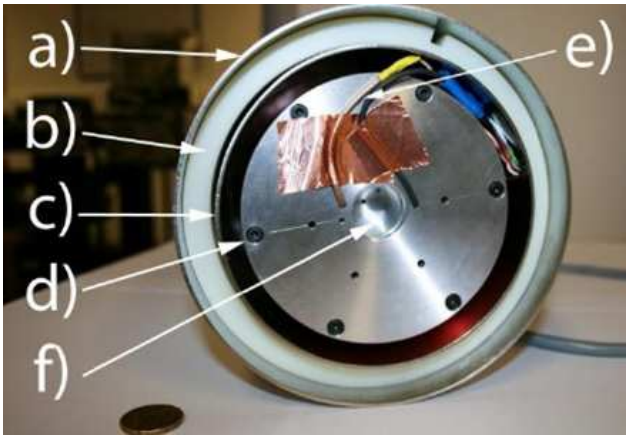

Figure 107: Photograph of the physics package of Cs vapor-buffer gas cell. (a): μ metal shell. (b): Foam to keep temperature. (c): μ metal shell. (d): mechanical tube with the wound coils. (e): oven. (f): support of vapor cell.

5 Continuous and Ramsey spectroscopy with push-pull optical pumping

This section is devoted to report CPT spectroscopy results we obtained with our experimental set-up. These results were reported in [149]. In the first part, we present the results of CPT characterization in continuous wave regime. The efficiency of the PPOP technique to increase greatly the number of atoms involved in the clock transition is demonstrated. The existence of $\Delta m = 2$ transitions, neighbours to the clock 0-0 transition, induced by the coexistence of left and right circular polarization in the PPOP scheme is pointed out. For different cells, we measured the impact of the laser intensity onto the CPT resonance line (linewidth, contrast, linewidth/contrast). CPT resonance with different beam diameters or under different optical transitions is also reported. CPT resonances with high-contrast are reported using the PPOP scheme. The contrast is found to be increased with increased laser intensity at the expense of the CPT line broadening. To circumvent this issue, we propose in the second part an original setup allowing the detection of high-contrast and narrow Ramsey fringes by combination of PPOP and a Ramsey-like temporal pulsed interrogation. These results were reported in [150].

5.1 CPT spectroscopy with PPOP in CW regime

5.1.1 Zeeman Spectrum : PPOP versus circular polarization

Figure 108(a) and 108(b) show a Zeeman spectrum obtained with the cell 2 with classical circular polarization and PPOP, respectively, for identical total incident laser intensity. It is clear that most of the atoms are lost in extreme Zeeman sublevels with circular polarization. At the opposite, the number of atoms that participate to the central clock transition is greatly favored with PPOP. In this case, the Zeeman spectrum is found to be well symmetrical and the clock resonance contrast is here 5.5 %. Figure 109 shows a Zeeman spectrum obtained in the cell 3 with PPOP. The 0-0 Zeeman transition in this case is even more favored. The static magnetic field is only homogeneous over 2 cm long, so the extreme Zeeman transitions are not so well symmetrical. On this figure, it is pointed out that neighbor Zeeman transitions are "dirty". This is explained by the fact that the physics package we used at this moment only ensured a homogeneous static magnetic field along a length of 2 cm as shown on figure 110. Figure 111 shows that extremely high contrasts can be obtained in the cell 3 by operating with high laser intensity. In this case, a CPT resonance with a contrast of 78 % is detected with a laser beam diameter of 6 mm. To our knowledge, this value is among the best contrasts ever measured on a CPT resonance.

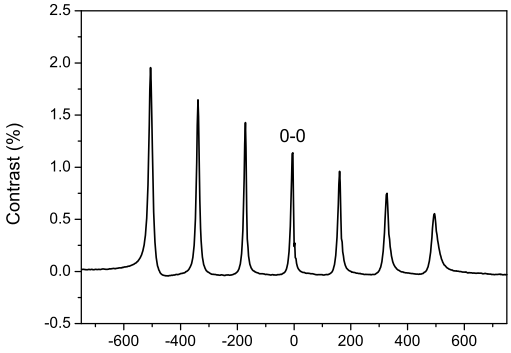

(a)

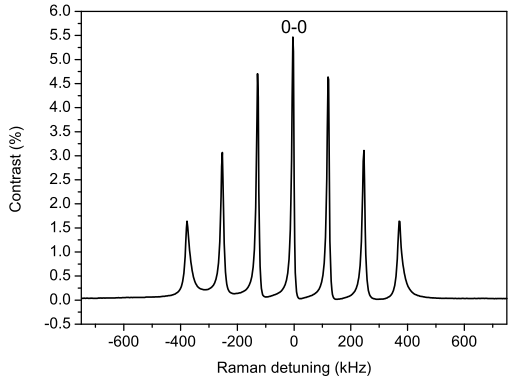

(b)

Figure 108: Zeeman spectrum detected in the cell 2. The total laser power is 1.05 mW. The beam diameter is 1 cm. The static magnetic field is not the same for both curves (without consequence on the CPT signal). (a): Circular polarization (b): Push-pull optical pumping.

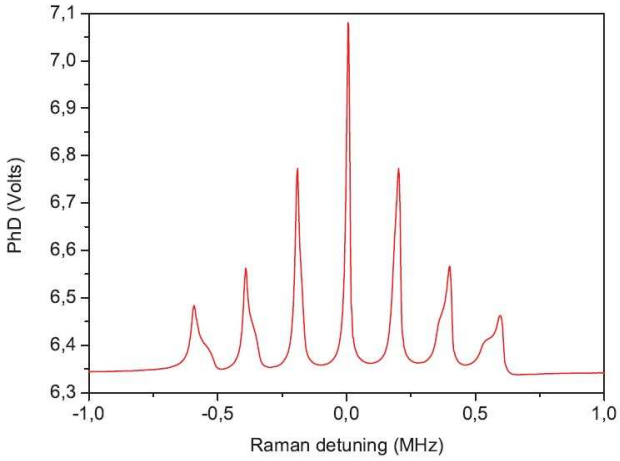

Figure 109: Zeeman spectrum detected in the cell 3. The total laser power is 800 μW. The beam diameter is 6 mm.

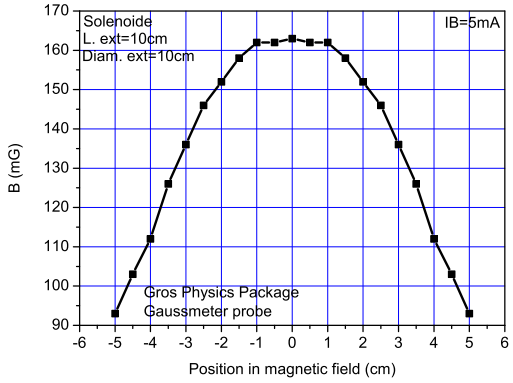

Figure 110: Magnetic field in the physic package as a function of the position in magnetic field.

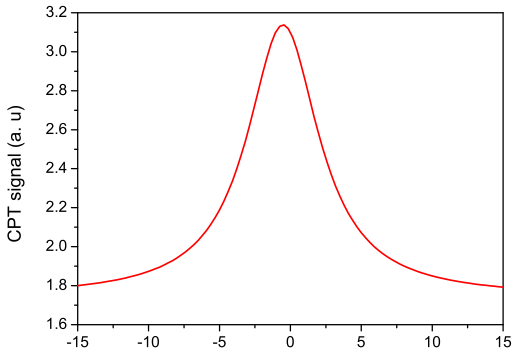

Figure 111: CPT resonance detected in the cell 3. The laser power is 3 mW. The beam diameter is 6 mm. The contrast is 78 %.

5.1.2 Impact of the mirror position

Figure 112 displays the light power transmitted through the cell 3 as a function of one mirror position the Michelson interferometer.

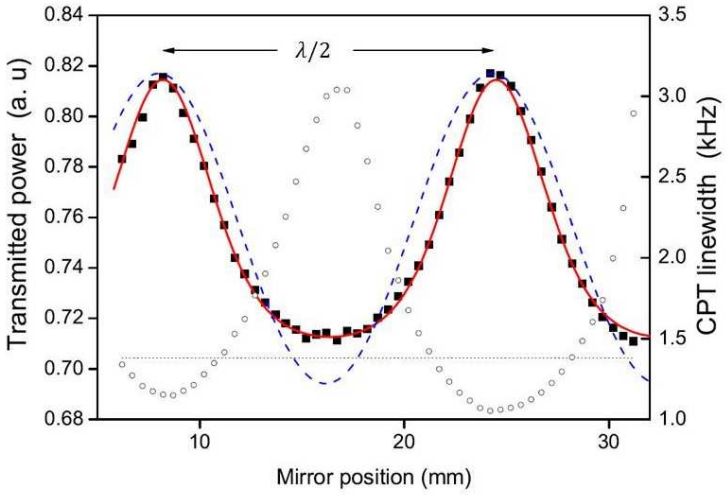

Figure 112: Transmitted light power through cell 3 and linewidth of the CPT resonance versus the position of the mirror of one arm of the interferometer. Squares: measured light power, dotted line: light power far from CPT resonance (large Raman detuning). The dashed line is a fit of Eq. 116. The solid line is a fit of Eq. (116) with an additional background. White dots: CPT resonance width.

The squares are the experimental data. The dotted line is the light power far from CPT resonance for a large Raman detuning. The distance between two maxima is 16 mm which is half the wavelength of the clock transition. The optical path difference between both arms of the interferometer can be written $\Delta\ell = 2(x - x_0)$, where x is the mirror position and x_0 the position where the optical path difference is null or a multiple of λ_0 (32.6 mm).

The theoretical output signal is given by Eq. (116). The dashed curve is a fit of experimental data with α_d and x_0 the adjustable parameters. The agreement is not good. The solid line on Fig. 112 is a fit of Eq. (116) with an additional background. Surprisingly, the agreement is found to be very good. Nevertheless, the fitted value of the background is significant and very close of the off-CPT resonance signal. We have no explanation for this and Eq. (116) with a background added can be considered as a phenomenological model.
In our experimental conditions, the last term of Eq. (91) is negligible and can not explain the disagreement between the theoretical expression and experimental data. At the opposite, the latter could be explained by an oversimplification of our model developed in section 3.6.3. Indeed, our model is based on analytical expressions from [117] calculated for a closed four level scheme whereas in our experience, atoms can circulate on the 16 Zeeman sublevels of the ground state. At CPT resonance ($\theta = \pi/2$), a significant part of the atoms are pumped in the dark state. When θ deviates from $\pi/2$, a growing part of these atoms leaks towards other sublevels by absorption and spontaneous emission. Then, the atomic population of the states involved in the dark state decreases. This implies that the absorption coefficients α_d, α_1, α_2 of Eq. (91) are not constant

but θ dependent. This could explain that experimental peaks are sharper than in the theoretical case. For further study, a complete analytical calculation does not seem possible. A full numerical calculation taking into account all the sublevels and all the optical transitions is required. The leak of the $(m = 0)$ clock level populations when θ deviates from $\pi/2$ corresponds to an increase of the hyperfine coherence relaxation γ_2, and consequently of the width of the CPT resonance. This is confirmed by the measurement of the resonance width as a function of θ, shown by white dots curve on Fig. 112. It is clearly seen that the CPT width and the signal are in opposite phase.

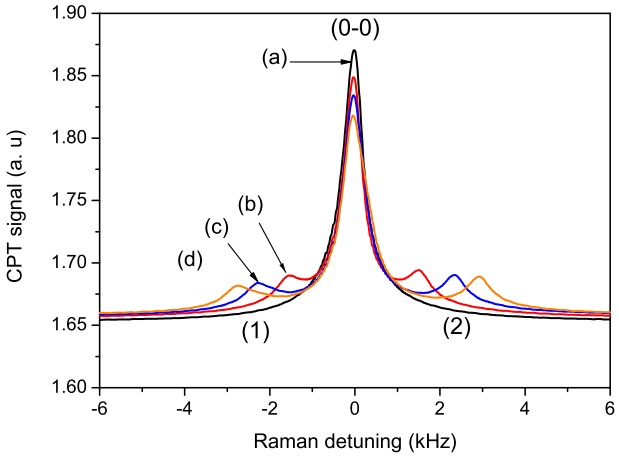

Figure 113: CPT spectra for various static magnetic fields: (a): 45 mG, (b): 1.335 G, (c): 2.07 G, (d): 2.531 G. Neighboring single Λ $\Delta m = 2$ transitions close to the central clock transition are noted (1) and (2). For clarity of the figure, the Zeeman frequency shift of the clock transition is compensated for each value of B.

On Fig. 112, the difference between minimum experimental values and the off-CPT resonance signal (dashed line) can be explained by the presence of neighboring Δm= 2 CPT resonances close to the clock transition. For illustration, Fig. 113 shows typical CPT spectra observed in the cell 3 for various static magnetic fields. Δm= 2 transitions connecting levels $2' \rightarrow 0 \rightarrow 1''$ and $2'' \rightarrow 0 \rightarrow 1'$ are noted on Fig. 113 (1) and (2) respectively. For low static magnetic fields, adjacent peaks from Δm= 2 transitions are not resolved. When the static magnetic field is increased, resonances (1) and (2) move apart the clock transition with opposite directions. We measured a sensitivity of $-$ 1141 Hz/G + 26 Hz/G^2 and + 1125 Hz/G + 24 Hz/G^2 for the frequency splitting $\nu_{(1)} - \nu_0$ and $\nu_{(2)} - \nu_0$ respectively, that is in reasonable agreement with theoretical values $\nu = \pm$1116.5 Hz/G +27 Hz/G^2. As expected by calculations, we observed that the amplitude of the neighboring Δm= 2 transitions resonances does not change with the mirror position. Compared to the clock transition, the relative amplitude of the $\Delta m = 2$ transitions was measured to be 6% in the experimental conditions of Fig. 112. Note that the presence of these Δm= 2 transitions induces a broadening of the CPT clock resonance and can cause a supplemental sensitivity to the static magnetic field.

5.1.3 Impact of the laser intensity

Figure 114(a), 114(b), 114(c), Figure 115(a), 115(b), 115(c) and Figure 116(a), 116(b), 116(c) display the linewidth, contrast and linewitdh-contrast ratio versus the laser intensity for the cells 1, 2 and 3 respectively.

As expected and already observed for single Λ schemes [78], the linewidth increases with higher laser intensity. For all the cells, the CPT linewidth-laser intensity dependence is well fitted by a linear function and is measured to be (0.21 I+ 1.32) kHz, (0.19 I+ 0.59) kHz and (0.058 I+ 0.42) kHz for the cells 1, 2 and 3 respectively (I is the laser intensity in μW/mm^2). The resonance contrast increases with higher laser intensity because of increased optical pumping rate. This behavior is similar to the one reported in [28]. For a laser intensity of 30 μW/mm^2, the contrast is measured to be 4.7 %, 10.2 % and 45 % for the cells 1, 2 and 3 respectively. For the cell 1 (microcell), the maximum contrast is measured to be about 6 %. This value is only 2-3 times higher than the contrast obtained with classical circular polarization. The linewidth-to-contrast ratio is minimized for laser intensities of about 3, 5 and 30 μW/mm^2 for cells 1, 2 and 3 respectively.

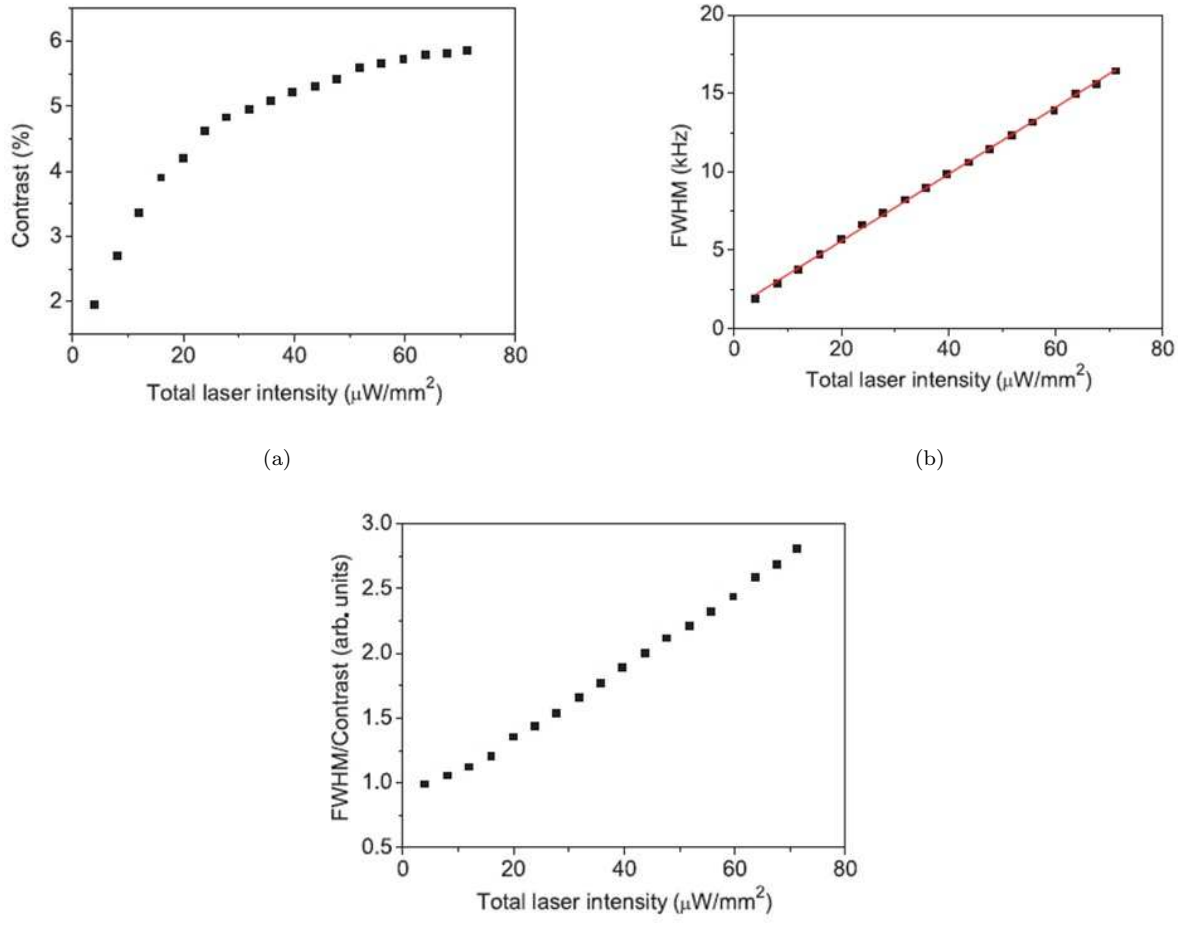

(a) (b)

(c)

Figure 114: CPT resonance contrast (a), FWHM (b) and FWHM/Contrast (c) as a function of the laser intensity for cell 1. The laser beam diameter is 2 mm. The cell temperature is 80 °C.

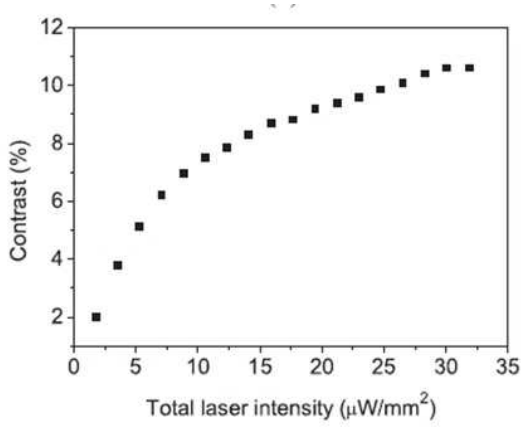

(a)

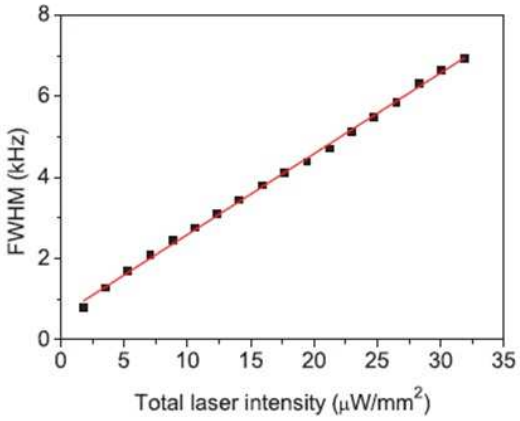

(b)

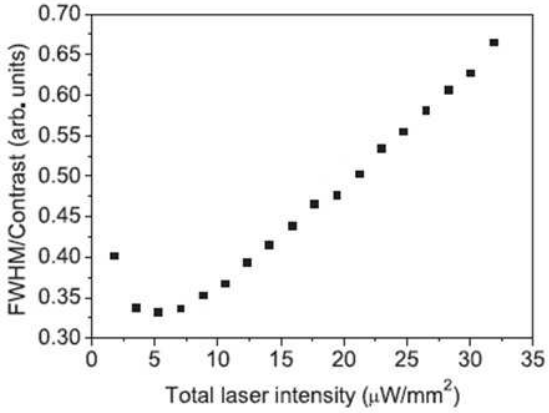

(c)

Figure 115: CPT resonance contrast (a), FWHM (b) and FWHM/Contrast (c) as a function of the laser intensity for cell 2. The laser beam diameter is 6 mm. The cell temperature is 32 °C.

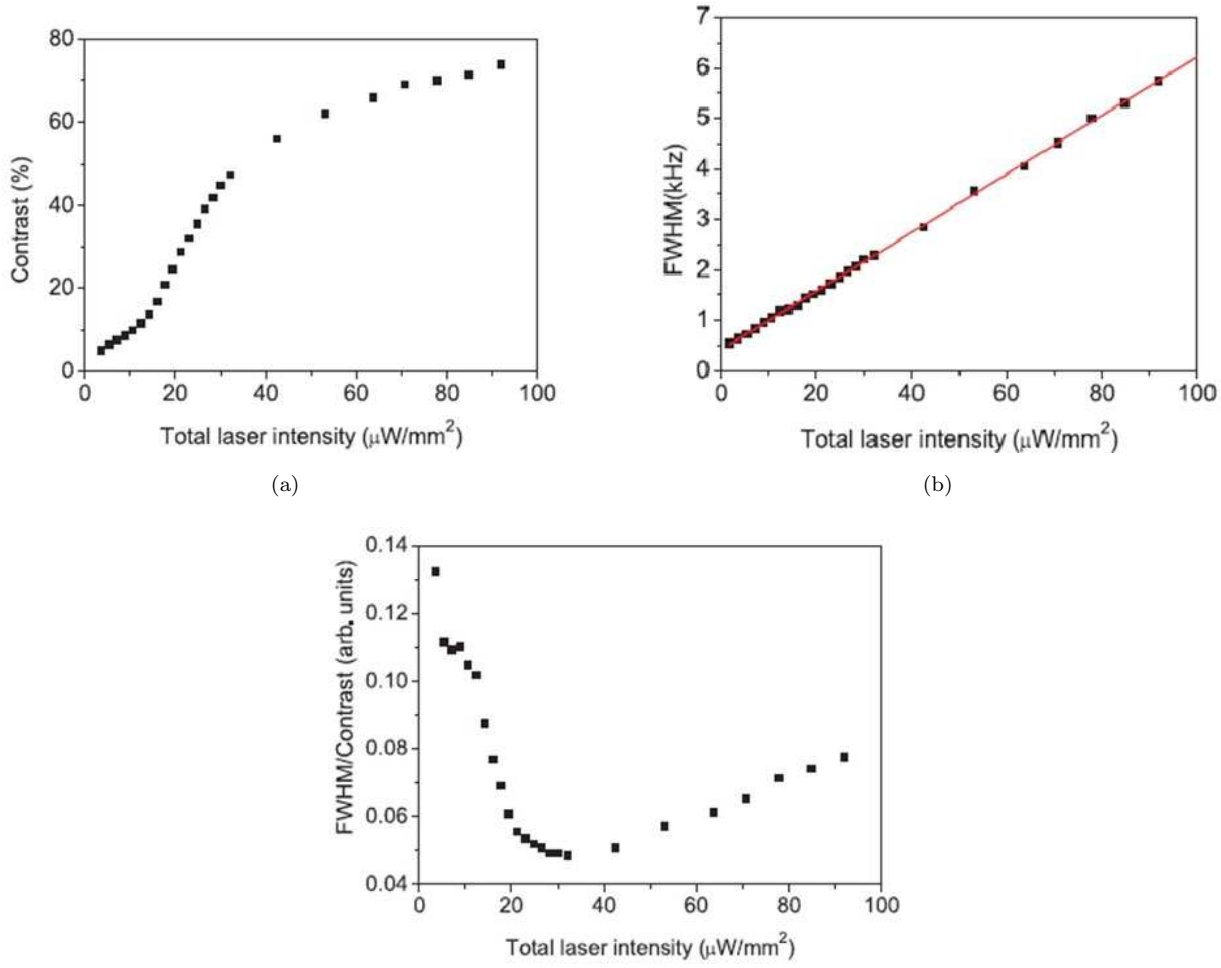

Figure 116: CPT resonance contrast (a), FWHM (b) and FWHM/Contrast (c) as a function of the laser intensity for cell 3. The laser beam diameter is 6 mm. The cell temperature is 38 °C.

From equations 34 and 20, the shot noise limited short-term frequency stability of an atomic clock can be derived by the CPT resonance FWHM/Contrast ratio. Figure 117 shows the shot noise limited short-term frequency stability as a function of the laser intensity for the three cells. For all the cells, the clock frequency stability is improved with increased laser intensity until a plateau after which the clock stability slightly degrades. The optimum laser intensity I_{opt} for best stability performances is measured to be 1-2 μW/mm^2, 10 μW/mm^2 and 33 μW/mm^2 for cell 1, cell 2 and cell 3, respectively. For the largest cell, the cell 3, only considering photon shot noise, the expected clock short-term frequency stability is close to 2×10^{-14} for a laser intensity of 33 μW/mm^2. This value is about one order of magnitude better than frequency stability performances of state-of-the-art vapor cell frequency standards [23].

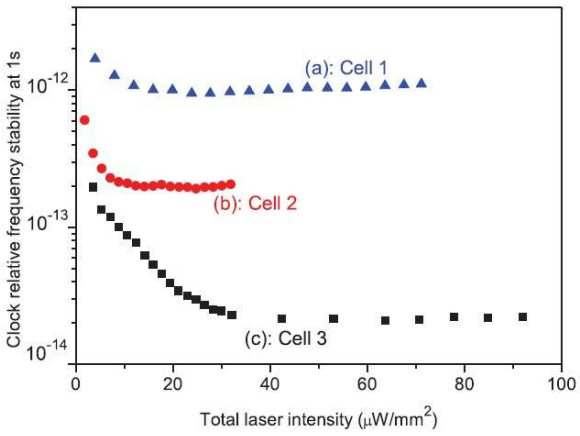

Figure 117: Estimated shot noise limited clock short-term frequency stability at 1 s for the different cells with PPOP interaction. The combination of Equations 34 and 20 is used for the calculation. The laser beam diameter is 2 mm for cell 1, 6 mm for cells 2 and 3.

5.1.4 Impact of the laser beam diameter

Figure 118(a), 118(b) and 118(c) shows in the case of the cell 3 the CPT contrast (a), FWHM (b) and FWHM/Contrast ratio (c) as a function of the laser intensity for two different laser beam diameter: 6 mm and 2 cm. As expected, a larger beam diameter, that allows to make interact more atoms with light, leads to a better contrast and a narrower linewidth. With a smaller beam diameter, the CPT linewidth is limited by the time-of-flight of the atoms across the laser beam.

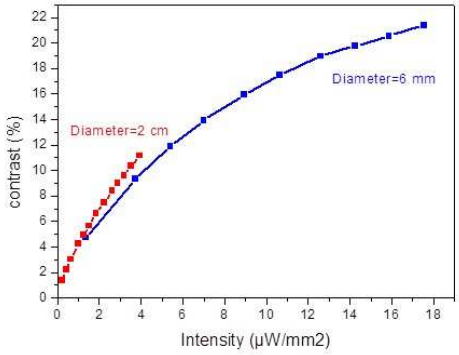

(a)

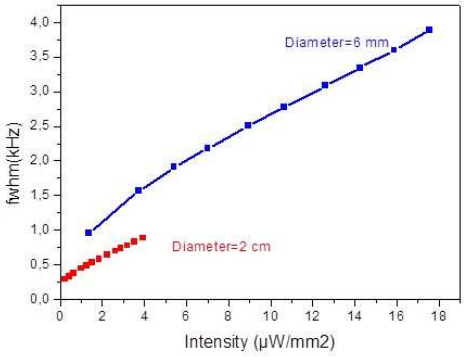

(b)

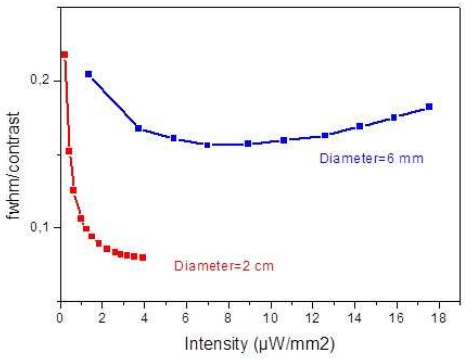

(c)

Figure 118: CPT resonance contrast (a), FWHM (b) and FWHM/Contrast (c) as a function of the laser intensity for different laser beam diameter: 6 mm (blue) and 2 cm (red). The cell temperature is 33°C. The optical sidebands are generated by a MZ EOM modulated at 9.192 GHz.

5.2 Detection of CPT Ramsey fringes

High-contrast CPT resonances were obtained in continuous regime with the PPOP scheme. However, high contrasts are obtained with high intensity laser beam that induces CPT FWHM broadening. To circumvent this issue, inspired by [26], we developed an original simple architecture laser system combining for the first time PPOP and Ramsey spectroscopy for the detection of high contrast and narrow Ramsey fringes. The experimental setup is presented in the section 5.2.1. Preliminary characterization of Ramsey fringes are presented and studied.

5.2.1 Experimental setup

Figure 119 shows the experimental setup for the detection of Ramsey fringes [150]. It is about perfectly similar to the one developed for the CW interaction. The only difference is that here, the signal from the microwave synthesizer that drives the EOM is switched on and off with a fast switch. The MZ EOM operates both as a a sideband generator and a light switch to make the atoms interact with a sequence of optical pulse trains. The operating point of the MZ EOM is fixed at the carrier signal suppression point. The use of the EOM MZ as a light switch prevents the use of an additional acousto-optic modulator (AOM) for light switching. In the first direction, the laser beam is analyzed by a Fabry-Perot interferometer (FPI) or a fast photodiode and a spectrum analyzer. In the second direction, the modulated light of fixed linear polarization is sent through the Michelson interferometer to create the PPOP scheme. The laser light is sent into the cell 3. The resulting signal is analyzed by a computer that drives the microwave switch and the synthesizer output frequency. CPT spectroscopy is realized by scanning the local oscillator frequency around 4.596 GHz.

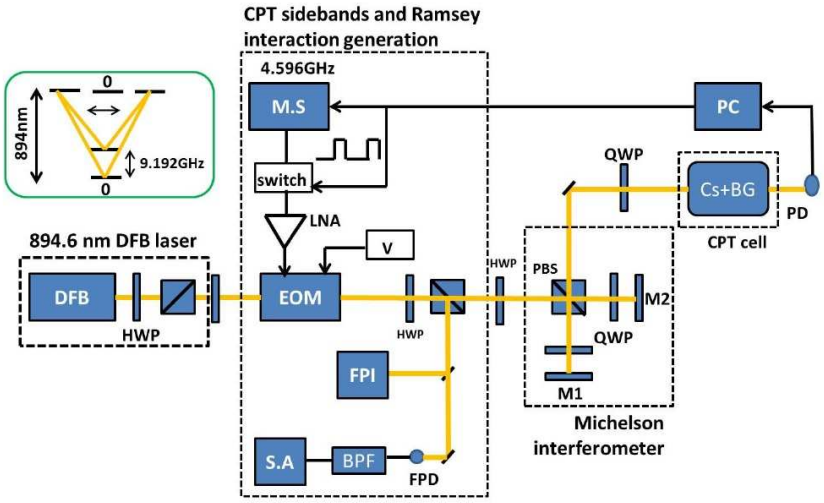

Figure 119: Ramsey fringes detection experimental setup. FPI: Fabry-Perot interferometer. S.A: microwave analyzer. M1 and M2: mirros. The inset shows the energy-level diagram involved in Cs vapor with PPOP. The clock transition is the ground state 0-0 transition.

5.2.2 Pulsed interaction with a MZ EOM

Figure 120 displays the optical harmonics power (height of the peaks at the output of the FPI) and the CPT signal (in continuous regime) at the output of the MZ EOM versus the bias voltage V when the RF power is continuously activated. The CPT signal height is found to be maximized for the so-called *dark point* $V = V_d = 2.6$ V where the optical carrier is optimally rejected and the power in first-order optical sidebands is maximized. At the opposite case, the CPT signal vanishes for $V = V_c = 5$ V where the optical carrier is maximized and first-order optical sidebands power minimized. We checked that when no RF modulation is applied, the output optical power is minimized (carrier suppression point) for $V = V_d$. According to the transfer functions reported above, we implemented the Ramsey sequence described in figure 121 to make the atoms interact with a sequence of optical pulse trains. This pulsed interaction scheme is inspired from [26].

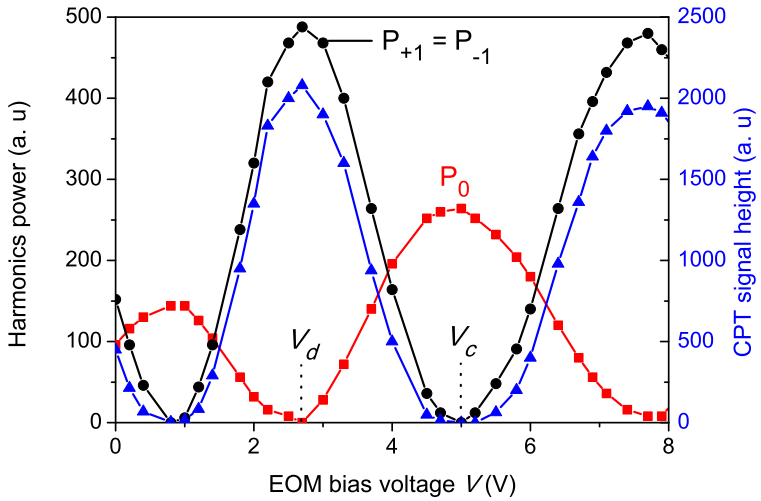

Figure 120: Optical power in the carrier (squares), first-order sidebands (circles) at the output of the MZ EOM and height of the CPT signal (triangles) versus the EOM bias voltage V.

The first pulse allows to pump the atoms in the CPT state during a time τ_p. For this purpose, the RF power is switched on using a microwave switch (Mini-Circuits ZASW-2-50-DR+) and the EOM bias voltage is adjusted to V_d to reject the optical carrier. Then, the RF power is turned off while the EOM bias voltage is kept to V_d to switch off the light. During this period, the atoms evolve freely in the *dark* for a time T. The next pulse is used both for the atomic signal detection and pumping again the atoms in the CPT state. The EOM-based light switching time was measured to be < 10 μs. The signal is typically detected a time $\tau_d = 10$ μs after the pulse trigger and averaged on a measurement time $t_m = 25$ μs. The Ramsey time T is ultimately limited by the microwave coherence relaxation time T_2 in the CPT cell.

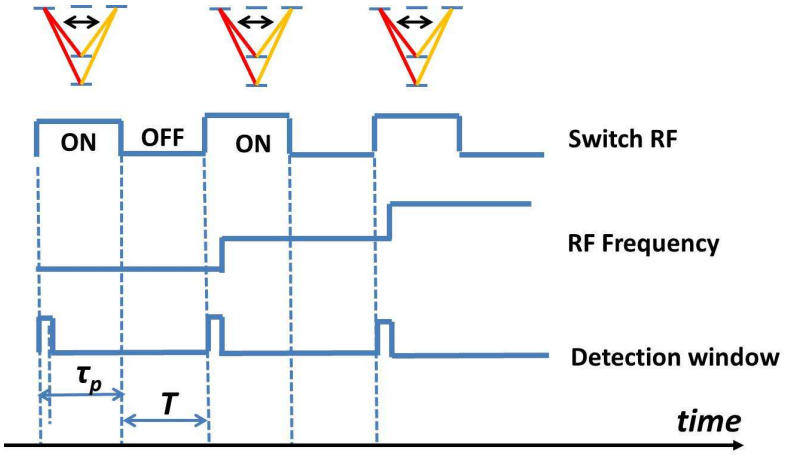

Figure 121: Pulsed sequence to scan and detect the CPT Ramsey fringes. The CPT pumping time τ_p is typically 1-2 ms. The Ramsey time T is of a few ms.

5.2.3 Detection and preliminary characterization of CPT Ramsey fringes

Fig. 122 reports, on a large span of 30 kHz, Ramsey fringes detected with $\tau_p = 2$ ms and $T = 3$ ms for a total laser input power of 3.8 mW. The central fringe exhibits a linewidth $\Delta\nu = 1/(2T) = 166$ Hz with a contrast C of 33 %. In order to highlight the efficiency of the PPOP technique, we compare on Fig. 123 Ramsey fringes obtained with standard circular polarization and push-pull optical pumping for identical experimental conditions. The contrast of the central fringe is found to be 31 % with push-pull interaction scheme whereas it is only 2.8 % with circular polarization.

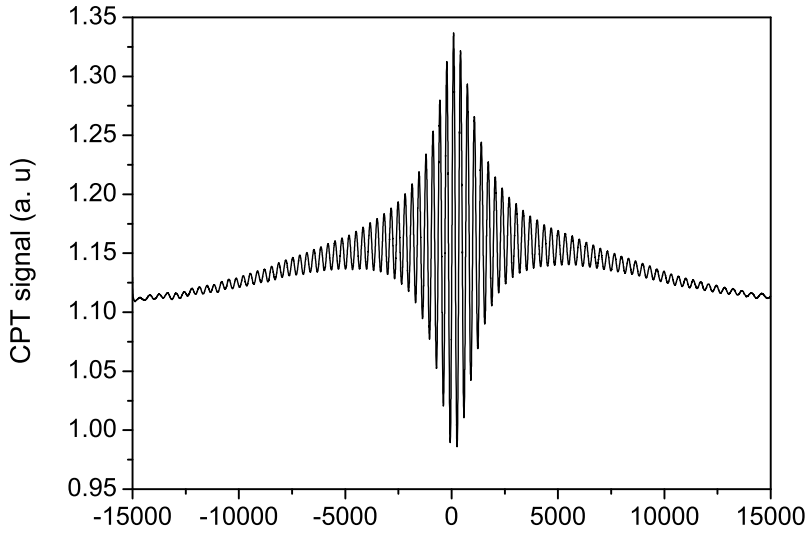

Figure 122: 166-Hz width Ramsey fringes with a contrast of 33 %. Experimental conditions: $T = 3$ ms, $\tau = 2$ ms, $P_L = 3.8$ mW.

Figures 124(a) and 124(b) show the contrast and the contrast/linewidth ratio of the central Ramsey fringe versus the Ramsey time T. We note that contrasts as high as 50 % and 24.2 % are obtained for $T = 1$ ms and $T = 3$ ms respectively. For $T = 10$ ms (fringe linewidth = 50 Hz), the contrast of the Ramsey fringe is still significant (3 %). Experimental data on Fig. 124(a) are well fitted by an exponential decay function with a time constant of about 3 ms. This value can be interpreted as an experimental estimation of the CPT hyperfine coherence lifetime T_2. The ratio contrast/linewidth is maximized for $T = T_2 = 3$ ms. This result indicates that a Ramsey time $T = T_2$ is a good trade-off between a large signal and a narrow fringe for atomic clocks applications, as already observed in [23] and [148].

Figure 125 plots the contrast of the central fringe versus the laser power P_L for $T = 5$ ms and $\tau_p = 2$ ms. The contrast of the resonance is increased with increased laser power until $P_L \simeq 3$ mW before reaching a plateau. For P_L=1 mW, the contrast is found to be about 10 %. For comparison, in [25], a contrast of 4.6 % was obtained at $T = 5$ ms for a laser intensity 2 times lower in a similar cell. Contrary to the CW regime where the CPT linewidth broadens with increased laser power, we measured in the pulsed case that the fringe linewidth does not depend on the laser power and narrows as $1/(2T)$.

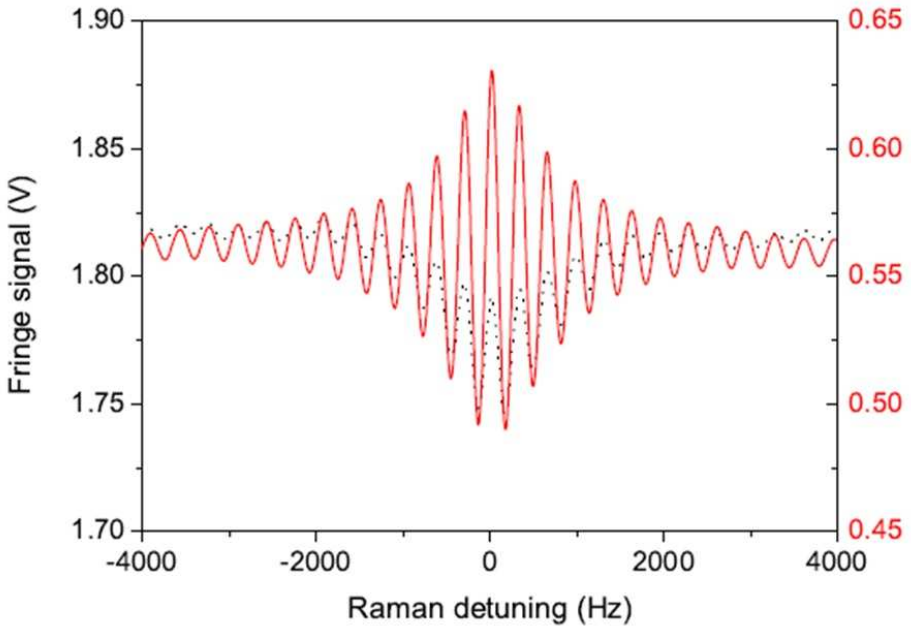

Figure 123: Comparison of Ramsey fringes obtained with standard circular polarization (dotted line) and push-pull optical pumping (solid line). Experimental conditions: $T = 3$ ms, $\tau = 2$ ms.

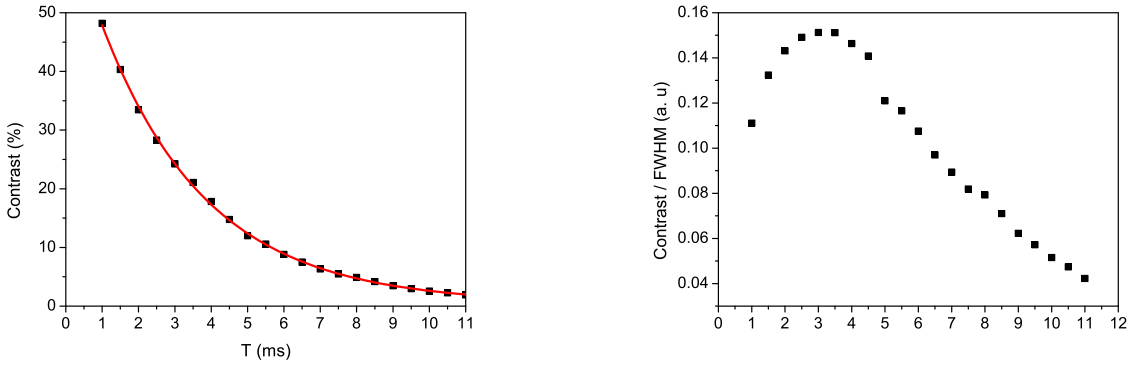

(a) (b)

Figure 124: Contrast (a) and contrast/linewidth ratio (b) of the central Ramsey fringe versus the dark time T. The solid line on (a) is an exponential decay function fit to experimental data. Experimental conditions are: $\tau = 2$ ms, $P_L = 3$ mW.

A possible drawback of the used MZ EOM is to exhibit a relatively low extinction ratio of only 24dB. In order to estimate its effect (see Fig. 126), we degraded intentionally the light extinction by changing the EOM bias voltage V during the free evolution time T. The laser power during the pumping time is 3.6 mW. Maximum and minimum optical power seen by the atoms in the dark time are respectively 4.6 mW and 25.6 μW, limited by the EOM extinction ratio. Note that MZ EOMs with extinction ratio of 60 dB are commercially available. Such devices could allow to reduce greatly the minimum optical power to a level of a few nW during the time T. The CPT fringe signal is measured to decrease rapidly when the laser power in

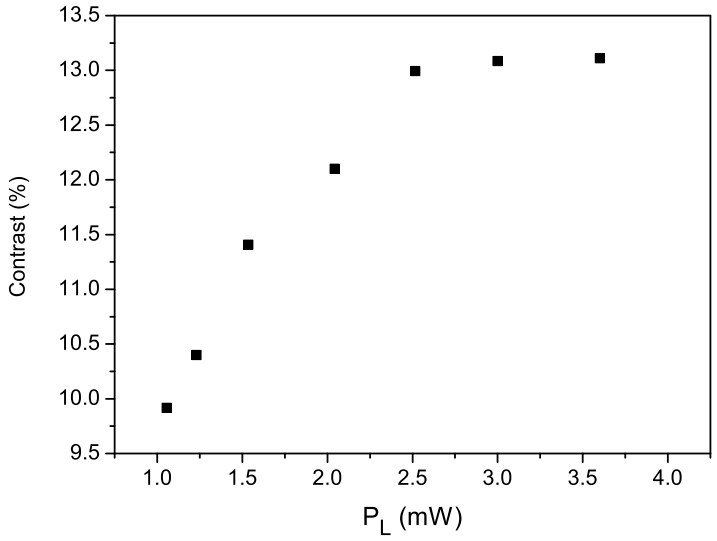

Figure 125: Contrast of the central fringe versus the laser power P_L. Experimental conditions are: $T = 5$ ms, $\tau_p = 2$ ms.

the time T is increased. The signal is found to vanish completely for $P_L > 1$ mW. Interestingly, for a residual light power < 100 μW, a plateau seems to be reached indicating that a better light extinction does not bring a relevant improvement on the clock signal. Nevertheless, we expect that a total light extinction during the time T is of great importance and to be preferred in order to minimize light shift effects for atomic clocks applications.

The shot-noise limited frequency stability of the pulsed atomic clock can be estimated by:

$$\sigma_y(\tau) \simeq \frac{\Delta\nu}{\nu_0}\frac{1}{C}\sqrt{\frac{h\nu}{P_o}}\sqrt{\frac{T_c}{t_m\tau}}, \tag{118}$$

where $\Delta\nu$ is the fringe width, ν_0 is the clock frequency, C is the contrast of the resonance, $h\nu$ is the energy of a single photon, P_0 is the laser power at the output of the cell, $T_c = T + \tau_p$ is the clock cycle time, t_m is the length of the detection window and τ is the averaging time of the measurement. From the clock signal shown in Fig. 122, Eq. (118) yields $\sigma_y(\tau) \simeq 9 \times 10^{-15}$ at 1 s averaging time. This value is about one order of magnitude better than shot-noise estimations in the CW regime [149]. In the real life, this result will be degraded by various noise mechanisms such as the detector noise, the laser intensity and frequency noise or the oscillator phase noise through the Dick effect [144]. In the first step, we estimate that demonstrating an experimental frequency stability better than 10^{-12} at 1 s integration time with our system is a reasonable objective.

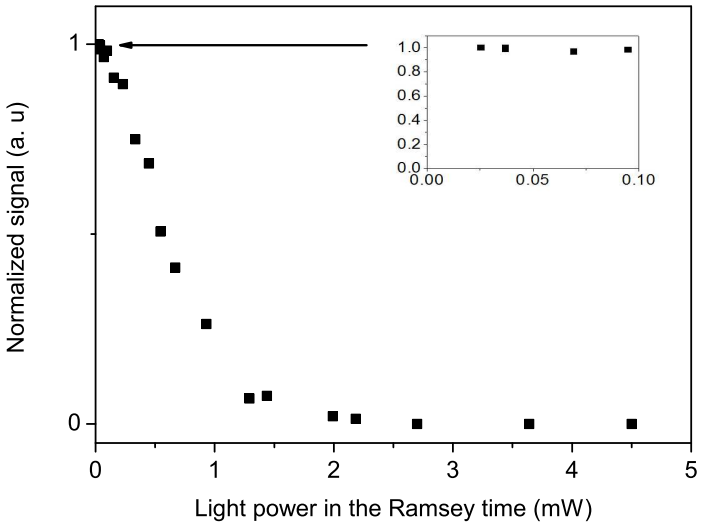

Figure 126: CPT fringe peak-peak signal versus laser power seen by the atoms in the Ramsey time T. The CPT signal for the lowest power point is normalized to 1. The inset shows a zoom on first points of the graph.

6 Annex Works

At the beginning of my thesis, all components of the laser system at 895 nm I presented were not available. Waiting for their reception, I started in collaboration with Eric Kroemer (master's degree) the development of a demonstration experiment at 1550 nm to produce two frequency-splitted orthogonally polarized optical lines with a simple laser system. These studies were realized thanks to the precious help of J. M. Merolla, CNRS researcher in Optics Department from FEMTO-ST. At this wavelength, numerous fiber-optics components are available, including Dual Phase Shift Key (DPSK) modulators we used for optical lines separation at the output of a MZ EOM. This section aims to report very preliminary results we obtained in this domain. An interesting point to highlight is that 780 nm wavelength (Rb atom transition line) can be generated from frequency-doubling of a 1560 nm source. Results presented here could be potentially used for Rb atom spectroscopy using telecom-wavelength based components. Some interesting results were reported recently to probe Rb atoms with 1.5 μm laser sources [151].

Moreover, during my thesis, I participated to different measurements focused on the use of microfabricated cells. When I started my thesis (october 2010), the European MAC-TFC project was in progress [19]. This section reports experimental setups we implemented to operate a Cs-Ne microcell-based table-top Cs CPT clock prototype. CPT spectroscopy on the Cs D_1 line was realized in Cs-Ne microcells to optimize the short-term frequency stability performances of the clock whereas all studies had been done with D_2 line VCSEL in the past of the project. Advanded light shift cancellation (LSC) techniques were implemented to improve the frequency stability performance of the clock for mid and long term integration times. Our reported results are among state-of-the-art frequency stability performances for a microcell-based CPT atomic clock. These results, published in IEEE UFFC [152], are presented in this section.

Moreover, in collaboration with FEMTO-ST MN2S department in charge of the microcell fabrication, I participated to study the impact of the presence of getters on hermetically sealed micromachined Cs-Ne cells. Our basic CPT tests allowed to confirm that the presence of getters allows to improve the microcell internal atmosphere purity and to reduce greatly undesired impurities. These results, detailed in this section, were published in Journal of Micromechanics and Microengineering [153].

6.1 Dual-frequency and dual-polarization modulated laser system at 1.5 μm

Figure 127 shows the basic scheme of a preliminary laser system we developed at 1.5 μm. A fiber pigtailed DFB diode laser is used. A MZ EOM is modulated by a microwave signal to generate two frequency-separated optical sidebands. The output carrier signal of the MZ EOM is suppressed by adjusting the bias voltage on the dc electrode of the MZ EOM. A DPSK demodulator (detailed later) is used to separate the two optical sidebands. At the output of the DPSK, one of the optical sidebands is rotated in polarization by 90° with a half wave plate. Eventually, both optical sidebands are recombined with a combiner into two orthogonally polarized sidebands. Figure 128 shows a photograph of the laser system.

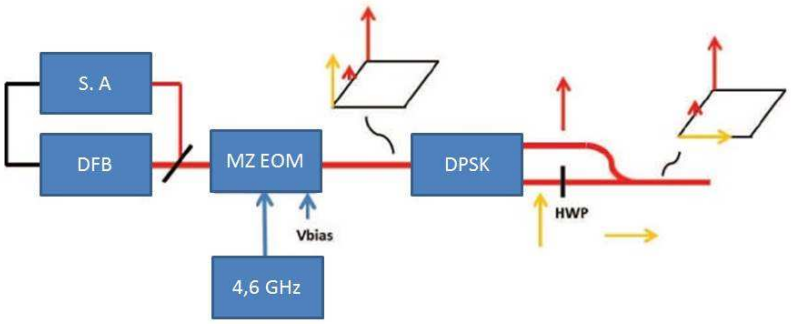

Figure 127: Basic scheme of the preliminary architecture at 1.5 μm.

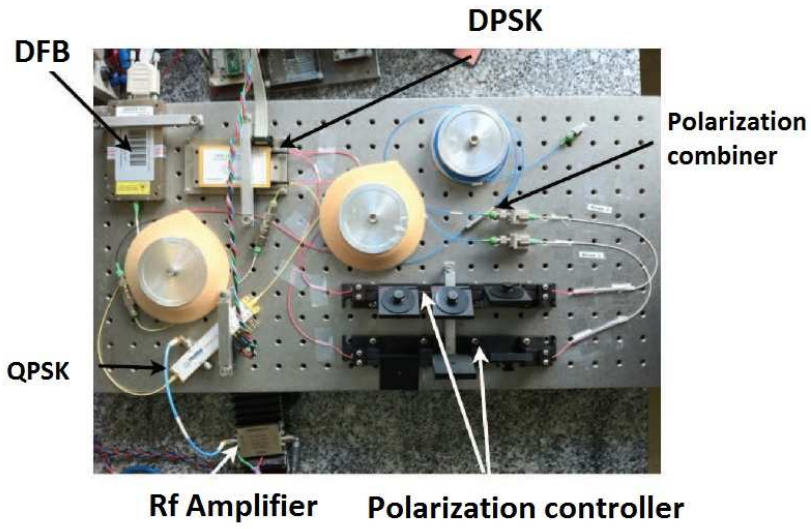

Figure 128: Photograph of the laser system at 1.5 μm.

6.1.1 1550 nm DFB laser source

A low noise and stable laser source at 1550 nm is needed in our system. Three different commercial laser sources were available in our laboratory when I started this project: a Agilent tunable laser source, a RIO Orion DFB laser diode and a Teraxion DFB laser diode. In order to select the best performance laser source, we built a measurement system, inspired by [154], to measure the frequency noise of each laser source. Figure 129 shows the frequency noise measurement system. In this measurement setup, frequency fluctuations of the laser are converted at the output of the DPSK demodulator as intensity fluctuations. This intensity noise is converted into a voltage signal by a photodiode and transimpedance amplifier. This signal is analyzed by a FFT analyzer. The system is duplicated to realize cross-correlation measurements and to reject no correlated noise sources in both arms. Preliminary RIN measurements are realized to check that we are not limited by laser amplitude noise. The DPSK demodulator transfer function is:

$$K(\nu) = \frac{1}{2} + \frac{\cos(2\pi\nu\tau)}{2} \tag{119}$$

with ν the optical frequency and $\tau = 1/FSR$ when FSR is the DPSK free spectral range. In our case, $\tau =$ 40 ps. We write:

$$\frac{\delta K(\nu)}{\delta\nu} = -\pi\tau\sin(2\pi\nu\tau) \tag{120}$$

For a given wavelength, τ is finely adjusted by adjusting the laser temperature or current such as we got $(\sin(2\pi\nu\tau) = 1)$. Then, we obtain:

$$K(\nu) = K_0 + \delta\nu(\frac{\delta K(\nu)}{\delta\nu})_{\nu_0} \tag{121}$$

The conversion factor to obtain the laser frequency noise is:

$$C_\nu = \frac{\delta\nu}{\delta V} = \frac{1}{\frac{\delta K(\nu)}{\delta\nu} P_{opt}\rho R_{PD} G} = \frac{1}{\pi P_{opt}\tau\rho R_{PD} G} \tag{122}$$

with P_{opt} the optical power at the input of the DPSK, ρ the photodiode quantum efficiency, R_{PD} the load resistance of the photodiode and G the amplifier gain. The average voltage V_{DC} at the output of the amplifier is:

$$V_{DC} = \frac{P_{opt}\rho R_{PD} G}{2} \tag{123}$$

The factor of conversion C_ν can be simplified by:

$$C_\nu = \frac{1}{2\pi\tau V_{DC}} \tag{124}$$

Before the measurement, we adjust the laser frequency (or the DPSK dc bias voltage) in order to put both outputs of the DPSK in quadrature. Voltages of both outputs of the DPSK are then equal. In this case, the DPSK is operating in the middle of the linear part of the transfer function.

Figures 130 shows the frequency noise of each laser source for 0 dBm laser power. The RIO DFB laser is found to be the best source with a frequency noise of -50 dBMHz^2/Hz at f= 10 Hz. We selected this diode laser for tests.

We measured the relative frequency stability of the beatnote signal between the RIO DFB and the Agilent laser source (Figure 131). The frequency stability is measured to be 9.5×10^{-10} at 1 second integration time, and increases to 3.5×10^{-8} at 1000 seconds. Figure 132 reports the relative intensity fluctuations of the RIO DFB diode along time. It is measured to be 2×10^{-4} at 1 second and lower than 1×10^{-3} to 2000 seconds.

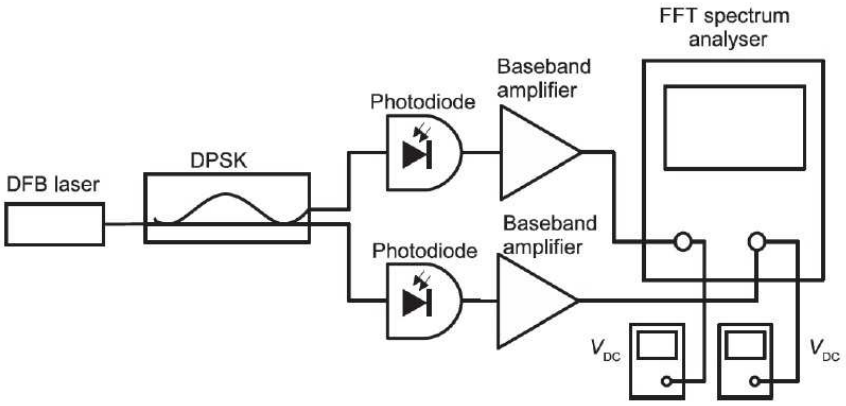

Figure 129: Frequency noise measurement system. The DPSK is used as a amplitude-frequency converter.

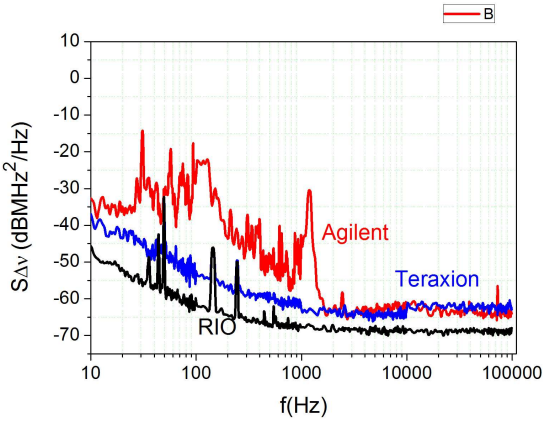

Figure 130: Frequency noise of the different laser sources: Agilent (Red), RIO (Black) and Teraxion (Blue).

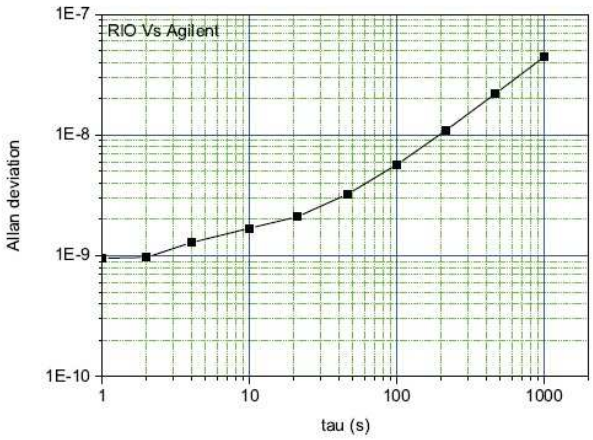

Figure 131: Relative frequency stability of the beatnote signal between the RIO DFB diode and the Agilent laser source.

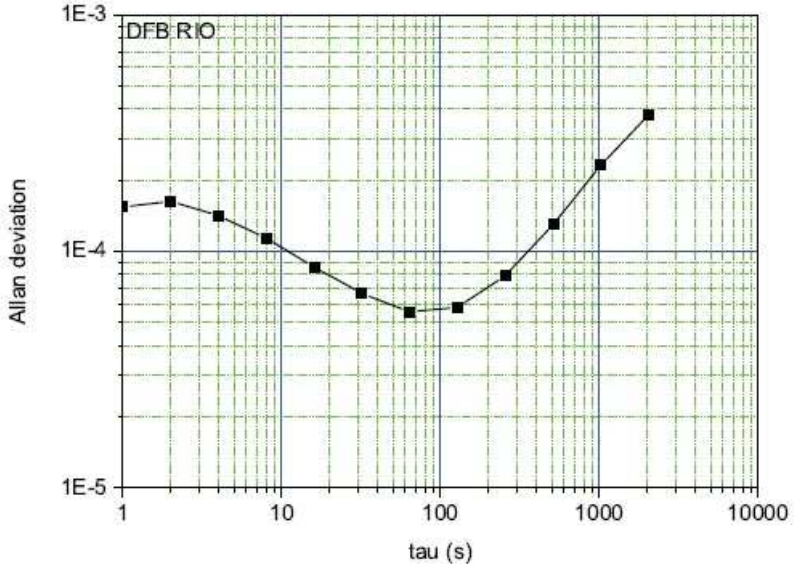

Figure 132: Relative intensity fluctuations of the RIO DFB diode.

6.1.2 Dual Phase Shift Key demodulator (DPSK)

The DPSK is used to separate both optical sidebands. The DPSK can be assimilated to an imbalanced Mach-Zehnder interferometer shown in figure 133.

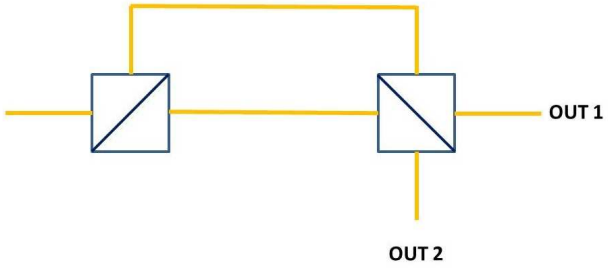

Figure 133: Simplified scheme of an imbalanced Mach-Zehnder interferometer.

Assuming a field E_{in} at the input of the DPSK, the output signals of the DPSK are given by:

$$\begin{aligned} E_{out1} &= \frac{1}{2}(E_{in}(t) - E_{in}(t+\tau)) \\ E_{out2} &= \frac{i}{2}(E_{in}(t) + E_{in}(t+\tau)) \end{aligned} \tag{125}$$

The first output signal can be rewritten to:

$$E_{out1} = \frac{E_{in}(t)}{2} \bigotimes (\delta(t) - \delta(t+\tau)) \tag{126}$$

If we apply the Fourier transformation on the first output signal, we can get:

$$\begin{aligned} E_{out1}(\omega) &= \frac{E_{in}(\omega)}{2}(1 - e^{j\omega\tau}) \\ \|E_{out1}(\omega)\|^2 &= \frac{E_{in}(\omega)}{4}(1 - \cos(\omega\tau)) \end{aligned} \tag{127}$$

where $\tau = L/\frac{c}{n} = \frac{nL}{c} = \frac{1}{FSR}$ is the differential delay time, with L is the optical path, n is the refraction index. FSR is the free spectral range. From the expression of τ, we have:

$$\begin{aligned} \|E_{out1}(\omega)\|^2 &= \frac{E_{in}(\omega)}{4}(1 - \cos(\frac{\omega}{FSR})) \\ \|E_{out2}(\omega)\|^2 &= \frac{E_{in}(\omega)}{4}(1 + \cos(\frac{\omega}{FSR})) \end{aligned} \tag{128}$$

Equation 128 indicates that the transfer functions of the DPSK output signals are sinusoidal. If we consider that the carrier signal is suppressed and the sidebands at $\omega_0 - \Omega$ and $\omega_0 + \Omega$ reach maximum, we have:

$$\begin{aligned} \omega_0 - \Omega &= 2k\pi FSR \\ \omega_0 + \Omega &= (2k+1)\pi FSR \end{aligned} \tag{129}$$

with $2\Omega = \pi FSR$. The two optical sidebands at the outputs of the DPSK are given by:

$$\begin{aligned} \|E_{out1}(\omega_0 - \Omega)\|^2 &= \frac{\|E_{in}(\omega_0 - \Omega)\|^2}{4}(1 - \cos(2k\pi)) = 0 \\ \|E_{out1}(\omega_0 + \Omega)\|^2 &= \frac{\|E_{in}(\omega_0 + \Omega)\|^2}{4}(1 - \cos((2k+1)\pi)) = \frac{\|E_{in}(\omega_0 + \Omega)\|^2}{2} \end{aligned} \tag{130}$$

and

$$\|E_{out2}(\omega_0-\Omega)\|^2=\frac{\|E_{in}(\omega_0-\Omega)\|^2}{4}(1+\cos(2k\pi))=\frac{\|E_{in}(\omega_0-\Omega)\|^2}{2}$$
$$\|E_{out2}(\omega_0+\Omega)\|^2=\frac{\|E_{in}(\omega_0+\Omega)\|^2}{4}(1+\cos((2k+1)\pi))=0 \tag{131}$$

Equation 130 and 131 show that there is only one frequency signal in each output of the DPSK. Figure 134 shows the output spectra of the DPSK.

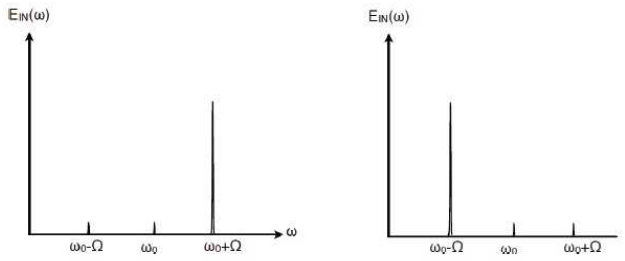

Figure 134: Spectra of output signals of the DPSK.

The differential delay between both arms of the DPSK is controlled by a dc voltage V_c. Figure 135 shows the voltages of the DPSK output signals versus the square voltage V_c^2. Figure 136 shows the carrier signal and the optical sidebands power at the output 1 of the DPSK as a function of the square voltage V_c^2.

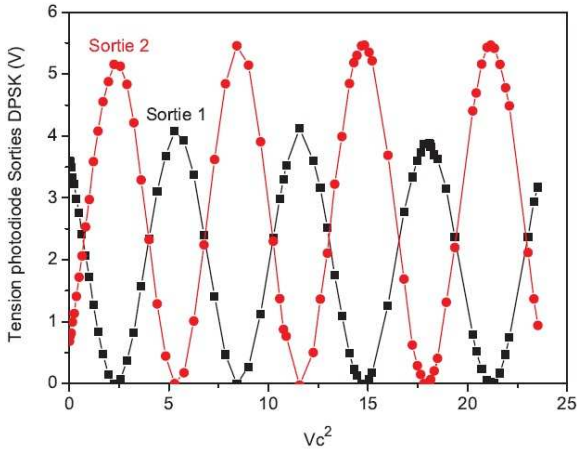

Figure 135: Optical powers of the two output signals of a DPSK as a function of the square voltage V_c^2.

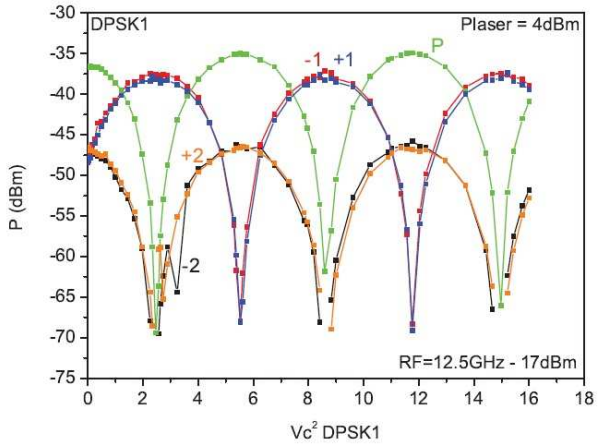

Figure 136: Optical power of the carrier signal and the sidebands at the output 1 of the DPSK as a function of the square voltage.

6.1.3 Laser system at 1550 nm

Our system uses a DPSK (FSR=25 GHz) at 1550 nm and a MZ EOM modulated at 6.25 GHz (quarter of the FSR). At one of the DPSK outputs, a polarization controller is used to rotate the polarization of the sideband. A fibered polarization combiner is used to recombine two orthogonally polarized optical sidebands. A Fabry-Perot fibered analyzer at the output of the system is used to observe the spectrum of the output signal. Figure 137 shows the spectrum of the output signal. The frequency difference between the sidebands is 12.5 GHz. The rejection rate of the carrier signal is 28 dB.

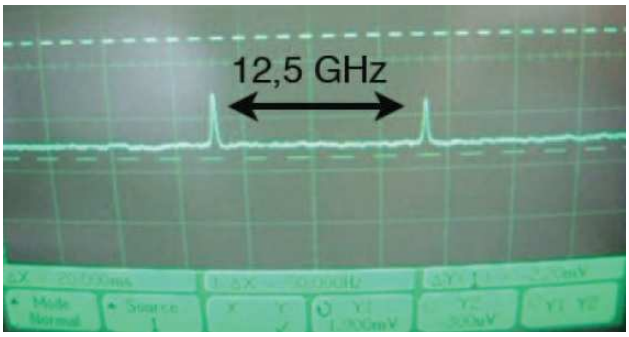

Figure 137: Spectrum of the recombined output signal. The frequency difference between the sidebands is 12.5 GHz.

Figure 138 shows the polarizations of the two optical sidebands as a function of the angle of the half wave plate at the output of the system. This figure confirms that the output signals are orthogonally polarized to each other. There is a light amplitude difference between two optical sidebands, which implies that the whole system would need to be stabilized for real operation.

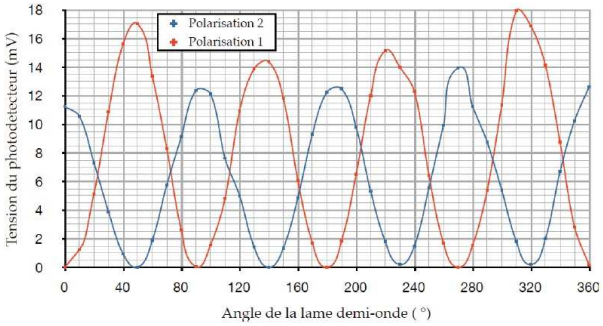

Figure 138: Polarizations of the optical sidebands as a function of the angle of the half wave plate.

6.1.4 Conclusion

A laser system at 1550 nm was built to generate two orthogonally polarized optical sidebands frequency-separated by 12.5 GHz. The system mainly consists of a laser source, a MZ EOM and a DPSK demodulator. Characterization of different components was reported. This architecture is simple. All the components are

commercially available and can be easily controlled. Further tests should be realized to validate fully this system for our application. In particular, we didn't have the opportunity to measure the phase noise of the optically carried microwave signal at the output of the DPSK. This test would be important to do to confirm the potential of this system.

6.2 A high-performance frequency stability compact clock based on a Cs-Ne microcell

In this section, we report a compact table-top micro-cell based Cs CPT clock with advanced frequency stability performance in this section. The heart of the clock is a single buffer gas Cs-Ne microfabricated cell realized in FEMTO-ST. As most microfabricated cells worldwide, the Cs microcell technology developed in FEMTO-ST is basically based on etching of a silicon wafer and subsequent anodic bonding of a thin glass wafer to each side [155]. However, our filling method differs from traditional ones [156], [157] in that the Cs vapor is generated only after complete sealing of the cell by local heating of a side-cavity Cs metallic dispenser with a high power infrared laser source [147]. This method is intended to reduce interactions with high-reactive Cs chemistry and to achieve a strong bonding quality. When I started my PhD thesis, best frequency stability results of a CPT clock with a Cs microcell in FEMTO-ST were measured to be 1.5×10^{-10} at 1 s and 10^{-10} at 1000 s [83]. During my thesis, in collaboration with Rodolphe Boudot, I participated to the implementation of advanced techniques to improve greatly these frequency stability performances. We developed a system using a DFB laser resonant on the Cs D_1 line and did CPT spectroscopy on a Cs-Ne microcell to improve greatly the short term frequency stability performances. Moreover, we implemented advanced noise reduction techniques, mainly a light shift cancelation technique inspired by [158] to improve the stability performances on the mid and long term. These results proved for the first time that the Cs-Ne cell technology solution developed in FEMTO-ST is compatible with the development of high-performance miniature atomic clocks. The following describes these studies.

6.2.1 Experimental setup

Figure 139 shows a scheme of the Cs CPT clock experimental setup. The laser source is a DFB diode at 894.6 nm on the Cs D_1 line. A Faraday optical isolator is placed at the output of the DFB laser to avoid optical feedback. Optical sidebands required to perform CPT spectroscopy are generated by driving an external pigtailed phase EOM at 9.192 GHz using a microwave frequency synthesizer. The fiber modulator ensemble is inserted into a box with insulating foam and is actively temperature-stabilized to the mK level to reduce output laser intensity fluctuations. No phase noise degradation was observed between the microwave frequency synthesizer output and the 9.192 GHz optically carried signal. The 2 mm diameter collimated laser beam is circularly polarized using a quatre wave plate. The laser power is 17 μW before entering the atomic resonator. The atomic resonator consists of a 2 mm diameter and 1.4 mm long cylindrical microfabricated Cs vapor cell filled with Ne. The cell temperature T_{cell} is stabilized close to 80°C, which corresponds to a Cs density of 4.05×10^{12} atom/cm^3. Temperature fluctuations of the microcell are below the mK level. A static magnetic field of a few microteslas parallel to the laser beam propagation direction is applied to split the hyperfine ground state Zeeman transitions. The ensemble is surrounded by a two layer μ metal magnetic shield as we presented in the section 4.6. The CPT resonance is detected by a low noise photodiode. The laser is frequency-stabilized near the center of the homogeneously broadened absorption line by modulating the DFB laser current at 60 kHz and demodulating it with the lock-in amplifier LA1. The atomic clock closed loop operation is achieved by a conventional synchronous modulation-demodulation technique (about 1 kHz frequency) applied to the local oscillator frequency through the lock in amplifier LA2.

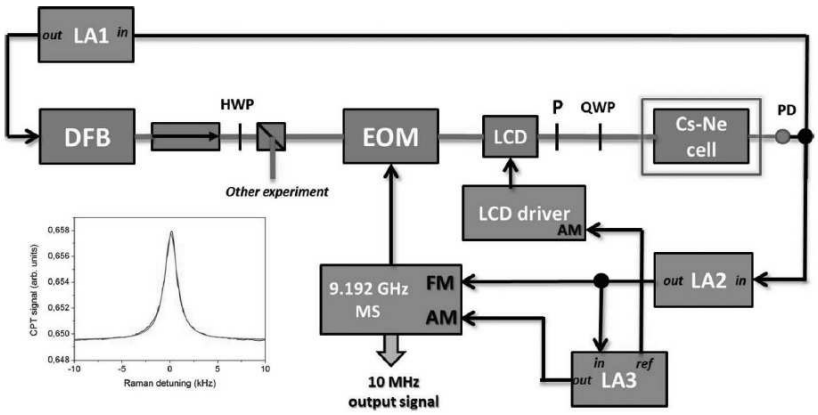

Figure 139: Schematic of the Cs-Ne microcell-based CPT clock. MS: 10 MHz quartz oscillator based microwave synthesizer; EOM: electro-optic modulator; LCD: voltage controlled liquid plate attenuator; P: polrizer; HWP: half wave plate; QWP: quarter wave plate; LA1: lock in amplifier based servo for DFB laser frequency stabilization through modulation at 60 kHz of the laser bias current; LA2: lock in amplifier based servo for locking the local oscillator frequency to the CPT resonance transition; LA3: lock in amplifier based servo for light shift correction.

6.2.2 Experimental investigations and results

A typical CPT resonance observed in the Cs-Ne cell for $T_{cell} = 80°C$ is reported in the inset of Figure 139. The resonance shape is well fitted by a Lorentzian function. The linewidth of the CPT resonance is 1.6 kHz in correct agreement with theoretical values. From [83], the hyperfine coherence relaxation rate γ_2 is calculated to be 4391 rad/s and the optical resonance homogeneous broadening $\Gamma^*/2\pi$ is 862 MHz. At 80°C, contributions to the CPT linewidth from wall-collisions and spin-exchange collisions are about equal and clearly dominant over buffer gas collisions. The contrast is measured to be about 1.25 %. Figure 140 shows both the CPT resonance contrast and the clock frequency shift versus the cell temperature. The CPT contrast is maximized in the 74°C to 81°C temperature range. For higher temperatures, the vapor medium becomes optically thick and causes a strong reduction of the CPT signal. In [83], with VCSEL emitting at 852 nm, the CPT signal maximum with temperature was measured to be in the 55°C to 60°C range for quite similar Cs-Ne microcells. This can be qualitatively explained by intrinsic differences between D_1 and D_2 excitation lines hyperfine structures. The Cs D_2 line excited state is composed of 4 hyperfine levels with a frequency separation (150 to 250 MHz) much lower than buffer-gas-induced optical broadening in microfabricated cells. Both hyperfine levels of the Cs D_1 line are well resolved and separated by about 1.16 GHz. Also, some excited states on the Cs D_2 line couple to only one of the ground states and act as loss-channels for the CPT interaction. Consequently, optical absorption is stronger for the Cs D_2 line and the alkali vapor becomes optically thick for lower temperatures than in the D_1 line case. Moreover, the Cs clock frequency temperature dependance is canceled close to 80°C in the presence of Ne. Using coefficient in [88], a fit of experimental points gives a Ne pressure of 79 Torr. This cell allows the overlap of a zero sensitivity of the clock frequency to temperature variations and a maximum of CPT contrast close to 80°C. This will lead to mutual improvements of the clock long term and short term frequency stability.

Combined with a greatly reduced sensitivity of the clock frequency to temperature variations, the light shift is continuously minimized using a method inspired by [158]. For this purpose, the laser power is slowly

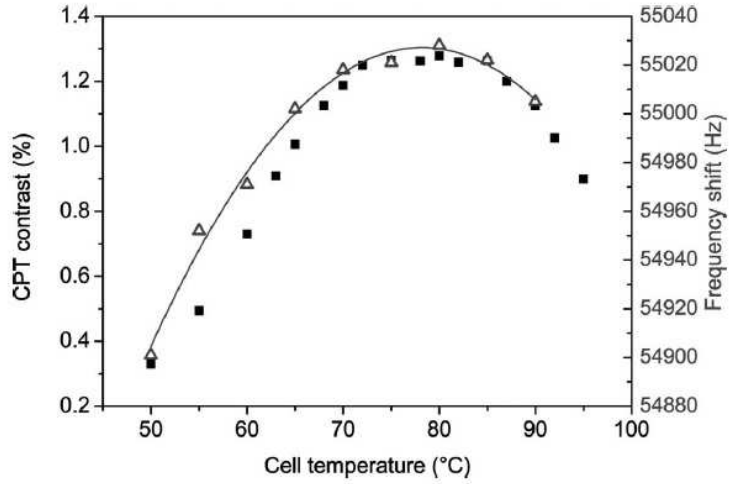

Figure 140: CPT resonance contrast (filled squares) and clock frequency shift (triangles) versus the cell temperature. The solid line is a second-order polynomial function fit to the frequency data. For a given temperature, each frequency shift is found from an extrapolation to zero intensity of the light shift curve. The CPT contrast is found to be optimized close to the clock frequency inversion temperature.

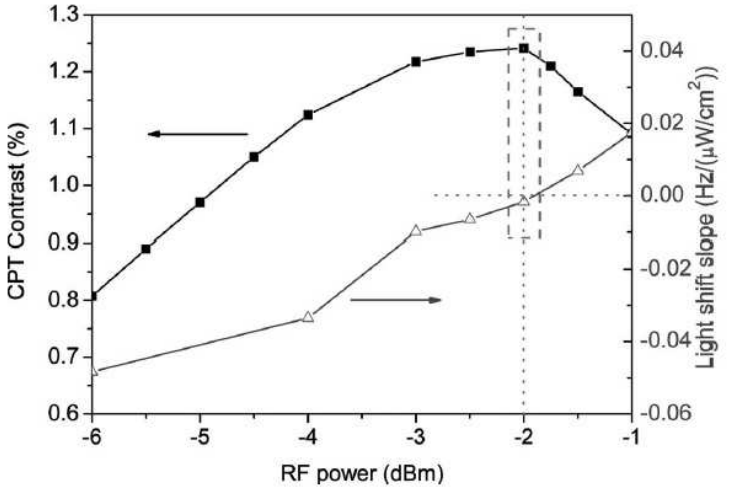

Figure 141: CPT resonance contrast (filled square) and light shift slope (triangles) versus the RF modulation power. The indicated RF power is before amplification of 24 dB. Close to P_{RF} = -2 dBm, the CPT resonance contrast is maximized and the light shift can be canceled. The cell temperature is 80°C. For each RF power, the frequency shift is measured for 5 to 6 different laser intensity values and is found to be well approximated by a linear function. Each triangle point corresponds to the slope of this function.

modulated at 15 Hz (12% depth) using a voltage-controlled liquid crystal display (LCD) attenuator. This laser power modulation is converted across the cell through the light shift effect into a slight clock frequency modulation that can be easily detected at the error signal output of the lockin amplifier LA2 used to stabilize the LO frequency. This modulation signal is found to vanish close to a so-called RF power zero-light-point driving the EOM. An additional servo loop based on the lock-in amplifier LA3 is eventually added to lock the RF power point where no light shift is present. For illustration, Fig. 141 plots both the light shift slope

and the CPT resonance contrast versus the RF modulation power. The light shift slope is measured to be negative for $P_{RF} < -2$ dBm, positive for $P_{RF} > -2$ dBm and can be nulled by finely adjusting the RF power to $P_{RF} \sim -2$ dBm. Moreover, as shown in Fig. 141, this RF power coincides with the one maximizing the CPT resonance contrast. It corresponds well to the RF power maximizing the optical power contained in the two resonant light fields.

Figure 142 reports the frequency stability of the CPT clock based on a Cs-Ne microcell. It is measured by a comparison with a reference hydrogen maser. In this figure, last results obtained with a D_2 line VCSEL and a Cs-Ne microcell are also reported for comparison. In our new experiment, the short term frequency stability was measured to be 3.8×10^{-11} at 1 second integration time. It is in agreement with a measured atomic Q-factor of 5.7×10^6 and a clock resonance signal-to-noise ratio of 4500 in a 1 Hz bandwidth. We measured that our laser power modulation for the light shift correction degrades the optimal short term stability by a factor of about 1.5. The Allan deviation curve decreases well with a $\tau^{-\frac{1}{2}}$ slope until 1000 s. After 1000 s, the Allan deviation increases again with a $\tau^{\frac{1}{2}}$ slope corresponding to a random walk frequency noise. The frequency stability is found to be 4×10^{-12} at 40000 s. These results obtained with optimal laboratory-scale electronics are comparable to those presented in [159] and [160] and are among best results reported for a microcell-based CPT clock [152].

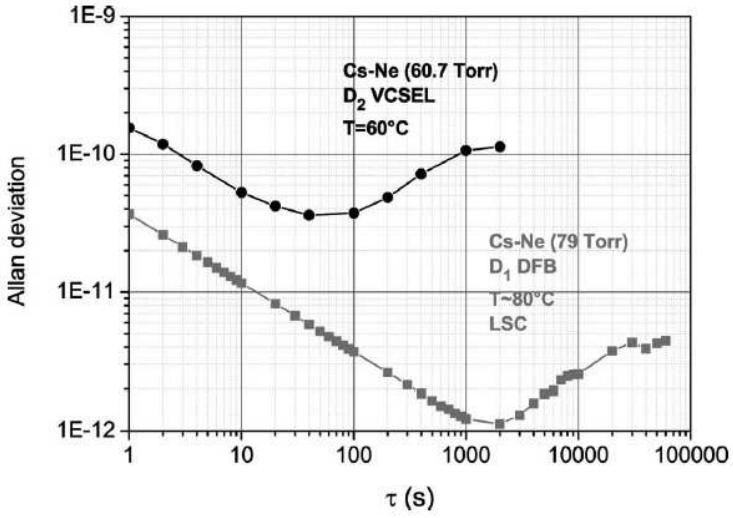

Figure 142: Allan deviation of the Cs CPT clock based on a Cs-Ne microcell. (circles): VCSEL D_2 line, no light shift correction, $T_{cell} = 60°$C, Ne pressure = 60.7 Torr [83]; (squares): DFB D_1 line, light shift correction, $T_{cell} \simeq 80°$C, Ne pressure = 79 Torr.

6.3 Effects of getters on hermetically sealed micromachined Cs-Ne cells for atomic clocks

6.3.1 Introduction

Hermetical sealing of MEMS structures is an important fabrication step to generate miniature devices such as atomic clocks. These miniature devices require a precisely controlled atmosphere for short and long term stability. In this fabrication process, the anodic bonding is the most reliable sealing technique to achieve such MEMS devices. Although different alkali atoms, such as Rb and Cs, as well as different techniques to fill the cavities with such atoms have been employed, most of them rely on anodic bonding in order to seal the cavities [156] [157] [161] [162]. However, it has been shown that the devices sealed by anodic bonding contain considerable amount of residual gases such as H_2, O_2, N_2 and CO_2 due to the bonding reaction and outgassing of glass substrate during high temperature processing [166]. Due to this reason, the inner cell atmosphere might be modified, especially for long-term use of the devices. In order to solve this problem, using getter materials to ensure vacuum in small cavities [164] is an effective solution. For instance, Ti coatings used in the vacuum cavity of a gyroscope has been reported to minimize such impurity gases [165]. In this section, the wafer-level integration technique of PageWafer (SAES Getters solution for getter film integration into wafer to wafer bonded devices) has been tested in hermetically sealed miniature Cs-Ne microcells similar to the one used in section 6.2. In frequency stability tests shown on Fig. 142, the clock frequency shift after 1000 s integration time could be due to the variation of the cell atmosphere that relates to reactions between very reactive alkali atoms and impurities. The integration of PageWafer to eliminate impurity gases seemed to be interesting in order to further improve the reliability of Cs vapor cells and to improve the purity of their internal atmosphere. Getter effects on the cell atmosphere were analyzed by quadruple mass spectroscopy and coherent population trapping (CPT) spectroscopy as reported below. I mainly participated to CPT measurements.

6.3.2 Micro Cs vapor cells

Figure 143 shows the Cs-Ne cells made of a Si wafer sandwiched between two borosilicate glass wafers. The cell contains two cavities connected through micro surface channels: one for CPT resonance detection and the other for Cs dispenser storage, achieving an inner volume of nearly 7.5 mm^3.

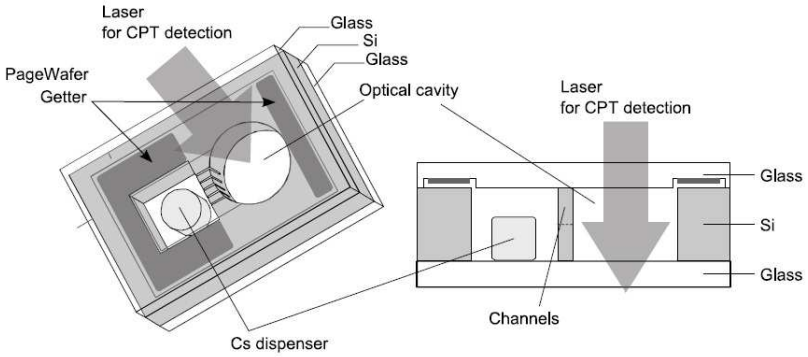

Figure 143: Schematic of the getter-integrated Cs vapor cell.

For getter-integrated cells, the PageWafer is deposited inside the cavity before the sealing of the cavity, in top-glass trenches located around the optical window and the dispenser cavity window, as shown in Figure 143. Figure 144 shows the fabrication process of the Cs vapor microcell. First, an array of cell cavities and filtration channels are patterned and etched in a Si wafer by using deep reactive ion etching (DRIE), followed by an additional KOH surface treatment for surface quality improvement. At the same time, a 10 μm deep cavity for getter deposition is etched in high frequency in a glass wafer, which is called cap wafer. For this purpose, a mask made of a layer of Au/Cr is sputtered on both surfaces of the glass wafer for high frequency etching. The cavity patterns are transferred into the mask layer by photolithography, and the sample is immersed in an high frequency aqueous solution. Thus, PageWafer is deposited inside the 10 μm deep cavities. Subsequently, the cell is sealed. Firstly, the getter-deposited top-glass wafer is anodically bonded to the Si wafer in vacuum. Once a Cs dispenser pill is placed in the cavity, the cell is sealed by anodic bonding in the chamber filled with Ne. For this step, we applied a two-step anodic bonding process in order to fill the cell cavity with Ne without the problem of electrical breakdown between electrodes when a high voltage is applied. After the sealing of the wafer, the array of microcells is diced into single cell chips. At last, Cs dispenser pill is locally heated with a high power laser source, so that the Cs vapor generated from the dispenser diffuses through the microchannels to the CPT detection cavity. Activation of the Cs dispenser is done after the cell is sealed, the most efficient gettering is done in a Ne atmosphere. PageWafer film sorption capacity for the various active gases is much higher under warm conditions, as it is during the bonding step, than at room temperature, which is almost two orders of magnitude at 450 °C. This is because higher temperatures promote the diffusion of the chemisorbed gases form the surface of the getter film into its bulk. This higher capacity allows the PageWafer film to also act as a process getter allowing the sorption of a larger quantity of gases desorbed during the high-temperature bonding process. Besides, use of Ne as a buffer gas prevents the undesired effect of pressure decrease inside the microcell because noble gases are not absorbed by the getter film. Therefore, with this cell configuration, the CPT resonance frequency is not expected to vary because of cell atmosphere variations. The top-glass wafer with deposited getters should be preferably bonded at last. Therefore, the getter would not undergo an activation during the first bonding process, as it is our case due to alignment restrictions in the employed bonding machine. In the following section, the efficiency of the getter and its great potential for purification of alkali vapor cell atmosphere are presented.

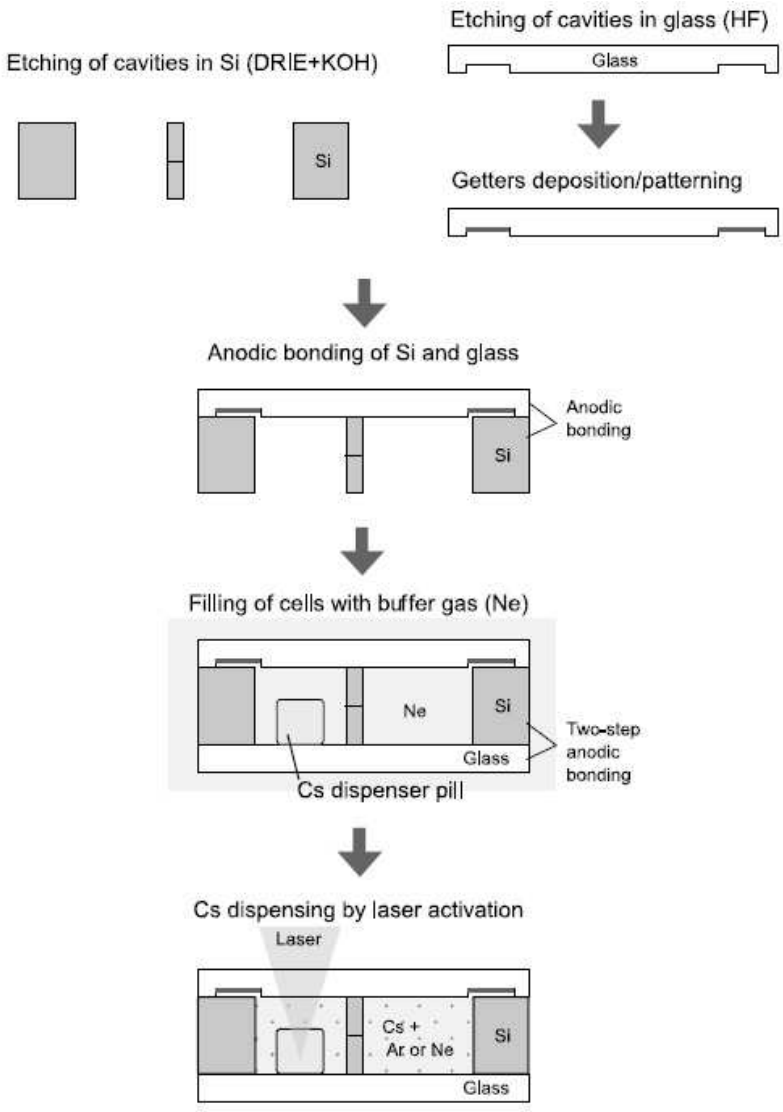

Figure 144: Fabrication steps of the getter-integrated Cs vapor microcell.

6.3.3 Residual gas analysis

The inner atmosphere of the cells are analyzed at room temperature in an ultrahigh vacuum chamber equipped with a high sensitivity quadrupole mass spectrometer (QMS). The microcells for this analysis contain Ne but neither a Cs dispenser nor Cs vapors in order to avoid possible partial gettering of Cs and also to simplify the residual gas analysis. A Cs-Ne microcell was placed in a small vacuum chamber equipped with an opening tool and a capacitance manometer. The chamber was evacuated and was isolated from the pumping system. Then, the cell was broken by an opening tool and the total pressure of the chamber was measured. The original pressure inside the cell is calculated by using the chamber and inner-cell volumes. After the total pressure was measured, a small part of the gas was introduced to another chamber and its composition was investigated with QMS. Table 8 shows the comparison the results of residual gas analysis from a getter-free cell and a getter-integrated cell. The main impurities in the getter-free cell are H_2, N_2, O_2 and CO_2, which are generated during anodic bonding reaction and to be active gas [166] [167]. These gases are not detected in the getter-integrated cell, which indicates that the PageWafer efficiently absorbed these gases. The pressure of Ne in both cells is comparable, which means Ne is not absorbed by the PageWafer. The value difference results from the precision of our Ne filling technique. In contrast to the above-mentioned gas species, it has to be mentioned that traces of hydrocarbons were detected (although four orders of magnitude lower than Ne pressure), which could be related to residual impurities of the manufacturing processes for getter patterning.

Table 8: Effects of getter films on cell atmosphere. Cells are filled with Ne (pressure=99.75 Torr.)

	Residual gas pressure (Torr)	
Gas	Cell A (Getter-free)	Cell B (Getter-integrated)
H_2	2.07×10^{-2}	0.00
He	2.783×10^{-3}	1.63×10^{-3}
CO	0.00	0.00
N_2	6.09×10^{-2}	0.00
CH_4	3.34×10^{-3}	2.79×10^{-2}
H_2O	0.00	0.00
Ne	1.05×10^{2}	1.42×10^{2}
O_2	6.07×10^{-1}	0.00
C_2H_6	0.00	5.28×10^{-3}
C_3H_8	5.72×10^{-3}	2.12×10^{-2}
Ar	5.46×10^{-3}	0.00
CO_2	1	0.00

Figure 145 summarizes the averages of residual gas pressure corresponding to each impurity in the getter-free and getter-integrated cells. Four samples of the getter-free cells and six samples of the getter-integrated cells are randomly chosen for gas analysis. All cells are filled with Ne but contain neither Cs vapor nor a Cs dispenser. The total residual gas pressure is significantly reduced in the getter-integrated cells by comparison with the getter-free cells. It is also important to note that the pressure errors among the cells are drastically reduced for the getter-integrated cells. The average pressure of total impurities was 3×10^{-2} Torr for the getter-integrated cells, whereas it was 1.5 Torr for the getter-free cells. In other terms, the residual gas remaining in the getter-integrated cells is 2% of that in the getter-free cells.

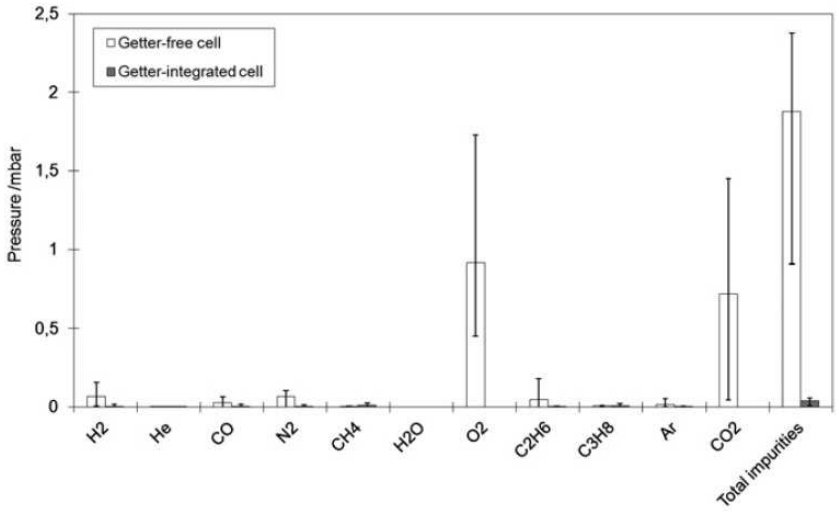

Figure 145: Residual gas pressure in Ne cells.

6.3.4 CPT spectroscopy

Cs-Ne cells were characterized by CPT spectroscopy employing a Cs CPT clock prototype. CPT spectroscopy is employed here for Ne pressure estimation. Indeed, presence of Ne buffer gas, in addition to narrowing of CPT resonance thanks to Dicke effect [34], is also responsible for a shift of the Cs hyperfine resonance frequency. This shift is proportional to Ne pressure, so pressure uniformity among the fabricated cells and process reproducibility can be estimated. The measured clock frequency f_{clk} is given by:

$$f_{clk} = f_0 + aB^2 + bI + \Delta f_{bg} \tag{132}$$

where f_0 is the frequency of the unperturbed Cs atom (9.192 631 770 GHz), aB^2 is the quadratic Zeeman shift due to the static magnetic field B (a=427 Hz/G^2), bI is the so-called light shift (frequency shift of the clock attributed to variations of the laser intensity I) and Δf_{bg} is the collisional frequency shift due to the presence of buffer gas. The value of Δf_{bg} should be determined in order to estimate the Ne pressure in the cell. For this purpose, the microcell temperature is fixed in the 60°C to 80°C range. The static magnetic field is 132 mG, inducing a fixed Zeeman shift of 7.4 Hz. Then, the clock frequency is measured for various laser intensities in order to determine the linear light shift function bI. At last, once the Zeeman shift taken into account, the collisional frequency shift Δf_{bg} due to the presence of buffer gas is measured by extrapolation at zero intensity of the light shift curve. For Ne, the collisional frequency shift Δf_{bg} is given by [88]:

$$\Delta f_{bg} = P_0 \times (686.014 + 0.266 \times (T - T_0) + (-0.001676) \times (T - T_0)^2) \tag{133}$$

where P_0 is the buffer gas pressure in Torr at the reference temperature of $T_0 = 0$ °C. In this experiment, the uncertainty on clock resonance frequency measurements was estimated to be only ±50 Hz because the LO frequency was not actively locked to the atomic transition. This uncertainty limits the estimation of Ne pressure value in the cell at a level of ±0.0975 Torr.

Batch pressure uniformity In the first step, Cs-Ne getter-cells were characterized from two different batches, called batch A and batch B, resulting from two fabrication runs. Cells are noted Axx and Bxx.

Eight or more samples from each batch were examined using CPT spectroscopy. For each batch, the Ne set pressure during fabrication is 99.75 Torr at 65 °C. Figure 146 shows a typical CPT resonance detected in the A04 cell. The resonance is well fitted by a lorentzian function with a FWHM of 1.88 kHz. Measured FWHM of cells from batch A are in the range of 1.66 kHz to 1.96 kHz (average: 1.76 kHz) and from batch B in the range of 1.59 kHz to 1.75 kHz (average: 1.66 kHz).

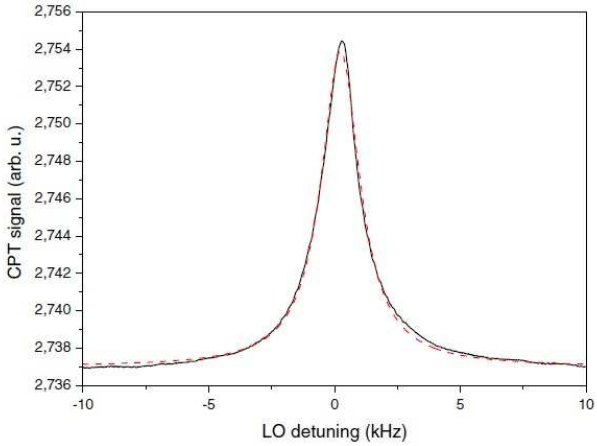

Figure 146: Typical 1.88 kHz linewidth CPT resonance detected in the A04 cell.

Figure 147 reports pressures in Cs-Ne cells derived from the measured collisional frequency shift of the CPT resonance for the two considered batches. Except for one cell, the Ne pressure is similar among the cells of the same batch. For cells Axx, the average pressure is 78.45 Torr. The minimum and maximum pressure is 77.475 and 81.15 Torr respectively. The pressure deviation is 4.5%. If we remove the exceptional cell (A08), the pressure deviation is reduced to 2%. For cells Bxx, average pressure is 91.575 Torr. The minimum and maximum pressure is 89.775 and 93.225 Torr respectively. The pressure deviation is 7.7%, and it is reduced to 3.7% if the B02 is not considered. For these two batches, the average pressures are 21.3 and 8.175 Torr lower than the set pressure, respectively. The difference in Ne pressure between the two batches is around 15% and is considered to result from the uncertainty of our Ne filling system.

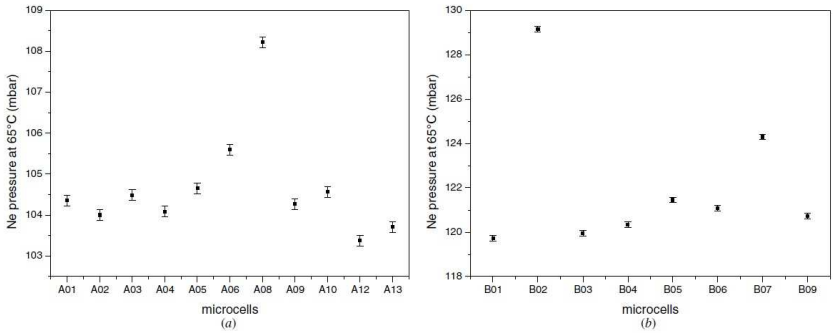

Figure 147: Estimated pressure at 65 °C of the (a) Axx and (b) Bxx Cs-Ne cells using CPT resonance frequency measurements.

Frequency stability measurements Accelerated aging tests were performed in order to evaluate the variation of the cell inner atmosphere along time. The clock signal lineshape and frequency were first measured in Cs-Ne cell at 80°C cell temperature. Then, the cells were placed in an oven at 110°C during 240 hours. This heating process can be considered as an aging test of $240 \times 8 = 1920$ h at 80°C [168]. The clock signal lineshape and frequency in the cell were then measured again at 80 °C. In both measurements, experimental parameters are kept identical. Figure 148 shows the evolution of the CPT resonance frequency as a function of the laser power for 3 different cell (A01, B03, B05) before and after aging. Experimental data are fitted by a linear function. Extrapolation to null laser power is performed to cancel the so-called frequency shift and isolate the collisional frequency shift value.

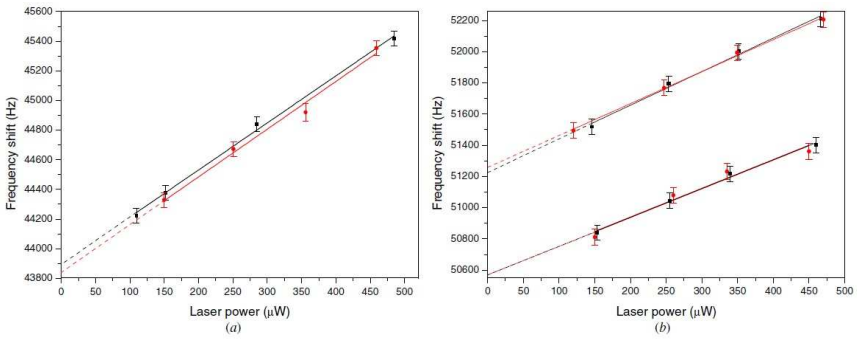

Figure 148: CPT resonance frequency measurements as a function of laser power of three different cells: (a) A01, (b) B03 (lower curve) and B05 (upper curve) before aging (black squares) and after aging (red circles). Experimental data are fitted by a linear function for extrapolation at null power.

Similar fit function results are obtained for cells B03 and B05 fabricated in the same batch. For the 3 cells, measured light shift slopes are found to be about 1 to 3 Hz/μW. The clock frequency variation at null laser power, during the aging test equivalent to 1920 hours at 80 °C, is lower than 53, 1 and 35 Hz for cells A01, B03 and B05 respectively, with uncertainties in the range of 100 Hz. This result demonstrates the excellent stability of the cell inner atmosphere. For comparison, a Cs vapor microcell-based miniature atomic clock characterized by relative frequency stability below 10^{-11} at 1 hour integration time has its frequency varying less than 0.1 Hz at 1 hour, i.e. less than 192 Hz in 1920 hours. The tested cells are below this limit. However, in order to further validate getter-cells, their compatibility to be used in a miniature atomic clock exhibiting a relative frequency stability of 10^{-11} at 1 day integration should be demonstrated. This will be analyzed by optimizing the frequency resolution of our setup or increasing the time duration of the aging test. Such tests will be led in a growing number of cells to check the repeatability of performances of our cells.

6.3.5 Conclusion

The PageWafer integration technology in Cs-Ne microcells for miniature atomic clocks was investigated. The residual gas analysis with quadruple mass spectroscopy revealed that PageWafer efficiently eliminates undesirable anodic-bonding-related gases such as H_2, O_2, N_2 and CO_2. Such cells achieve the impurity pressure in the order of 10^{-2} Torr which is 2% of that of the getter-free cells. CPT spectroscopy of the getter-integrated Cs-Ne cells showed that Ne pressure is almost identical among the cells fabricated in one

run (less than 5% deviation). We performed preliminary aging tests showing that these cells are compatible with the development of miniature atomic clocks exhibiting a relative frequency stability better than 10^{-11} at 1 hour integration.

7 Conclusion

In this thesis, a research work on CPT spectroscopy on Cs vapor cells was presented. Since classical CPT atomic clocks generate low contrast CPT signals, we developed an experimental setup to detect high-contrast CPT resonances using the push-pull optical pumping (PPOP) technique. Theoretical analysis of PPOP was reported and allowed to be compared with the so-called $lin \perp lin$ interaction scheme. CPT resonance signals with contrasts as high as 78 % were detected in the CW regime, that represents almost an improvement of two orders of magnitude compared to standard interaction schemes. The impact of some experimental parameters on the CPT resonance lineshape was studied. In order to reduce the CPT resonance linewidth, we developed an original simple-architecture laser system combining for the first time PPOP and Ramsey interrogation for the detection of high-contrast and narrow CPT-Ramsey fringes. In this system, an EOM is used both for CPT sidebands generation and light switch. Consequently, atoms interact with a sequence of optical pulse trains where each pulse is used both for CPT pumping and CPT signal detection. The central Ramsey fringe, for a free-evolution time $T = 3$ ms exhibits a linewidth of 166 Hz and a contrast of 33 %. This laser system could be interesting for the development of a high-performance Cs CPT vapor cell frequency standard.

Our system combines basically a DFB laser at 895 nm, a pigtailed intensity Mach-Zehnder EOM, a Michelson system and a low noise microwave frequency synthesizer. We developed a DFB laser system that can be frequency stabilized by standard saturation absorption scheme on Cs Doppler-free D1 line. In the free running regime, the short term relative frequency stability of the laser is measured to be 1.5×10^{-9} at 1 s integration time, increasing to reach about 8×10^{-9} at 100 s integration time. With the frequency stabilizatipon system, it exhibits a fractional frequency instability better than 10^{-11} at 1 s integration time and lower than 5×10^{-12} at 200 s. The laser power can be stabilized using a commercial voltage controlled LCD attenuator-based servo loop. In stabilized regime, the relative laser power fluctuations are 2×10^{-6} at 500 s integration time, which is almost 4 orders of magnitude lower than fluctuations in the free running regime.

We compared phase and intensity EOMs for sidebands generation. Intensity MZ EOM, with bias voltage adjusted to reject the optical carrier, was found to give better CPT signals. We implemented a technique to stabilize the optical carrier signal suppression at the output of the MZ EOM to ensure that atoms interact with "only" two optical lines. The carrier signal power fluctuations at the output of the MZ EOM are reduced by a factor of about 100 compared to the one in free running regime.

We developed and measured phase noise performances of a frequency-multiplied quartz oscillator based low phase noise microwave synthesizer. This one is used to drive EOM. The absolute phase noise of the 9.192 GHz signal at the output of the EOM was measured to be better than $-$ 85 dBc/Hz at $f=$ 100 Hz. No relevant phase noise degradation was observed between the synthesizer direct output and the 9.192 GHz optical beatnote at the output of the EOM. Performances are compatible with the development of an atomic clock with a relative frequency stability at the level of 2×10^{-13} at 1 s.

In our experiments, we tested three Cs vapor-buffer gas cells with different dimensions and buffer gas contents. Contrasts up to 78% were achieved in a 5 cm long and 2 cm diameter Cs-N_2-Ar cell in the CW regime. The PPOP technique was found to be more efficient to obtain high contrasts when the cell dimensions are increased. Consequently, our study suggests that optimized CPT pumping schemes such as PPOP or lin$\perp$lin cannot be used efficiently to improve the performances of chip-scale atomic clocks, but are very promising for more conventional atomic clock using cm-size cells. We pointed out that high-contrast CPT resonances are achieved with increased laser intensity, at the expense of laser power broadening. A Ramsey pulsed

interaction technique was then implemented to allow the detection of narrow Ramsey fringes, that should constitute a good reference for the development of a high-performance CPT clock. Typical Ramsey fringes with a linewidth of 166 Hz and a contrast of 33% were detected in a cm-scale buffer gas filled Cs vapor cell. Besides the main work of my thesis, I participated into the development of a high performance frequency stability compact clock based on a Cs-Ne microfabricated cell. The clock frequency stability was measured to be 3.8×10^{-11} at 1 s integration time and below 10^{-11} until 50000 s thanks to the implementation of light shift cancellation techniques. These results demonstrate the possibility to develop high performance chip-scale atomic clocks using vapor cells containing a single buffer gas. Moreover, I participated to study the impact of the presence of getters in hermetically sealed micromachined Cs-Ne cells.

The laser system we developed in this PhD thesis will be further studied and improved along the MClocks project, funded by EURAMET. This project combines the competence of best european laboratories in the field of vapor cell clocks. Significant efforts remain to be done to validate fully our laser system for the development of a high-performance CPT atomic clock. The first next step is to realize clock frequency measurements and to evaluate the influence of the laser system components and parameters onto the clock frequency. Clock frequency shifts linked to laser frequency variations, intensity variations, EOM bias voltage variation, Michelson system length fluctuations, polarization fluctuations need to be measured in detail to know how experimental parameters must be controlled to reach frequency stability objectives. **This is really the clock frequency metrology and this will be the most important step in the validation of our system.** Note also that we're confident that the volume of our laser system architecture is compatible to be strongly reduced. In particular, we expect to replace nextly the TO3-packaged DFB laser we used by a "butterfly-packaged" pigtailed diode laser. This would allow to connect directly the output of the laser to the MZ EOM and will simplify greatly the system. Nevertheless, commercially-available pigtailed diode lasers resonant at 895 nm are not easy to find. We contacted recently different suppliers (Eagleyard, Nanoplus, Toptica, Photodigm) for this purpose but none of them is currently able to deliver such diodes at this wavelength. The Michelson system ensemble will be inserted in a small mechanical duralumin box with active temperature control and active control of the optical path difference. At the end, the aim is to insert the total laser system into an elegant A3-A2 format rack that would be easily transportable. Some insulating foam will be used to stabilize passively fiber lengths of the system.

Annex

Cesium Properties

Table 9 shows basic cesium physical properties [84].

Table 9: Cesium Physical Properties.

Atomic Number	Z	55
Total Nucleons	Z+N	133
Relative Natural Abundance	$\eta(^{133}Cs)$	100%
Nuclear Lifetime	τ_n	stable
Atomic Mass	m	2.206 946 50(17) $\times 10^{-25}$ kg
Density at 25°C	ρ_m	1.93 g/cm^3
Melting Point	T_M	28.44°C
Boiling Point	T_B	671°C
Specific Heat Capacity	c_p	0.242 J/g·K
Molar Heat Capacity	C_p	32.210 J/mol·K
Vapor Pressure at 25°C	P_v	1.3×10^{-6} torr
Nuclear Spin	I	7/2
Ionization Limit	E_I	3.893 905 32(14) eV

Table 10 shows cesium D_1 line transition optical properties [84].

Table 10: Cesium D_1 ($6^2S_{1/2}$-$6^2P_{1/2}$) Transition Optical Properties.

Frequency	ω_0	$2\pi \cdot$ 335.116 048 807(41) THz
Transition Energy	$\hbar\omega_0$	1.385 928 475(50) eV
Wavelength (Vacuum)	λ	894.592 959 86(11) nm
Wavelength (Air)	λ_{air}	894.353 09 nm
Wave Number (Vacuum)	$k_L/2\pi$	11 178.268 160 7(14) cm^{-1}
Lifetime	τ	34.894(44) ns
Decay Rate / FWHM	Γ	28.659(36) $\times 10^6$ s^{-1} / $2\pi \cdot$ 4.5612(57)
Absorption Oscillator Strength	f	0.3438(13)
Recoil Velocity	υ_r	3.3561 mm/s
Recoil Energy	ω_r	$2\pi \cdot$ 1.8758 kHz
Recoil Temperature	T_r	180.05 nK
Doppler Shift ($\nu_{atom} = \nu_r$)	$\Delta\omega_d(\nu_{atom} = \nu_r)$	$2\pi \cdot$ 3.7516 kHz
Frequency Shift for Standing Wave Moving with $\nu_{SW} = \nu_r$	$\Delta\omega_{SW}(\nu_{SW} = \nu_r)$	$2\pi \cdot$ 7.5031 kHz

Table 11 shows cesium D transition hyperfine structure constants [84].

Table 11: Cesium D Transition Hyperfine Structure Constants.

Magnetic Dipole Constant, $6^2S_{1/2}$	$A_{6^2S_{1/2}}$	$h \cdot$ 2.298 157 942 5 GHz (exact)
Magnetic Dipole Constant, $6^2P_{1/2}$	$A_{6^2P_{1/2}}$	$h \cdot$ 291.920(19) MHz
Magnetic Dipole Constant, $6^2P_{3/2}$	$A_{6^2P_{3/2}}$	$h \cdot$ 50.275(3) MHz
Magnetic Dipole Constant, $6^2P_{3/2}$	$B_{6^2P_{3/2}}$	$h \cdot$ -0.53(2) MHz

Table 12 shows cesium D transition magnetic and electric field interaction parameters [84].

Table 12: Cesium D Transition Magnetic and Electric Field Interaction Parameters.

Electron spin g-factor	g_S	2.002 319 304 373 7(80)
Electron orbital g-factor	g_L	0.999 995 87
Fine structure Landé g-factor ($6^2S_{1/2}$)	$g_J(6^2S_{1/2})$	2.002 540 32(20)
Fine structure Landé g-factor ($6^2P_{1/2}$)	$g_J(6^2P_{1/2})$	0.665 90(9)
Fine structure Landé g-factor ($6^2P_{3/2}$)	$g_J(6^2P_{3/2})$	1.3340(3)
Nuclear g-factor	g_I	-0.000 398 853 95(52)
Clock transition Zeeman shift	$\Delta\omega_{clock}/B^2$	$2\pi \cdot$ 427.45 Hz/G^2
Ground-state polarizability	$\alpha_0(6^2S_{1/2})$	$h \cdot$ 0.1001(20) Hz/(V/cm)^2
D_1 scalar polarizability	$\alpha_0(6^2P_{1/2})$ - $\alpha_0(6^2S_{1/2})$	$h \cdot$ 0.2415(24) Hz/(V/cm)^2
D_2 scalar polarizability	$\alpha_0(6^2P_{3/2})$ - $\alpha_0(6^2S_{1/2})$	$h \cdot$ 0.308 60(60) Hz/(V/cm)^2
D_2 tensor polarizability	$\alpha_2(6^2P_{3/2})$	$h \cdot$ -0.065 29(37) Hz/(V/cm)^2

Figure 149 shows cesium D_1 line hyperfine structure [84].

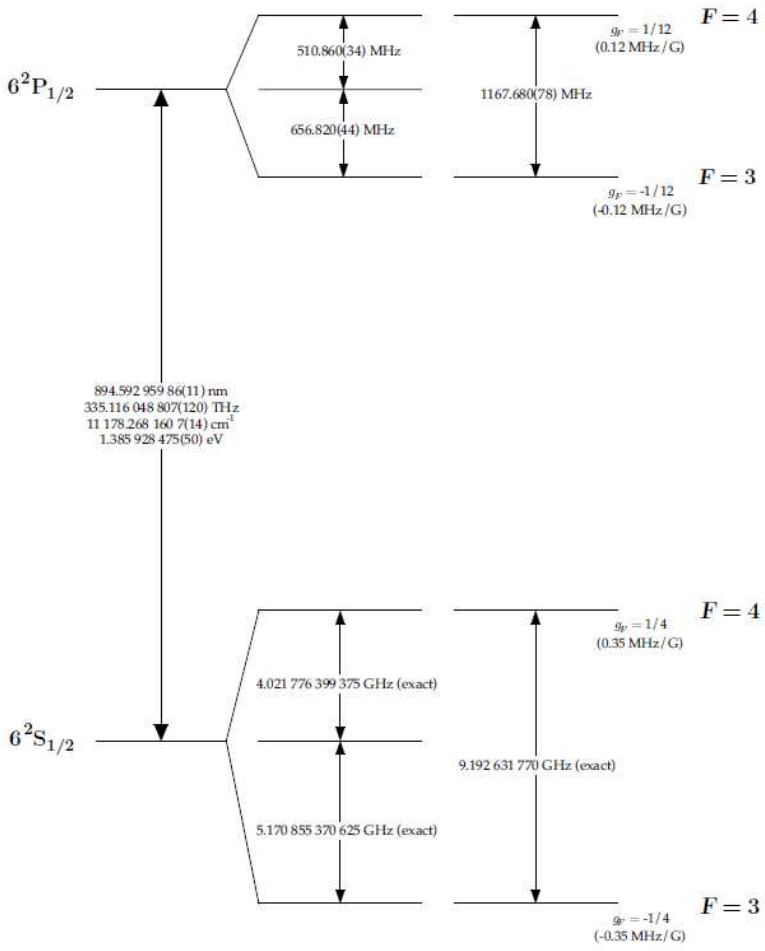

Figure 149: Cesium D_1 transition hyperfine structure, with frequency splittings between the hyperfine energy levels. The approximate Landé g_F-factors for each levels are given, with corresponding Zeeman splittings between adjacent magnetic sublevels.

Circuit Diagram

We applied different electronic drive circuits and feedback loops in our experimental setups. The circuit diagrams of each part are shown in the following parts. Figure 150 shows the circuit diagram of the laser drive.

Figure 151, 152 and 153 shows the circuit diagram of the variable dc source applied on the MZ EOM.

Figure 154, 155 and 156 shows the circuit diagram of the cell temperature regulator.

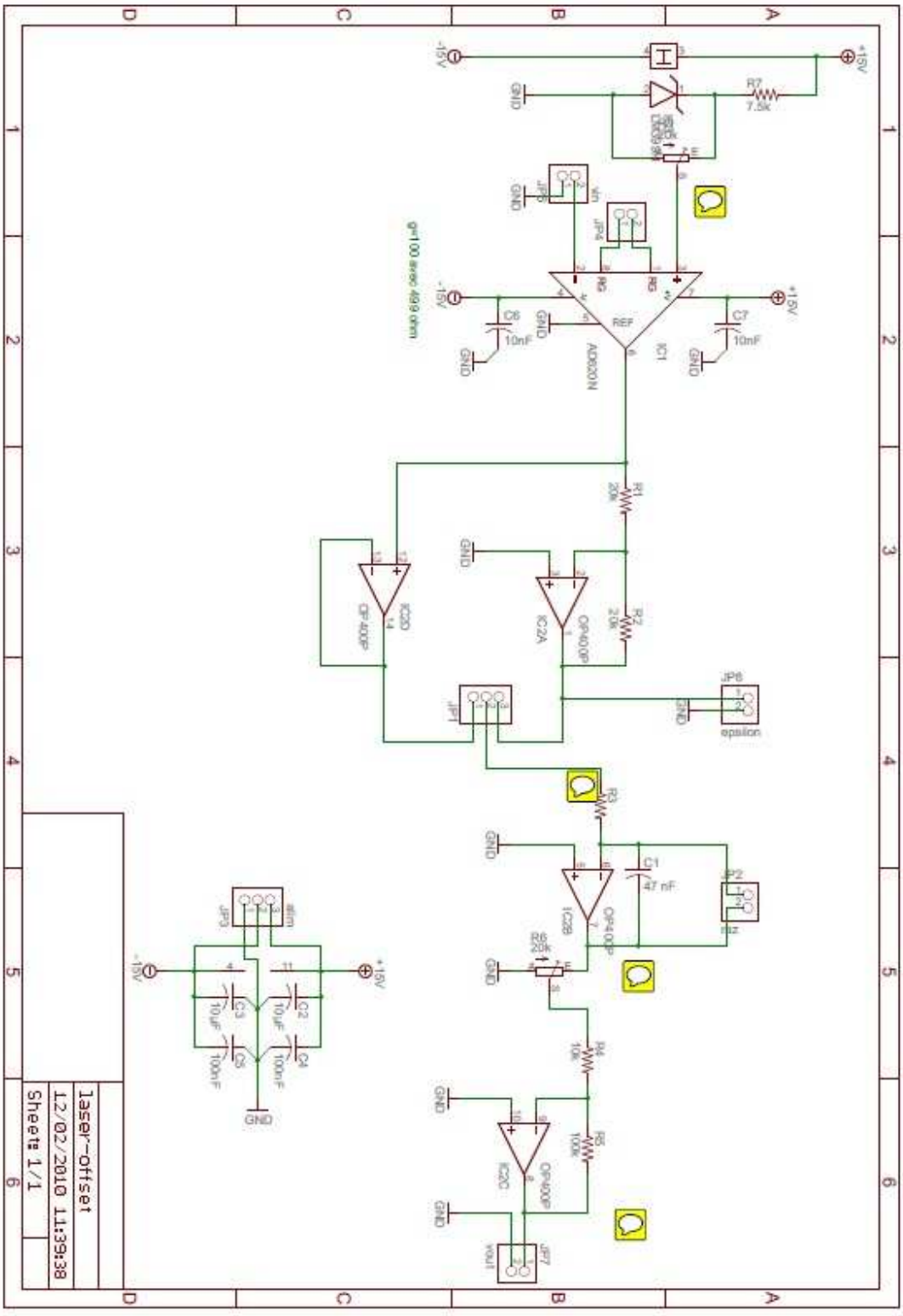

Figure 150: Circuit diagram of the laser drive.

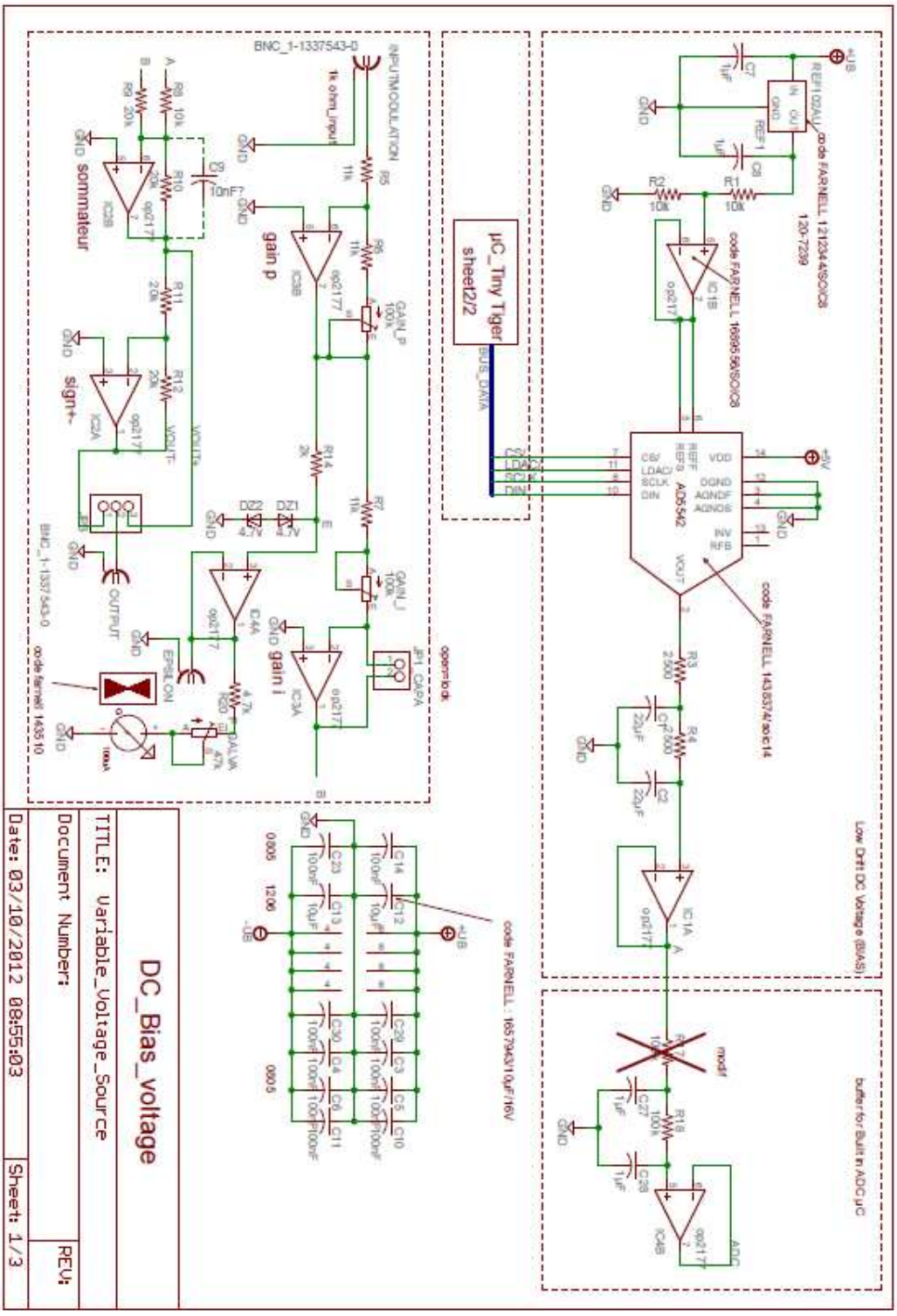

Figure 151: Circuit diagram of DC bias voltage of the variable dc source applied on the MZ EOM.

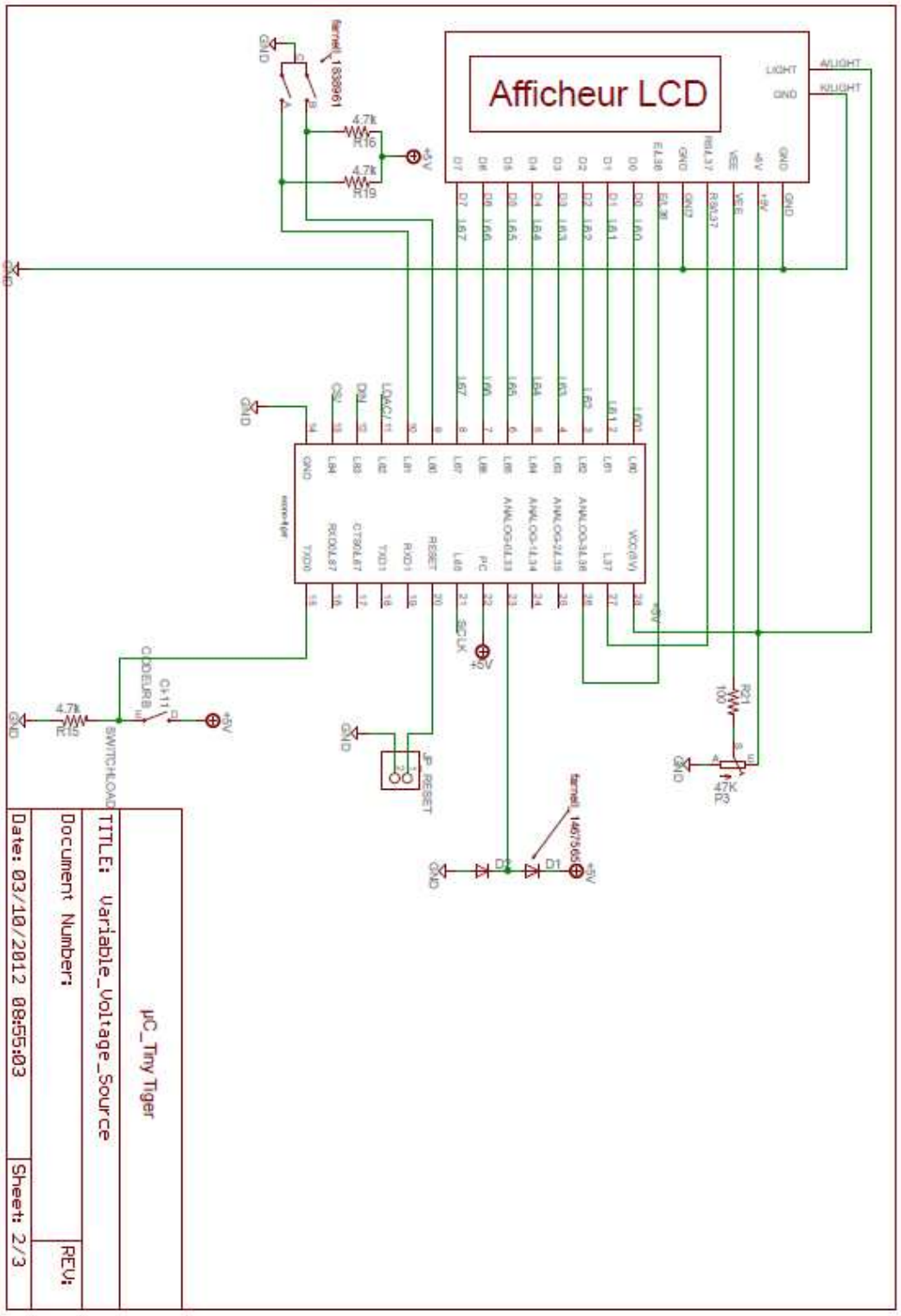

Figure 152: Circuit diagram of tiny tiger of the variable dc source applied on the MZ EOM.

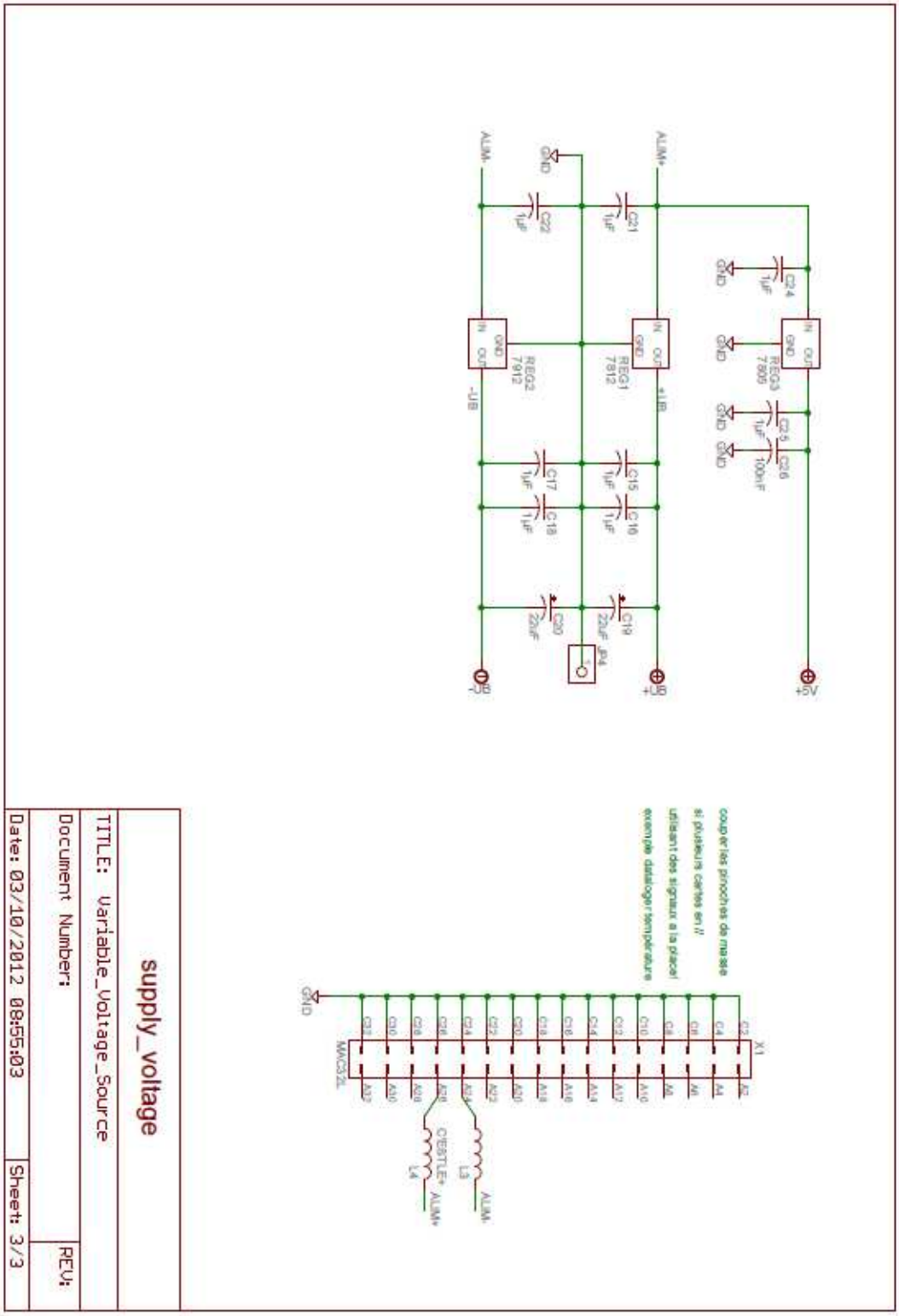

Figure 153: Circuit diagram of supply voltage of the variable dc source applied on the MZ EOM.

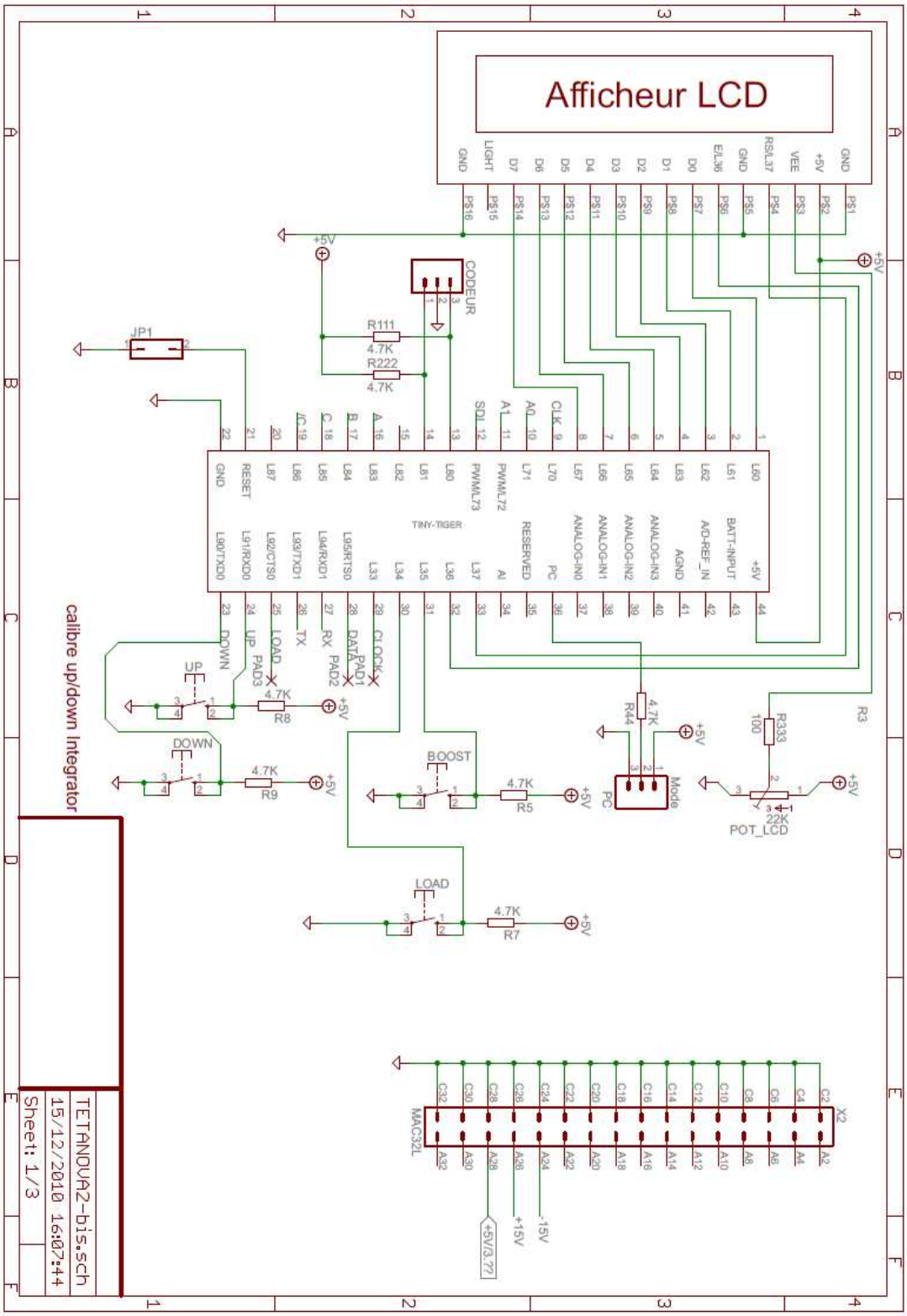

Figure 154: Circuit diagram of the cell temperature regulator.

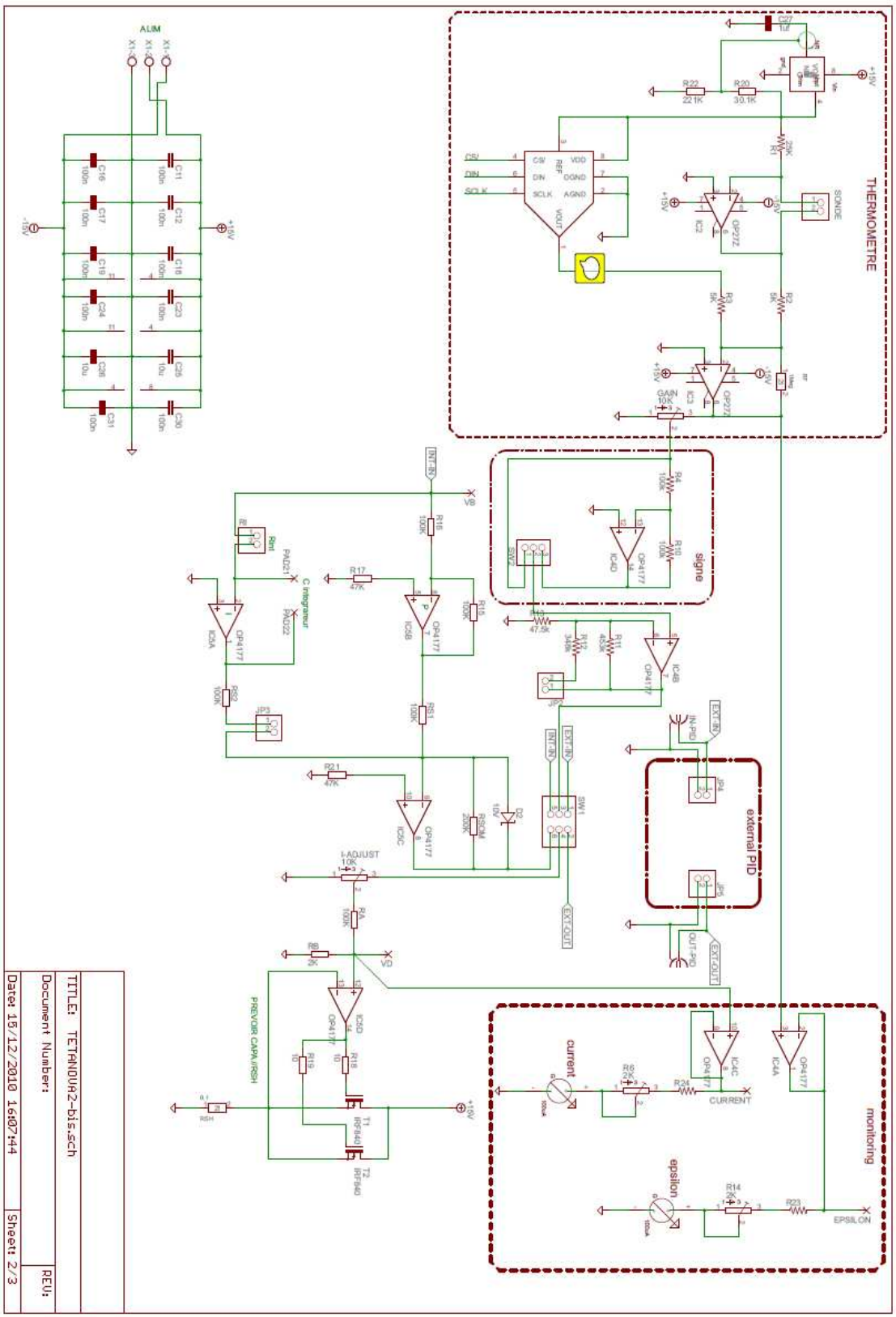

Figure 155: Circuit diagram of the cell temperature regulator.

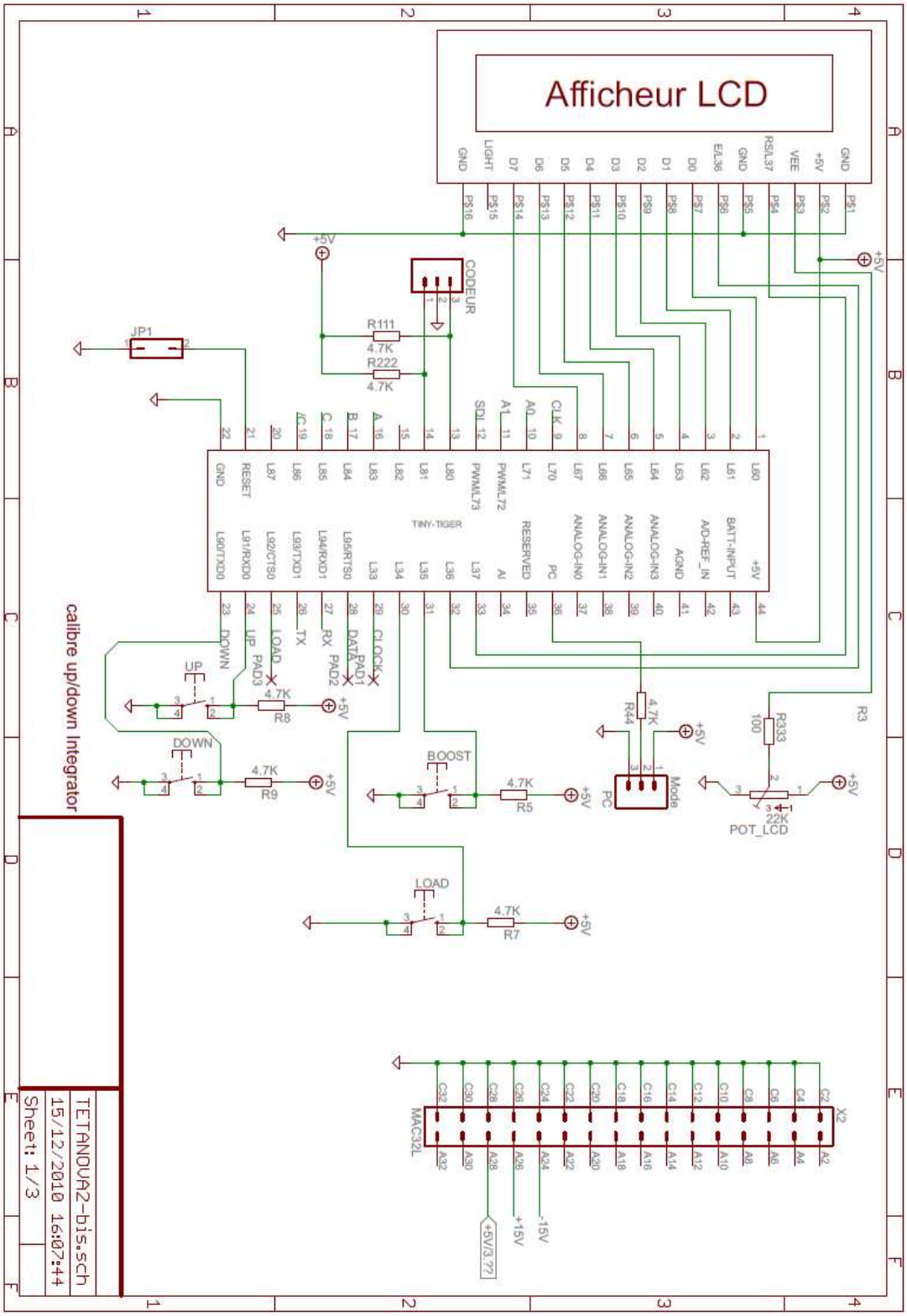

Figure 156: Circuit diagram of the cell temperature regulator.

References

[1] B. de Beauvoir, F. Nez, L. Julien, B. Cagnac, F. Biraben, D. Touahri, L. Hilico, O. Acef, A. Clairon, and J. J. Zondy, Phys. Rev. Lett., **78** , pp. 440−443 (1997)

[2] T. Rosenband, D. B. Hume, P. O. Schmidt, C. W. Chou, A. Brusch, L. Lorini, W. H. Oskay, R. E. Drullinger, T. M. Fortier, J. E. Stalnaker, S. A. Diddams, W. C. Swann, N. R. Newbury, W. M. Itano, D. J. Wineland and J. C. Bergquist, Science, **319** , 1808 − 1812 (2008).

[3] Ph. Laurent, M. Abgrall, Ch. Jentsch, P. Lemonde, G. Santarelli, A. Clairon, I. Maksimovic, S. Bize, Ch. Salomon, D. Blonde, J. F. Vega, O. Grosjean, F. Picard, M. Saccoccio, M. Chaubet, N. Ladiette, L. Guillet, I. Zenone, Ch. Delaroche, Ch. Sirmain, Appl. Phys. B, **84** , 683 (2006).

[4] S. Bhaskaran. The application of noncoherent doppler data types for deep space navigation. The Telecommunications and Data Acquisition Progress Report 42-121, January−March 1995, pages 54 − 65, 1995. JPL, http://tmo.jpl.nasa.gov/tmo/progressreport/42-121/121B.pdf.

[5] L. Essen and J. V. L. Parry, Nature, **176** (4476): 280-282 (1955).

[6] I. Rabi, Phys. Rev., 51:652 (1937).

[7] N. F. Ramsey, A Molecular Beam Resonance Method with Separated Oscillating Fields, Phys. Rev., **78,** 695 (1950).

[8] A. Kastler, J.Phys. et rad., 11:255−265 (1950).

[9] A. Aspect, E. Arimondo, R. Kaizer, N. Vansteenkiste and C. Cohen-Tannoudji, "Laser cooling below the one-photon recoil energy by velocity-selective coherent population trapping: theoretical analysis," J. Opt. Soc. Am. B **6** , 2112-2124 (1989).

[10] R. Holzwarth, Th. Udem, T. W. Hänsch, J. C. Knight, W. J. Wadsworth, and P. St. J. Russell, Phys. Rev. Lett., **85** , 11, 2264 (2000).

[11] S. A. Diddams, Th. Udem, J. C. Bergquist, E. A. Curtis, R. E. Drullinger, L. Hollberg, W. M. Itano, W. D. Lee, C. W. Oates, K. R. Vogel and D. J. Wineland, Phys. Rev. Lett., **84** , 22, 5102 (2000).

[12] C. W. Chou, D. B. Hume, J. C. J. Koelemeij, D. J. Wineland and T. Rosenband, Phys. Rev. Lett., **104** , 070802 (2010).

[13] P. G. Westergaard, J. Lodewyck, L. Lorini, A. Lecallier, E. A. Burt, M. Zawada, J. Millo and P. Lemonde, Phys. Rev. Lett., **106** , 210801 (2011).

[14] T. L. Nicholson, M. J. Martin, J. R. Williams, B. J. Bloom, M. Bishof, M. D. Swallows, S. L. Campbell and J. Ye, Phys. Rev. Lett., **109** , 230801 (2012).

[15] N. Hinkley, J. A. Sherman, N. B. Phillips, M. Schioppo, N. D. Lemke, K. Beloy, M. Pizzocaro, C. W. Oates and A. D. Ludlow, Sciencexpress, 1240420, 22 Aug. (2013)

[16] B. J. Bloom, T. L. Nicholson, J. R. Williams, S. L. Campbell, M. Bishof, X. Zhang, W. Zhang, S. L. Bromley and J. Ye, arxiv.org/abs/1309.1137 (2013).

[17] J. Deng, P. Vlitas, D. Taylor, L. Perletz and R. Lutwak. In Proc. of 22th European Freq. and Time Forum, Toulouse, France, 2008.

[18] http://www.symmetricom.com/products/frequency-references/chip-scale-atomic-clock-csac/SA.45s-CSAC/

[19] http://www.mac-tfc.eu/

[20] J. Haesler, J. Bennes, T. Overstolz, J. Pierer, R. J. James, D. Ruffieux and S. Lecomte, Proc. EFTF, Gothenbury, Sweden (2012).

[21] http://www.darpa.mil/

[22] J. Camparo. Physics today, Novembre, 2007.

[23] S. Micalizio, C. E. Calosso, A. Godone and F. Levi, "Metrological charaterization of the pulsed Rb clock with optical detection", Metrologia **49,** 425 (2012).

[24] T. Bandi, M. Pellaton, D. Miletic, C. Affolderbach, F. Gruet, R. Matthey, G. Mileti, C. Stefanucci, M. Violetti, F. Merli, J. Zurcher and A. K. Skriverviky, In Proc. of Frequency Control Symposium, (2012).

[25] R. Boudot, S. Guerandel, E. De Clercq, N. Dimarcq, and A. Clairon, IEEE Trans. Instrum. Meas. **58,** 1217 (2009).

[26] T. Zanon, S. Guérandel, E. de Clercq, D. Holleville, N. Dimarcq and A. Clairon, Phys. Rev. Lett. **94,** 193002 (2005).

[27] N. Castagna, R. Boudot, S. Guerandel, E. De Clercq, N. Dimarcq, and A. Clairon, IEEE Trans. Ultrason. Ferroelec. Freq. Contr. **56,** 246 (2009).

[28] Y. Y. Jau, E. Miron, A. B. Post, N. N. Kuzma and W. Happer, Phys. Rev. Lett. **93** , (16) 160802 (2004).

[29] S. A. Zibrov, V. L. Velichansky, A. S. Zibrov, A. V. Taichenachev and V. I. Yudin, JETP Lett. **82** , 8, 534 (2005)

[30] D. Allan, Statistics of Atomic Frequency Standards. Proc. of IEEE, **54** (2): 221-230 (1966).

[31] A. Barnes, et al., Characterization of frequency stability. IEEE Transactions on Instrumentation and Measurement, **20** (2):105-200 (1971)

[32] J. Rutman and F. L. Walls, "Characterization of frequency stability in precision frequency sources", Proc. of the IEEE **79** , 953-960 (1991).

[33] E. Rubiola, "Phase Noise and Frequency Stability in Oscillators", ISBN 978-0-521-15328-7, Cambrige University Press, (2009).

[34] R. H. Dicke, Phys. Rev. **89** , 472 (1953).

[35] M. A. Bouchiat and J. Brossel, Phys. Rev. **147** , $41 - 54$ (1966).

[36] M. V. Balabas, T. Karaulanov, M. P. Ledbetter, and D. Budker, Phys. Rev. Lett., **105** , 070801 (2010).

[37] J.Prestage et al. Compact microwave mercury ion clock for deep-space applications. In Proc. of the 2007 UFFC-IFCS EFTF joint meeting, Geneva, Switzerland, (2007).

[38] E. De Clercq. L'étalon primaire de fréquence à jet de césium du BNM-SYRTE

[39] E. De Clercq. L'étalon primaire de fréquence à jet de césium du bnm-syrte. Bulletin du BNM, **125** , (2004).

[40] P. Berthoud et al. Optically-pumped space cesium clock for galileo:firrst results of the breadboard. In Proc. of 22th European Freq. and Time Forum, Toulouse, France, (2008).

[41] B. Guinot and C. Audoin. Les fondements de la mesure du temps. MASSON, ISBN 2225 83261 7, (1997).

[42] G. Mileti, J. Deng, F. L. Walls, D. A. Jennings, and R. E. Drullinger. Laser-pumped rubidium frequency standards: New analysis and progress. IEEE Journal of Quantum Electronics, **34** , 233-237, (1998).

[43] R. Dupuis, T. Lynch and J. Vaccaro. Rubidium frequency standard for the gps iif program and modifications for the rafsmod program. In Proc. of the 2008 IEEE UFFC - IFCS meeting, Honolulu, USA, (2008).

[44] P. Rochat et al. The onboard galileo rubidium and passive maser,status and performance. In Proc. of the 2005 UFFC-IFCS, Vancouver, Canada, (2005).

[45] P. Waller, S. Gonzalez, S. Binda, I. Sesia, I. Hidalgo, G. Tobias and P. Tavella, IEEE Trans. Ultrason. Ferroelectr. Freq. Control. **57** , 738 (2010).

[46] C. Stefanucci, T. Bandi, F. Merli, M. Pellaton, C. Affolderbach, G. Mileti and A. K. Skrivervik, "Compact microwave cavity for high performance rubidium frequency standards", Rev. Sci. Instrum. **83,** 104706-1/8 (2012).

[47] A. Godone, S. Micalizio, F. Levi and C. Calosso, Phys. Rev. A **74** , 043401 (2006).

[48] A. Godone, S. Micalizio and F. Levi, Phys. Rev. A **70** , 023409 (2004).

[49] M. Zhu, Proc. of the 2003 IEEE IFCS, Tampa, FL, USA (2003).

[50] S. Knappe, Thesis (2001).

[51] J. Lin, J. Deng, Y. Ma, H. He and Y. Wang, Opt. Lett. **37** , 24 (2012).

[52] G. Alzetta, A. Gozzini, L. Moi and G. Orriols, Nuovo Cimento B **36** , 5 (1976).

[53] E. Arimondo, Prog. Opt., **35** , 257 (1996).

[54] J. E. Thomas, P. R. Hemmer, C. Ezekiel, C. Leiby, R. H. Picard and C. R. Wills, Phys. Rev. Lett. **48** , 867 (1982).

[55] R. Lutwak, D. Emmons, T. English, W. Riley, A. Duwel, M. Varghese, D. K. Serkland and G. M. Peake. In Proc. of the 2003 PTTI meeting, San Diego, CA, USA, (2003).

[56] S. Knappe, V. Shah, P. D. D. Schwindt, L. Hollberg, J. Kitching, L-A. Liew and J. Moreland, Appl. Phys. Lett. **85** , 1460 (2004)

[57] R. Lutwak, A. Rashed, M. Varghese, G. Tepolt, J. LeBlanc, M. Mescher, D. K. Serkland, K. M. Geib, G. M. Peake and S. Römish, PTTI, 269-290 (2011)

[58] R. Lutwak, A. Rashed, M. Varghese, G. Tepolt, J. Leblanc, M. Mescher, D. K. Serkland and G. M. Peake. In Proc. of the 2007 UFFC-IFCS EFTF joint meeting, Geneva, Switzerland, (2007).

[59] O. Kozlova, Thesis UPMC (2012).

[60] M. Kasevich, E. Riis, S. Chu, and R. G. De Voe, rf spectroscopy in an atomic fountain. Phys. Rev. Lett. **63** , 612 (1989).

[61] M. Vengalattore et al. High-Resolution Magnetometry with a Spinor Bose-Einstein Condensate. Phys. Rev. Lett. **98** , 200801 (2007).

[62] A. Peters, K. Y. Chung and S. Chu, Measurement of gravitational acceleration by dropping atoms. Nature **400** , 849 – 852 (1999).

[63] T. L. Gustavson, P. Bouyer and M. A. Kasevich, Precision Rotation Measurements with an Atom Interferometer Gyroscope. Phys. Rev. Lett. **78** , 2046 (1997).

[64] J. L. Hall, M. Zhu and P. Buch, Prospects for using laser-prepared atomic fountains for optical frequency standards applications. J. Opt. Soc. Am. B **6** , 2194 – 2205 (1989).

[65] F.-X. Esnault, D. Holleville, N. Rossetto, S. Guerandel and N. Dimarcq, Phys. Rev. A **82** , 033436 (2010).

[66] J. Prestage et al. One-liter ion clock: New capability for space ight applications. In Proc. of the 2003 PTTI meeting, San Diego, CA, USA, (2003).

[67] J. Prestage, S. Chung, T. Le and L. Lim, In Proc. of the 2005 IEEE IFCS meeting, Vancouver, BC, Canada (2005).

[68] Y. -Y. Jau, H. Partnet, P. D. D. Schwindt, J. D. Prestage, J. R. Kellogg and N. Yu, Appl. Phys. Lett. **101** , 253518 (2012)

[69] P. D. D. Schwindt, R. Olsson, K. Wojciechowski, D. Serkland, T. Statom, H. Partner, G. Biedermann, L. Fang, A. Casias and R. Manginell. In Proc. of the 2003 PTTI meeting, Santa Ana Pueblo, NM, USA (2009)

[70] V. Shah, R. Lutwak, R. Stoner and M. Mescher, In Proc. of the 2012 Frequency Control Symposium (FCS), Baltimore, MD, USA (2012).

[71] F.-X. Esnault, J. Kitching and E. A. Donley, In Proc. of the 2012 Frequency Control Symposium (FCS), Baltimore, MD, USA (2012).

[72] E. N. Ivanov, F.-X. Esnault and E. A. Donley, "Offset phase locking of noisy diode lasers aided by frequency division," Rev. Sci. Instrum. 82, 083110, 2011.

[73] M. Fleischhauer, A. Imamoglu, and J. P. Marangos, "Electromagnetically induced transparency: Optics in Coherent Media", Rev. Mod. Phys. **77,** 633 (2005).

[74] A. Nagel, L. Graf, A. Naumov, E. Mariott, V. Biancalna, D. Meschede and R. Wynands, "Experimental realization of coherent dark-state magnetometers," Europhys. Lett. **44** , 31-36 (1998).

[75] M. Bajcsy, A. S. Zibrov and M. D. Lukin, "Stationary pulses of light in an atomic medium," Nature **426** , 638-641 (2003).

[76] J. Vanier, "Atomic clocks based on coherent population trapping: a review," Appl. Phys. B Lasers Opt., **81** , 421-442 (2005).

[77] V. Shah and J. Kitching, "Advances in atomic, molecular, and optical physics: chapter 2", Elsevier Inc. (2010).

[78] S. Knappe, R. Wynands, J. Kitching, H. G. Robinson and L. Hollberg, J. Opt. Soc. Am. B **18,** 1545 (2001).

[79] J. Vanier and C. Audoin, "The Quantum Physics of Atomic Frequency Standards," (Adam Hilger, Bristol 1989).

[80] W. Happer, Rev. Mod. Phys. **44** , 169 (1972).

[81] G. Pitz, D. Wertepny and G. Perram, Phys. Rev. A **80** , 062718 (2009).

[82] S. Knappe, J. Kitching, L. Hollberg and R. Wynands, Appl. Phys. B **74** , 217 − 222 (2002).

[83] R. Boudot, P. Dziuban, M. Hasegawa, R. K. Chutani, S. Galliou, V. Giordano and C. Gorecki, J. Appl. Phys. **109** , 014912 (2011).

[84] D. A. Steck, "Cesium D Line Data" (1998).

[85] F. Strumia, N. Beverini, A. Moretti and G. Rovera, "Optimization of the buffer gas mixture for optically pumped Cs frequency standard," Proceedings of the 30th Annual Symposium Frequency Control, Atlantic City, NJ, pp. 468−472 (1976).

[86] N. Beverini, F. Strumia and G. Rovera, Opt. Commun. **37** , 394 (1981).

[87] J. Vanier, R. Kunski, N. Cyr, J. Y. Savard and M. Tetu, J. Appl. Phys. **53** , 5387 (1982).

[88] O. Kozlova, S. Guérandel and E. De Clercq, Phys. Rev. A **83** , 062714 (2011).

[89] O. Kozlova, R. Boudot, S. Guérandel and E. De Clercq, "Temperature dependence cancellation of the Cs clock frequency in presence of Ne buffer gas," IEEE Trans. Instr. Meas. **60** , 2262-2266 (2011).

[90] C. W. Beer and R. A. Bernheim, Phys. Rev. A **13** , (1976).

[91] N. Beverini, F. Strumia and G. Rovera, Opt. Commun. **37** , 394 (1981).

[92] K. Dorenburg, M. Gladisch and G. zu Pulitz, Z. Phys. A **289** , 145 (1979).

[93] S. Brandt, A. Nagel, R. Wynands and D. Meschede, Phys. Rev. A **56** , 1063 (1997).

[94] D. Miletic, P. Dziuban, R. Boudot, M. Hasegawa, R. K. Chutani, G. Mileti, V. Giordano and C. Gorecki, Electron. Lett. **46** , 15, 1069 − 1071 (2010).

[95] C. Cohen-Tannoudji and J. Dupont-Roc, Phys. Rev. A, **5** , 968 − 984 (1972).

[96] F. Levi, A. Godone and J. Vanier, IEEE Trans. Ultrason. Ferroelectr. Freq. Control **47** , 466 (2000).

[97] D. Miletic, C. Affolderbach, M. Hasegawa, R. Boudot, C. Gorecki and G. Mileti, Appl. Phys. B, **109** , 89 − 97 (2012)

[98] V. Shah, V. Gerginov, P. D. D. Schwindt, S.Knappe, L.Hollberg and J. Kitching, Appl. Phys. Lett. **89** , 151124 (2006).

[99] B. H. McGuyer, Y. Y. Jau, and W. Happer, Appl. Phys. Lett. **94** , 251110 (2009).

[100] A. Nagel, S. Brandt, D. Meschede and R. Wynands, Europhys. Lett. **48** , 385 (1999).

[101] R. Lutwak, D. Emmons, W. Riley and R. M. Garvey, in Proc of the 34th PTTI, **1** , (2002).

[102] J. Vanier, A. Godone and F. Levi, Phys. Rev. A **58** , 2345-2358 (1998).

[103] T. Zanon, E. de Clercq and E. Arimondo, Ultrahigh-resolution spectroscopy with atomic or molecular dark resonances: Exact steady-state line shapes and asymptotic profiles in the adiabatic pulsed regime. Phys. Rev. A, **84** , 062502 (2011).

[104] M. Stähler, R. Wynands, S. Knappe, et al., Opt. Lett. **27,** , 16, 1472 (2002).

[105] Y. Y. Jau and W. Happer, Phys. Rev. Lett. **99** , 223001 (2007).

[106] Y. Zhang, S. Qu and S. Gu, Opt. Exp. **20** , 6400 (2012).

[107] E. Breschi and A. Weis, In Proc. of the 2012 EFTF meeting, Gothenburg, Sweden (2012).

[108] S. H. Yim, T. H. Youn, and D. Cho, Rev. Sci. Instrum. **79** , 126104 (2008).

[109] P. Yun, B. Tan, W. Deng, and S. Gu, Rev. Sci. Instrum. **82** , 123104 (2011).

[110] P. Yun, B. Tan, W. Deng, J. Yang, and S. Gu, Rev. Sci. Instrum. **83** , 093111 (2012).

[111] A. V. Taichenachev, V. I. Yudin, V. L. Velichanslky, S. V. Kargapoltsev, R. Wynands, J. Kitching and L. Hollberg, JETP Lett. **80** , 477 (2004).

[112] A. V. Taichenachev, V. I. Yudin, V. L. Velichanslky and S. A. Zibrov, JETP Lett. **82** , 398 (2005).

[113] E. E. Mikhailov, T. Horrom, N. Belcher and I. Novikova, J. Opt. Soc. Am. B **27** , 417 (2010).

[114] S. A. Zibrov, I. Novikova, D. F. Phillips, R. L.Walsworth, A. S. Zibrov, V. L. Velichansky, A. V. Taichenachev and V. I. Yudin, Phys. Rev. A **81** , 013833 (2010).

[115] K. Watabe, T. Ikegami, A. Takamizawa, S. Yanagimachi, S. Ohshima and S. Knappe, Appl. Opt. **48** , 1098 (2009).

[116] C. Cohen-Tanoudji, Cours Collège de France, 1991 − 1992, http://www.phys.ens.fr/cours/college-de-france/1991-92/cours4/cours4.pdf.

[117] E. A. Korsunsky and D. V. Kosachiov, Phys. Rev. A **60** , 4996 (1999).

[118] M. B. Gornyi, B. G. Matisov and Y. V. Rozhdestvenskii, Sov. Phys. JETP **68** , 728 (1989).

[119] W. Demtröder, "Laser Spectrocopy : Basic concepts and instrumentation - Third edition", Springer-Verlag ISBN 1439 − 2674, Section 5.4.5 (2002).

[120] R. W. P. Drever, J. L. Hall, F. V. Kowalski, J. Hough, G. M. Ford, A. J. Munely and H. Ward, Appl. Phys. B **31** , 97 − 105 (1983).

[121] A. D. Ludlow, X. Huang, M. Notcutt, T. Zanon-Wilette, S. M. Foremand, M. M. Boyd, S. Blatt and J. Ye, Opt. Lett. **32** , 641 − 643 (2007).

[122] S. A. Webster, M. Oxborrow, S. Pugla, J. Millo and P. Gill, Phys. Rev. A **77** , 033847 (2008).

[123] J. Millo et al., Phys. Rev. A **79** , 053829 (2009).

[124] Y. Y. Jiang et al., Nature Photon. **5** , 158 – 161 (2011).

[125] G. A. Cranch, Opt. Lett. **27** , 1114 – 1116 (2002).

[126] F. Kefelian, H. Jiang, P. Lemonde and G. Santarelli, Opt. Lett. **347** , 914 – 916 (2009).

[127] W. K. Lee, C. Y. Park, J. Mun and D. H. Yu, Rev. Sci. Instr. 82073105 (2011).

[128] G. D. Rovera, G. Santarelli and A. Clairon, Rev. Sci. Instrum. **65** , 5 (1994).

[129] C. Affolderbach and G. Mileti, Optics and Lasers in Engineering **43** , 291−302 (2005).

[130] C. Affolderbach and G. Mileti, Rev. Sci. Instr. **76** , 073108 (2005).

[131] F. J. Vermersch, V. Ligeret, S. Bansropun, M. Lecomte, O. Parillaud, M. Calligaro, M. Krakowski and G. Giuliani IEEE Photon. Tech. Lett. **20** , 13, 1145 – 1147 (2008).

[132] A. Klehr, H. Wenzel, O. Brox, F. Bugge, G. Erbert, T. P. Nguyen and G. Trankle, Opt. Exp. **15** , 18, 11364 – 11369 (2006).

[133] K. G. Libbrecht and J. L. Hall Rev. Sci. Instr. **64** , 8, 2133 – 2135 (1993).

[134] R. Boudot, C. Rocher, N. Bazin, S. Galliou and V. Giordano, Rev. Sci. Instr. **76** , 095110 (2005).

[135] X. Liu and R. Boudot, IEEE Trans. Instr. Meas. **61** , (10), 2852-2855 (2012).

[136] F. Bertinetto, P. Cordiale, G. Galzerano and E. Bava, IEEE Trans. Instr. Meas. **50** , 2, 490 – 492 (2001).

[137] T. Hori, A. Araya, S. Moriwaki and N. Mio, Rev. Sci. Instrum. **78** , 026105 (2007).

[138] http://www.photline.com/product/Modulators/

[139] R. A. Becker and R. C. Williamson, Appl. Phys. Lett. **47** , 1024 (1985).

[140] G. T. Harvey, "The photorefractive effect in directional coupler and Mach-Zehnder LiNbO3 optical modulators at a wavelength of 1.3 μm," Journ. Light. Tech. **6** , 872-876 (1998).

[141] J. Snoody, Y. Li and F. Ravet, Appl. Opt. **469** , 1482 – 1485 (2007).

[142] K. Zhang and Y. X. Zhang, Appl. Mech. and Mat. **71** , 1200 (2011).

[143] D. T. Bui, Meas. Sci. Technol. 22125105 (2011).

[144] G. J. Dick, Proc. Precise Time and Time interval, Redondo Beach, CA, pp 133 – 147 (1987).

[145] B. Onillon, P. Danès, B. Bénazet and O. Llopis, Microwave and Optical Tech. Lett. **49** , 7, 1634 (2007).

[146] C. Audoin, V. Candelier and N. Diamarcq, IEEE Trans. Instrum. Meas., **40** , 2, pp 121 – 125 (1991).

[147] M. Hasegawa, R. K. Chutani, C. Gorecki, R. Boudot, P. Dziuban, V. Giordano, S. Clatot, and L. Mauri, Sens. Actuators, A **167** , 594 (2011).

[148] S. Guérandel, T. Zanon, N. Castagna, F. Dahes, E. De Clercq and A. Clairon, IEEE Trans. Instr. Meas. **56** (2), 383 – 387 (2007).

[149] X. Liu, J. M. Merolla, S. Guérandel, C. Gorecki, E. De Clercq and R. Boudot, Phys. Rev. A **7** , 013416 (2013).

[150] X. Liu, S. Guérandel, J. M. Merolla, E. De Clercq and R. Boudot, "Ramsey spectroscopy of hihg-contrast CPT resoances with push-pull optical pumping in Cs vapor" Opt. Exp. **21** , 12451-12468 (2013)

[151] V. Ménoret, R. Geiger, G. Stern, N. Zahzam, B. Battelier, A. Bresson, A. Landragin and P. Bouyer, Opt. Lett. **36** , 21, 4128 – 4130 (2011).

[152] R. Boudot, X. Liu, P. Abbé, R. Chutani, N. Passilly, S. Galliou, C. Gorecki and V. Giordano, IEEE Trans. Ultrason. Ferroelec. Freq. Contr. **59** , 2584-2587 (2012)

[153] M. Hasegawa, R. K. Chutani, R. Boudot, L. Mauri, C. Gorecki, X. Liu and N. Passilly, J. Micromech. Microeng. **23** , 055022 (2013)

[154] K. Volyanskiy, Y. K. Chembo, L. Larger and E. Rubiola, Journ. Light. Tech. **28** , 18, 2730 – 2735 (2010).

[155] J. Kitching, S. Knappe and L. Hollberg, Appl. Phys. Lett. **81 (3)**, 553-555 (2002).

[156] L. A. Liew, S. Knappe, J. Moreland, H. Robinson, L. Hollberg, and J. Kitching, Appl. Phys. Lett. **84** , 14, 2694 – 2696 (2004).

[157] S. Knappe, V. Gerginov, P. D. D. Schwindt, V. Shah, H. Robinson, L. Hollberg, and J. Kitching, Opt. Lett. **30** , 18, 2351 – 2353 (2005).

[158] V. Gerginov, V. Shah, S. Knappe, L. Hollberg and J. Kitching, Opt. Lett., **31** , 12, 1851 – 1853 (2006)

[159] R. Lutwak, A. Rashed, M. Varghese, G. Tepolt, J. LeBlanc, M. Mescher, D. K. Serkland, K. M. Geib, G. M. Peake and S. Römisch, in Proc. 39th Annu. Precise Time and Time Interval Meeting, 269 – 290 (2007).

[160] S. Knappe, V. Shah, V. Gerginov, A. Brannon, L. Hollberg, and J. Kitching, in Proc. 38th Annu. Precise Time and Time Interval (PTTI) Meeting, 241 – 250 (2008).

[161] S. Knappe, H. Robinson and L. Hollberg, Opt. Exp., **15** , 6293 – 9 (2007).

[162] W. C. Griffith, S. Knappe and J. Kitching, Opt. Exp., **18** , 27167 – 72 (2010).

[163] S. Mack, H. Baumann, U. Gösele, H. Werner and R. Schlögl, J. Electrochem. Soc. **144** , 1106 – 11 (1997).

[164] D. Farkas, K. Hudek, E. Salim, S. Segal, M. Squires and D. Anderson, Appl. Phys. Lett. **96** , 093102 (2010).

[165] S-H. Choa, Microsyst. Technol. **11** , 1187 – 96 (2005).

[166] S. Mack, H. Baumann, U. Gösele, H. Werner and R. Schlögl, J. Electrochem. Soc., **144** , 1106 – 1111 (1997).

[167] SAES, PageWafer specs : http://www.saesgetters.com/

[168] B. J. Lambert and F. W. Tang, Radiat. Phys. Chem. **57** , 349 – 53 (2000).

Abstract

This thesis reports the development of a simple-architecture laser system resonant at 895 nm used for the detection of high-contrast coherent population trapping (CPT) resonances in Cs vapor cells. The laser system combines a distributed feedback-diode (DFB) laser, a pigtailed Mach-Zehnder intensity electro-optic modulator (EOM) driven at 4.596 GHz for the generation of optical sidebands frequency-splitted by 9.192 GHz and a Michelson delay-line system to produce a bichromatic optical field that alternates between right and left circular polarization. This polarization pumping scheme, pioneerly proposed by Happer's group in Princeton on K atoms, allows to pump optically a maximum number of Cs atoms into the 0-0 magnetic field insensitive clock transition. Advanced noise reduction techniques were implemented in order to stabilize the laser power, the optical carrier suppression at the output of the EOM and the DFB laser frequency. Using this system, we demonstrated the detection of CPT resonances with a contrast of 80% in cm-scale Cs vapor cells. This contrast was measured to be increased until a saturation effect with the laser power at the expense of the CPT line broandening. To circumvent this issue, we proposed with a simple setup Ramsey spectroscopy of CPT resonances in vapor cells to combine high-contrast and narrow linewidth of the CPT resonances. In this setup, the EOM is used both for optical sidebands generation and light switch to produce Ramsey interaction. Ramsey fringes of 166 Hz linewidth with a contrast better than 30% were detected with this setup. This laser system will be in a near future devoted to be used for the development of a high-performance CPT-based atomic clock.

Keywords: coherent population trapping (CPT), Cs vapor cells, electro-optic modulator, atomic clock.

Résumé

Cette these reporte le développement d'un système d'architecture simple, resonant à 895 nm, utilisé pour la detection de resonances à piégeage coherent de population (CPT) de fort contraste dans des cellules à vapeur de cesium. Le système laser combine une diode laser DFB, un modulateur électro-optique d'intensité type Mach-Zehnder piloté à 4.596 GHz pour la génération de bandes latérales optiques séparées de 9.192 GHz et un système de type Michelson pour produire à terme un champ optique bichroamatique dont la polarisation est alternativement circulaire gauche et circulaire droite au rythme de la fréquence de Bohr des atomes. Ce schéma de polarisation CPT optimisé, proposé par le groupe de Happer à Princeton en 2004, permet de pomper optiquement un grand nombre d'atomes sur la transition d'horloge entre les sous-niveaux Zeeman 0-0 de l'état fondamental. Des techniques avancées ont été implémentées pour stabiliser la puissance laser, la suppression de porteuse optique en sortie de l'EOM et la fréquence laser. En utilisant ce montage, nous avons démontré la détection de résonances CPT avec un contraste de 80% dans des cellules Cs de dimensions centimétriques. Le contraste augmente avec la puissance laser au dépit d'un élargissement de la résonance CPT. Pour contourner ce problème, nous avons proposé la spectroscopie Ramsey de résonances CPT pour combiner fort contraste et faible largeur de raie. Dans ce montage, l'EOM est utilisé et pour la génération de bandes latérales optiques et comme un obturateur de lumière pour produire l'interaction Ramsey. Des franges de Ramsey de largeur 166 Hz et de contraste supérieur à 30% ont été détectées avec ce système. Ce système laser sera utilisé dans un future proche au sein d'une horloge atomique CPT de haute-performance.

Mots-clés : piégeage cohérent de population (CPT), cellule à vapeur de césium, modulateur électro-optique, horloge atomique.